Tidal Dynamics of Moons with Fluid Layers

From Ice to Lava Worlds

Rovira Navarro, M.

DOI
10.4233/uuid:c6d607fe-11d7-4c14-870e-97d1a9d6e0d5

Publication date
2022

Document Version
Final published version

Citation (APA)
Rovira Navarro, M. (2022). *Tidal Dynamics of Moons with Fluid Layers: From Ice to Lava Worlds*. [Dissertation (TU Delft), Delft University of Technology]. https://doi.org/10.4233/uuid:c6d607fe-11d7-4c14-870e-97d1a9d6e0d5

Tidal Dynamics of Moons with Fluid Layers

From Ice to Lava Worlds

Marc Rovira-Navarro

Tidal Dynamics of Moons with Fluid Layers

From Ice to Lava Worlds

TIDAL DYNAMICS OF MOONS WITH FLUID LAYERS

FROM ICE TO LAVA WORLDS

Proefschrift

ter verkrijging van de graad van doctor
aan de Technische Universiteit Delft,
op gezag van de Rector Magnificus Prof. dr. ir. T.H.J.J. van der Hagen,
voorzitter van het College voor Promoties,
in het openbaar te verdedigen op Dinsdag 27 september 2022 om 15:00 uur

door

Marc ROVIRA-NAVARRO

ingenieur luchtvaart-en ruimtevaart
Technische Universiteit Delft, Delft, Nederland
geboren te Barcelona, Spanje.

Dit proefschrift is goedgekeurd door de promotoren

Samenstelling promotiecommissie bestaat uit:

Rector Magnificus	voorzitter
Prof. dr. L.L.A. Vermeersen	Technische Universiteit Delft, promotor
Dr. ir. W. van der Wal	Technische Universiteit Delft, copromotor

Onafhankelijke leden:

Prof. dr. Breuer	Deutsches Zentrum für Luft- und Raumfahrt , Duitsland
Prof. dr. C. Sotin	Nantes Université, Frankrijk
Prof. dr. D.G. Simons	Technische Universiteit Delft
Dr. K.M. Soderlund	The University of Texas at Austin, Verenigde Staten
Prof. dr. ir. P.N.A.M. Visser	Technische Universiteit Delft, reservelid

Overige leden:

Dr. T. Gerkema	Nederlands Instituut voor Zeeonderzoek

The work presented in this dissertation was financially supported by the User Support Programme Space Research, a program of the Netherlands Organization for Scientific Research, under the project number ALW-GO/16-19.

Keywords: Icy moons, Io, exomoons, tides, thermal-orbital evolution, interiors

Printed by: Ipskamp Printing

Front & Back: Front: Enceladus and Io (center) surrounded by a cut of tidal dissipation in Enceladus' ocean due to internal inertial waves (left) and in Io's partially molten asthenosphere (right). Back: Rossby wave mode excited by the obliquity tide (top) and surface gravity wave mode excited by the eccentricity tide (bottom). Images courtesy of NASA/JPL/University of Arizona (Io) and NASA/JPL (Enceladus).

ISBN 978-94-6421-819-0

An electronic version of this dissertation is available at
http://repository.tudelft.nl/.

3.14159265...
I walked to the horizons of my world
to find a wall where I could lounge
but all there was were deep blue skies
...3589793...
Where do horizons end?
...2384626...

M. Rovira-Navarro

CONTENTS

SUMMARY

In the last fifty years, the space missions Voyager, Galileo, Cassini-Huygens and Juno explored the moons of the outer Solar System and revealed a wide spectrum of worlds. While some of these worlds are barren, others are among the most geologically active of the Solar System. The innermost Jovian moon, Io, showcases spectacular volcanic activity; its three companions, Europa, Ganymede and Callisto, are likely ocean worlds that harbour subsurface oceans beneath their icy crusts. Similarly, the biggest Saturnian moon, Titan, is believed to have a subsurface ocean concealed beneath its icy surface and dense atmosphere. Saturn's collection of smaller icy bodies feature different levels of activity, Enceladus being the most remarkable. Above its limb, water plumes rise more than hundred kilometers spilling its internal ocean into Saturn's E-ring. In Neptune, the captured moon Triton orbits in a peculiar retrograde orbit; its barely cratered surface is similar to that of other ocean worlds and shows signs of cryovolcanic activity. The spectrum of geological activity displayed by the moons of the outer Solar System is thought to be mainly the consequence of tides.

If a moon is in a circular orbit co-planar to its equatorial plane, the planet —as seen from the moon— remains frozen in the sky. Instead, if the moon is in an elongated eccentric orbit, the planet dances. As the moon moves closer and further away from the planet, its apparent size changes and its right ascension librates. This causes the gravitational pull experienced by the moon to change in time, which give rise to eccentricity tides. Coherent gravitational interactions between moons —mean-motion resonances— pump their orbital eccentricity and cause strong eccentricity tides. Moreover, if the moon's orbital plane is inclined with respect to its equator, the planet's declination also changes as the moon orbits, causing the so-called obliquity tides. As a result of eccentricity and obliquity tides, the moons of the outer Solar System are periodically deformed as they orbit their planet. Such deformation is not adiabatic: different dissipative processes within the moon transform the tidal energy into heat, which warms up the interior of the moon and drives its internal engine; a process know as tidal heating.

Traditionally, the study of tides in the moons of the outer Solar System has focused on their solid layers —ice crusts and rocky mantles. When computing the moon's tidal response, the dynamic response of fluid layers has been mostly ignored. However, ocean tides can play a key role in the evolution of planets and moons. Just as the Moon stirs the Earth's oceans and seas, tidal currents can be excited in the internal liquid layers of Solar System satellites. Robert H. Tyler proposed that ocean tides can drive strong currents and lead to intense energy dissipation in ocean worlds and in Io, which could have a molten liquid 'magma ocean' beneath its lithosphere. Since then, several advances have been made in the study of liquid tides; however, our understanding of it is still shallow. In this thesis, we present new advances in the modelling of the tidal dynamics of moons

with fluid layers.

We start by considering the tidal dynamics of subsurface oceans. The investigations of extraterrestrial ocean tides have relied on the equations Pierre-Simon Laplace used to study the tides of Earth's oceans, the so-called Laplace tidal equations. The solutions of the Laplace tidal equations are given by two types of surface waves: surface gravity waves —where gravity acts as the restoring force— and Rossby-Haurwitz waves —where the Coriolis force is the restoring force. Ocean currents and tidal dissipation due to tidal forcing are generally negligible unless the ocean resonates at the tidal frequency. Gravity-wave resonances can be excited by eccentricity tides, however these resonances occur in oceans much thinner than those predicted for icy moons. In contrast, strong Rossby-Haurwitz waves can be excited in thick oceans by the obliquity tide. Rossby-Haurwitz waves can produce tidal dissipation above that resulting from solid tides provided the satellite has a high obliquity; as it is the case of the Neptunian moon Triton.

Previous studies of ocean tides in subsurface oceans have relied on the assumption that the oceans are of constant thickness. However, oceans might be of variable thickness. The most evident example is Enceladus. Gravity and topography data indicates that Enceladus' ocean is not of uniform thickness but varies from ~ 30 km at the equator to ~ 50 km at the south pole. We investigate what are the effect of ocean thickness variations on the response of a subsurface ocean (Chapter 3). We show that the occurrence of gravity waves resonances is controlled by the equatorial ocean thickness. Moreover, we find that ocean thickness variation hinders the excitation of Rossby-Haurwitz waves. This is even more relevant for Triton, as it has been suggested that obliquity ocean tides might be the prevalent heating mechanism maintaining its subsurface ocean. Our results show that this only occurs if the moon's ocean is of nearly constant thickness.

The Laplace tidal equations make use of the shallow water approximation, which is valid if the ocean is thin with respect to the moon's radius. This approximation greatly simplifies the equations involved in computing the tidal response of an ocean; however, this comes at the expense of filtering out internal waves. In Chapter 4, we study tidally excited internal waves in Enceladan and Europan unstratified subsurface oceans. The properties of these waves are notably different from surface waves; upon reflection, instead of keeping their wavelength constant, the wavelength can change. Depending on ocean geometry, this can lead to wave focusing and the formation of internal shear layers. We show that internal shear layers form in Europa's and Enceladus' oceans whose strength (i.e., velocity gradient) depends on the ocean geometry. While currents of few centimeters per second can develop in these internal boundary layers, the integrated tidal dissipation due to inertial waves is small compared to the amount of radiogenic heating for both moons.

In some circumstances both solid and liquid phases can coexist in the same layer of the moon. When this is the case, neither the theory of solid tides nor that of liquid tides alone applies; the complex dynamics of multiphase media should be considered. The presence of a liquid affects how the solid deforms; additionally, the flow of liquid through the solid skeleton (Darcian flow) opens a new avenue for energy dissipation. The inferred low density of Enceladus' core together with evidence of hydrothermal activity suggest that the moon's core consists of a porous solid matrix throughout which ocean water can

circulate. Io's 'magma ocean' is another example of two phases (rock and magma) in one layer.

Tides in multiphase media have received very little attention. Nevertheless, recent work on the topic has suggested that Darcian dissipation in Enceladus' core is behind Enceladus' geological activity. This is particularly relevant, as it is still uncertain where (ice, ocean or rocky core) and how the energy that powers the moon's plumes and prevents its internal ocean from freezing is produced. As discussed above, tides in an unstratified ocean are unlikely to account for the moon's thermal output, and dissipation in the ice shell can only rise to the observed values if the ice shell viscosity is very low. In Chapter 5, we extend the theory of tides for solid viscoelastic self-gravitating bodies to bodies with porous layers and apply it to Enceladus to assess whether tides in its porous core can explain its thermal activity. We show that tides excite Darcian flow in the moon's core but that the ocean prevents high velocities from being attained, making viscous dissipation in the rocky matrix the leading source of energy dissipation in the core. Tidal dissipation in the core can only rise to values comparable to Cassini observations if the core has a very low viscosity compared to that of silicates. Previous work has suggested that this might be the case if Enceladus' core resembles an unconsolidated rubble pile core. We propose that a future Enceladan mission could test this hypothesis by measuring the phase lags in the tidal-induced gravitational field and surface displacements.

While the main body of this thesis focuses on the moons of the Solar System, in the last part (Chapter 6), we consider the role that tidal heating might have in exomoons. With more than four thousands exoplanets discovered so far, it is not bold to assume that some of them harbour exomoons. Their detection is fraught with technical challenges. Different detection methods have been proposed, some specifically targeting tidally heated exomoons. Extreme tidal heating can increase a moon's surface temperature, rendering it observable in the infrared. Additionally, extensive volcanism leaves a fingerprint on the spectrum of the system that could be detected in transits.

To asses to which degree these two factors can make an exomoon observable, it is necessary to consider its thermal and orbital evolution. We identify thermal equilibrium states attained for moons of sizes ranging from Io- to Earth-sized with different orbits. Large moons in high eccentricity, low-period orbits experience high levels of tidal dissipation. An Earth-sized moon in Io's orbit would see its surface temperature increased to around 300 K —at the verge of the James Webb Space Telescope sensitivity for the closest stars. However, such amount of tidal dissipation comes at the expense of quickly circularizing the moon's orbit. In an isolated moon-planet system, high eccentricity orbits cannot be sustained for very long. Alternatively, in systems with multiple moons, mean motion resonances —akin to those responsible for the eccentricity of the moons of the outer Solar System— can sustain a high orbital eccentricity for a long time. We show that the inner moon of a pair of Mars-sized exomoons in a mean-motion resonance can present tidally boosted temperatures for millions of years before orbital migration reduces their activity. Furthermore, we show that the moon can remain tidally active for billions of years and feature Io-like levels of volcanism, thus giving ample opportunity for the formation of a secondary atmosphere that might be detected in transits.

In this thesis, new advances have been made on the modeling front; however, several

questions remain open. In Chapter 7, we revise the assumptions behind the models we use and underline how future space missions will inform modellers studying the tidal dynamics of moons with fluid layers. New missions to the outer planets like JUICE and Europa Clipper will provide a wealth of new data that will help constraining the bathymetry and composition of subsurface oceans, and thus allow to build more detailed ocean dynamics models than those used in this thesis. Furthermore, these missions might return the first remote measurements of extraterrestrial ocean currents against which the output of extraterrestrial ocean tidal models can be compared. We argue that a future Enceladan mission will bring similar benefits and resolve the outstanding question about how and where energy is dissipated within the moon. A dedicated Io mission would shed new light into the workings of moons experiencing high amounts of tidal heating, and particularly help understanding the unexplored regime that lays in-between solid and liquid tides. In the meantime, the James Webb Space Telescope (JWST) is on its way to L2. The discovery of a super-Io by the JWST would add a new member to the family of tidally active worlds, revealing what occurs in extreme instances of tidal heating, and bringing new insight into the interior of gas giants and the architecture of gas giant systems. We have good reason to believe that the future holds great promise for the topics explored in this thesis.

SAMENVATTING

De afgelopen vijftig jaar hebben de ruimtemissies Voyager, Galileo, Cassini-Huygens en Juno de manen van andere planeten in ons zonnestelsel verkend. Deze missies hebben een grote verscheidenheid aan manen aangetroffen. Sommige zijn ruig en onherbergzaam en andere behoren tot de geologisch meest actieve lichamen van ons zonnestelsel. De binnenste Joviaanse maan, Io, vertoont een spectaculaire vulkanische activiteit; de drie andere Joviaanse manen, Europa, Ganymede en Callisto, zijn werelden die waarschijnlijk een ondergrondse oceaan herbergen onder de ijzige korst. Verder herbergt de grootste Saturniaanse maan, Titan, ook een ondergrondse oceaan en heeft het een dichte atmosfeer. De verzameling kleinere ijzige manen van Saturnus verschillen in hoe actief deze zijn. Van deze kleinere manen is Enceladus de meest opmerkelijke. De waterpluimen van Enceladus komen meer dan 100 kilometer boven het oppervlak en daarmee brengen ze water van de oceaan naar de E-ring van Saturnus. Binnen Neptunus zit de gevangen maan Triton in een bijzondere retrograde baan. Het oppervlak van Triton bevat nauwelijks kraters, lijkt op dat van andere oceaanwerelden en laat tekenen zien van cryovulkanische activiteit. De grote verscheidenheid aan geologische activiteit van de manen wordt verondersteld te zijn veroorzaakt door getijden.

Wanneer een maan in een circulaire baan zit die coplanair is met zijn equatoriale vlak dan staat de planeet – gezien vanaf de maan – stil aan de hemel. Als de maan zich daarentegen in een langwerpige excentrische baan bevindt dan 'danst' de planeet. Wanneer de maan dichterbij de planeet komt en vervolgens weer verder weg beweegt dan verandert zijn ogenschijnlijke grootte en varieert zijn rechte klimming. Dit zorgt ervoor dat de zwaartekrachtsaantrekking van de maan verandert met de tijd waardoor de excentriciteitgetijden ontstaan. Zwaartekrachtsinteracties tussen manen – baanresonanties – verhogen de excentriciteit van de baan en kunnen zorgen voor sterke excentriciteitgetijden. Door getijden, veroorzaakt door de excentriciteit en door de schuine stand van de as, zijn de buitenste manen van ons zonnestelsel periodisch vervormt wanneer ze om hun planeet bewegen. Deze vervorming is niet adiabatisch: verschillende processen binnen de maan zetten de getijdenenergie om in warmte, waardoor het binnenste van de maan in temperatuur toeneemt en de 'motor' in het binnenste van de maan wordt aangedreven; dit proces staat bekent als getijdenverhitting.

Traditioneel gezien heeft het onderzoek naar getijden van de buitenste manen in ons zonnestelsel zich altijd beziggehouden met de vaste lagen – de ijzige korst en de rotsachtige mantels – van deze manen. Bij het berekenen van de reactie van de maan op de getijden wordt de dynamische reactie van de vloeibare lagen meestal niet meegenomen. De oceaangetijden kunnen echter een belangrijke rol spelen in de evolutie van planeten en manen. Op dezelfde manier als dat de Maan de oceanen en de zeeën van de Aarde aanstuurt, kunnen getijdenstromingen aangewakkerd worden in de binnenste vloeibare

lagen van manen in het zonnestelsel. Robert H. Tyler suggereerde dat oceaangetijden sterke stromingen kunnen aandrijven en dat deze kunnen leiden tot intens energieverlies in oceaanplaneten en in Io, waarin zich een gesmolten vloeibare magmaoceaan zou kunnen bevinden onder de lithosfeer. Vanaf dat moment zijn er verschillende vorderingen gemaakt wat betreft het bestuderen van vloeibare getijden. Echter,ons begrip hiervan is nog laag. In deze scriptie presenteren we nieuwe vorderingen in het modelleren van de getijdendynamiek van manen met vloeibare lagen.

We beginnen deze scriptie met het beschouwen van de getijden dynamiek van werelden met ondergrondse oceanen. De onderzoeken van buitenaardse oceaangetijden zijn gebouwd op de vergelijken die Pierre-Simon Laplace gebruikt heeft tijdens zijn onderzoek naar de getijden van de oceanen op Aarde. Dit zijn de Laplace vergelijkingen voor getijden. De oplossingen van deze vergelijkingen kunnen beschreven worden door twee soorten oppervlaktegolven: zwaartekrachtsgolven aan het oppervlak – hier werkt de zwaartekracht als een terugwerkende kracht – en de Rossby-Haurwitz golven – waar de Coriolis kracht herstellend werkt. Getijdendissipatie en oceaanstromingen veroorzaakt door de getijden zijn over het algemeen verwaarloosbaar klein, tenzij de oceaan resoneert met de frequentie van de getijden. Resonanties van zwaartekrachtsgolven kunnen aangedreven worden door de excentriciteitgetijden. Deze resonanties komen echter alleen voor in oceaan die vele malen minder diep zijn dan de oceanen die we verwachten te vinden in ijzige manen. Daarentegen kunnen sterke Rossby-Haurwitz golven veroorzaakt worden in diepere oceanen door getijden die veroorzaakt worden door de schuine stand van de as van de maan. Rossby-Haurwitz golven kunnen meer getijdendissipatie produceren dan getijden in vaste lagen wanneer het lichaam een hoge scheefstand heeft, zoals het geval is bij de Neptuniaanse maan Triton.

Eerdere studies naar getijden in ondergrondse oceanen zijn afhankelijk van de aanname dat de oceanen een constante diepte hebben. Dit hoeft echter niet het geval te zijn. Het meest duidelijke voorbeeld is de oceaan van Enceladus. Metingen van de zwaartekracht en topografie laten zien dat de diepte van de oceaan van Enceladus niet constant is, maar varieert van 30 km op de evenaar tot 50 km op de zuidpool. We onderzoeken wat het effect is van een variabele oceaandiepte op de reactie van een ondergrondse oceaan (Hoofdstuk 3). We laten zien dat het voorkomen van resonanties met de zwaartekrachtsgolven bepaald wordt door de diepte van de oceaan op de evenaar. Daarnaast vinden we dat variaties in de dikte van de oceaan het ontstaan van de Rossby-Haurwitz golven kan verhinderen. Dit is relevant voor Triton, aangezien gesuggereerd wordt dat de oceaangetijden door de scheefstand van de as als het dominante verhittingsmechanisme geldt voor het in stand houden van de ondergrondse oceaan. Onze resultaten laten zien dat dit alleen het geval is als de oceaan van de maan een nagenoeg constante diepte heeft.

De getijdenvergelijkingen van Laplace maken gebruik van de ondiep water benadering, die alleen geldig is als de oceaan ondiep is in vergelijking met de straal van de maan. Deze benadering vereenvoudigt de vergelijkingen voor het berekenen van de getijden binnen een oceaan enorm. Door deze benadering filteren we echter ook de interne golven eruit. In Hoofdstuk 4 bestuderen we interne golven veroorzaakt door getijden in ongelaagde ondergrondse oceanen, met focus opEuropa en Enceladus. De eigenschap-

pen van deze interne golven zijn aanzienlijk anders dan die van oppervlaktegolven; wanneer de interne golven reflecteren kan de golflengte veranderen, in plaats van dat deze constant blijft. Afhankelijk van de geometrie van de oceaan kan dit leiden tot het focusseren van een golf en het formeren van interne afschuiflagen. We laten zien dat interne afschuiflagen gevormd worden in de oceanen van Europa en Enceladus waarvan de grootte van de kracht (i.e., de gradiënt van de snelheid) afhankelijk is van de geometrie van de oceaan. Ondanks dat stromingen van enkele centimeters per seconde zich kunnen ontwikkelen in deze interne grenslagen is de totale hoeveelheid getijdendissipatie door interne golven klein in verhouding tot de hoeveelheid radiogene verhitting voor beide manen.

In sommige gevallen kunnen zowel een vaste als een vloeibare fase naast elkaar bestaan in dezelfde laag van een maan. Wanneer dit het geval is kunnen de theorieën voor vaste en vloeibare getijden niet meer toegepast worden. De complexe dynamica van meerfase media moet hiervoor beschouwd worden. De aanwezigheid van een vloeistof beïnvloedt namelijk hoe de vaste laag deformeert. Daarbovenop komt dat het stromen van de vloeistof door de vaster matrix (Darcische stroom) een extra manier is om energie te dissiperen. De lage dichtheid van de kern van Enceladus suggereert samen met het bewijs voor hydrothermische activiteit dat de kern van de maan bestaat uit een poreuze vaste matrix waardoor het oceaanwater kan stromen. De magma-oceaan van Io is een ander voorbeeld van twee fasen (gesteente en magma) in één laag.

Getijden in meerfase media hebben tot nu toe weinig aandacht gekregen. Desondanks suggereert recent werk dat Darcische dissipatie in de kern van Enceladus de reden kan zijn voor de geologische activiteit van de maan. Dit is relevant, aangezien het nog steeds onzeker is wáár (in het ijs, in de oceaan of in de rotsachtige kern) en hoe de energie wordt gegenereerd die zorgt voor het aandrijven van de pluimen van de maan en voor het voorkómen van bevriezing van de interne oceaan. Zoals hierboven al genoemd, zijn getijden in ongelaagde oceanen waarschijnlijk niet de reden voor de thermische output van de maan. Bovendien kan dissipatie in de ijsschil alleen de geobserveerde waarden bereiken wanneer de viscositeit van het ijs erg laag is. In Hoofdstuk 5 breiden we de theorie voor getijden in vaste, viscoelastische, zelf-aantrekkende lichamen uit naar lichamen met poreuze lagen. Deze nieuwe theorie passen we toe op Enceladus om te beoordelen of getijden in een poreuze kern de thermische activiteit zouden kunnen verklaren. We laten zien dat getijden een Darcische stroom veroorzaken in de kern van de maan, maar dat de oceaan voorkómt dat hoge snelheden kunnen worden bereikt. Hierdoor wordt de viskeuze dissipatie in het rotsachtige skelet de voornaamste bron van energiedissipatie in de kern. Getijdendissipatie in de kern kan waardes vergelijkbaar met die van Cassini's observaties bereiken als de kern een erg lage viscositeit heeft in vergelijking tot die van silicaten. Eerder werk suggereert dat dit het geval kan zijn wanneer de kern van Enceladus veel weg heeft van een niet-geconsolideerde 'rubble pile' (een collectie losse stenen die samengehouden worden door hun eigen zwakke zwaartekracht). We stellen ons voor dat een toekomstige missie naar Enceladus zou kunnen testen of deze hypothese waar is door het meten van de fasevertraging in het zwaartekrachtsveld veroorzaakt door getijden en door het meten van de verplaatsingen op het oppervlakte.

Het grootste deel van deze scriptie gaat over de manen in ons zonnestelsel, maar in

het laatste onderdeel (Hoofdstuk 6) bestuderen we de rol die getijdenverhitting kan hebben in exomanen. Op dit moment zijn er meer dan vierduizend exoplaneten ontdekt en het is aannemelijk dat een aantal hiervan exomanen hebben. De detectie van deze exomanen zit vol technische uitdagingen. Verschillende detectiemethodes zijn voorgesteld, enkele hiervan specifiek voor exomanen met getijdenverhitting. Extreme getijdenverhitting kan namelijk de oppervlaktetemperatuur van een maan doen toenemen, waardoor deze waar te nemen is in het infrarood. Daarnaast laat vulkanisme een voetprint achter die gedetecteerd zou kunnen worden bij astronomische transities.

Om te beoordelen in welke mate deze twee factoren een exomaan waarneembaar maken, is het noodzakelijk om de thermische evolutie en de baanevolutie te beschouwen. We identificeren toestanden van thermisch evenwicht voor manen met een grootte variërend van Io tot Aarde in verschillende baantrajecten. Veel getijdendissipatie vindt plaats in grote manen die in een baan zitten met een hoge excentriciteit en een lage periode. Wanneer een maan ter grootte van de Aarde in de baan van Io zou zitten, dan kan de oppervlaktetemperatuur stijgen tot ongeveer 300 K – op de grens van wat de James Webb Space Telescoop aankan wat betreft gevoeligheid voor de dichtstbijzijnde sterren. Echter zorgt de grote hoeveelheid getijdendissipatie ervoor dat de baan snel circulair wordt. In een geïsoleerd maan-planeet systeem kunnen banen met een hoge excentriciteit niet lang bestaan. Als alternatief bekijken we systemen met meerdere manen, met daarin baanresonanties vergelijkbaar met die verantwoordelijk voor de excentriciteit van de manen in het buitenste deel van het zonnestelsel. Hierdoor kunnen de banen een hoge excentriciteit hebben gedurende een langere tijd. Bij een maan-planeet systeem met een paar manen ter grootte van Mars kan de binnenste maan in een baanresonantie zorgen dat de aanwezigheid van hogere temperaturen door getijden vastgehouden kan worden voor miljoenen jaren, voordat de banen migreren en de activiteit minder wordt. Verder laten we zien dat in dit geval de getijden van de maan actief kunnen blijven gedurende miljarden jaren met een vulkanische activiteit vergelijkbaar met Io. Dit alles biedt genoeg mogelijkheden voor het ontstaan van een tweede atmosfeer die gedetecteerd zou kunnen worden tijdens astronomische transities.

In deze scriptie zijn nieuwe vorderingen gemaakt op het modelleervlak. Enkele vragen zijn echter nog niet beantwoord. In Hoofdstuk 7 kijken we opnieuw naar de aannames achter de modellen en benadrukken we hoe toekomstige ruimtemissies modelleurs zullen informeren over de getijdendynamica van manen met vloeibare lagen. Nieuwe missies naar planeten aan de rand van ons zonnestelsel, zoals JUICE en Europa Clipper, zullen zorgen voor een grote hoeveelheid nieuwe gegevens. Deze gegevens gaan ons helpen om de bathymetrie en de compositie van ondergrondse manen beter te begrijpen. Hiermee kan een gedetailleerder model worden gemaakt van de oceaandynamica. Verder zou het kunnen dat deze missies de eerste metingen op afstand voor buitenaardse oceaanstromingen op gaan leveren waartegen de output van modellen vergeleken kan worden. We betogen dat een toekomstige missie naar Enceladus vergelijkbare voordelen met zich mee zal brengen, en ervoor kan zorgen dat de vraag beantwoord kan worden over waar en hoe de dissipatie van energie binnen de maan plaatsvindt. Een |missie gewijd aan Io zou nieuw licht kunnen werpen op de werking van manen met een hoge getijdenverhitting. Dit helpt specifiek voor het begrijpen van het onontdekte regime dat

ligt tussen vaste en vloeibare getijden. In de tussentijd is de James Webb Space Telescoop (JWST) op weg naar L2. De ontdekking van een super-Io door de JWST kan een nieuwe toevoeging betekenen aan de familie van werelden die actieve getijden hebben. Dit kan onthullen wat er gebeurt in extreme gevallen van getijdenverhitting en kan ook nieuwe inzichten brengen over het binnenste van gasreuzen en de architectuur van de systemen van gasreuzen. We hebben goede redenen om aan te nemen dat de toekomst veel goeds belooft voor de besproken onderwerpen van deze scriptie.

1

INTRODUCTION

If we're stuck in one world, we're limited to a single case; we don't know what else is possible[...] By contrast, when we explore other worlds, what once seemed the only way a planet could turn to be turns out to be somewhere in the middle range of a vast spectrum of possibilities.

—Carl Sagan, *Pale Blue Dot*

Point your backyard telescope towards Jupiter and you will have a similar —yet improved— view of what Galileo Galilei and Simon Marius had when they looked through their telescopes in the early 17th century. Floating around the mighty planet, four bright dots. Repeat the observation every night and you will see how the dots gently move around Jupiter. Named after Zeus' lovers, the Galilean moons —Io, Europa, Ganymede and Callisto— dance to the beat of gravity.

If you are lucky, on the same night you might also get the chance to point your telescope towards Saturn. The rings will surely catch your attention, but look closer and you may be able to spot some bright dots around it. Titan will be the most evident but Rhea, Tethys, Dione, Enceladus, Iapetus and Mimas might also be visible.

Since the discovery of the Jovian and Saturnian moons, some of the most prominent astronomers and mathematicians have tried to understand the music of the moons' motions. Today, thanks to space probes and the improvement of ground-based and space-borne telescopes, these bright dots have turned to worlds. Io's volcanic lava lakes, Titan's hydrocarbon lakes and Europa's and Enceladus' subsurface oceans are among the most interesting views in the Solar System (see Figure 1.1). What do these geologically active moons have in common? They are shaped by tides.

The geological activity of a body depends on how much energy is produced within

it. If we consider two bodies of different sizes, we can expect one producing a higher amount of heat per square meter to be more active. Earth's internal energy is powered by primordial heat still being released from its formation and radiogenic heat produced by the decay of radioactive isotopes. For bodies of same age, the heat flux resulting from these two sources is roughly proportional to the body's radius; consequently, we could expect the comparatively smaller moons of the gas giants to be geologically inert. Surprisingly, they are not. Just as tidal waves raised by the Moon and the Sun wash the shores of our planet, the gravitational attraction of gas giants raise tides in their moons. Because the moons are viscous, part of the tidal energy is converted into heat, a process known as tidal heating.

On Earth, tidal heating is relatively small compared with the two other heat sources, but in other bodies tidal heating can be dominant and drive vigorous geological activity. The most prominent example is the Jovian moon Io, where tidal heating results in an average surface heat flux more than 20 times higher than that of Earth that manifests as widespread volcanism. In the icy moons Enceladus and Europa, tidal heating partially melts their ice-cover forming subsurface oceans, habitable oases outside of the traditional habitable zone. Tidal heating modulates the geological activity of tidally active moons and results in a spectrum of tidally active worlds.

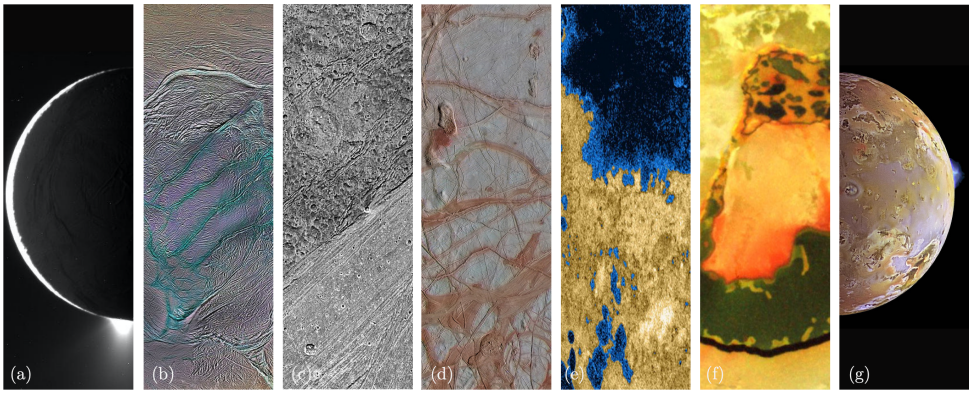

Figure 1.1 A glimpse of some tidally active moons of the outer Solar System. Enceladus' limb with a plume rising from its cracked South Polar Terrain (a); ridges crisscrossing the icy surfaces of Enceladus (b), Ganymede (c) and Europa (d); Titan's hydrocarbon lakes as seen by Cassini's radar (e); a magma-filled patera on Io's surface (f) and volcano erupting over Pillan Patera (g). Images courtesy of NASA

1.1. A SPECTRUM OF TIDALLY ACTIVE WORLDS

We got our first close look of the outer Solar System moons thanks to Voyager 1 and Voyager 2. The Voyager mission was designed to exploit a very rare opportunity to visit the gas and ice giants in one go, an opportunity that will not take place in the next hundred years. Voyager 1 was put in a course designed to study up close the Jovian moon Io and

Saturnian moon Titan, but incompatible with a visit to Uranus and Neptune. Voyager 2's trajectory, on the other hand, was planned so that it could visit Uranus and Neptune after flying through the Jovian and Saturnian system.

The Voyager missions remains one —if not the most— of the most successful planetary exploration missions. It revealed a rich spectrum of worlds ranging from volcanic Io to icy Triton, redefining our understanding of the outer Solar System. Subsequent missions such as Galileo and Cassini-Huygens, together with remote observations made with ground and space telescopes, allowed to unveil more details of these fascinating worlds. In what follows, we will visit these diverse bodies and concisely review their main features, placing special emphasis in what we know about their interiors.

THE JOVIAN SYSTEM

Among the most important discoveries made by the Voyager missions was the first detection of active extraterrestrial volcanism. When navigation engineer L. A. Morabito, in an effort to improve the satellite's ephemeris, was examining images of Io taken by the camera onboard Voyager on 8 March 1979, she was surprised to see a strange bright anomaly close to Io's limb. After ruling out different explanations for the origin of the anomaly (a previously unknown Jovian satellite, a defect in Voyager's camera), Voyager's science team confirmed the first detection of active extraterrestrial volcanism (*Morabito et al.*, 1979)[1]. Remarkably, the discovery was made just a few days after Peale, Cassen and Reynolds published a paper predicting tidally driven volcanism in Io (*Peale et al.*, 1979). Since then, Io's spatially and temporally changing volcanic landscape has been monitored by different space missions, and ground-based and orbital telescopes (e.g., *de Pater et al.*, 2004; *de Pater et al.*, 2020; *Lopes and Spencer.*, 2007; *Mura et al.*, 2020; *Spencer et al.*, 1997, 2007).

Io's volcanism was not the only surprise awaiting Voyager. Images of Europa taken by Voyager 1 (*Smith et al.*, 1979a) and by Voyager 2 (*Smith et al.*, 1979b) during a closer encounter revealed a surprisingly young surface with fewer craters than Ganymede and Callisto, and crisscrossed by a complex network of cracks and ridges. The same group that predicted tidally driven volcanism in Io proposed that the same mechanism was behind Europa's geological activity and that tides could even maintain a subsurface ocean there (*Cassen et al.*, 1979). At more than five astronomical units from the Sun, Europa's icy surface has a mean temperature of 102 K and pressure of just about 0.1 μPa, making it impossible for liquid water to exist at its surface. However, radiogenic and tidal heat produced within the moon can prevent a subsurface ocean beneath its ice shell from freezing.

The geological activity of Io and Europa is linked with their peculiar orbits. The orbits of the three innermost Galilean satellites are tightly related; every time Ganymede completes one orbit, Europa completes two and Io four, a configuration known as the Laplace resonance in honor of Pierre-Simon Laplace, who studied the resonance's long-term stability. Because of this orbital configuration, the moons mutually exert a coherent periodic gravitational perturbation to each other that distorts their orbits. In particular,

[1] A personal account of the discovery by L.A. Morabito can be read in *Morabito* (2012)

the orbits of the moons are more elongated than they would be if they were not in this orbital configuration.

A moon in an elongated orbit experiences strong tides. As it moves from pericenter to apocenter, the strength of the planet's gravitational pull changes. Consequently, the moon is periodically stretched and compressed. This process is not adiabatic; friction within the moon results in energy dissipation in the form of heat that can power geological activity. Apart from this, tides have an important effect on the moon's orbit. Energy dissipation within the moon comes at the expense of losing orbital energy and causes the moon's orbit to shrink and circularize. Similarly, tides raised by the moons on their planet deform the planet. This alters the gravitational field of the planet and consequently affects the moon's orbit causing a slow drift in the orbital size. The intricate connection between interior and orbit renders precise information of the satellites' ephemerides extremely useful in constraining their interior properties.

The discovery of active geology in Io and Europa evidenced these processes and demonstrated how tidal heating in Io drives the evolution of the Laplace resonance (e.g., *Yoder*, 1979). In the years after Voyager's visit to the Jovian system, advances in the understanding of the orbital dynamics and the interior dynamics of the Galilean satellites were made. *Segatz et al.* (1988) showed that tidal heating affects the interior structure and dynamics of Io, controlling the location of its volcanoes; and *Yoder and Peale* (1981) and *Ojakangas and Stevenson* (1986) explored how interior and orbital evolution are linked. Tests of these models had to await for a return to the Jovian system.

In 1995, the Galileo spacecraft arrived at the Jovian system. In contrast to the Voyager mission, which only flew by Jupiter, Galileo orbited Jupiter during eight years during which it flew by the Galilean moons and returned a wealth of data. Among this data is the radio tracking of the spacecraft, which can be used to obtain precise ephemeris of the spacecraft and details of the moons' gravity fields. The deviation of the gravity field of a moon compared with that of a perfectly spherical body can be used to obtain the moon's moment of inertia (*Murray and Dermott*, 2000, Chapter 4), which holds important clues about how mass is distributed within the interior of the moon[2].

Using the moment of inertia and average density of the satellites (Table 1.1) (non-unique) models of the interior of the satellites can be obtained. For Io, the data is consistent with a 500 to 900 km metallic Fe-FeS core overlaid by a rocky mantle (*Anderson et al.*, 2001). For the icy satellites, the interior structure consists of possibly a metallic core, a silicate mantle and an H_2O layer. The decrease in average density of the moons with distance to Jupiter indicates that the water/rock mass ratio changes from 5% for Europa to roughly 50% for Callisto (*Soderlund et al.*, 2020). Callisto's highest moment of inertia indicates that it is the least differentiated of the Jovian icy moons. The H_2O compositional gradient has implications for the interior structure of the satellites. Because of their thicker water envelopes, pressures exceeding those required for the crystallization of high pressure ices ($\sim$ 210 MPa) are attained inside Ganymede and Callisto. Apart from the common Ice I, higher pressure ices with different crystal structure (Ice III, Ice V and Ice VI) are expected in these two moons.

[2] The moment of inertia for a sphere of uniform density is $I = \frac{2}{5}MR^2$, a lower moment of inertia suggests a body whose density increases with depth.

While the average density and moment of inertia can be used to determine how the moon's mass is partitioned between rock and water, these two observations hold little clue about whether the water layer is completely frozen or partially molten. Theoretical models based on the thermal budget of the moons can be used to infer the existence of a subsurface ocean (*Cassen et al.*, 1979); however, such a claim becomes stronger when supported by observational evidence. Galileo's magnetometer was key to providing this evidence. The tilt of Jupiter's magnetic dipole results in a synodic variation of the magnetic field at the moons' positions. If a conductor (e.g., a subsurface water ocean, a molten magma layer) is present within the moon, these variations induce a magnetic field. Galileo's magnetometer measured the spatially and temporally varying magnetic field around the Galilean moons and provided evidence for the existence of a subsurface ocean in Europa (*Khurana et al.*, 1998; *Kivelson et al.*, 2000). For Ganymede and Callisto the magnetometer data was less conclusive; magnetometer data (*Kivelson et al.*, 2002) together with aurora observations (*Saur et al.*, 2015) supports the existence of a subsurface ocean in Ganymede, for Callisto the measured magnetic field (*Khurana et al.*, 1998) can also be caused by the ionosphere (*Hartkorn and Saur*, 2017).

An Europan subsurface ocean is also consistent with geological observations (*Pappalardo et al.*, 1999). The high resolution imagery returned by Galileo revealed tectonic features that include mobile blocks of ice known as chaos terrain, ridges and cycloids (Figure 1.1). These features have been interpreted as being the result of tidal deformations of an Europan floating ice shell (e.g., *Carr et al.*, 1998; *Greenberg et al.*, 1998; *Hoppa et al.*, 1999).

Magnetic observations were also used to probe Io's interior. *Khurana et al.* (2011) suggested that variations of the magnetic field around Io are evidence of a partially molten magma ocean; however, this claim has been challenged (*Blöcker et al.*, 2018; *Roth et al.*, 2017). Current models of Io's interior range from an almost melt-depleted mantle to a fully molten magma ocean (see *Steinke*, 2021, Chapter 1 for a comprehensive overview). These models have different merits when compared to observations such as the type of volcanism (*McEwen et al.*, 1998), distribution of volcanoes (e.g., *Hamilton et al.*, 2013; *Steinke et al.*, 2020a), or the height of Io's mountains (*Jaeger et al.*, 2003) (see *Lopes and Spencer.* (2007) for a review). A partially-molten Io provides an efficient way to transport the tidal heat produced inside the moon. *Moore* (2001) proposed that Io's tidal heat is transported by the advection of melt, a mechanism that might be important for the early evolution of planets including Earth (*Moore*, 2003), making Io an archetype to study the early evolution of terrestrial planets and moons.

THE SATURNIAN SYSTEM

The Saturnian system is markedly different from the Jovian system. While almost all the mass of the Jovian moon system ($\sim 99.997\%$) is split between the four Galilean moons, Titan makes roughly 95% of Saturn's moons' mass. The remaining percentage corresponds to a collection of smaller icy satellites, the most massive being —ordered by proximity to Saturn— Mimas, Enceladus, Tethys, Dione, Rhea and Iapetus. Voyager 1 and 2 showed that these icy satellites are remarkably diverse (*Smith et al.*, 1981, 1982) (see *Rothery* (1999) for a pre-Cassini and *Castillo-Rogez et al.* (2018) for a post-Cassini

overview).

Images of Saturn's icy moons returned by Voyager showed surfaces with different crater densities. Mimas, Rhea and Iapetus are heavily cratered and show little sign of recent activity, because of this they have been labelled as dead bodies. Tethys and Dione, on the other hand, show resurfacing features evidencing they have been active after the Big Bombardment Era (e.g., *Czechowski*, 2006). But most surprising of all is the tiny moon Enceladus.

Enceladus presents distinct types of terrains. The oldest cratered terrains have crater densities comparable to the other icy moons, but the moon has also heavily tectonized regions almost free of impact craters (*Crow-Willard and Pappalardo*, 2015; *Porco et al.*, 2006; *Smith et al.*, 1982). The low crater density implies that the moon is or has very recently been active. The geological activity of Enceladus was quickly associated to tides. Enceladus is in an orbital resonance with Dione, because of this *Yoder* (1979) already anticipated that Voyager might observe a very active world with a young surface. *Terrile and Cook* (1981) went one step further and postulated that tidally driven water eruptions could be the source of Saturn's E-ring, whose densest region happens to coincide with Enceladus' location. The confirmation of this hypothesis had to wait for two decades.

On 1 July 2004, Cassini-Huygens entered orbit around Saturn. For almost 13 years, the spacecraft studied the planet, its rings and moons. Given the observations of Voyager, one of the most anticipated parts of the mission was a series of close flybys of Enceladus. Between February and July 2005, Cassini performed three flybys of the moon (*Porco et al.*, 2006) that demonstrated that Enceladus has a tenuous atmosphere around it —denser in the South Pole. High resolution images of the region taken with the Imaging Science Subsystem (ISS) showed that the South Polar Terrain (SPT) is barely cratered but carved by tectonic features, the most prominent being ~ 100 km long fractures nicknamed "Tiger Stripes" (Figure 1.1b), and the Composite Infrared Spectrometer (CIRS) detected high thermal emissions emanating from the region. But most striking of all were the images returned by the ISS that showed water plumes emanating from Enceladus' SPT.

Two possible origins of Enceladus' water plumes were considered: melt pockets within the ice shell and a subsurface ocean. Contrary to Jupiter, Saturn's magnetic field is not tilted, making it much more difficult to sample the interior of Enceladus using magnetic field measurements. The answer had to come from another instrument onboard of Cassini, the Cosmic Dust Analyser (CDA). The detection of salt grains and silicate particles in the material ejected by the plumes indicates that the plumes originate from a subsurface ocean in contact with Enceladus' silicate core (*Hsu et al.*, 2015; *Postberg et al.*, 2009, 2011). At first, the subsurface ocean was postulated to be restricted to the SPT, where most of the geological activity is located (*Iess et al.*, 2014), but later work proved a global ocean to be also consistent with observations (*McKinnon*, 2015). To test this hypothesis, *Thomas et al.* (2016) measured the libration (periodic changes in the spin rate) of Enceladus' ice shell by tracking the motion of the moon's surface craters —an ice shell pinned at the core would librate less than one decoupled from it— and demonstrated that the subsurface ocean is global, albeit not necessarily of constant thickness.

More recently, gravity, libration and topography data have been combined to constrain the geometry of Enceladus' ice shell. This data shows that Enceladus' ocean and ice shell are on average ~ 40 and ~ 20 km thick, respectively. The ice shell thickness varies from 5 km at the south pole to 35 km at the equator (*Beuthe et al.*, 2016; *Čadek et al.*, 2016). The core density, 2.4 $\mathrm{g\,cm^{-3}}$, is low compared to that of the minerals expected to form the bulk of the core, 3–4 $\mathrm{g\,cm^{-3}}$, suggesting the core could be porous (e.g., *Choblet et al.*, 2017). Evidence of hydrothermal activity supports this hypothesis (*Hsu et al.*, 2015; *Matson et al.*, 2007; *Waite et al.*, 2017) and holds promise for astrobiology; Enceladus' seafloor might resemble terrestrial hydrothermal vents where life might have originated on Earth.

The discovery of intense geological activity and of a global subsurface ocean in Enceladus posed an important challenge to modellers. Preventing Enceladus' ocean from freezing requires an amount of internal heat difficult to reconcile with existing models (e.g., *Nimmo et al.*, 2018). A way out of the problem is that Enceladus' ocean might indeed be freezing; however, precise ephemerides of the Saturnian moons indicate that this is not the case. The migration rate of Enceladus can be related to the amount of tidal dissipation within the moon. The measured migration rate of Enceladus is consistent with the moon being close to thermal equilibrium, the amount of tidal heating can be reconciled with the moon's thermal activity and is sufficient to maintain its subsurface ocean (*Lainey et al.*, 2012). While it has long been theorized that eccentricity tides could heat Enceladus interior and drive geological activity (*Yoder*, 1979), where in the moon and precisely how this occurs remains a mystery. Different hypothesis ranging from intense heating in the moon's rocky core (e.g., *Choblet et al.*, 2017; *Liao et al.*, 2020), the ocean (e.g., *Tyler*, 2009; *Wilson and Kerswell*, 2018), or in a very low-viscosity, convective ice shell (e.g., *Hemingway and Mittal*, 2019) have been proposed.

Saturn's biggest moon, Titan, is also remarkably interesting. At the beginning of the 20th century, observations made from the Fabra Observatory in Barcelona revealed that Titan has an atmosphere (*Comas Solá*, 1908). Decades later, observing from the McDonald Observatory, Texas, Kuiper identified methane in Titan's atmosphere (*Kuiper*, 1944). The Voyager 1 radio occultation experiments determined the thickness and composition of Titan's atmosphere with more precision (*Lindal et al.*, 1983). The atmosphere is mostly made of nitrogen (~ 95%) and methane (~ 5%), and the pressure at the moon's surface is roughly 1.5 bar. Because of the low surface temperatures, ethane and methane can condensate and form seas, lakes and rivers, and an hydrologic cycle akin to that of Earth (e.g., *Lunine et al.*, 1983).

Titan has a high orbital eccentricity (Table 4.1) that can excite tidal waves in Titan's hydrocarbon seas. However, as opposed to the previously considered moons, Titan is not in an orbital resonance. Without an orbital resonance to pump the eccentricity, Titan's orbit is currently being circularized. *Sagan and Dermott* (1982) and *Dermott and Sagan* (1995) showed that if Titan's hydrocarbon hydrosphere would resemble the Earth's (with oceans and continents), tidal dissipation would quickly circularise its orbit; the high eccentricity of Titan should then be the result of a recent disruption such as a big impact. On the other hand, if Titan had a global hydrocarbon ocean or a series of small disconnected lakes and seas, Titan's present eccentricity could be maintained during billions of

years.

The second hypothesis turned out to be the correct one. Cassini's Radar showed that Titan's surface is dotted with lakes (*Stofan et al.*, 2007), the biggest ones being the Kraken (roughly the size of Spain), Ligeia and Punga Mare, located at high latitudes (*Hayes*, 2016). The Mare are estimated to be ~ 100 m deep and their tides have a small amplitude (~ 1 m) (*Tokano*, 2010). Hydrocarbon seas are not the only liquid bodies that Titan has. On January 15th 2005, after travelling with Cassini, Huygens entered the history books when it landed on Titan. During its decent, Huygens observed Extremely Low Frequency electromagnetic waves that *Beghin et al.* (2010) attributed to a resonance between Titan's ionosphere and a subsurface conductive layer, most likely a subsurface ocean. Topography, gravity and rotation data is also consistent with the presence of a subsurface ocean ~ 100 km below Titan's ice layer (*Durante et al.*, 2019; *Iess et al.*, 2012; *Lorenz et al.*, 2008; *Nimmo and Bills*, 2010).

BEYOND SATURN

Although we know much less about the moons of Uranus and Neptune, Voyager 2 gave us a glimpse of these two systems. Among the different moons, Neptune's Triton proved to be very interesting. Triton's orbit largely differs from that of the regular moons of the Solar System (Table 1.1). Instead of being in a prograde orbit, Triton orbits in a retrogade orbit tilted with respect to the ecliptic. The peculiar orbit of Triton has led to the conclusion that Triton is a Kuiper-belt object captured by Neptune (e.g., *McKinnon*, 1984). This is further supported by the similarities between Triton and Pluto —they have similar densities, composition, and an ice shell overlaid by a layer of frost nitrogen in equilibrium with a N_2 atmosphere.

Just as Europa and Enceladus, Triton has just a few craters, presents tectonic features and evidence of cryovolcanism (*Smith et al.*, 1989); characteristics of a satellite that is presently active (*Schenk and Zahnle*, 2007; *Stern and McKinnon*, 2000). Voyager 2 observed nitrogen plumes ~ 8 km high, which are likely driven by the sublimation of nitrogen frost due to solar heating (*Kirk et al.*, 1990). In contrast to the other moons, Triton has a very small eccentricity. Nevertheless, it probably experienced strong tides during its capture. Furthermore, the inclination of Triton's rotational axis with respect to its orbital plane (obliquity) can drive strong tides. The geological activity of Triton is most likely powered by a combination of radiogenic and tidal heating and could have resulted in the formation of an ammonia rich subsurface ocean (*Gaeman et al.*, 2012; *Nimmo and Spencer*, 2015).

We should not presume tidally active worlds to be a particular of the Solar System. Although the detection of exomoons remains elusive (e.g., *Heller*, 2017), we can expect exoplanets to host satellites. Tidally heated exomoons are interesting targets for exomoon hunters. *Peters and Turner* (2013) suggested that thermal emissions from a body several times more active than Io could be detected using the James Webb Telescope. *Oza et al.* (2019) went further and proposed that the spectra of some short-period gas giants show features that hint at ongoing tidally powered volcanism from an orbiting nearby moon. The known spectrum of tidally active worlds might soon widen.

1.2. RESEARCH QUESTIONS AND THESIS OUTLINE

As we have seen in the previous section, the spectrum of tidally active moons spans from frozen worlds to worlds with magma oceans (Figure 1.2). Because of this diversity, computing the tidal response of these bodies requires different approaches. However, until very recently, most studies of the tidal dynamics of the moons of the outer Solar System focused on solid tides. With few exceptions (e.g., *Sagan and Dermott*, 1982; *Sears*, 1995), the dynamical tidal response of the liquid layers of tidally active moons was largely ignored.

Tyler (2008) put liquid tides back at the center of the discussion when he suggested that strong tides stir Europa's subsurface ocean. He later generalized this idea to other icy moons including Enceladus (*Tyler*, 2011, 2009, 2020), Ganymede, Callisto, Mimas, Dione, Rhea, Titan and Triton (*Tyler*, 2014), and to Io's magma ocean (*Tyler et al.*, 2015). This work, together with advances in our understanding of the interiors of the moons of the outer Solar System, has triggered a wave of new research into the tidal dynamics of moons with liquid layers (e.g., *Chen et al.*, 2014; *Chen and Nimmo*, 2011; *Hay and Matsuyama*, 2017, 2019; *Hay et al.*, 2020; *Kamata et al.*, 2015; *Matsuyama*, 2014; *Matsuyama et al.*, 2018; *Nimmo and Spencer*, 2015; *Rekier et al.*, 2019; *Wilson and Kerswell*, 2018).

Despite this effort, many questions remain unanswered. In this thesis several new aspects relevant to understanding tidally active moons with liquid layers are addressed. We challenge common assumptions made in modelling moons with fluid layers with the aim to interpret observations of the moons of the outer Solar System and inform the planning of future space missions. While the overarching topic of tidal dynamics of moons with fluid layers vertebrates the work presented here, the problems we tackle are diverse. Below, we detail the specific topics we investigate.

To place the work presented in this thesis into context, Chapter 2 presents a brief overview of the different aspects of the topic. We start by introducing the character pulling the strings behind this tale: the tidal force. We then examine the dynamic effects of the tidal force in moons with solid, fluid and porous layers. We place special emphasis on the different assumptions and approximations that can be used to study tidal dynamics in these different contexts and point out their shortcomings to derive the research questions tackled in chapters 3, 4 and 5. The effect of tides in the orbital evolution of moons is then explained and the link between astronomical observations and the interior properties of the moons established. This allows us to better appreciate the relevance of the research questions tackled in chapters 3, 4 and 5 as well as to prepare the grounds for the study of tidally heated exomoons presented in Chapter 6.

Chapters 3 and 4 are concerned with the study of subsurface ocean tides. Three main research questions are addressed:

1. How does the tidal response of a subsurface ocean of variable thickness differ from that of a constant thickness ocean?

2. What are the patterns and intensity of ocean currents resulting from tidally induced inertial waves in subsurface oceans?

3. Do tidally induced inertial waves heat the subsurface ocean of Europa and Enceladus?

In Chapter 3, a model to study tides in subsurface oceans with variable thickness is developed. The model relies on the classic Laplace tidal equations, which we solve using a Finite Element Method. We apply it to Enceladus and also discuss the implication of our findings for Triton. In Chapter 4, we challenge some of the assumptions behind the widely-used Laplace tidal equations. We show that internal waves are excited by the tidal force in Europa's and Enceladus' oceans and discuss their relevance for the dynamics of subsurface oceans.

In Chapter 5, a model to study tides in porous media is developed to tackle two research questions:

4. How does the presence of a porous layer alter the tidal response of a tidally active moon?

5. What is the contribution of Darcy dissipation to Enceladus' energy budget?

The model relies on the viscoelastic theory of tides which is extended to include Biot's poroviscoelasticity theory. The new model can be used to study the tidal dynamics of moons with porous layers such as Enceladus' porous core and Io's partially molten asthenosphere. We focus on Enceladus, we apply the new model to this moon and discuss the implication of our result for its energy budget.

In Chapter 6, we take an excursion outside of the Solar System to consider the existence and detection of tidally heated exomoons. Moons undergoing extreme levels of tidal heating, super-Ios, are prime targets in the exomoon hunt (*Oza et al.*, 2019; *Peters and Turner*, 2013). To assess how likely it is to discover a super-Io, it is important to understand the internal and orbital dynamics of moons experiencing extreme levels of tidal heating. With this goal in mind, we address the following research questions:

6. What is the thermal state of a super-Io?

7. How long can a super-Io persist in an observable state?

The different elements of the tidal problem come now into full view, the coupling between internal and orbital evolution becomes evident. We first consider the thermal state of a super-Io for different orbital configurations to assess its thermal output and potential volcanic activity. We then investigate how longevous this activity could be and what the discovery of a super-Io would imply.

Finally, Chapter 7 gathers the answers to the research questions presented here and discussed in the body of the thesis. As it is often the case, our answers prompt new questions, which open avenues for future research. The last chapter of the thesis discusses these questions and puts them in the broader context of the planetary exploration of the outer Solar System.

	Moon	Io	Europa	Ganymede	Callisto	Enceladus	Dione	Titan	Triton	Pluto	Charon
Radius [km]	1737.5	1821.6	1560.8	2631.2	2410.3	252.1	561.7	2574.7	1353.4	1188.3	603.6
Mass [10^{22}kg]	7.3	8.9	4.8	14.8	10.8	0.01	0.1	13.5	2.1	1.3	0.16
Average density [10^{3}kgm^{-3}]	3.35	3.53	3.01	1.94	1.84	1.61	1.47	1.88	2.06	1.87	1.66
Surface Gravity [ms^{-2}]	1.62	1.80	1.32	1.36	1.25	0.11	0.23	1.35	0.78	0.30	0.62
MoI [-]	0.393	0.377	0.346	0.310	0.355	0.335	-	0.34	-	-	-
Tidal period [days]	27.32	1.77	3.55	7.16	16.69	1.37	2.73	15.95	5.88	6.39	6.39
Eccentricity [10^{-3}]	55.4	4.1	9.4	1.3	7.4	4.7	2.2	28.8	-	0.2	0.2
Obliquity [deg]	6.68	0.0021	0.053	0.033	0.24	0.00014	0.0020	0.32	0.35	-	-
Amp. eccentricity tide [m]	2.3	40.9	23.4	2.2	2.1	24.4	6.8	9.4	0	2.6	1.3
Amp. obliquity tide [m]	2.21	0.17	1.05	0.04	0.54	0.006	0.05	0.83	3.2	-	-
Surface heat flux [Wm^{-2}]	0.018	2.24	0.02	–	–	0.02 – 0.04	-	0.005	–	0.085	-

Table 1.1 Physical parameters of a selection of tidally active bodies of the Solar System. Mass, radius, surface gravity, orbital period, eccentricity and obliquity are from NASA/JPL's Solar System Dynamics database. The moment of inertia factor (I/MR^2) is from: Moon (*Konopliv et al.*, 1998), Io (*Anderson et al.*, 1996a), Europa (*Anderson et al.*, 1998), Ganymede (*Anderson et al.*, 1996b), Callisto (*Anderson et al.*, 2001), Enceladus (*Iess et al.*, 2014), Titan (*Iess et al.*, 2010). Note that for a body of uniform density $MoI = 0.4$. Only the obliquity of the Moon and Titan correspond to measured values (*Lang*, 2011; *Stiles et al.*, 2008); for the remaining satellites the obliquity is computed by assuming the satellite is in a Cassini state, see *Chen et al.* (2014) for the icy moons, and *Baland et al.* (2012) for Io. For the Moon the heat flux comes from Apollo 15 and 17 measurements (*Langseth et al.*, 1976); for Io, it is estimated from astrometric measurements *Lainey et al.* (2009); for Enceladus, it is obtained from Cassini's infrared observations of the South Pole (*Howett et al.*, 2011) and heat flux estimates obtained assuming the moon is in thermal equilibrium (*Hemingway et al.*, 2018); for Europa, it is estimated assuming Europa is in thermal equilibrium (*Hussmann et al.*, 2002); and for Titan and Pluto a maximum is inferred from topography (*Conrad et al.*, 2019; *Nimmo and Bills*, 2010). The amplitude of the eccentricity and obliquity tide are computed as explained in Section 2.2.1; the given values correspond to the maximum amplitude attained during the tidal period.

1

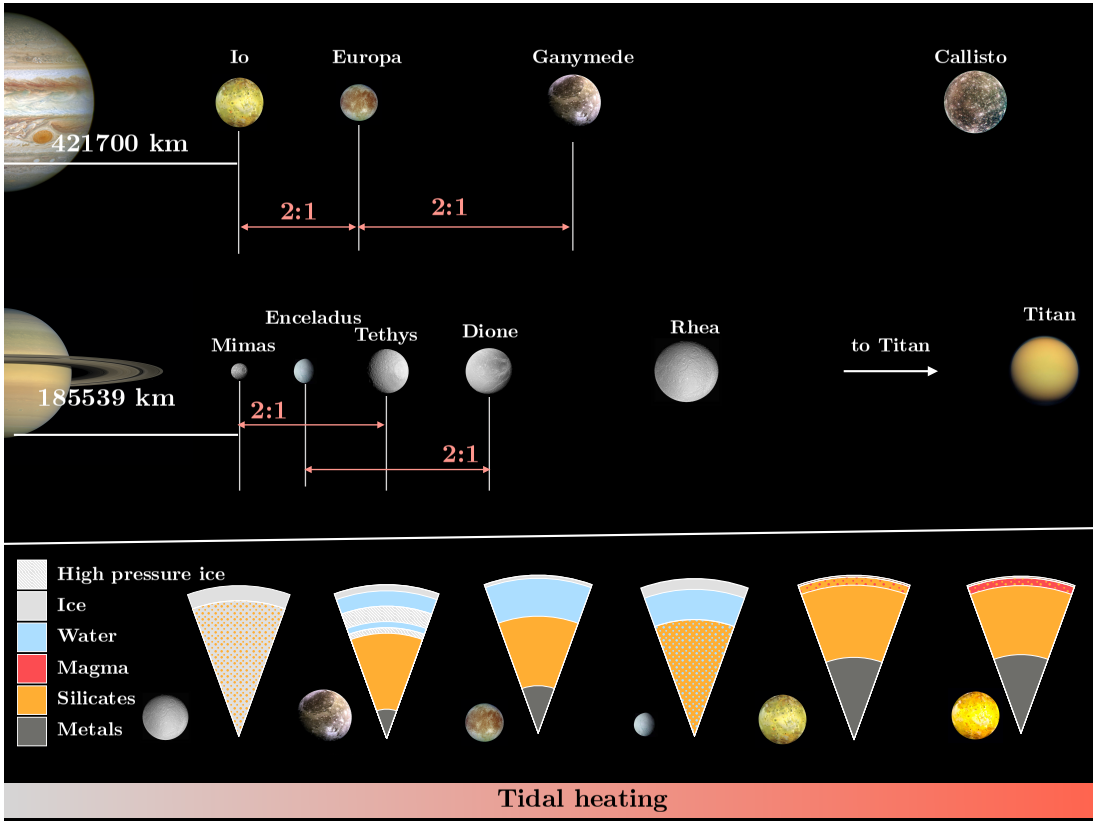

Figure 1.2 Overviews of the Jovian and Saturnian systems. For both systems, planetocentric distances are to scale and pairs in mean-motion resonances are indicated. The sizes of the moons are to scale except for Mimas, Enceladus, Tethys, Dione and Rhea, which have been enlarged by a factor of three. The lower panel illustrates representative interior structures for a selection of moons that show different amounts of tidal activity, from left to right: Rhea, which resembles a dirty snowball; Ganymede, with various subsurface oceans sandwiched between high pressure ices; Europa, and its subsurface ocean in contact with the mantle; Enceladus and its porous core; Io, with a partially molten asthenosphere; and a super-Io with a fully molten magma ocean. Images courtesy of NASA.

2

TIDES: A BRIEF OVERVIEW

The construction of a model, therefore, was for him a miracle of equilibrium between principles (left in shadow) and experience (elusive), but the result should be more substantial than either

— Italo Calvino, *Mr. Palomar*

To tackle the research questions of this thesis, we need to understand very diverse processes that range from the deformation of a grain of sand to the large-scale gravitational interactions that govern the motion of the moons of gas giants. This chapter has the ambitious goal to concisely review these processes.

In Section 2.1, we start by introducing the tidal force. We then discuss how this force deforms a body with solid, liquid and porous layers; we present the equations of motion and underline the assumptions and approximations often used to obtain the tidal response of a body (Section 2.2). Finally, we examine how the tidal deformation of the body alters its orbit, linking the internal properties of a body to its orbit (Section 2.3). Throughout the chapter, the research questions from Chapter 1 are contextualized and their relevance discussed.

2.1. THE PULL OF TIDES

Almost everybody who has lived on or visited Earth's coastlines has experienced tides; the almost magical periodic flooding and ebbing of the sea. Yet for millennia nobody could understand the cause of this daily phenomenon. From the Copernican Revolution to general relativity, the study of tides has shaped our understanding of one of the fundamental forces of nature: gravity (see *Cartwright* (1999) for a comprehensive historical review). Before Newton, the theories on the origin of tides were very diverse, it was

not until his *Principia* that the connection between tides and gravity was made evident and the theory of tides as we know it today started to take shape.

2

THE TIDAL POTENTIAL

Newton showed that tides arise because of the difference in gravitational attraction experienced by two separate points of a body. The point closer to the tide-raising body experiences a stronger attraction as compared to the other [1]. The gradient in the gravitational force provokes the relative motion between the two points and the everyday experience of tides. The strength of the tidal acceleration ($\boldsymbol{a}_{tidal}$) experienced by a point P of the perturbed body (primary) with co-latitude θ and longitude φ depends on its location relative to the tide-rising body. It is given by the tidal potential ($\boldsymbol{a}_{tidal} = -\nabla\phi^T$)[2]:

$$\phi^T = -\frac{GM^*}{d^*}\sum_{l=2}^{\infty}\left(\frac{r}{d^*}\right)^l P_l(\cos\psi). \tag{2.1}$$

M^* is the mass of the tide-raising body (secondary), d^* the distance between the centers of the primary and the secondary, r the distance from point P to the center of the primary and Ψ the angle between $\boldsymbol{r}$ and $\boldsymbol{d}^*$ (see Figure 2.1). P_l is a Legendre polynomial of degree l. Note that the previous expression can be used to compute the tidal deformation of a planet due to moon tides or the tidal deformation of a moon due to planet tides by exchanging the role of the primary and the secondary.

Equation 2.1 is not practical for computing the deformation of a body due to tides. The distance d^* and angle Ψ change in a complicated way as the relative position between the tide-rising body and point P changes. If the secondary is orbiting around the primary, d^* and Ψ can be written using the orbital elements of the secondary, the coordinates of point P, and the rotation of the primary as given by its angular velocity Ω (see Figure 2.1):

$$d^* = f(a^*, e^*, \nu^*), \tag{2.2a}$$

$$\psi = f(\theta, \varphi, i^*, \gamma^*, \omega^*, \nu^*). \tag{2.2b}$$

a^* is the semi-major axis, e^* the eccentricity, i^* is the angle between the rotational axis and the normal to the orbital plane and ν^* is the true anomaly. Longitudes in the frame rotating with the primary are φ, while those referring to the non-rotating reference frame are given by φ^*, φ_0^* being the sidereal time of the reference meridian – the angle formed between an inertially fixed point in the equator and the intersection of the meridian of the body from which longitude is measured with the equator. The remaining angles are indicated in Figure 2.1. Eq. (2.2) can be expanded in a series and substituted in Eq. (2.1) to obtain an expression of the tidal potential (*Kaula*, 1961):

[1] In the modern relativistic interpretation of gravity, tidal forces are the consequence of the curvature of space-time

[2] Other authors (e.g., *Jara-Orué and Vermeersen*, 2011; *Kaula*, 1964) use $\boldsymbol{a}_{tidal} = \nabla\phi^T$ instead and hence their formulas differ in a sign.

$$\phi^T = -\frac{GM^*}{a^*}\sum_{l=2}^{\infty}\left(\frac{r}{a^*}\right)^l \sum_{m=0}^{l}\frac{(l-m)!}{(l+m)!}(2-\delta_{0m})P_{lm}(\cos\theta)\sum_{p=0}^{l}\sum_{q=-\infty}^{\infty}F_{lmp}(i^*)G_{lpq}(e^*)$$
$$\left[\cos(m\varphi)\begin{Bmatrix}\cos\\ \sin\end{Bmatrix}_{l-m\text{ odd}}^{l-m\text{ even}}\left(v^*_{lmpq}-m\varphi_0^*\right)+\sin(m\varphi)\begin{Bmatrix}\sin\\ -\cos\end{Bmatrix}_{l-m\text{ odd}}^{l-m\text{ even}}\left(v^*_{lmpq}-m\varphi_0^*\right)\right] \tag{2.3}$$

with

$$v^*_{lmpq} = (l-2p)\omega^* + (l-2p+q)\mathcal{M}^* + m\gamma^*. \tag{2.4}$$

P_{lm} are Legendre functions of degree l and order m, and F_{lmp} and G_{lpq} are the eccentricity and obliquity polynomials. $\mathcal{M}^*$ is the mean anomaly, which is related to the orbital frequency as $\dot{\mathcal{M}}^* = n^*$.

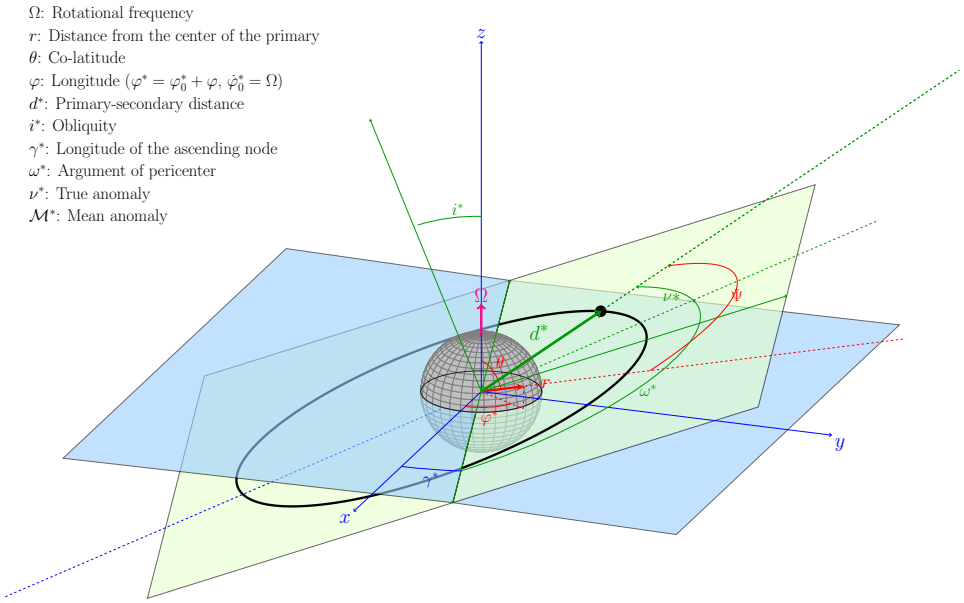

Figure 2.1 Relative motion of the tide-raising body (secondary) around the perturbed body (primary). The orbital and equatorial plane are indicated in green and blue, respectively. Longitudes in the rotating frame rotating with the object are given by φ while longitudes in the non-rotating reference frame (x,y,z) are indicated with φ^*.

TIDAL CONSTITUENTS

Eq. (2.3) makes more evident the different components of the tidal force; by examining it, we can evaluate which are the leading components of the tidal force. We start by

noting that a tidal component of degree l is proportional to $(r/a^*)^l$, hence the higher the degree the smaller the tidal amplitude; terms of order $l = 2$ are dominant. F_{lmp} and G_{lpq} are polynomials of the eccentricity and obliquity. In most cases, eccentricity and obliquity are small; if this is the case, F_{lmp} and G_{lpq} rapidly converge and it is sufficient to only consider the lower order terms of these two polynomials.

To illustrate this, let us consider tides raised by the Moon (secondary) on the Earth (primary) and by the Earth (secondary) on the Moon (primary). The lowest order term is $O(1)$ and corresponds to $q = 0$, $p = 0$, $m = 2$. This term has frequency $2(\dot{\omega}^* + n^* + \dot{\gamma}^* - \Omega)$, which on Earth corresponds to the familiar semidiurnal lunar tide M_2 that circles the planet approximately every twelve hours and a half. On the other hand, because the Moon is tidally locked in synchronous rotation ($\dot{\omega}^* + n^* + \dot{\gamma}^* - \Omega_{Moon} \approx 0$), this tidal component has zero frequency with respect to the Moon. It causes a frozen tidal bulge but does not produce dynamic tides. For the Moon, higher order terms in e and i become the leading components of the dynamical tide.

Similarly to the Moon, most moons of the Solar System are tidally locked in synchronous rotation. If their orbits were circular ($e^* = 0$) and co-planar with respect to the equatorial plane ($i^* = 0$), the relative position between the planet and a point at the surface of the moon would not change; the planet's location in the sky as seen from the moon would remain fixed. The tidal force would be constant and there would not be dynamic tides. However, the orbit is slightly eccentric and the equatorial plane of the moon is inclined with respect to the orbital plane, which means that in the course of an orbit the planet's location with respect to a point on the moon's surface slightly changes as illustrated in Figure 2.2. The leading terms of the tidal potential (2.3) are then (e.g., *Jara-Orué and Vermeersen*, 2011; *Murray and Dermott*, 2000):

$$\phi^T = -(nR)^2 \left(\frac{r}{R}\right)^2 \left(\phi_0^T + \phi_e^T + \phi_i^T\right) \tag{2.5}$$

with:

$$\phi_0^T = -\frac{1}{2} P_{2,0}(\cos\theta) + \frac{1}{4} P_{2,2}(\cos\theta)\cos\varphi, \tag{2.6a}$$

$$\begin{aligned}\phi_e^T = e^* \Big(-\frac{3}{2} P_{2,0}(\cos\theta)\cos\big(n^* t\big) + \frac{3}{4} P_{2,2}(\cos\theta)\cos\big(2\varphi\big)\cos\big(n^* t\big) \\ + P_{2,2}(\cos\theta)\sin\big(2\varphi\big)\sin\big(n^* t\big)\Big) + O(e^{*2}),\end{aligned} \tag{2.6b}$$

$$\phi_i^T = \sin\big(i^*\big) P_{2,1}(\cos\theta)\cos\big(\varphi\big)\sin\big(\omega^* + n^* t\big) + O(\sin^2 i^*). \tag{2.6c}$$

θ and φ indicate the co-latitude and longitude of the point in the moon's reference frame.

The tidal potential (2.5) has three components. The first component, ϕ_0^T, is the tide that the moon would experience if the orbit were circular and contained in its equatorial plane. As mentioned above, it produces a frozen tidal bulge. The two remaining components have a diurnal frequency and produce dynamic tides. ϕ_e^T is known as the eccentricity tide and, as its name indicates, is the consequence of the elongation of the moon's orbit. It can be split into two parts: one does not have a longitudinal dependence and

the other does. The first part arises because the planet moves closer and further away from the moon's surface as the moon shifts from pericenter to apocenter. The second appears because conservation of angular momentum implies that the moon does not move at a constant velocity in its eccentric orbit, producing a longitudinal libration of the subplanet point in the moon's surface (Figure 2.2). ϕ_i^T is the obliquity tide, produced by the latitudinal libration of the subplanet point resulting from the inclination of the orbital plane with respect to the moon's equator. As mentioned above, (2.6) only contains the leading order terms of the tidal potential. Due to the small obliquity and eccentricity of the moons of the Solar System, this is normally sufficient. However, in bodies with high eccentricities ($e > 0.1$), higher order terms start to play an important role in the tidal dynamics (e.g., *Renaud et al.*, 2021).

The time-varying tidal potential drives periodic deformations of the moon. In what follows, we discuss how this periodic deformation can be computed. While our treatment is general, we will place it in the context of previous work on tides in the moons of the outer Solar System, paying special attention to the assumptions and shortcomings of previous work, and, in this way, introducing the research questions that will be tackled in the succeeding chapters.

2.2. TIDAL DYNAMICS

The changing tidal force induces motions in the solid and liquid layers of moons. If we consider a small parcel of a moon, the effect of the tidal potential is given by Newton's second law ($F = m\frac{\mathrm{d}v}{\mathrm{d}t}$). As the moon is rotating, it is convenient to study the relative motion of the parcels in a reference frame that is rotating with it. Conservation of momentum implies that:

$$\rho\left(\frac{\mathrm{D}\boldsymbol{v}}{\mathrm{D}t} + 2\boldsymbol{\Omega}\times\boldsymbol{v}\right) = \nabla\cdot\boldsymbol{\sigma} - \rho\nabla\phi, \tag{2.7}$$

where $\boldsymbol{v}$ is the velocity of the parcel and D indicates the Lagrangian derivative. The first term on the left-hand side gives the acceleration of the parcel and the second term is the Coriolis acceleration, which arises because of the rotational frame. The forces acting on the parcel are on the right hand of the equation, with the first term being the surface forces given by the stress tensor ($\boldsymbol{\sigma}$) and the second term being body forces arising from a potential (ϕ) that includes the tidal potential (ϕ^T), the self-gravitation of the body in question and the centrifugal force. The self-gravitation of the body depends on how mass is distributed within the body and is given by Poisson's equation:

$$\nabla^2\phi = 4\pi G\rho. \tag{2.8}$$

To obtain the tidal motions, we need to consider additional conservation equations. Mass is conserved,

$$\frac{\partial\rho}{\partial t} + \nabla\cdot(\rho\boldsymbol{v}) = 0. \tag{2.9}$$

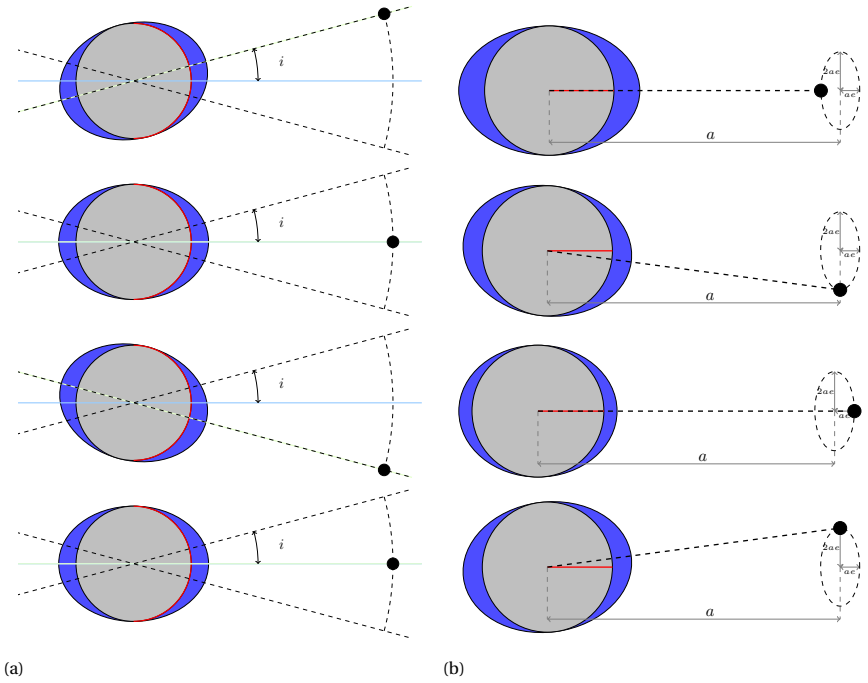

Figure 2.2 Obliquity (a) and eccentricity (b) tide for a tidally locked moon in a moon-fixed reference frame. A meridian corresponding to the average location of the subplanet point is indicated in red, the tidal bulge is shown in blue and the planet is represented by the black circle. For (a) the equatorial and orbital planes of the moon are shown in blue and green, respectively. The semi-major axis (a), eccentricity (e) and obliquity of the satellite's (i) are indicated.

Additionally, a constitutive equation for the stress tensor and an energy conservation equation are needed to close the system of equations. In the subsequent sections, we will briefly describe how tides can be modelled for different media, underline some commonly made assumptions in the study of tides and show the kind of tidal motions that can be expected.

2.2.1. TIDAL DYNAMICS OF LIQUID MEDIA

While Newton was the first to accurately explain the origin of tidal forces, he did not study their dynamical effect on the ocean. This task was undertaken by the French mathematician Laplace who set to study *l'action du soleil et de la lune sur la mer et sur l'atmosphère* (*Laplace*, 1798). Laplace used the now-called Laplace tidal equations to study ocean tides. Since then, these equations have been widely used to study Earth's tides. More recently, they have also been applied to study tidally active moons (e.g., *Beuthe*, 2016; *Kamata et al.*, 2015; *Matsuyama*, 2014; *Sagan and Dermott*, 1982; *Tyler*, 2008) and exoplanets (e.g., *Blackledge et al.*, 2020) with oceans. As we will see, however, the Laplace tidal equations rely on important assumptions that filter some solutions out of the Navier-Stokes equations.

Starting with the momentum and mass conservation equations, we will present the different waves that the tidal force can induce and examine in which cases they can(not) be neglected. We will then examine which tidal waves are expected to dominate the tidal response of subsurface oceans, finally leading to three of the research questions tackled in this thesis.

GOVERNING EQUATIONS

We start by introducing a constitutive equation for the stress tensor. To do so, we split the stress tensor into two components, the thermodynamic fluid pressure p, independent of the fluid velocity, and the viscous stress tensor $\boldsymbol{\tau}$, which depends on the flow velocity,

$$\boldsymbol{\sigma} = \boldsymbol{\tau} - p\boldsymbol{I}. \tag{2.10}$$

For a Newtonian fluid, the viscous stress tensor is given by:

$$\boldsymbol{\tau} = \zeta \,\mathrm{tr}(\dot{\boldsymbol{\epsilon}})\boldsymbol{I} + 2\eta\left(\dot{\boldsymbol{\epsilon}} - \frac{1}{3}\,\mathrm{tr}(\dot{\boldsymbol{\epsilon}})\boldsymbol{I}\right), \tag{2.11}$$

where η and ζ are the dynamic and second viscosity, respectively associated with volumetric and shear deformations, and $\dot{\boldsymbol{\epsilon}}$ is the rate of strain tensor:

$$\dot{\boldsymbol{\epsilon}} = \frac{1}{2}\left(\nabla\boldsymbol{v} + (\nabla\boldsymbol{v})^T\right). \tag{2.12}$$

Taking the continuity, momentum and Poisson equations (2.7-2.8) together with the constitutive equation (2.11), we note that we have six unknown variables ($\boldsymbol{v}$, p, ρ and ϕ) and five equations.

Parts of Section 2.2.1 are based on an unfinished survey paper on tides in extraterrestrial oceans that the author worked on with Gerkema, Maas, Hay, Matsuyama, Tyler and Beuthe, and Chapter 7 of *Gerkema* (2019).

An additional equation relating density and pressure can be obtained from thermodynamic principles. Assuming local thermodynamic equilibrium, the density of a parcel can be written in terms of a state function that depends on three independent state variables: pressure p, entropy s and salinity S, for a certain function that we can leave unspecified here $\rho(p,s,S)$. Material changes in density, i.e., following a parcel, can then be expressed as

$$\frac{D\rho}{Dt} = \left(\frac{\partial\rho}{\partial p}\right)_{sS}\frac{Dp}{Dt} + \left(\frac{\partial\rho}{\partial s}\right)_{pS}\frac{Ds}{Dt} + \left(\frac{\partial\rho}{\partial S}\right)_{ps}\frac{DS}{Dt}. \tag{2.13}$$

The subscripts on the right-hand side of (2.13) are added to indicate that these variables are kept constant in the respective partial derivatives. The first partial derivative on the right-hand side has a special significance, for it is related to the speed of sound c_s (see *Vallis* (2006), Section 1.8). Assuming that the movement of water parcels is adiabatic[3], i.e., they exchange no heat or salinity with their surroundings, we have $Ds/Dt = 0$ and $DS/Dt = 0$, so that (2.13) reduces to

$$\frac{D\rho}{Dt} = \frac{1}{c_s^2}\frac{Dp}{Dt}. \tag{2.14}$$

Without loss of generality, we can split pressure and density and perturbing potential into two components: a time-independent hydrostatic component (denoted by subscript 0) and a dynamic one (denoted by superscript Δ):

$$p = p_0(r) + p^{\Delta}(\boldsymbol{r},t) \tag{2.15a}$$

$$\rho = \rho_0(r) + \rho^{\Delta}(\boldsymbol{r},t) \tag{2.15b}$$

$$\phi = \phi_0(r) + \phi^{\Delta}(\boldsymbol{r},t) \tag{2.15c}$$

Note that ϕ^{Δ} includes both the external perturbing potential (i.e., the tidal potential ϕ^T) and the gravitational potential that arises due to the ensuing deformation of the body. In the hydrostatic state, $\boldsymbol{v} = 0$, the density is ρ_0 and the gravitational force is balanced by a hydrostatic pressure field p_0:

$$\nabla p_0 = -\rho_0\nabla\phi_0 = -\rho_0 g_0 \boldsymbol{e_r}. \tag{2.16}$$

g_0 is the gravity of the unperturbed body and $\boldsymbol{e_r}$ the radial vector.

[3]The adiabatic assumption can be made to study processes that occur at timescales smaller than those at which the background thermal state (temperature, density and salinity) of the medium changes. An apparent contradiction occurs when these very same processes influence the thermal structure of the medium in the long-term, here a coupling arises between the short and long timescales. A clear example is the study of internal waves in Earth's oceans; even though mixing provoked by internal waves plays a crucial role in the stratification of Earth's oceans, their short-term dynamics (for timescales comparable to the forcing period) are normally modelled using the adiabatic approximation and their long-term effects on the ocean's thermal structure are assessed a posteriori or in a parametrized way.

COMMON APPROXIMATIONS

A major simplification can be made by assuming that the flows of interest have a small amplitude. This assumption allows to linearize the previous set of equations and immensely simplifies the study of waves. Unfortunately, it removes important phenomena including wave-wave and wave-flow interactions, and wave-breaking, all of which can trigger instabilities and turbulence in the system. By plugging (2.15) into (2.7,2.8,2.9,2.14) and linearizing we get:

$$\frac{\partial \rho^\Delta}{\partial t} + \boldsymbol{v}\cdot\boldsymbol{e}_r \frac{\mathrm{d}\rho_0}{\mathrm{d}r} = -\rho_0 \nabla\cdot\boldsymbol{v}, \tag{2.17a}$$

$$\frac{\partial \rho^\Delta}{\partial t} + \boldsymbol{v}\cdot\boldsymbol{e}_r \left[\frac{\mathrm{d}\rho_0}{\mathrm{d}r} + \frac{\rho_0 g_0}{c_s^2}\right] = \frac{1}{c_s^2}\frac{\partial p^\Delta}{\partial t}, \tag{2.17b}$$

$$\rho_0\left(\frac{\partial \boldsymbol{v}}{\partial t} + 2\boldsymbol{\Omega}\times\boldsymbol{v}\right) = -\nabla p^\Delta + \nabla\cdot\tau - \rho_0\nabla\phi^\Delta - \rho^\Delta\nabla\phi_0, \tag{2.17c}$$

$$\nabla^2\phi^\Delta = 4\pi G\rho^\Delta. \tag{2.17d}$$

Eqs. (2.17) describe a rich spectrum of waves including: sound waves, barotropic and baroclinic waves, as well as various kinds of waves that are affected by the Coriolis force. Because the tidal perturbation propagates slow compared to the speed of sound, we can filter sound waves from our equations by assuming $c_s \to \infty$. (2.17a,b) become

$$\rho_0\nabla\cdot\boldsymbol{v} = 0, \tag{2.18a}$$

$$\frac{\partial \rho^\Delta}{\partial t} + \boldsymbol{v}\cdot\boldsymbol{e}_r N^2 = 0. \tag{2.18b}$$

$N^2 = \mathrm{d}\rho_0/\mathrm{d}r + \rho_0 g_0/c_s^2$ is the so-called Brunt-Väisälä or buoyancy frequency N. If $N^2 > 0$, it indicates that the fluid is stably stratified; radial perturbations can then excite internal waves where gravity is the restoring force . If $N^2 < 0$, the fluid is gravitationally unstable. For $N = 0$ the fluid is unstratified. In that case, the Coriolis force acts as the sole restoring force; the associated waves are called gyroscopic or inertial.

While we have made several approximations, we have not yet obtained the well-known Laplace tidal equations. The Laplace tidal equations rely on the shallow water approximation which is based on the fact that the fluid occupies a thin layer compared to the wavelength of the forcing, which in the case of tides can be approximated with the body's radius. Much has been written on the validity of the Laplace tidal equations (see *Gerkema et al.* (2008); *Miles* (1974); *Vallis* (2006) for an in-depth analysis), here we will only sketch the idea behind it. We write the continuity equation in spherical coordinates,

$$\frac{1}{r}\frac{\partial r^2 v_r}{\partial r} + \frac{1}{\sin\theta}\frac{\partial \sin\theta\, v_\theta}{\partial\theta} + \frac{1}{\sin\theta}\frac{\partial v_\varphi}{\partial\varphi} = 0; \tag{2.19}$$

and non-dimensionalize it considering a characteristic vertical length-scale H equal to the ocean depth, and two characteristic velocities V_r, $V_{\theta,\varphi}$ corresponding to characteristic radial and lateral velocities. Assuming that $r = R + \delta$ where δ is a small number, we find that:

$$\frac{V_r}{V_{\theta,\varphi}} \sim \frac{H}{R}. \tag{2.20}$$

It follows that if $H/R \ll 1$, radial flows are much smaller than meridional and zonal ones, $\mid v_r \mid \ll \mid v_{\theta,\varphi} \mid$. The radial component of the momentum equation simplifies to

$$\frac{\partial p^\Delta}{\partial r} = -\rho^\Delta g_0 - \rho_0 \frac{\partial \phi^\Delta}{\partial r} + 2\Omega \sin\theta v_\varphi, \tag{2.21}$$

where v_φ is the zonal component of the velocity. A very common approximation is to neglect the Coriolis term ($2\Omega \sin\theta v_\varphi$), thus assuming that the vertical dynamics are governed by hydrostatic balance,

$$\frac{\partial p^\Delta}{\partial r} = -\rho^\Delta g_0 - \rho_0 \frac{\partial \phi^\Delta}{\partial r}. \tag{2.22}$$

If this is done, energy considerations require that the Coriolis terms containing $\sin\theta$ are also removed from the horizontal momentum equations, an approximation known as the "traditional approximation". This approximation was introduced by Laplace and has been widely employed since then. Using (2.22) and averaging the continuity and momentum equations in the radial direction, the Laplace tidal equations are finally obtained:

$$\frac{\partial \eta}{\partial t} + \nabla \cdot h \bar{\boldsymbol{v}}_{\theta,\varphi} = 0 \tag{2.23a}$$

$$\frac{\partial \bar{\boldsymbol{v}}_{\theta,\varphi}}{\partial t} - f \bar{\boldsymbol{v}}_{\theta,\varphi} \times \boldsymbol{e}_r = -g_0 \nabla \eta - \nabla \phi^\Delta - \boldsymbol{f}_d(\bar{\boldsymbol{v}}_{\theta,\varphi}). \tag{2.23b}$$

η is vertical displacement of the water surface, $\bar{\boldsymbol{v}}_{\theta,\varphi}$ is the radially averaged zonal and meridional velocity, h is the ocean thickness, and $f = 2\Omega\cos\theta$ the Coriolis parameter. $\boldsymbol{f}_d(\boldsymbol{v}_{\theta,\varphi})$ is a dissipation function used to account for momentum dissipation, a function of the form

$$\boldsymbol{f}_d(\boldsymbol{v}_{\theta,\varphi}) = \alpha \bar{\boldsymbol{v}}_{\theta,\varphi} + \frac{c_D}{h} \bar{\boldsymbol{v}}_{\theta,\varphi} \mid \bar{\boldsymbol{v}}_{\theta,\varphi} \mid, \tag{2.24}$$

is normally assumed with either one or the two terms. α and c_D are the Rayleigh and bottom drag coefficients, respectively.

Compared to the set of equations (2.17c,d) and (2.18a,b), (2.23) remove the possibility of internal inertial waves (see Table 2.1). Solutions to (2.23) are given by two types of surface waves: surface gravity waves —with gravity as the restoring force— and Rossby-Haurwitz waves — with the Coriolis force as the restoring force.

Approximation/Assumptions	Filtered waves	Equations	Chapters
Linearization	Wave-breaking, wave-wave and wave-flow interactions	(2.17)	Ch. 3, 4
Infinite speed of sound ($c_s \to \infty$)	Sound waves	(2.18)	Ch.3 4
Unstratified ocean ($N^2 = 0$)	Internal gravity waves		Ch. 3, 4
Hydrostatic approximation ($h/R \to 0$)	Internal inertial waves	(2.22,2.23)	Ch. 3
Equilibrium tide ($c_0 \to \infty$)	Surfaces wave	(2.25)	Ch. 5

Table 2.1 Approximations that can be used to study tidal flows and flow phenomena that they filter. The third column refers to the equations that result from these approximations and the last column indicates which assumptions are used in some of the Chapters of the thesis.

If the wave speed c_0 is much higher than the velocity at which the tidal perturbation propagates ($c_t = \Omega R$), the ocean can quickly adjust to the tidal perturbation. When this occurs, $\bar{\boldsymbol{v}}_{\theta,\varphi} \approx 0$ and the ocean response can be approximated by the equilibrium tide,

$$\eta_{eq} = -\frac{\phi}{g_0}, \tag{2.25}$$

or, if we ignore self-gravitation, $\eta_{eq} = -\phi^T / g_0$.

The equilibrium tide is an excellent proxy to measure the strength of tides. Table1.1 shows the amplitude of the equilibrium tide for different bodies. Moreover, the equilibrium tide is normally used to assess the efficiency of dissipative processes within the ocean (e.g., friction, wave-breaking). The amount of energy dissipation ($\mathrm{d}E/\mathrm{d}t$) can be compared to the peak energy contained in the equilibrium tide (E_0) via the quality factor Q (e.g., *Efroimsky*, 2012a)

$$Q \equiv \frac{2\pi E_0}{\int (\mathrm{d}E/\mathrm{d}t)\mathrm{d}t}. \tag{2.26}$$

Q is analogous to the quality factor of an oscillator; it is frequency dependent and it indicates how efficiently tidal energy is dissipated in the ocean. Its meaning can be understood as follows: if the tidal force would stop, it would take $2Q/n$ time for the oceans to come to rest. The quality factor can also be associated with a phase lag between the tidal force and the ocean response ϵ:

$$\sin\epsilon = \frac{1}{Q}. \tag{2.27}$$

The previous definition is not restricted to liquid tides. The quality factor Q can be used to account for all the dissipative processes at play. As we will see in Section 2.3, the quality factor is central to understanding the link between tides and orbital evolution.

EXTRATERRESTRIAL OCEAN TIDES

The Laplace tidal equations have been widely used to study Earth's ocean tides and have proven very successful in explaining their general characteristics. It should not come as a surprise that this set of equations is the go-to tool to study tides in other planetary bodies. *Sagan and Dermott* (1982) first considered the tides of Titan's hydrocarbon seas using a simple analytical method that ignores the Coriolis force. Later, *Sears* (1995) addressed this issue and used a numerical approach to solve the Laplace tidal equations and investigate the tides of Titan. More recently, Tyler used these equations to study tides in subsurface and magma oceans (*Tyler*, 2011, 2014, 2008, 2009, 2020; *Tyler et al.*, 2015). Using the work of *Longuet-Higgins* (1968) on tides in global surface oceans, *Tyler* (2008, 2009) showed that two kinds of waves can be excited by obliquity and eccentricity tides: surface gravity waves and Rossby waves. The first kind are excited by both the eccentricity and the obliquity tide; the second kind are only excited by the obliquity tide. As shown in Figure 2.3, their characteristics are markedly different: surface gravity waves are characterized by ripples of the ocean surface that propagate at $c_g^2 = gh$. In contrast, Rossby waves are nearly divergence-free, they feature small surface displacements.

Since the pioneering work of *Tyler* (2008, 2009), several improvements have been made to the theory of tides in subsurface and magma oceans. The work of Tyler did not consider the effects of self-gravity and ignored the presence of an ice shell. These two issues have been resolved (*Beuthe et al.*, 2016; *Kamata et al.*, 2015; *Matsuyama*, 2014; *Matsuyama et al.*, 2018). *Beuthe* (2016) and *Matsuyama et al.* (2018) showed that the role of the ice shell depends of the effective rigidity of the moon. For moons with a high effective rigidity, such as Enceladus, the ice shell plays an important role, for moons with low effective rigidity, such as Europa, the effect of the ice shell is smaller. Nevertheless, all previous studies of tides in subsurface ocean still considered liquid layers of constant thickness. Yet, it is possible that subsurface oceans feature thickness variations.

The most evident case is Enceladus. Gravity and topography data from the Cassini mission shows that Enceladus' ocean thickness varies from ~ 30km at the equator to ~ 60 km at the South Pole (e.g., *Beuthe et al.*, 2016; *Čadek et al.*, 2016; *Hemingway and Mittal*, 2019). On Earth, ocean bathymetry and the configuration of the continents shape the ocean's response to tides, something similar could occur in Enceladus. We explore this idea in Chapter 3, where we address the following research question:

1. How does the tidal response of a subsurface ocean of variable thickness differ from that of a constant thickness ocean?

As evidenced by the discussion above, up until now the Laplace tidal equations have been the standard tool to study tides in moons with subsurface oceans. However, it is important to recall that the Laplace tidal equations filter out internal waves. Internal waves are key to energy dissipation on Earth's ocean (*Garrett*, 2003; *Garrett and Munk*, 1979; *Munk*, 1997; *Munk and Wunsch*, 1997). Moreover, the h/R ratio of some ocean worlds is higher than Earth's ($h/R \sim 0.15$ for Enceladus versus 0.001 for Earth), which suggests that internal waves might be more relevant there. *Vermeersen et al.* (2013) proposed that inertial waves could play a central role in the dynamics of Enceladus' ocean and could

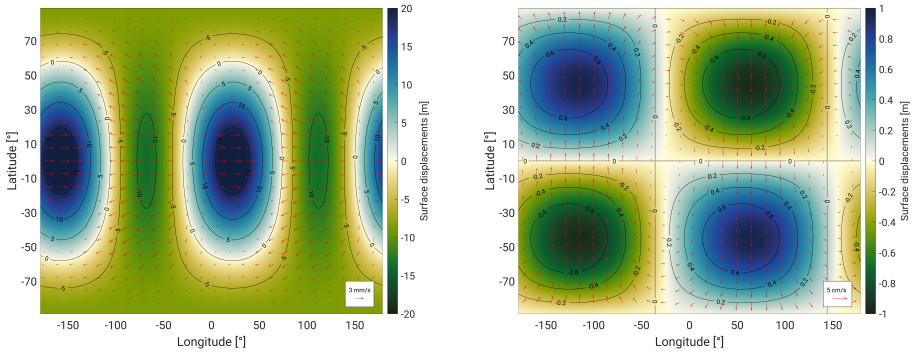

(a) (b)

Figure 2.3 Snapshots of surface waves in Europa excited by eccentricity (a), and obliquity tides (b). The arrows indicate flow velocities and the colormap corresponds to surface displacements η. Contours of the equilibrium tide are superimposed. A 80 km thick ocean and a 20 km thick ice shell is assumed. Figure from *Soderlund et al.* (2020).

even be behind the formation of Enceladus' Tiger Stripes. An investigation of the role of internal waves in the tidal dynamics of subsurface oceans is necessary. In Chapter 4, we investigate the role of internal inertial waves in the ocean dynamics of Enceladus and Europa. We tackle the following research questions:

2. What are the patterns and intensity of ocean currents resulting from tidally induced inertial waves in subsurface oceans?

3. Do tidally induced inertial waves heat the subsurface ocean of Europa and Enceladus?

2.2.2. TIDAL DYNAMICS OF SOLID MEDIA

It should not come as a surprise that the theory of solid tides received attention later than the theory of ocean tides. While the effect of ocean tides is readily noticed by anyone standing on a beach, solid tides are more subtle. The study of solid Earth tides was pioneered by Lord Kelvin (*Thomson*, 1863; *Thomson and Tait*, 1911), who suggested that the solid Earth deformation could be used to infer its rigidity. However, the modern theory of tides owes much to the work of A.E.H. Love, who studied the deformation of a self-gravitating elastic Earth due to tides (*Love*, 1906, 1911) and established the firm basis upon which later work rested. A comprehensive review of the theory of tides for a viscoelastic body can be found in *Sabadini et al.* (2016). Here we summarize the main ideas and give some insight into the role of interior properties on the tidal response of a body. A more detailed explanation can be found in Chapter 5.

GOVERNING EQUATIONS

We start with Eqs. (2.7, 2.8, 2.9). As was the case of liquid tides, a constitutive equation for the stress is required. Again, we split the stress tensor into two components —a volumetric and a deviatoric component— and do the same for the strain tensor:

$$\boldsymbol{\sigma} = -p\boldsymbol{I} + \boldsymbol{\sigma}^d, \tag{2.28a}$$

$$\boldsymbol{\epsilon} = \epsilon^M \boldsymbol{I} + \boldsymbol{\epsilon}^d, \tag{2.28b}$$

where the mean strain ϵ^M and pressure p are given by:

$$p = -\frac{\mathrm{tr}(\boldsymbol{\sigma})}{3}, \tag{2.29a}$$

$$\epsilon^M = \frac{\mathrm{tr}(\boldsymbol{\epsilon})}{3}. \tag{2.29b}$$

The pressure defined here is equivalent to that defined for a liquid only if the liquid is incompressible. The mean strain is related to volume changes $\frac{\Delta V}{V} = 3\epsilon^M$. For an elastic solid, the volumetric and deviatoric component of the stress and strain tensors are proportional to each other:

$$p = -3K\epsilon^M = -K\frac{\Delta V}{V_0}, \tag{2.30a}$$

$$\boldsymbol{\sigma}^d_{el} = 2\mu\boldsymbol{\epsilon}^d_{el}. \tag{2.30b}$$

K and μ are respectively the bulk and shear modulus of the material. Eq. (2.30a) is closely related with the thermodynamic identity (2.14) used to relate density and pressure in a liquid; in fact the bulk modulus is related to the speed of sound (for a liquid, K=$c_s^2\rho_0$).

Apart from elastic behaviour, most materials also exhibit a viscous fluid-like behaviour: when a stress is applied, the material flows just like a fluid would do. This behaviour can be modelled using an expression analogous to that we used for the viscous stress tensor of a liquid, the stress is proportional to the strain rate via the viscosity η:

$$\boldsymbol{\sigma}^d_{vis} = 2\eta\dot{\boldsymbol{\epsilon}}^d. \tag{2.31}$$

A viscoelastic material exhibits both elastic and viscous behaviour. To capture this behaviour, Eqs. (2.30) and (2.31) can be combined in different ways. The simplest one is the Maxwell model in which it is assumed that the stress is the same in the viscous and elastic elements. The total strain of the material is then the combination of the elastic and viscous strain:

$$\dot{\boldsymbol{\sigma}}^d + \frac{\mu}{\eta}\boldsymbol{\sigma}^d = 2\mu\dot{\boldsymbol{\epsilon}}^d. \tag{2.32}$$

The Maxwell model captures the elastic deformation of a material followed by an irrecoverable viscous deformation. Other deformation mechanisms are also possible. For example, for an anelastic material, once a stress is applied, the deformation is recovered;

but unlike an elastic material, the recovery does not occur instantaneously. This kind of behaviour can be represented using the Voigt-Kelvin model. Both the elastic and viscous element experience the same strain and the total stress is the result of adding the elastic and viscous stresses:

$$\dot{\boldsymbol{\sigma}}^d = 2\mu\boldsymbol{\epsilon}^d + 2\eta\dot{\boldsymbol{\epsilon}}^d. \tag{2.33}$$

More complex material responses can be obtained by combining the Maxwell and Voigt-Kelvin mechanisms (see *Renaud and Henning* (2018) for an overview).

The shear and bulk modulus and the viscosity are macroscopic parameters that depend on the microscopic structure of the material. The viscosity of a solid can be approximated by (*Karato and Wu*, 1993; *Reese et al.*, 1999)

$$\eta = A\frac{d^m}{s^{n-1}}\exp\left(\frac{E+pV^*}{RT}\right), \tag{2.34}$$

where A is a material constant, s is the second invariant of the deviatoric stress tensor, d is the grain size, E and V^* are the activation energy and activation volume, R the ideal gas constant, n and m the stress and grain size exponents and p and T the pressure and temperature. From the previous expression it is evident that as temperature increases, the viscosity decreases, which agrees with our everyday experience. The value of n depends on the dominant micromechanic flow mechanism. If the prevalent deformation mechanism is the diffusion of defects in the crystal lattice (diffusion creep), $n = 1$, and the viscosity does not have an explicit dependence on the stress state. This is not the case for other deformation mechanisms, such as the movement of dislocations within the crystal lattice (dislocation creep), which has $n \approx 3$–3.5 (e.g., *Reese et al.*, 1999). Although it might not always be the case, for tidal studies it is normally assumed that diffusion creep dominates.

Even though a solid can flow as a liquid, the viscosity of a solid is much higher than that of a fluid. Moreover, inside a solid, perturbations propagate as seismic waves. As the speed at which seismic waves propagate is high compared to the speed at which the tidal perturbation does, the body quickly adjusts to the external perturbation. These two facts combined imply that inertial terms (left side of (2.7)) are generally much smaller than the other terms in the momentum equation and thus can be ignored:

$$\nabla\cdot\boldsymbol{\sigma} - \rho\nabla\phi = 0 \tag{2.35}$$

As we did for liquid tides (Eq. (2.15)), we can split the different fields into their hydrostatic and dynamic components. Doing so and linearizing Eqs. (2.9, 2.8, 2.35), we get:

$$\nabla\cdot\boldsymbol{\sigma}^{\boldsymbol{\Delta}} - \nabla\left(\rho_0 g\boldsymbol{u}\cdot\boldsymbol{e}_r\right) - \rho_0\nabla\phi^\Delta - \rho^\Delta\nabla\phi_0 = 0, \tag{2.36a}$$

$$\rho^\Delta = -\boldsymbol{u}\cdot\boldsymbol{e_r}\frac{\partial\rho_0}{\partial r} - \rho_0\nabla\cdot\boldsymbol{u}, \tag{2.36b}$$

$$\nabla^2 \phi^{\Delta} = 4\pi G \rho^{\Delta}. \tag{2.36c}$$

To obtain the response of a solid body to tides, the previous set of equations should be solved under appropriate boundary conditions. Different sets of boundary conditions apply depending on the interior structure of the body. It is generally assumed that there are no loads on the surface ($\sigma_{rr} = \sigma_{r,\theta} = \sigma_{r,\varphi} = 0$) and the gravitational potential ϕ is continuous at the surface, but its gradient is not. More details on the specific set of surface and internal boundary conditions can be found in Chapters 5 and 6.

LOVE NUMBERS AND TIDAL HEATING

Different approaches can be used to solve the previous set of partial differential equations. If the body is close to spherically symmetric, spherical harmonics are often employed to solve the previous set of equations (e.g., *Alterman et al.*, 1959; *Love*, 1911; *Peltier*, 1974; *Sabadini et al.*, 2016; *Segatz et al.*, 1988; *Tobie et al.*, 2005, chs. 5 and 6). In case the body is not spherically symmetric, spherical harmonics (*Beuthe*, 2018, 2019) can still be used, but other numerical techniques such as finite elements become an attractive option (e.g., *Steinke et al.*, 2020b; *Wu*, 2004).

The solution of the tidal problem is normally expressed in terms of tidal Love numbers, complex numbers that relate the perturbing tidal potential to the response of the body:

$$u_r(r,\theta,\varphi,t) = \mathrm{Re}\left\{ \frac{h(r,\theta,\varphi)}{g_0} \phi^T(R,\theta,\varphi,t) \right\} = -\frac{|h|}{g_0} \left[\phi^T\right]_{lag}, \tag{2.37a}$$

$$\boldsymbol{u}_{\theta,\varphi}(r,\theta,\varphi,t) = \mathrm{Re}\left\{ \frac{l(r,\theta,\varphi)}{g_0} \nabla_{\theta,\varphi} \phi^T(R,\theta,\varphi,t) \right\} = -\frac{|l|}{g_0} \left[\nabla_{\theta,\varphi} \phi^T\right]_{lag}, \tag{2.37b}$$

$$\phi(r,\theta,\varphi,t) = \mathrm{Re}\left\{ \left[\left(\frac{r}{R}\right)^l + k(r,\theta,\varphi) \right] \phi^T(R,\theta,\varphi,t) \right\} = \left(\frac{r}{R}\right)^l \phi^T + |k| \left[\phi^T\right]_{lag}, \tag{2.37c}$$

with $\nabla_{\theta,\varphi} = (\frac{\partial}{\partial\theta}, \frac{1}{\sin\theta}\frac{\partial}{\partial\varphi})$. The h and l tidal Love numbers relate a unit tidal perturbation to radial and lateral displacements. The k tidal Love number indicates how the ensuing tidal deformation of the body affects its gravitational field.

The Love numbers depend on the internal properties of the body, and the wavelength and frequency of the forcing. If the body is spherically symmetric, they are independent of θ and φ. For $|h| = 1$, we recover the equilibrium tide (2.25); however, due to the body's rigidity $|h| < 1$. The Love numbers are generally complex numbers. The notable exception is if the body is perfectly elastic; in such a case the tidal response is instantaneous and the Love numbers are real. In contrast, for a viscous body, there is a phase lag ϵ between the tidal force and the tidal response, which is reflected in the phase of the tidal Love numbers. The phase lag is the result of energy dissipation within the body. The average amount of tidal dissipation over a tidal period (T) can be obtained as:

$$\dot{E} = \frac{1}{T} \int_0^T \boldsymbol{\sigma} : \dot{\boldsymbol{\epsilon}} \, dt. \tag{2.38}$$

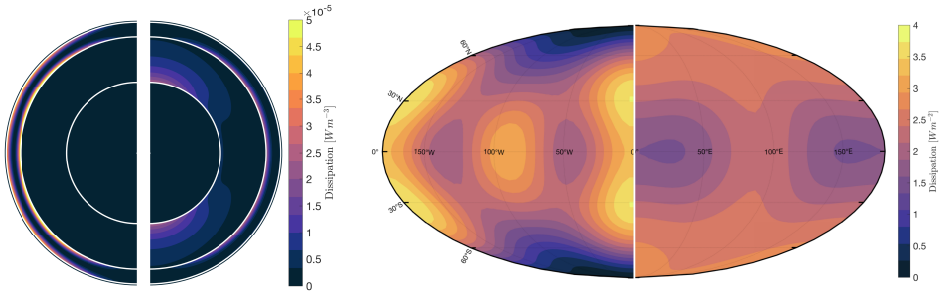

(a) (b)

Figure 2.4 Tidal dissipation for two interior models of Io with a $|\,\mathrm{Im}\{k_2\}\,|$ consistent with observations (0.015). (a) shows a meridional cut going through the sub-Jovian point, (b) shows the surface heat flow. For both (a) and (b), the interior model of the left has a weaker asthenosphere than that on the right. Model parameters are from *Steinke et al.* (2020b) models A and B.

The amount and location of tidal dissipation strongly depends on the interior properties of a body. As an example, Figure 2.4 depicts tidal dissipation for two models of Io that produce an amount of tidal dissipation compatible with observations (*Steinke et al.*, 2020b). Even though the total amount of dissipated energy is the same, its distribution is markedly different.

The total amount of tidal dissipation can be obtained by integrating the volumetric heating rate given by (2.38) over the volume of the body. For spherically symmetric bodies, this integral can be performed in the Fourier domain using the Love numbers. For a tidal perturbation given by (2.3), the total tidal dissipation is (*Renaud et al.*, 2021):

$$\dot{E} = -\frac{GM^{*2}}{a^*}\sum_{l=2}^{\infty}\left(\frac{R}{a^*}\right)^{2l+1}\sum_{m=0}^{l}\frac{(l-m)!}{(l+m)!}(2-\delta_{0,m})\sum_{p=0}^{l}F^2_{lmp}(i^*)\sum_{q=-\infty}^{\infty}G^2_{lpq}(e^*) \\ |\,\dot{\nu}^*_{lmpq}-m\Omega\,|\,\mathrm{Im}\Big\{k_l(\dot{\nu}^*_{lmpq}-m\Omega)\Big\}, \tag{2.39}$$

where M^* is the mass of the tide-raising body and R the radius of the primary . As evidenced by the previous expression, tidal dissipation depends on the interior structure of the body via the imaginary component of the Love numbers, k_l. $\mathrm{Im}\{k_l\}$ can be related to the quality factor we defined in Eq. (2.26), and the phase lag (ε) mentioned before:

$$-\,\mathrm{Im}\{k_l\} = \frac{|\,k_l\,|}{Q} = |\,k_l\,|\sin\varepsilon. \tag{2.40}$$

For a synchronous satellite with eccentricity e^* and obliquity i^* whose tidal potential is given by (2.3), (2.39) reduces to:

$$\dot{E} = -\operatorname{Im}(k_2)\frac{(n^* R)^5}{G}\left(\frac{21}{2}e^{*2} + \frac{3}{2}\sin^2 i^*\right) + O(e^{*4}) + O(\sin^4 i^*), \tag{2.41}$$

with k_2 evaluated at the orbital frequency.

The theory of solid tides has been very successful in explaining some of the main features of the tidally active moons of the Solar System. It has been used to link the timing of Enceladus plumes to its interior properties (*Běhounková et al.*, 2015; *Nimmo et al.*, 2014), explain the formation of cracks in Europa (e.g., *Greenberg et al.*, 1998; *Harada and Kurita*, 2006; *Hoppa et al.*, 1999; *Hurford et al.*, 2007; *Poinelli et al.*, 2019), and link the location of Io's volcanoes to the interior structure of the moon (e.g., *Hamilton et al.*, 2013; *Segatz et al.*, 1988). Additionally, it has proved central to understanding the interior of tidally active moons, helping to predict the presence of melt in Io and resulting volcanism (*Peale et al.*, 1979), and allowing to constrain the thickness and stability of subsurface oceans (e.g., *Cassen et al.*, 1979; *Hussmann et al.*, 2002; *Ojakangas and Stevenson*, 1989; *Roberts and Nimmo*, 2008). In Chapter 6, we will use the ideas presented in this section to compute tidal dissipation in exomoons. Additionally, in the next section, the theory of tides for a solid body will serve as a starting point to develop a theory for the tidal response of bodies with porous or molten layers.

2.2.3. TIDAL DYNAMICS OF MULTIPHASE MEDIA

Some tidally active worlds have layers in which solid and liquid phases coexist. This is the case of Enceladus, which likely has a porous core (e.g., *Choblet et al.*, 2017) and Io, which probably has a partially molten asthenosphere (*Khurana et al.*, 2011). While solid and liquid tides have been widely studied before, tides in porous media have received much less attention. In this section, we first obtain the equations governing the tidal deformation of a body with porous layers and discuss the brief history of the study of tides in porous media, leading us to two of the research questions tackled in subsequent chapters.

GOVERNING EQUATIONS

If we want to compute the tidal response for a body with porous layers, we need to simultaneously consider the mass, momentum and Poisson's equations (Eqs. (2.7, 2.9, 2.8)) for the liquid and the solid phases. We consider a parcel of the body with volume V, whose volume is partitioned between a solid V_s and a liquid V_l with densities ρ_s and ρ_l, respectively (Figure 2.5). The porosity is given by:

$$\Phi = \frac{V_l}{V}, \tag{2.42}$$

and the bulk density is just $\rho = \Phi\rho_l + (1-\Phi)\rho_s$. Mass and momentum conservation for the two phases reads (*Ganesan and Poirier*, 1990),

$$\frac{\partial \Phi\rho_l}{\partial t} + \nabla\cdot\left[\Phi\rho_l \boldsymbol{v}_l\right] = 0, \tag{2.43a}$$

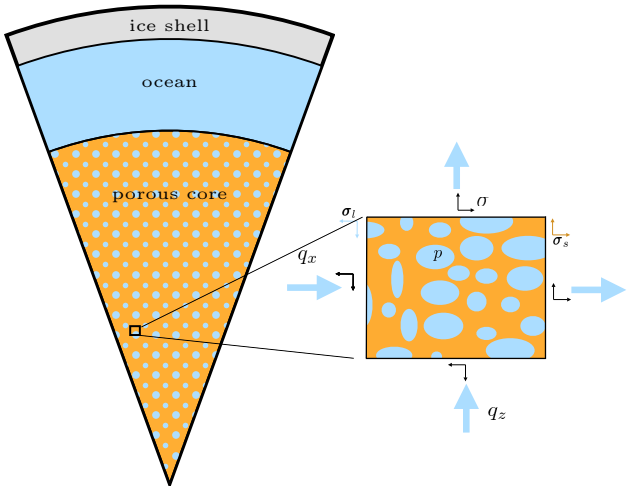

Figure 2.5 Model of Enceladus' interior. The inset shows a parcel of the porous core, the total stress tensor and those of the liquid and solid phases are indicated. The big blue arrows show the relative velocity of the liquid with respect to the solid.

$$\frac{\partial(1-\Phi)\rho_s}{\partial t} + \nabla\cdot\left[(1-\Phi)\rho_s \boldsymbol{v}_s\right] = 0, \tag{2.43b}$$

$$\Phi\rho_l\left(\frac{\mathrm{D}\boldsymbol{v}_l}{\mathrm{D}t} + 2\boldsymbol{\Omega}\times\boldsymbol{v}_l\right) = \nabla\cdot\Phi\boldsymbol{\sigma}_l - \Phi\rho_l\nabla\phi - \boldsymbol{F}, \tag{2.43c}$$

$$(1-\Phi)\rho_s\left(\frac{\mathrm{D}\boldsymbol{v}_s}{\mathrm{D}t} + 2\boldsymbol{\Omega}\times\boldsymbol{v}_s\right) = \nabla\cdot(1-\Phi)\boldsymbol{\sigma}_s - (1-\Phi)\rho_s\nabla\phi + \boldsymbol{F}. \tag{2.43d}$$

$\boldsymbol{q}$ is the segregation flux given by the relative velocity of the liquid phase with respect to the solid phase, $\boldsymbol{q} = \Phi(\boldsymbol{v}_l - \boldsymbol{v}_s)$ and $\boldsymbol{F}$ is an interaction force resulting from the viscous interaction between the solid and liquid phases given by (*Mckenzie*, 1984):

$$\boldsymbol{F} = \Phi\frac{\eta_l}{\kappa}\boldsymbol{q} - p\nabla\Phi. \tag{2.44}$$

η_l is the liquid viscosity, κ the matrix permeability, which depends on the geometry of the solid matrix (grain size, tortuosity of the pore space), and p the pore pressure. It is also useful to introduce an additional kinematic variable known as the variation of fluid content ζ that gives the volume of liquid entering the control volume per unit of solid frame volume, $\zeta = \Phi\nabla\cdot(\boldsymbol{u}_s - \boldsymbol{u}_l)$ (*Cheng*, 2016). As noted in the previous section, the inertial terms of the momentum equation for the solid phase can be neglected. For the fluid phase, the interaction force is larger than the inertial terms, which results in a low Reynolds number indicative of laminar flow. If this is the case, the inertial terms of the liquid phase momentum equation can also be neglected. It is common to assume that the stress tensor of the liquid is isotropic, $\boldsymbol{\sigma}_l = -p\boldsymbol{I}$ (see Chapter 5). With these approximations the mass and momentum equations can be written as:

$$\frac{\partial\rho}{\partial t} + \nabla\cdot\left[\rho_l\boldsymbol{q} + \rho\boldsymbol{v}_s\right] = 0, \tag{2.45a}$$

$$\nabla\cdot\boldsymbol{\sigma} - \rho\nabla\phi = 0, \tag{2.45b}$$

$$\frac{\partial \zeta}{\partial t} = -\nabla \cdot \boldsymbol{q}, \tag{2.45c}$$

$$\boldsymbol{q} = -\frac{\kappa}{\eta_l}\left(\nabla p + \rho_l \nabla \phi\right), \tag{2.45d}$$

where we have introduced the total stress $\boldsymbol{\sigma} = (1-\Phi)\boldsymbol{\sigma}_s - \Phi p \boldsymbol{I}$. Eqs. (2.45a, b) are the total mass and momentum conservation equations, and Eqs. (2.45c, d) are the mass and momentum conservation equations for the liquid phase, the second one being the well-known Darcy law for porous media.

To close the system, a constitutive equation relating stress and strain is required. It is very similar to the one used for a solid, except that instead of using the total stress ($\boldsymbol{\sigma}$), an effective stress ($\boldsymbol{\sigma}'$) should be employed (*Biot*, 1941),

$$\boldsymbol{\sigma}' = \boldsymbol{\sigma} + \alpha p \boldsymbol{I}. \tag{2.46}$$

$\alpha \in (0,1)$ is Biot's coefficient. The rheology parameters that appear in the constitutive equation (bulk modulus, shear modulus and viscosity) are not those of the solid phase alone. We can understand why this is the case if we consider how a porous and a solid deform if a pressure is applied. For a solid parcel, all compression arises from volume changes of the solid phase. In contrast, for a porous parcel, compression is split into three components: the compression of the solid phase, the compression of the liquid phase, and the compression arising due to the rearrangement of the pore matrix. For homogeneous isotropic material, the relation between the bulk modulus of the solid phase (K_s) and the porous matrix (K) is given by Biot's coefficient α as:

$$\alpha = 1 - \frac{K}{K_s}. \tag{2.47}$$

As we did for the solid phase, we can split the different fields into an unperturbed and a perturbed state to obtain a linearized version of the equations:

$$\nabla \cdot \boldsymbol{\sigma}^{\Delta} - \nabla(\rho_0 g \boldsymbol{u} \cdot \boldsymbol{e}_r) - \rho_0 \nabla \phi^{\Delta} - \rho^{\Delta} g \boldsymbol{e}_r = 0, \tag{2.48a}$$

$$\frac{\rho^{\Delta}}{\rho_0} = -\nabla \cdot \boldsymbol{u} + \frac{\rho_{l,0}}{\rho_0}\zeta, \tag{2.48b}$$

$$\boldsymbol{q} = -\frac{\kappa}{\eta_l}\left(\nabla p^{\Delta} + \rho_{l,0}\nabla \phi^{\Delta} + g\rho_l^{\Delta}\boldsymbol{e}_r\right), \tag{2.48c}$$

$$\frac{\partial \zeta}{\partial t} = -\nabla \cdot \boldsymbol{q}, \tag{2.48d}$$

$$\nabla^2 \phi^{\Delta} = 4\pi G \rho^{\Delta}. \tag{2.48e}$$

Comparing these equations with those obtained for solid and liquid phases alone, we can see some similarities and differences. The presence of a fluid introduces an additional pressure (the pore pressure) that can affect how the solid matrix responds to

tides. Additionally, pressure gradients induce a Poisseuille-like flow of water through the porous matrix, introducing an additional source of energy dissipation, Darcy dissipation, that can be computed as:

$$\dot{E}_l = \frac{1}{T}\int_0^T \frac{\eta_l}{\kappa}\boldsymbol{q}\cdot\boldsymbol{q}\,dt. \tag{2.49}$$

A LARGELY UNCHARTED TERRITORY

As mentioned above, the tidal response of bodies with porous tides has received little attention. *Vance et al.* (2007) provided a first estimate of energy dissipation due to Darcian flow on Europa and Enceladus hydrothermal system. They used the approach *Wang and Davis* (1996) and *Wang et al.* (1999) employed to study dissipation in Earth's subsea formations due to the M2 tide. The approach of *Vance et al.* (2007); *Wang and Davis* (1996); *Wang et al.* (1999), however, did not consider how the pore pressure affects the tidal response of the body.

Liao et al. (2020) addressed the previous issue and accounted for the interactions between the solid and liquid phases. They applied Biot's poroviscoelasticity theory (*Biot*, 1941) to Enceladus and showed that tidal dissipation can be enhanced due to poroviscoelastic effects. Nevertheless, they introduced several simplifications that require further examination, the most important ones being: they ignored self-gravitation, considered only the moon's core and ignored ocean and ice shell, and used a simplified set of boundary conditions at the core's surface. In Chapter 5, we present an extension of the model of *Liao et al.* (2020) that does not rely on such simplifications. We use the model to tackle the following research questions:

4. How does the presence of a porous layer alter the tidal response of a tidally active moon?

5. What is the contribution of Darcy dissipation to Enceladus' energy budget?

2.3. TIDES AND ORBIT

So far, we have considered how a body's orbit results in a changing tidal potential (Section 2.1) and how the body responds to this tidal potential (Section 2.2) as two separate problems. However, as we will see in this section, orbit and tides are closely related. When Neil Armstrong and Buzz Aldrin landed on the Moon, they left more than footprints on the surface. In the Mare Tranquillitatis, next to the remnants of the Eagle landing module, a half meter wide array of retroreflectors stand facing the Earth. These retroreflectors can be used to obtain with precision the distance between the Earth and the Moon by firing a laser and measuring how much time it takes for the signal to get back. By periodically repeating this measurement, it is found that the moon is on average moving away from the Earth at a rate of approximately 4 cm per year (e.g., *Munk and Wunsch*, 1997).

Why is the Moon moving away from the Earth? The answer is again tides. As we will see, the rate at which the Moon moves away from the Earth is closely linked with how much energy is dissipated in the Earth's oceans, shallow seas and interior due to tides. For this reason, measurements of a moon's position and how it changes over time provide invaluable insights into the tidal response of a body. These observations range from precise measurements of an object's angular position in the sky (astrometry) obtained from both Earth-based observations and spacecraft measurements, to laser ranging measurements (such as those done using the retroreflectors left on the Moon's surface) and the radio tracking of space probes. In this section, we will explain how tides and orbital changes are interlinked and underline what observations of the orbits of the Solar System moons tell us about the interior of planets and their satellites.

As opposed to the Earth-Moon pair, the tidally active moons of gas giants are in systems with multiple moons. To understand the interplay between tides and orbit we need to consider the orbital interaction between moons. In what follows, we will first study the tidal effects in a relatively simple system consisting of one planet and one moon (Sec. 2.3.1), and then examine how gravitational interactions between multiple moons alter this picture (Sec. 2.3.2). There, we will place special emphasis on two bodies: Enceladus and Io, for which we will discuss how astrometric observations can be used to constrain their thermal budget and forecast their orbital evolution.

2.3.1. ISOLATED MOON-PLANET SYSTEM

The first rigorous study of how tides affect the rotation and orbit of planetary objects was done by the son of the British naturalist Charles Darwin, George Darwin (*Darwin*, 1880). Darwin's work was later generalized by *Kaula* (1964) and led to a myriad of applications. Here, we briefly review the theory, for a more in-depth treatment of the problem we refer the interested reader to *Boué and Efroimsky* (2019); *Efroimsky and Williams* (2009); *Kaula* (1964).

TIDAL-INDUCED PERTURBING POTENTIAL

As showed in Section 2.2, tidal forces exerted by a secondary deform the primary. The tidal distortion of the primary produces a perturbing potential (T) proportional to the tidal potential (2.37). The tidal response is not instantaneous, but is characterized by a phase lag given by the quality factor Q (Eq. (2.27)). We can write the perturbing potential at the surface of the primary as (2.37)

$$T = \sum_{l=2}^{\infty} | k_l | \left[\phi_l^T(R)\right]_{lag}, \tag{2.50}$$

where k_l is the tidal Love number of spherical harmonic degree l of the primary. The perturbing potential at a point outside the primary located at distance d can be found by solving Laplace's equation, $\nabla^2 T = 0$, in spherical coordinates (see *Dermott and Sagan*, 1995, Chapter 4) and using that the tidal potential should be given by (2.50) at $d = R$ and vanish at $d \to \infty$;

$$T(d) = \sum_{l=2}^{\infty} \left(\frac{R}{d}\right)^{l+1} \mid k_l \mid \left[\phi_l^T(R)\right]_{lag}. \tag{2.51}$$

Let us imagine now that we want to compute what the effect of this perturbation is in a body M orbiting the primary. Firstly, we note that the tidal potential ϕ^T is given by Eq. (2.3), secondly, we can expand d in similar way as we did for d^* in the tidal potential (Eq. (2.1)) and we get (e.g., *Efroimsky and Williams*, 2009; *Kaula*, 1964):

$$\begin{aligned} T = &-\frac{GM^*}{a^*} \sum_{l=2}^{\infty} \left(\frac{R}{a}\right)^{l+1} \left(\frac{R}{a^*}\right)^{l} \sum_{m=0}^{l} \frac{(l-m)!}{(l+m)!}(2-\delta_{0m}) \\ &\sum_{p=0}^{l} F_{lmp}(i^*) \sum_{q=-\infty}^{\infty} G_{lpq}(e^*) \sum_{h=0}^{l} F_{lmh}(i) \sum_{j=-\infty}^{\infty} G_{lhj}(e) \\ &\mid k_{lmpq} \mid \cos\Big((v^*_{lmpq} - m\varphi_0^*) - (v_{lmhj} - m\varphi_0) - \epsilon_{lmpq}\Big). \end{aligned} \tag{2.52}$$

ϵ_{lmpq} and k_{lmpq} are the phase lag in the tidal response and the tidal Love numbers of the primary, which depend on the forcing frequency $\dot{v}^*_{lmpq} - m\Omega$ as indicated by the subscripts. Orbital elements with and without (*) correspond to the tide-raising body and the body whose orbital changes we want to study, respectively. Both φ_0' and ${\varphi_0'}^*$ indicate the sidereal time of the primary and are equal, the reason we keep them will become evident shortly. Of particular interest is the situation where we want to study the effects of the tidal deformation of the primary in the orbit of the secondary (e.g., how does the tidal response of the Earth to lunar tides affect the Moon's orbit?). If this is the case, we have that $(a, e, i, \mathscr{M}, \omega, \gamma) = (a^*, e^*, i^*, \mathscr{M}^*, \omega^*, \gamma^*)$ and using the definitions of v_{lmpq} and v^*_{lmhj} (2.4), the angular argument reduces to:

$$v^*_{lmpq} - v_{lmhj} - \epsilon_{lmpq} = (2h - 2p + q - j)\mathscr{M} + (2h - 2p)\omega - \epsilon_{lmpq}. \tag{2.53}$$

TIDAL EFFECT ON ORBIT AND SPIN

The perturbing potential has two effects: (1) it changes the orbit of the secondary, and (2) it alters the spin of the primary (Figure 2.6). As noted before, the role of the primary and the secondary can be exchanged: in the same way M_1 raises tides in M_2 that alter the spin of M_2 and orbit of M_1, M_2 raises tides in M_1 that alter the spin of M_1 and the orbit M_2. Considering M_1 and M_2 to be a planet and a moon, we consider the tidal effects on spin and orbit of the two bodies.

The attraction of the secondary on the tidal bulge of the primary produces a gravitational torque that affects the spin of the primary. The gravitational torque is given by:

$$\tau = -M^* \frac{\partial T}{\partial \varphi_0}. \tag{2.54}$$

Taking the derivative of Eq. (2.52), using that $\varphi_0 - \varphi_0^* = 0$, Eq. 2.53 and averaging over an orbital-period, we get (e.g., *Efroimsky and Williams*, 2009):

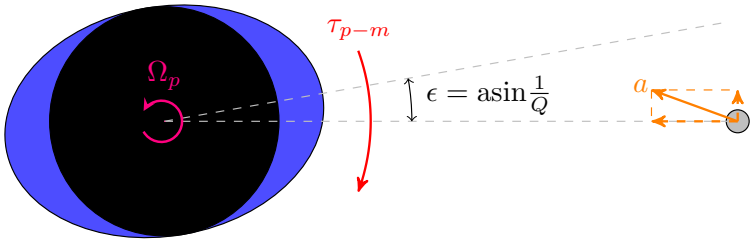

Figure 2.6 Sketch showing the effects of the tidal bulge raised by the moon on the planet on the planet's spin and moon's orbit. It is assumed that the spin-rate of the planet is higher than the moon's orbital frequency. The phase lag in the planet's tidal response provokes a tidal torque τ_{p-m} that spins down the planet and produces a tangential acceleration that causes outward orbital migration.

$$\bar{\tau} = \frac{GM^{*2}}{a}\sum_{l=2}^{\infty}\left(\frac{R}{a}\right)^{2l+1}\sum_{m=0}^{l}2m\frac{(l-m)!}{(l+m)!}\sum_{p=0}^{l}F^2_{lmp}(i)\sum_{q=-\infty}^{\infty}G^2_{lpq}(e)\,|\,k_{lmpq}\,|\,\sin(\epsilon_{lmpq}). \tag{2.55}$$

The spin change of the planet and the moon simply follow from the conservation of angular momentum:

$$I_p\frac{\mathrm{d}\Omega_p}{\mathrm{d}t} = \bar{\tau}_{p-m}, \tag{2.56a}$$

$$I_m\frac{\mathrm{d}\Omega_m}{\mathrm{d}t} = \bar{\tau}_{m-p}, \tag{2.56b}$$

where I_p and I_m are respectively the moon and planet moment of inertia, and τ_{p-m} and τ_{m-p} are the torques exerted by the moon to the planet and by the planet to the moon, respectively.

The effect of tides in orbit can be computed using Lagrange-type planetary equations (see *Boué and Efroimsky*, 2019, for the explicit equations and their derivation), which allow to compute the change in orbital elements due to a perturbing potential $\mathscr{R}$

$$\frac{\mathrm{d}\beta_i}{\mathrm{d}t} = b_{ij}\frac{\partial\mathscr{R}}{\partial\beta_j}. \tag{2.57}$$

β_i stands for the orbital elements, b_{ij} are a series of coefficients that depend on the orbital elements, and $\mathscr{R}$ is the total perturbing potential, which accounts for both the effect of the deformation of the planet due to moon tides (T_{m-p}) and of the deformation of the moon due to planet tides (T_{p-m}) (*Boué and Efroimsky*, 2019; *Kaula*, 1964)

$$\mathscr{R} = \frac{M_p + M_m}{M_p M_m}\left(M_m T_{m-p} + M_p T_{p-m}\right). \tag{2.58}$$

Eqs. (2.57), (2.56) provide a consistent and robust way to compute the effects of tides in orbit and spin state. However, they are not always transparent and intuitive. We can try to understand the first order effects by considering the first order terms in the previous equations and using conservation principles. To do so, we assume a moon orbiting a planet with zero inclination.

As noted before, if neither the moon nor the planet are synchronous, the leading term in eccentricity is the semidiurnal tide (i.e., $l = 2, m = 2, p = 0, q = 0$). In such a case, the tidal torque exerted by the moon to the planet τ_{p-m}, and by the planet to the moon τ_{m-p} are given by (2.55):

$$\tau_{p-m} = -\frac{3}{2}\frac{|k_{2,p}|}{Q_p}\frac{GM_m^2R_p^5}{a^6}\text{sign}(\Omega_p - n), \tag{2.59a}$$

$$\tau_{m-p} = -\frac{3}{2}\frac{|k_{2,m}|}{Q_m}\frac{GM_p^2R_m^5}{a^6}\text{sign}(\Omega_m - n). \tag{2.59b}$$

If the planet or moon rotates faster than the moon's orbital frequency, the torque slows it down. Using the conservation of angular momentum, we can compute how fast the planet and the moon slow down. Comparing the expression obtained for the moon and the planet, we get:

$$\frac{\mathrm{d}\Omega_m/\mathrm{d}t}{\mathrm{d}\Omega_p/\mathrm{d}t} = \frac{|k_{2,m}|/Q_m}{|k_{2,p}|/Q_p}\frac{\rho_p}{\rho_m}\left(\frac{M_p}{M_m}\right)^2 \tag{2.60}$$

Rocky bodies have a $|k_2|/Q$ larger than that of gas giants. Additionally, moons are smaller or much smaller than their planet ($M_m \ll M_p$). This implies that a moon slows down much faster than the planet, which explains why the Moon and other satellites of the Solar System are tidally locked while planets are not. The tidal torque has an additional consequence; conservation of angular momentum implies that if the moon exerts a torque τ_{p-m} to the planet, a torque of the same magnitude and opposite sign acts on the moon. Such torque changes the angular momentum of the moon, $J^2 = M_m^2 G(M_p + M_m)a(1-e^2)$, as $\dot{J} = -\tau_{p-m}$. Assuming the eccentricity is small and $M_p \gg M_m$, the change in semi-major axis follows from:

$$\frac{\mathrm{d}a}{\mathrm{d}t} = \frac{2a}{J}\frac{\mathrm{d}J}{\mathrm{d}t} = 3na\frac{M_m}{M_p}\left(\frac{R_p}{a}\right)^5\frac{|k_{2,p}|}{Q_p}\text{sign}(\Omega_p - n) = \frac{a}{\tau_a}\text{sign}(\Omega_p - n) \tag{2.61}$$

where we have introduced the migration time scale τ_a. If the planet rotates faster than the moon orbits, the moon migrates outwards. This is the case for our Moon and most moons in the Solar System with the notable exception of the Martian moon Phobos. From (2.61), it follows that measurements of $\dot{a}$ can be used to obtain the value of $|k_{2,p}|/Q_p$. Using the $\dot{a}$ obtained using the retroreflectors installed on the Moon by the

Apollo astronauts, we find[4] $|k_{2,p}|/Q_p = 2.4 \cdot 10^{-2}$, which corresponds to 3.2 TW of energy dissipated due to Lunar tides (2.39). Similarly, precise astrometric observations of the Jovian and Saturnian moons done over the last centuries — and radiometric observations for the Saturnian system— allow to estimate the drifts in semi-major axis of the moons and constrain the Q_p of the planet (*Lainey et al.*, 2009, 2012, 2017, 2020), as we will discuss in more detail in the next section.

Finally, we also examine how tidal dissipation within the moon affects the orbit. As in the case of the planet, the tidal distortion of the moon gives rise to a perturbing potential T_{m-p} that also affects its orbit (see (2.58)). Again, some insight can be obtained applying conservation principles. Energy dissipated within the moon (Eq. 2.41) results in a decrease of the orbital energy, $E_{orbit} = -0.5GM_mM_p/a$:

$$\frac{\mathrm{d}a}{\mathrm{d}t} = 2\frac{a^2}{GM_mM_p}\left(\frac{\mathrm{d}E}{\mathrm{d}t}\right)_{tides} = -21na\left(\frac{R_m}{a}\right)^5 \frac{M_p}{M_m}\frac{|k_{2,m}|}{Q}e^2 \tag{2.62}$$

Additionally, energy dissipation within the moon modifies the orbital eccentricity. The change in eccentricity is related to the change in semi-major axis and orbital angular momentum J, if the eccentricity is small:

$$\frac{2J}{GM_pM_m^2}\frac{\mathrm{d}J}{\mathrm{d}t} = \frac{\mathrm{d}a}{\mathrm{d}t} - 2ae\frac{\mathrm{d}e}{\mathrm{d}t}. \tag{2.63}$$

If tidal dissipation occurs at constant angular momentum, we find:

$$\frac{\mathrm{d}e}{\mathrm{d}t} = \frac{1}{2ae}\frac{\mathrm{d}a}{\mathrm{d}t} = -\frac{e}{\tau_e} \tag{2.64}$$

with the circularization time-scale τ_e. Combining Eqs. (2.61, 2.62 and 2.64) we can get the total effect of tides on the moon's orbit:

$$\frac{1}{a}\frac{\mathrm{d}a}{\mathrm{d}t} = \frac{1}{\tau_a} - \frac{p_e e^2}{\tau_e}, \tag{2.65a}$$

$$\frac{1}{e}\frac{\mathrm{d}e}{\mathrm{d}t} = -\frac{1}{\tau_e}, \tag{2.65b}$$

with

$$\tau_a = \frac{1}{3n}\left(\frac{a}{R_p}\right)^5 \frac{M_p}{M_m}\frac{Q_p}{|k_{2,p}|}\mathrm{sign}(\Omega_p - n), \qquad \tau_e = \frac{2}{21}\frac{1}{n}\left(\frac{a}{R_m}\right)^5 \frac{M_m}{M_p}\frac{Q_m}{|k_{2,m}|}. \tag{2.66}$$

Note that we have introduced an additional constant p_e. For energy dissipation at constant angular momentum it equals 2, but, in general, the assumption that energy dissipation within the moon occurs at constant angular momentum J is not correct and $p_e = 38/7$ (see Section 6.7).

[4] Note that the 4 cm yr^{-1} corresponds to the total tidal dissipation in the Earth and here we have just considered the semidiurnal component of the lunar tide (M_2), hence the value we obtain should be understood as an upper bound

2.3.2. MULTIPLE MOON SYSTEM

Comparing the migration and the circularization time-scales, we can get some insight into how fast a moon migrates and how fast its orbit is circularized:

$$\frac{\tau_e}{\tau_a} = \frac{2}{7}\left(\frac{\rho_m}{\rho_p}\right)^2 \frac{R_m}{R_p}\frac{|\,k_{2,p}\,|\,/Q_p}{|\,k_{2,m}\,|\,/Q_m}. \tag{2.67}$$

For a moon around a gas giant, $R_m \ll R_p$ and $|\,k_{2,p}\,|\,/Q_p \ll |\,k_{2,m}\,|\,/Q_m$; consequently, we can expect that a moon's orbit is circularized much faster than the time it takes for it to migrate in the system. This introduces a new question: Why do some of the moons of the outer Solar System have a non-zero eccentricity? Two possible answers exist: (1) the eccentricity is a remnant of a past event that altered the moon's orbit (impact, resonance crossing, etc.) and the moon orbit is currently being circularized, or (2) a third body in orbit around the planet is modifying the orbit of the moon and constantly pumping the eccentricity. (1) is likely the case of Titan, (2) is the case of the three Galilean moons Io, Europa and Ganymede, as well as Saturnian moons Enceladus and Dione. Here, we will briefly explain how third body perturbations can excite the eccentricity of a moon.

MOON-MOON GRAVITATIONAL INTERACTIONS AND MEAN-MOTION RESONANCES

If there are multiple moons in a planetary system, they gravitationally interact. We consider two moons located at planetocentric distances $\boldsymbol{r}_i$, and $\boldsymbol{r}_o$, with i and o indicating inner and outer, respectively. The gravitational potential experienced by the inner moon is:

$$\mathscr{R}_{i-o} = -GM_o\left(\frac{1}{|\,r_i - r_o\,|} - \frac{\boldsymbol{r}_i\cdot\boldsymbol{r}_o}{r_o^3}\right). \tag{2.68}$$

The first term is called the direct term and results from the direct gravitational attraction of the outer moon to the inner moon, the second term is the indirect term, which accounts for the fact that we are using a planetocentric reference frame rather than an inertial reference frame (the planet orbits around the planet-moon barycenter). As we did to go from Eq. (2.1) to (2.3), we can expand $\boldsymbol{r}_i$ and $\boldsymbol{r}_o$ by using the orbital elements of the two moons to obtain the perturbing potential (e.g., *Le Verrier*, 1855; *Murray and Dermott*, 2000). The full expansion can be found in *Murray and Dermott* (2000), the leading terms are of the form

$$\mathscr{R}_{i-o} = -\frac{GM_o}{a_o} f(\alpha) e_i^{|q_1|} e_o^{|q_2|} \left(\sin\frac{i_i}{2}\right)^{|q_3|} \left(\sin\frac{i_o}{2}\right)^{|q_4|} \cos\left(\Phi_{pq_1q_2q_3q_4}\right), \tag{2.69}$$

with $\alpha = a_i/a_o$ and $f(\alpha)$ is a sum of Laplace coefficients and their derivatives (see *Murray and Dermott* (2000) for details about the $f(\alpha)$ function). Additionally, the condition $q = \sum_{i=1}^{4} q_i$ applies. The angular variable $\Phi_{pq_1q_2q_3q_4}$ is:

$$\Phi_{pq_1q_2q_3q_4} = p\lambda_i - (p+q)\lambda_o + q_1\tilde{\omega}_i + q_2\tilde{\omega}_o + q_3\gamma_i + q_4\gamma_o, \tag{2.70}$$

where λ is the mean longitude ($\lambda = \tilde{\omega} + M$), and $\tilde{\omega}$ the longitude of pericenter ($\tilde{\omega} = \omega + \gamma$).

Due to the small mass of the moons compared to the planet, the perturbing potential is much smaller than the planet's gravitational potential. Moreover, the perturbing potential often changes fast during an orbital revolution; consequently, its average over an orbital period is close to zero ($\bar{\mathscr{R}} = 0$) and the effect of moon-moon perturbations is small. However, if $\dot{\Phi}_{pq_1q_2q_3q_4} \approx 0$, the moon experiences a net force ($\bar{\mathscr{R}} \neq 0$) that can alter its orbit. If this occurs, we speak of a $p : (p+q)$ mean-motion resonance (MMR); q is the order of the resonance and indicates every how many conjunctions of the moons a conjunction occurs at the same mean longitude.

MMRs are common in the Solar System and have also been observed in exoplanetary systems, the most well-known being the TRAPPIST-1 system (*Gillon et al.*, 2017). In the Solar System the most classic example is the Laplace resonance, which involves the three inner Galilean moons. The study of the Galilean moons has played a central role in the development of astronomy (see *de Sitter* (1931) for a historical overview of the problem). The mean longitudes and longitudes of pericenter of the three moons obey the following relations:

$$\lambda_1 - 2\lambda_2 + \tilde{\omega}_1 \approx 0^\circ, \tag{2.71a}$$

$$\lambda_1 - 2\lambda_2 + \tilde{\omega}_2 \approx 180^\circ, \tag{2.71b}$$

$$\lambda_2 - 2\lambda_3 + \tilde{\omega}_2 \approx 0^\circ. \tag{2.71c}$$

An expression involving the three satellites can be found:

$$\lambda_1 - 3\lambda_2 + 2\lambda_3 \approx 180^\circ. \tag{2.72}$$

The previous equations are not exact identities, in fact the angles librate around the values indicated. For the last angle, the libration period is 2074 days (*Lieske*, 1980). If we look closer at (2.71), we see that the Laplace resonance is a chain of two 2:1 MMRs involving the pairs Io-Europa and Europa-Ganymede.

The stability of the Laplace resonance was a puzzle until Lagrange presented a mathematical theory of the motion of the moons that demonstrated that it naturally arises from the gravitational interaction of the moons[5]. Nevertheless, the origin of the Laplace resonance is, even today, a topic of intense debate. Two competing theories exist: the Laplace resonance is either primordial in origin or not. The first theory postulates that the Laplace resonant chain was assembled in the protoplanetary disk due to the inward migration of the Galilean moons (*Peale and Lee*, 2002). In contrast, the second theory defends that the resonance was assembled once the protoplanetary disk dissipated and the moons migrated outwards due to tides via the process explained in the previous section (e.g., *Malhotra*, 1991; *Yoder*, 1979).

[5]The work of the French mathematicians Lagrange and Laplace on the Galilean moons was closely related to another question that had troubled Newton and the answer of which involved creating the mathematical machinery that today is so central to celestial mechanics. This question was: is the Solar System stable?

ECCENTRICITY PUMPING AND THE EQUILIBRIUM ECCENTRICITY

Regardless of its origin, the orbital commensurability given by (2.71) results in a coherent gravitational perturbation that can increase the eccentricity of the moons involved. The change in eccentricity close to a resonance can be obtained using Lagrange's planetary equations (Eq. (2.57)). It can be shown that the change of orbital eccentricity of the inner moon in a MMR is given by (*Dermott et al.*, 1988, Equation 21):

$$\begin{aligned}\frac{1}{e_i}\left(\frac{\mathrm{d}e_i}{\mathrm{d}t}\right)_{res} = -\frac{q_1}{3n_i e_i^2}\left(p^2+(p+q)^2\frac{M_i}{M_o}\alpha^2\right)^{-1}\left[p\left(\frac{\mathrm{d}n_i}{\mathrm{d}t}\right)_t-(p+q)\left(\frac{\mathrm{d}n_o}{\mathrm{d}t}\right)_t\right]\approx \\ \frac{1}{2}\frac{q_1}{e_i^2}\left(p^2+(p+q)^2\frac{M_i}{M_o}\alpha^2\right)^{-1}\left[\frac{p}{\tau_{a,i}}-\frac{(p+q)\alpha^{3/2}}{\tau_{a,o}}\right].\end{aligned} \tag{2.73}$$

$\dot{n}_t$ indicates the change in orbital frequency due to the action of tides alone. Note that for simplicity in the last step we ignored the change in semimajor axis due to dissipation in the satellite. If the inner moon migrates outwards faster than the outer moon ($\tau_{a,i} < p(p+q)^{-1}\alpha^{-3/2}\tau_{a,o}$), its eccentricity is pumped. This is indeed normally the case. Recalling the tidal migration time-scale (Eq. (2.66)), we see that, unless $k_{2,p}/Q$ is frequency dependent —as seems to be the case for Saturn (*Lainey et al.*, 2017, 2020)— or the outer moon is much more massive than the inner moon, the inner moon migrates faster than the outer moon. This seems to suggest that as the inner moon moves deeper into resonance its eccentricity increases until outward migration causes the moon to move out of resonance. However, we need to remember that tidal dissipation within the moon tends to decreases its eccentricity, (2.65). As a consequence, an equilibrium configuration can be attained in which

$$\left(\frac{\mathrm{d}e_i}{\mathrm{d}t}\right)_{res}+\left(\frac{\mathrm{d}e_i}{\mathrm{d}t}\right)_{tides}\approx 0. \tag{2.74}$$

Using (2.65) and (2.73), we find that this occurs for an eccentricity of:

$$e_i^2 \sim \frac{\tau_{e,1}}{\tau_{a,1}} = \frac{2}{7}\left(\frac{M_i}{M_p}\right)^2\left(\frac{R_p}{R_i}\right)^5\frac{|k_{2,p}|/Q_p}{|k_{2,m}|/Q_m} \tag{2.75}$$

The equilibrium configuration can be understood as follows: if the inner moon is perfectly elastic and there is no tidal dissipation, conjunction occurs when the inner moon is at its pericenter and the outer moon is at its apocenter; the tangential component of the gravitational force exerted by the inner to the outer moon during an orbital period averages out to zero. In contrast, if there is tidal dissipation in the inner satellite, conjunction occurs when the inner moon is slightly past its pericenter. This breaks the symmetry and results in a net tangential force exerted by the inner moon to the outer moon. Angular momentum is transferred from the inner to the outer moon; the inner moon "pushes" the outer moon. If the amount of transferred angular momentum is such as that (2.74) is satisfied, the eccentricity stops growing and the two moons can remain in a stable configuration for a long period of time.

Plugging (2.75) into the expression of tidal dissipation for a synchronous moon, Eq. (2.41), we can compute the amount of tidal dissipation when this configuration is attained:

$$\dot{E} \sim \frac{n^5 R_p^5}{G} \left(\frac{M_m}{M_p}\right)^2 \frac{|\, k_{2,p}\,|}{Q_p}. \tag{2.76}$$

Interestingly, in equilibrium dissipation does not depend on the structure of the satellite but on how much energy dissipation occurs within the planet —dissipation within the planet prompts a transfer of rotational energy from the planet to the moon where it is dissipated. The previous equation makes evident that the more dissipative a planet is, the higher tidal dissipation in one of its moons can be.

As mentioned above, the value of $|\, k_{2,p}\,|/Q_p$ can be estimated from the observations of the moon's dynamics. Using observations spanning more than a century, the migration rate of the moons of Jupiter and Saturn have been obtained (*Lainey et al.*, 2009, 2012, 2017, 2020) and the value $|\, k_{2,p}\,|/Q_p$ for these planets inferred. In the case of the Jovian system, intense tidal dissipation within Io has such a prominent role in the dynamics of the Laplace resonance that the value of $|\, k_{2,Io}\,|/Q_{Io}$ has also been estimated from astrometric data — albeit with a high correlation with the $|\, k_{2,p}\,|/Q_p$ of Jupiter (*Lainey et al.*, 2009). Apart from this, direct measurements of $\dot{E}$ are available for two moons, Io and Enceladus. Below we discuss what this ensemble of observations implies for the thermal and orbital state of these two moons.

ENCELADUS

Enceladus' thermal output has been measured by Cassinis' CIRS instrument: the South Polar Terrain radiates around 16 GW of energy (*Howett et al.*, 2011). An additional constraint on Enceladus' thermal output can be obtained by considering the amount of heat conducted through the ice shell. If we assume Enceladus is in thermal equilibrium (the amount of heat produced inside is conducted through the shell and radiated to space), it can be shown that (*Nimmo et al.*, 2018):

$$\dot{E} \approx 20 \left(\frac{25}{h_{ice}}\right) \quad [\text{GW}] \tag{2.77}$$

where h_{ice} is the mean ice thickness in km.

Using the concepts introduced in the previous section, we can compare these two estimates with the amount of energy dissipation Enceladus would experience in its current 2:1 MMR with Dione if it was in orbital equilibrium. Using (2.76), we get

$$\dot{E} \approx 1.5 \left(\frac{18000}{Q_\hbar}\right) [\text{GW}], \tag{2.78}$$

where we have retained the prefactors and assumed that $k_{2,\hbar} = 0.34$ (*Lainey et al.*, 2017). As noted above, the thermal output of Enceladus in orbital equilibrium solely depends on the dissipative properties of Saturn, and not those of the moon. A lower bound of

$|k_{2,\text{♄}}|/Q_{\text{♄}}$ can be obtained by considering the time it would take for Saturn's moons to migrate from the planet's Roche limit or synchronous radius to their current position during the age of the Solar System. For the innermost icy moon, Mimas, this yields $Q_{\text{♄}} > 18000$ (*Peale et al.*, 1980). Inserting this value in (2.78) and comparing the result with the observed $\dot{E}$ or that given by (2.77), this would imply Enceladus is not in orbital equilibrium. If this was the case, it would indicate that we are witnessing Enceladus in a transient state of anomalously high thermal activity, probably associated with an episodic release of tidal heat built up in its interior during many years.

As mentioned above, rather than inferring the value of $Q_{\text{♄}}$ from theoretical considerations, we can try to measure it using precise observations of the moons' positions. Combining Earth-based astrometric observations of Saturn's moons with accurate ephemerides of the moons obtained using the Cassini space probe, *Lainey et al.* (2012, 2017, 2020) obtained a $Q_{\text{♄}}$ about ten times lower. The low quality factor of Saturn can imply a late-formation of the Saturnian moons as proposed by *Asphaug and Reufer* (2013) or be indicative of a $Q_{\text{♄}}$ strongly dependent on frequency. Most important for our present discussion is the fact that a low $Q_{\text{♄}}$ reconciles the observed thermal output of the moon with the moon being in thermal-orbital equilibrium.

If Enceladus is in thermal-orbital equilibrium, a major question arises. Using traditional viscoelastic models, tidal dissipation in the solid layers (ice and core) cannot easily account for this high level of tidal dissipation. The core and conductive ice shell are expected to be too rigid to generate sufficient heat (e.g., *Roberts and Nimmo*, 2008; *Souček et al.*, 2016). This has puzzled the scientific community in the last decades (e.g., *Lainey et al.*, 2012; *Meyer and Wisdom*, 2007; *Nimmo et al.*, 2018) and has prompted research into other processes that can close Enceladus' thermal budget such as ocean tides (e.g., *Chen and Nimmo*, 2011; *Tyler*, 2009; *Wilson and Kerswell*, 2018) or tides in an unconsolidated porous core (*Choblet et al.*, 2017; *Liao et al.*, 2020). In this context, we can appreciate the relevance of research questions 3 and 5 in new light.

IO

Io's volcanic activity is so prominent that its thermal emissions can be observed and measured using ground-based telescopes (e.g., *Matson et al.*, 1981; *Veeder et al.*, 1994). The moon's thermal emissions were also accurately measured thanks to the Galileo mission (*Spencer et al.*, 2000). Average surface heat flux estimates obtained using the two methods cluster around $2\,\mathrm{W\,m^{-2}}$. This value is consistent with the $|k_{2,Io}|/Q_{Io}$ obtained from astrometric observations indicating that the moon is in thermal equilibrium (Io radiates approximately as much heat as it produces inside). Even though the value of $|k_{2,Io}|/Q_{Io}$ is well constrained, how and where energy is dissipated within Io is still a matter of debate. Io's volcanic activity might be primarily driven by tidal dissipation in a thin partially-molten asthenosphere, in the deep mantle (e.g., *Segatz et al.*, 1988, Figure 2.4), or, alternatively, in a liquid magma ocean (*Tyler et al.*, 2015). As for Saturn, Jupiter's $|k_{2,♃}|/Q_{♃}$ has been constrained using astrometric observation (*Lainey et al.*, 2009). The obtained value indicates that Io is not in orbital equilibrium: it is losing more orbital energy than it is gaining due to the transfer of angular momentum from Jupiter. While it is unknown whether this is a trend or a long-term period variation, it evidences that the

Laplace resonance is not static but it is presently evolving.

The fact that Io's volcanic activity can be observed from Earth has prompted an interest in the detection of tidally heated exomoons. Just as our Io, it is possible that similar tidally heated moons might exist in other planetary systems. *Peters and Turner* (2013) hypothesized that future telescopes such as the James Web Telescope could observe the thermal emission of a tidally heated exomoon with a thermal output higher than that of Io, a super-Io. Furthermore, *Oza et al.* (2019) proposed that some of the chemicals expelled via volcanism in a tidally heated moon leave a distinct signature in the spectra of gas giants.

We have seen that for Io to exist, several aspects need to converge: a mean-motion resonance, the moon needs to have certain internal structure and rheology, Jupiter must be quite dissipative, etc. The same is true for a super-Io. Moreover, as evidenced by astrometric observations, the Laplace resonance is not static, it has evolved and will evolve throughout the life of the Solar System. This exemplifies that a super-Io is not necessarily active during its whole life —we can expect that as it migrates away from the planet tides become weaker and so does tidal dissipation. In Chapter 6, we study these elements to answer the following research questions:

6. What is the thermal state of a super-Io?

7. How long can a super-Io persist in an observable state?

3

TIDES IN SUBSURFACE OCEANS WITH MERIDIONAL VARYING THICKNESS

M. ROVIRA-NAVARRO , T. GERKEMA, L. R.M. MAAS, W. VAN DER WAL, R. VAN OSTAYEN,B. VERMEERSEN

Tidal heating can play an important role in the formation and evolution of subsurface oceans of outer-planet moons. Up until now tidal heating has only been studied in subsurface oceans of spatially uniform thickness. We develop a numerical model to consider oceans of spatially variable thickness. We use the Laplace Tidal Equations for the ocean and model the ice shell using membrane theory. The problem is solved using the commercial Finite Element software Comsol Multiphysics ®. We use this new model to study the tidal response of Enceladus' ocean with a twofold objective: to understand how ocean thickness variations modify the tidal response of a subsurface ocean and to assess if tidal dissipation in an Enceladan ocean with varying ocean thickness can explain the high heat flux emanating from Enceladus' South Polar Terrain and the perdurance of a subsurface ocean. We consider the effect of meridional ocean thickness changes of spherical harmonic degree two and three as suggested by topography and gravimetry data. We observe that an ocean with degree two topography responds with the same eigenmodes as an ocean of constant thickness but resonances occur for thicker oceans. However, resonant ocean thick-

An earlier version of this chapter is published in Icarus (*Rovira-Navarro et al.*, 2020): Rovira-Navarro, M., Gerkema, T., Maas, L. R., van der Wal, W., van Ostayen, R., & Vermeersen, B. (2020), Tides in subsurface oceans with meridional varying thickness, Icarus, 343, 113,711.

nesses are still thin compared to current estimates for Enceladus ocean thickness. Rossby-Haurwitz waves, excited by the obliquity tide for thick oceans of constant thickness, are not excited at the tidal frequency when oceans of variable thickness are considered. This result implies that the role of the obliquity tide in ocean tidal-dissipation might have been overestimated for Enceladus and other icy worlds. An antisymmetric, degree-three ocean thickness variation mixes the ocean modes excited in a constant thickness ocean by the eccentricity and obliquity tide.

3.1. INTRODUCTION

The discovery of subsurface oceans in the outer Solar System (e.g., *Beghin et al.*, 2010; *Beuthe et al.*, 2016; *Iess et al.*, 2014; *Khurana et al.*, 1998; *Kivelson et al.*, 1996; *Saur et al.*, 2015; *Thomas et al.*, 2016) has raised new questions on the thermal evolution of icy moons. Because they receive little energy from the Sun, the persistence of subsurface oceans in these bodies needs to be explained by internal heat sources such as radiogenic heating and tidal dissipation and/or the presence of dissolved salts or ammonia that decrease water's melting temperature. Tidal dissipation arises due to the non-zero obliquity and eccentricity of synchronously rotating icy satellites. It has long been recognised that tidal dissipation in solid viscoelastic layers can generate enough heat to maintain subsurface water reservoirs (e.g., *Cassen et al.*, 1979). This is the case of the Jovian satellites Europa, Ganymede and Callisto, where models including radiogenic and tidal heating predict the presence of subsurface oceans (e.g., *Hussmann et al.*, 2002; *Ojakangas and Stevenson*, 1989; *Spohn and Schubert*, 2003). However, for Enceladus, tidal heating in the solid layers of the moon is not enough to explain the presence of a global ocean (*Běhounková et al.*, 2017; *Souček et al.*, 2019; *Tobie et al.*, 2008) unless the satellite rocky core is unconsolidated (*Choblet et al.*, 2017). Neither can it account for the $10-50$ GW of average tidal dissipation suggested by astrometric observations (*Lainey et al.*, 2012, 2017; *Nimmo et al.*, 2018) and the 4.2 GW of heat emanating from Enceladus' South Polar Terrain (SPT) observed by Cassini's CIRS instrument (*Spencer et al.*, 2013). This fact has led to the speculation that oceanic tidal dissipation contributes significantly to the thermal budget of subsurface oceans (e.g., *Tyler*, 2008).

In the last decade, the role of ocean dynamics in tidal-dissipation has been investigated. *Tyler* (2011, 2014, 2008, 2009) considered the response of an ice-free ocean to tides, *Matsuyama* (2014) expanded the formulation to consider the effect of self-gravity and a deformable rocky core. More recently, models that consider the overlying ice shell have been developed (*Beuthe*, 2016; *Hay and Matsuyama*, 2017, 2019; *Matsuyama et al.*, 2018). The ocean response highly depends on the surface gravity wave speed (c) which is given by $\sqrt{gh}$, with g being the ocean surface gravity and h the ocean thickness. The time it takes for a perturbation to travel around the moon is $2\pi R/c$, with R the moons's radius. If this time is much smaller than the tidal period, the ocean responds following nearly the equilibrium tide and oceanic tidal dissipation becomes negligible. Otherwise, the dynamic response of the ocean needs to be considered. Resonant ocean thicknesses exist for which tidal dissipation becomes very high. However, these resonances happen for oceans considerably thinner than those present on the moons of the outer Solar System (e.g., *Matsuyama et al.*, 2018; *Tyler*, 2014). It has been suggested that these resonances can prevent subsurface oceans from freezing as they get thinner (*Tyler*, 2011), although this may not be the case for small satellites like Enceladus where the effective rigidity of the ice shell is large (e.g., *Hay and Matsuyama*, 2019).

The obliquity tide can also excite (planetary) Rossby-Haurwitz waves (*Tyler*, 2008). Contrary to surface gravity waves, the restoring force lies in the conservation of potential vorticity (the fluid dynamical analog of angular momentum conservation) arising in a field where background vorticity varies spatially (such as due to a latitudinal gradient in planetary vorticity, or due to thickness-variations of a rotating fluid). These waves are

characterised by an ocean flow that is tangentially non-divergent implying that there are no surface displacements in the radial direction. Rossby-Haurwitz waves were argued to play a major role in preventing Enceladus and Europa' ocean from freezing (*Tyler*, 2011, 2008, 2009). However, this argument relied on what is likely a two orders of magnitude overestimate of the obliquity of Enceladus (*Chen and Nimmo*, 2011) and the debate on the role of tidal heating in the ocean of Enceladus was reopened.

All of the previous studies are restricted to oceans of constant thickness. However, it is expected that subsurface oceans have thickness variations. For instance, gravity and topography data suggests that Enceladus' ocean thickness is not constant: the ice shell has degree two and three meridional thickness variations (*Beuthe et al.*, 2016; *Čadek et al.*, 2016; *Hemingway and Mittal*, 2019). On Earth, tides are greatly affected by ocean bathymetry, which raises the question of how the tidal response of a subsurface ocean of variable thickness differs from that of an ocean of constant thickness. In particular, we want to understand what the effect of ocean thickness variations is on gravity waves resonances and the excitation of Rossby-Haurwitz waves.

To tackle these questions we use a finite element software package Comsol Multiphysics ® to solve the Laplace Tidal Equations for an ocean with varying thickness. To account for the ice shell we use the thin shell theory of *Beuthe* (2008, 2016) in the membrane limit. We consider a subsurface ocean overlying a rigid spherical core and neglect the effects of self-gravity. While our method can illustrate the effect of ocean thickness changes for subsurface oceans in general, we focus on Enceladus as there is compelling evidence for meridional ocean thickness variations and closing its thermal budget has proven to be more problematic than for other icy worlds (*Nimmo et al.*, 2018). We start by considering an ocean of constant thickness and its solutions and then add meridional degree two and three ocean thickness variations via the dependence of phase speed on ocean thickness, while formally keeping the thickness of the elastic lid constant. This implicitly corresponds to an ocean with bedrock topography (Figure 3.1). Even though our model has limitations (no self-gravity, a rigid core and constant ice shell thickness), it provides the first insight on how ocean thickness variations change the dynamic tidal response of subsurface oceans.

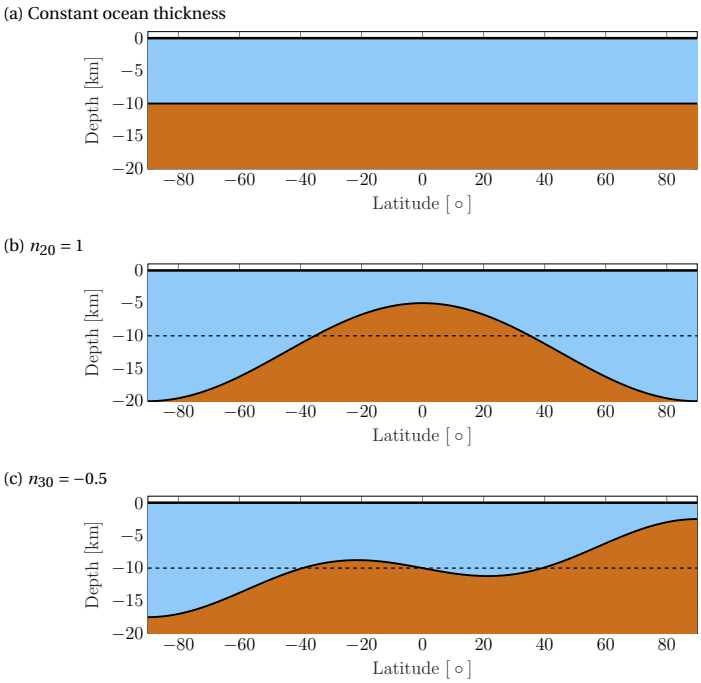

Figure 3.1 Ocean thickness for a uniform ocean 10 km thick (a) and oceans with degree two (b) and three (c) meridional thickness variations.

3.2. PROBLEM FORMULATION AND ASSUMPTIONS

The Laplace Tidal Equations (LTE) were presented by *Laplace* (1798) in his study of barotropic (surface) tides. We use the formulation given in *Tyler* (2011). The linearised LTE for an ocean of variable thickness h and surface gravity g on a spherical body with radius R rotating at angular frequency Ω are given by:

$$\partial_t \boldsymbol{s} - f\,\boldsymbol{s} \times \boldsymbol{r} = -c^2 \nabla (m + m_f) - F_{diss}, \tag{3.1a}$$

$$\partial_t m + \nabla \cdot \boldsymbol{s} = 0, \tag{3.1b}$$

where c is the local surface gravity wave phase speed that is a function of ocean thickness, f the Coriolis parameter ($2\Omega\cos\theta$ with θ being co-latitude), m_f a potential forcing term and $\boldsymbol{r}$ the unit radial vector. m and $\boldsymbol{s}$ are respectively a surface density and a vertically integrated momentum flow defined as:

$$m = \rho_w \eta, \tag{3.2}$$

$$\boldsymbol{s} = \int_h \rho_w \boldsymbol{u} dr. \tag{3.3}$$

ρ_w is the ocean density (assumed to be constant), and η and $\boldsymbol{u}$ are the radial surface displacement and tangential flow velocity. The forcing term m_f follows from the tidal potential ϕ:

$$m_f = \frac{\rho_w}{g}\phi. \tag{3.4}$$

The term F_{diss} is a dissipative term that can take different forms. It is often described using a linear drag term, a quadratic drag terms or a combination of both:

$$F_{diss} = \alpha \boldsymbol{s} + \left(\frac{c_D g^2}{c^4 \rho_w}\right) \boldsymbol{s} \,|\, \boldsymbol{s} \,|\,. \tag{3.5}$$

α and c_D are the Rayleigh and the bottom drag coefficient, respectively. Differences between both approaches are discussed in detail in *Hay and Matsuyama* (2017). For a given bottom drag coefficient, scaling relations can be used to estimate a linear drag coefficient (*Matsuyama et al.*, 2018). As most studies have considered the simpler case of linear drag (e.g., *Matsuyama*, 2014; *Matsuyama et al.*, 2018; *Tyler*, 2011) and we want to investigate how the response of an ocean with variable thickness compares with an ocean of constant thickness we adopt the simpler linear approach.

If a pressure load q (positive inwards) acts on the ocean surface (e.g., atmospheric pressure, force exerted by an elastic lid), Eq. (3.2a) can be modified as:

$$\partial_t \boldsymbol{s} - f \boldsymbol{s} \times \boldsymbol{r} = -c^2 \nabla (m + m_f + q/g) - \alpha \boldsymbol{s} \tag{3.6a}$$

$$\partial_t m + \nabla \cdot \boldsymbol{s} = 0. \tag{3.6b}$$

A problem that can arise depending on the choice of coordinates is the “pole-problem": nodes located at the poles become singular as the definition of east-west becomes singular (*Hay and Matsuyama*, 2017; *Platzman*, 1978). To avoid this problem the equations can be rewritten using a Helmholtz decomposition. The momentum flow is split into curl-free (Φ) and divergence-free (Ψ) components:

$$\boldsymbol{s} = \nabla \Phi + \nabla \times (\Psi \boldsymbol{r}). \tag{3.7}$$

By using this definition and taking the curl and divergence of (3.6a), (3.6) becomes (*Tyler*, 2011):

$$\partial_t m + \nabla^2 \Phi = 0, \tag{3.8a}$$

$$(\partial_t + \alpha)\nabla^2\Phi + f\nabla^2\Psi - \nabla f \cdot [(\nabla\Phi + \nabla\times(\Psi\boldsymbol{r}))\times\boldsymbol{r}] = -c^2\nabla^2\left(m + m_f + q/g\right) - \nabla c^2 \cdot \nabla(m + m_f + q/g), \tag{3.8b}$$

$$(\partial_t + \alpha)\nabla^2\Psi - f\nabla^2\Phi + \boldsymbol{r}\cdot\left[\nabla f \times (\nabla\Phi + \nabla\times(\Psi\boldsymbol{r}))\times\boldsymbol{r}\right] = \boldsymbol{r}\cdot\left[\nabla c^2 \times \nabla(m + m_f + q/g)\right]. \tag{3.8c}$$

From (3.8b) and (3.8c) it becomes clear that ocean thickness variations enter the equations through the implicit dependence of c^2 on ocean thickness. In case of uniform c^2, we recover the equations for an ocean of constant thickness.

The term q couples the ocean and the ice shell response. Two different approaches have been used to account for this term: the thick and the thin shell approaches. The thick shell approach considers all the elements of the stress and strain tensor (*Matsuyama et al.*, 2018). The thin shell theory is a $2D$ analogue of the $1D$ beam theory. It can be used if the shell is thin compared with the radius of the body (i.e., five to ten percent of the radius) (*Beuthe*, 2008). Under this circumstance it can be assumed that the transverse stress is negligible and that normals to the reference surface remain normal after deformation. The membrane limit is a further simplification that consists in neglecting bending within the ice shell. *Matsuyama et al.* (2018) and *Hay and Matsuyama* (2019) used the thick shell approach to study tidal dissipation in subsurface oceans, and showed that the membrane approach is accurate to 4% for Enceladus.

We use the thin shell approximation in the membrane limit. *Beuthe* (2008) derived a set of equations to study the deformation of a membrane of changing thickness under transverse and tangential loads. However these equations proved to be difficult to be efficiently implemented using Comsol's Multiphysics® tools. The equations are fourth order differential equations which imply that quintic or higher order elements need to be used together with a high spatial resolution. This fact highly increases the computational time making it difficult to explore the parameter space. Due to this limitation we consider an ice shell of constant thickness, which implies that changes in ocean thickness are implicitly represented by bedrock topography. In this case, the relation between surface displacements (η) and pressure exerted by the ice shell (q) is given by a second order differential equation:

$$\frac{1}{R}\Delta'\eta - \beta R\Delta' q + (1+\nu)\beta R q = 0. \tag{3.9}$$

ν is the Poisson ratio and β is extensional rigidity of an ice shell of constant thickness h_i and Young modulus E and is given by (*Beuthe*, 2008, 2016):

$$\beta = \frac{1}{E h_i}. \tag{3.10}$$

Δ' is a differential operator equal to $R^2\nabla^2 + 2$.

Equations (3.8) and (3.9) can be solved to obtain the ocean response to tidal forcing. Once the ocean tidal response is obtained, the momentum flow $\boldsymbol{s}$ can be used to compute the amount of tidal dissipation for each time-step:

$$D = \int_S \frac{\alpha}{\rho_w h} \boldsymbol{s} \cdot \boldsymbol{s} dS. \tag{3.11}$$

D changes over a tidal-period. We are interested in the average tidal dissipation over a tidal-period, which is obtained as:

$$\bar{D} = \frac{1}{T} \int_T D dt \tag{3.12}$$

where T is the tidal period.

Equations (3.8) are forced through the tidal potential ϕ, which arises due to the eccentricity (e) and obliquity (θ_o) of the satellite. The tidal potential can be written in terms of the satellite's orbital elements (*Jara-Orué and Vermeersen*, 2011):

$$\phi = -(nR)^2 (\phi_0 + \phi_{e0} + \phi_{e2e} + \phi_{e2w} + \phi_{o1e} + \phi_{o1w}), \tag{3.13}$$

where n is the mean motion of the satellite, which equals its rotational frequency Ω. ϕ_0 is the static component of the tidal-potential, which does not have any dynamic effect. The eccentricity and obliquity tide can be written in terms of spherical harmonics of degree two and different harmonic orders. The eccentricity tide consists of an order zero component (ϕ_{e0}) and an order two component that can be further split into an eastward (ϕ_{e2e}) and a westward component (ϕ_{e2w}). The obliquity tide is an order one forcing that can also be split into eastward and westward components (ϕ_{o1e},ϕ_{o1w}). These components are given by:

$$\phi_{e0} = -\frac{3e}{2} P_{2,0}(\cos\theta) \cos(nt), \tag{3.14a}$$

$$\phi_{e2e} = \frac{7e}{8} P_{2,2}(\cos\theta) \cos(2\varphi - nt), \tag{3.14b}$$

$$\phi_{e2w} = -\frac{e}{8} P_{2,2}(\cos\theta) \cos(2\varphi + nt), \tag{3.14c}$$

$$\phi_{o1e} = -\frac{\sin(\theta_o)}{2} P_{2,1}(\cos\theta) \sin(\varphi - nt - \omega) \tag{3.14d}$$

$$\phi_{o1w} = \frac{\sin(\theta_o)}{2} P_{2,1}(\cos\theta) \sin(\varphi + nt + \omega). \tag{3.14e}$$

where e, θ_o and ω are the satellite's eccentricity, obliquity and argument of pericenter, φ is the longitude and $P_{l,m}$ are associated Legendre polynomials of degree l and order m. The physical parameters used for Enceladus are given in Table 3.1.

3.3. SOLVING THE LTE USING FEM

Different approaches exist to solve the previous set of partial differential equations. If the ocean thickness is constant, spectral methods are very efficient (*Beuthe*, 2016; *Longuet-Higgins*, 1968; *Matsuyama*, 2014; *Matsuyama et al.*, 2018; *Tyler*, 2011, 2014). In such methods, m, Φ, Ψ are expanded in a series of spherical harmonics and Equations (3.8) are reduced to a set of algebraic equations that can be inverted to obtain the spherical harmonic coefficients. However, if c^2 is not constant this approach is more problematic and other numerical approaches are more suitable.

For example, for Earth, *Platzman* (1975) used a finite difference method to study the eigenmodes of the Atlantic ocean. The finite difference method presents some challenges, one of them being the previously mentioned "pole-problem". *Platzman* (1978) developed an alternative approach using a Finite Element Method (FEM) and applied it to study the eigenfrequencies and modes of Earth's ocean basins. In the context of planetary sciences, *Sears* (1995) used a finite difference approach to solve for tides in Titan's hydrocarbon lakes. This approach was incorporated in the first version of ODIS (Ocean Dissipation in Icy Satellites) (*Hay and Matsuyama*, 2017) to study tides in icy satellites with non-linear bottom drag. A finite volume method is used in the most recent version of ODIS (*Hay and Matsuyama*, 2019).

We use the commercial Finite Element software Comsol Multiphysics® to solve the system of partial differential equations. Comsol Multiphysics ® allows to solve user-defined partial differential equations and has extensively tested build-in integration methods that can be employed (*Comsol Multiphysics®*, 2012). More specifically, we use the Boundary PDE module to solve the PDEs in the boundary of a $3D$ domain, in our case a sphere of radius R. The equations are discretised using a mesh of quadratic triangular elements. The use of quadratic elements gives a smooth representation of the derivatives of m, Φ, Ψ and therefore of the flow momentum $\boldsymbol{s}$ (see Eq. (3.7)) which results in a more accurate estimation of tidal dissipation for a given mesh size.

The eigenmodes and eigenfrequencies of the system are obtained using the eigenvalue solver algorithm of Comsol ® which uses the implicitly restarted Arnoldi method (IRAM). Different methods can be used to integrate the system forward in time. *Hay and Matsuyama* (2017, 2019); *Sears* (1995) use an explicit method. This implies that the time step should fulfill the Courant-Friedrichs-Lewy (CFL) stability conditions, which dictates that $\Delta t \leq \Delta l / c$ with Δl being the mesh size, and places a stringent constraint on time-step for thick oceans. In contrast, we decide to use the Generalized-Alpha method, an implicit second-order integration method (*Chung and Hulbert*, 1993). The use of an implicit method has the advantage that the CFL condition can be relaxed.

The system is forced with the eccentricity and obliquity tide and integrated forward in time until a periodic solution is reached. The accuracy of the solution depends on the mesh-size and time step. Appendix 3.6 shows a benchmark of the FEM model as well as a study of the effect of mesh-size and time step. Based on the results presented there we decide to use a mesh with 834 elements (Figure 3.7) and a time step of 0.008 Enceladus orbital period for the simulations presented below. Using these parameters the error is shown to be smaller than 3% in most of the parameter space with the exception of few

Parameter	Value
R [km]	252.1
g [m·s^{-2}]	0.11
Ω [rad·s^{-1}]	$5.31 \cdot 10^{-5}$
e [-]	0.047
θ_o [°]	0.00045
ω [rad]	0
ρ_w [kg·m^{-3}]	1007
E [10^9Pa]	8.778
ν [km]	0.33
h_{ocean} [km]	$0.01 - 45$
h_{ice} [km]	$0, 1, 10$
α [s^{-1}]	$1 \cdot 10^{-5,-6,-7}$

Table 3.1 Enceladus physical parameters used for this study. Physical and orbital parameters are obtained from the JPL ephemerides (`http://ssd.jpl.nasa.gov/?sat_elem`). Enceladus' obliquity is an upper bound obtained considering Enceladus is in a Cassini state (*Baland et al.*, 2016). We use the same Young modulus (E), Poisson ratio (ν) and ocean density (ρ_w) as in *Souček et al.* (2016). Ocean (h_{ocean}) and ice shell thickness (h_{ice}) are varied within the indicated range.

cases close to resonant states for which the error can be up to 20%.

3.4. RESULTS

We use the FEM presented above to compute the response of subsurface oceans to the time-varying eccentricity and obliquity tidal potential (3.14). We consider ocean thicknesses between 10 m and 45 km. For each ocean thickness we force the system with the eccentricity and obliquity tide, the solution approaches the periodic steady solution asymptotically. In order to speed-up convergence we follow the approach of *Hay and Matsuyama* (2017). Instead of using initial conditions of the rest state, we use the converged solution of the previous ocean thickness as starting point. For some ocean thicknesses, the ocean response exhibits oscillations with a period of few Enceladan orbits diminishing in amplitude (see Figure 3.8). For these cases we compute tidal dissipation by averaging tidal dissipation for the last oscillation.

The Rayleigh coefficient depends on the dissipation mechanism at work in the ocean. Using values of Earth's Rayleigh and bottom drag coefficients, *Matsuyama et al.* (2018) argues that its value can range from 10^{-5} s^{-1} to 10^{-11} s^{-1}. We consider a nominal Rayleigh coefficient of 10^{-7} s^{-1} and briefly discuss the effect of changing this parameter by exploring two more dissipative scenarios ($10^{-5,-6}$ s^{-1}).

We are interested in studying the effect of ocean thickness variations on the ocean response. However, to put our results into context, we start by considering the very thoroughly studied case of a global ocean of constant thickness without any ice-cover, then

discuss the effects of adding an elastic ice shell of constant thickness and, finally, we study how ocean thickness variations alter the ocean response.

3.4.1. OCEAN OF UNIFORM THICKNESS

The case of a global ocean with a free surface (no ice shell) has been widely studied in the past in the context of geosciences (e.g., *Hough*, 1898; *Longuet-Higgins*, 1968) and recently revisited in the context of planetary sciences (e.g., *Beuthe*, 2016; *Hay and Matsuyama*, 2017; *Matsuyama*, 2014; *Tyler*, 2008). The behaviour of the system can be understood in terms of its eigenmodes and eigenfrequencies. Resonances can occur when the system is forced at one of its eigenfrequencies with a forcing that has a spatial pattern similar to that of the eigenmode. We will first consider the eigenmodes of Equations (3.8,3.9) without a forcing term and then the response of an ocean forced with the tidal potential. For the discussion that follows, we will name the different modes as follows: the first letter indicates whether the mode is symmetric (S) or antisymmetric (A) with respect to the equator; the number that follows indicates the order of the mode (wave number in the longitudinal direction), and the second letter indicates the propagation direction: east (E), west (W) or standing non-propagating wave (-). As some modes share the previous characteristics we will use subindices to distinguish modes belonging to the same family, with 1 corresponding to the mode excited for the thickest ocean.

It is very common to study the LTE in terms of the non-dimensional Lamb parameter $\epsilon = 4\Omega^2 R^2/gh$ (e.g., *Hough*, 1898; *Longuet-Higgins*, 1968). In his pioneering work, *Hough* (1898) studied the response of a non-dissipative ocean in the limit of a thick ocean $h \to \infty$ (or $\epsilon \to 0$) and identified two classes of waves: waves of the first class (gravity-waves), and waves of the second class (vorticity waves)[1]. He showed that the eigenfrequencies (in the asymptotic limit) are respectively given by:

$$\frac{n}{2\Omega} = \sqrt{\frac{l(l+1)}{\epsilon}} \tag{3.15a}$$

$$\frac{n}{2\Omega} = \frac{m}{l(l+1)} \tag{3.15b}$$

where l and m are the degree and order of the ocean response. Class 2 oscillations propagate westward, while class 1 oscillations can propagate either east- or west- ward. Figure 3.2 shows a representative Class 1 $(S2E)_1$ and Class 2 $(A1W)_1$ mode. The plots show the amplitude and phase of surface displacements (η) as well as the tangential flow velocity ($\boldsymbol{u}$) at $t = 0$ (in red) and tidal ellipses showing the change of magnitude and direction of the current vector over a tidal period. The difference between these two modes can

[1] Vorticity waves were first discovered by Laplace (*Laplace*, 1798). These oscillations were forgotten until *Margules* (1893) and *Hough* (1898) rediscovered them independently and called them oscillations of second class. Rossby and Haurwitz (*Haurwitz*, 1940; *Rossby*, 1939) rediscovered the waves of the second class again and since then the term "Rossby-Haurwitz waves" or "planetary waves" is also widely used to refer to Class 2 oscillations. We use both terms depending on the context

be further appreciated by computing the ratio of potential energy to total energy (kinetic plus potential). For an ocean thickness of 10000 km this ratio equals 0.4659 for the Class 1 $(S2E)_1$ mode and 0.016 for the Class 2 $(A1W)_1$ mode, indicating that surface displacements are small for the $(A1W)_1$ mode, which means that the flow is nearly non-divergent. As ocean thickness increases, the ratio approaches 0.5 and 0 for Class 1 and 2 modes, respectively (*Longuet-Higgins*, 1968, Figures 14,15).

The eigenfrequencies of the system for different ocean thicknesses are shown in Figure 3.3. The modes that have the right spatial structure to be excited by the eccentricity and obliquity tide are labeled. For an ocean of constant thickness symmetric and antisymmetric modes with respect to the equator are decoupled. Therefore the symmetric eccentricity tide excites symmetric modes while the antisymmetric obliquity tide excites antisymmetric modes. These modes are shown in Figures 3.9 and 3.10, where the distinction between symmetric and antisymmetric modes can be identified as a 180° phase lag between the Northern and Southern Hemisphere. The order of the mode is evident as the number of cycles in the zonal direction. Class 2 modes can be distinguished in Figure 3.3 as modes that asymptotically approach a constant frequency. This is the case of the $(A1W)_1$ mode, which in the asymptotic limit has an eigenfrequency equal to that of the tidal forcing $n/2\Omega = 0.5$. By contrast, the other indicated modes are Class 1 modes whose frequency in the thick ocean limit is proportional to $h^{1/2}$ and therefore show up as straight lines of slope 1/2 in Figure 3.3.

As the ocean becomes thinner the spectrum becomes denser and we cannot use the classification into Class 1 and 2 modes anymore. In the limit $h \to 0$ ($\epsilon \to \infty$), *Longuet-Higgins* (1968) distinguished three types of modes. For the first type, the eigenfrequency is proportional to $h^{1/4}$ while for the second and third type it is proportional to $h^{1/2}$. The second and third type can be distinguished because they propagate westward and eastward respectively. All modes labelled in Figure 3.3 are type 1 except mode $(S2E)_1$, which is type 3 as evidenced by its slope. In between the two asymptotic limits ($\epsilon \to \infty$ and $\epsilon \to 0$) the eigenfrequency curves change their slope as they transition to class 1 and 2 oscillations.

(a) $(S2E)_1$

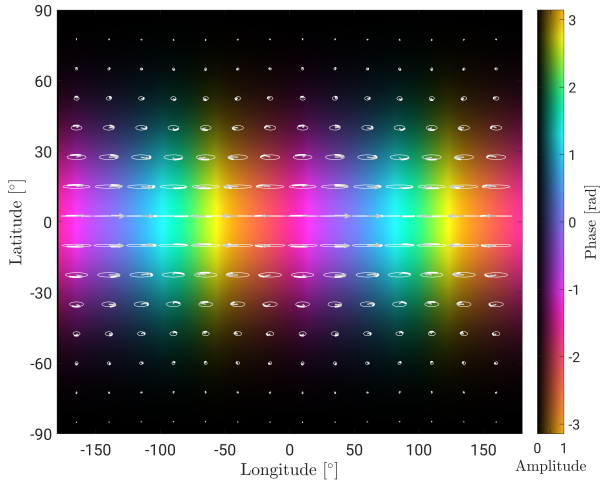

(b) $(A1W)_1$

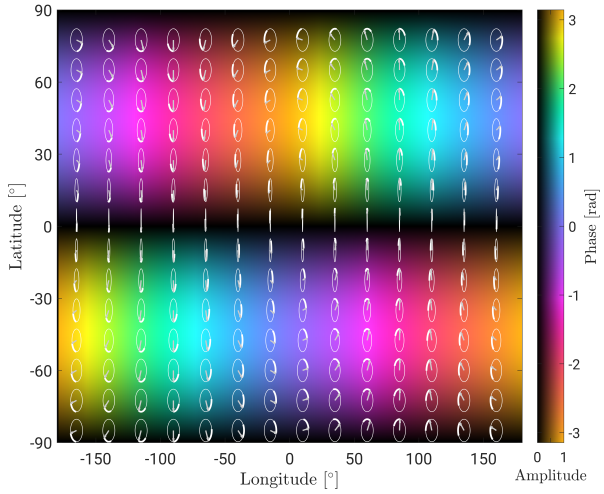

Figure 3.2 Class 1 (a) and Class 2 mode (b). The arrows show the flow velocity at $t = 0$, the surrounding ellipses show the change of the flow velocity during a tidal period. The phase and amplitude of surface displacements are shown in the background, with the phase represented by the colour and amplitude by brightness. Black indicates diminishing amplitude.

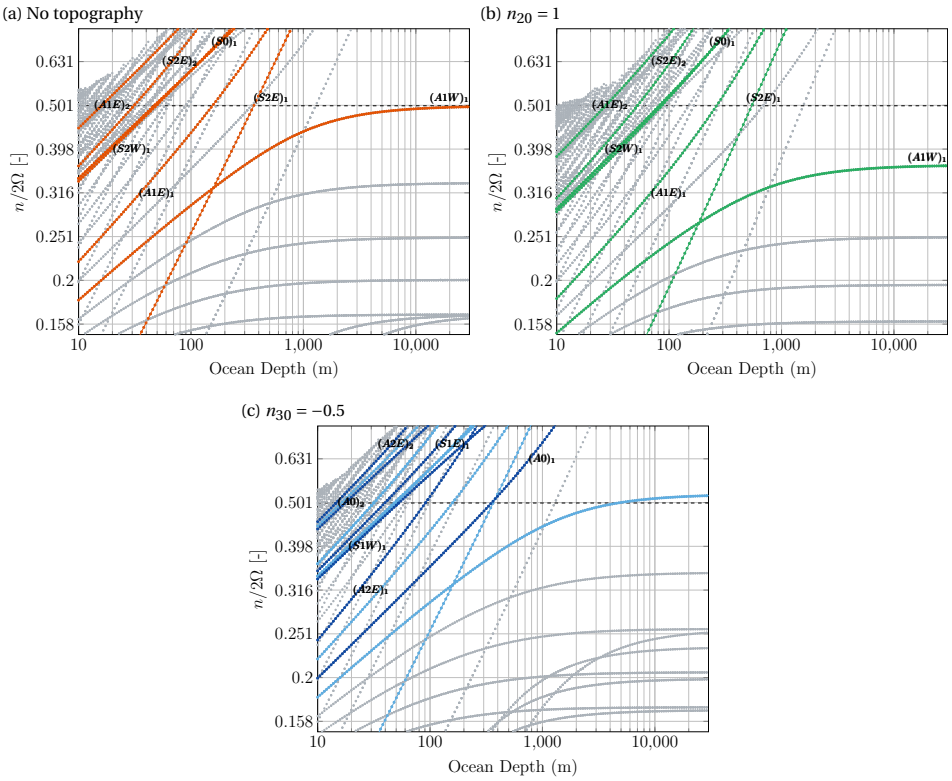

Figure 3.3 Eigenfrequencies for an ocean without ice cover and different ocean thickness changes. The modes excited by the obliquity tide and the eccentricity tide are indicated. For the ocean with degree three order zero topography only the new excited modes (indicated in darker blue) are labeled. High frequency eigenmodes corresponding to thin oceans (upper left corner) are not shown.

When forced with the tidal potential, the response of the system is given by a combination of the previous eigenmodes. The tidal response is maximized if the eigenfrequency of the mode is the same as the tidal frequency, which can be visualised as a mode crossing the horizontal line corresponding to $n/2\Omega = 1/2$ in Figure 3.3. When this happens a resonance occurs. Figure 3.4 shows the average tidal dissipation for different ocean thicknesses due to the eccentricity and obliquity tide. The ocean response is characterised by a series of resonance peaks, i.e. ocean thicknesses for which tidal dissipation is enhanced by several orders of magnitude. For these resonant peaks, tidal dissipation can be above Enceladus' observed thermal flux (*Spencer et al.*, 2013). The resonance peak corresponding to a thicker ocean occurs for an ocean thickness of $h_o = 363$ m. However, as noted before, the actual ocean on Enceladus is expected to be much thicker (*Beuthe et al.*, 2016). Surface heat flux patterns due to the eccentricity tide for a resonant and non-resonant configuration are shown in Figure 3.5 a,b. In both cases tidal dissipation

is symmetric and maximum in equatorial regions, for the resonant ocean thickness tidal dissipation is increased by 7 orders of magnitude. Dissipation patterns depend on flow amplitudes, from the eigenmodes depicted in Figure 3.9, it follows that tidal dissipation in polar regions is very small for the eccentricity tide, which does not agree with Cassini's observation of enhanced heat flux in Enceladus SPT.

The curves corresponding to the eccentricity and the obliquity tides are markedly different. Dissipation due to Enceladus' obliquity is lower than that due to its eccentricity, mainly because the obliquity of Enceladus is predicted to be very small (see Table 3.1). Moreover, the behaviour for an increasing ocean thickness differs. For the eccentricity tide we observe that tidal dissipation decreases with ocean thickness. As the ocean thickness increases the surface gravity wave-speed increases too, thus the ocean can adjust faster to the varying tidal potential. Interestingly, this is not the case for the obliquity tide, which shows the opposite behaviour. This is because the ocean response is mainly given by the Rossby-Haurwitz mode $(A1W)_1$. We should not label this behaviour as a resonance (*Beuthe*, 2016). In contrast to the other resonance peaks, where in the inviscid limit kinetic energy diverges as the difference between eigenfrequency and forcing frequency becomes smaller, the excitation of the $(A1W)_1$ mode does not result in a divergent response. Dissipation patterns for this mode are shown in Figure 3.5c. Contrary to the eccentricity tide, where tidal dissipation is maximum at the equator, tidal dissipation is enhanced at the poles for the obliquity tide. However, dissipation patterns remain symmetric and the values are still small compared with the estimated radiogenic heating ($\sim 4 \times 10^{-4}$ Wm^{-2}) making it difficult to explain Enceladus dichotomy through this mechanism.

The ocean response is influenced by the value of the Rayleigh coefficient. As expected, for more dissipative oceans (higher α) resonant peaks are smoothed (Figure 3.4 d,e). Similarly, lower values result in narrower resonance peaks but do not alter the ocean thickness for which they occur provided $\alpha \ll \Omega$. When damping is increased, the obliquity tide in the thick ocean limit is no longer only described by the Rossby-Haurwitz alone, gravity waves are added to the solution. In such cases, the maximum value of tidal dissipation is not obtained in the limit $h \to \infty$ (*Beuthe*, 2016; *Hay and Matsuyama*, 2019; *Matsuyama*, 2014).

If an ice shell is added, the response of the system is altered. We compute the tidal response of an ocean of constant thickness covered by a 1 or 10 km ice shell. As in *Beuthe* (2016) and *Matsuyama et al.* (2018) we find that the effect of adding an elastic ice shell is twofold (Figure 3.4): (1) it shifts the gravity mode resonance peaks to thinner oceans and (2) for thick oceans it dampens the ocean response. Using the $(S2E)_1$ mode as an example we can see that the ocean thickness for which this mode has an eigenfrequency equal to that of the tidal force decreases with increasing ice shell thickness (Figure 3.6b), resulting in the shift of the resonance peaks. The $(A1W)_1$ mode still has an eigenfrequency equal to $n/2\Omega = 0.5$ in the thick ocean limit and thus Rossby-Haurwitz waves are still excited by the obliquity tide in an ocean covered by an ice shell.

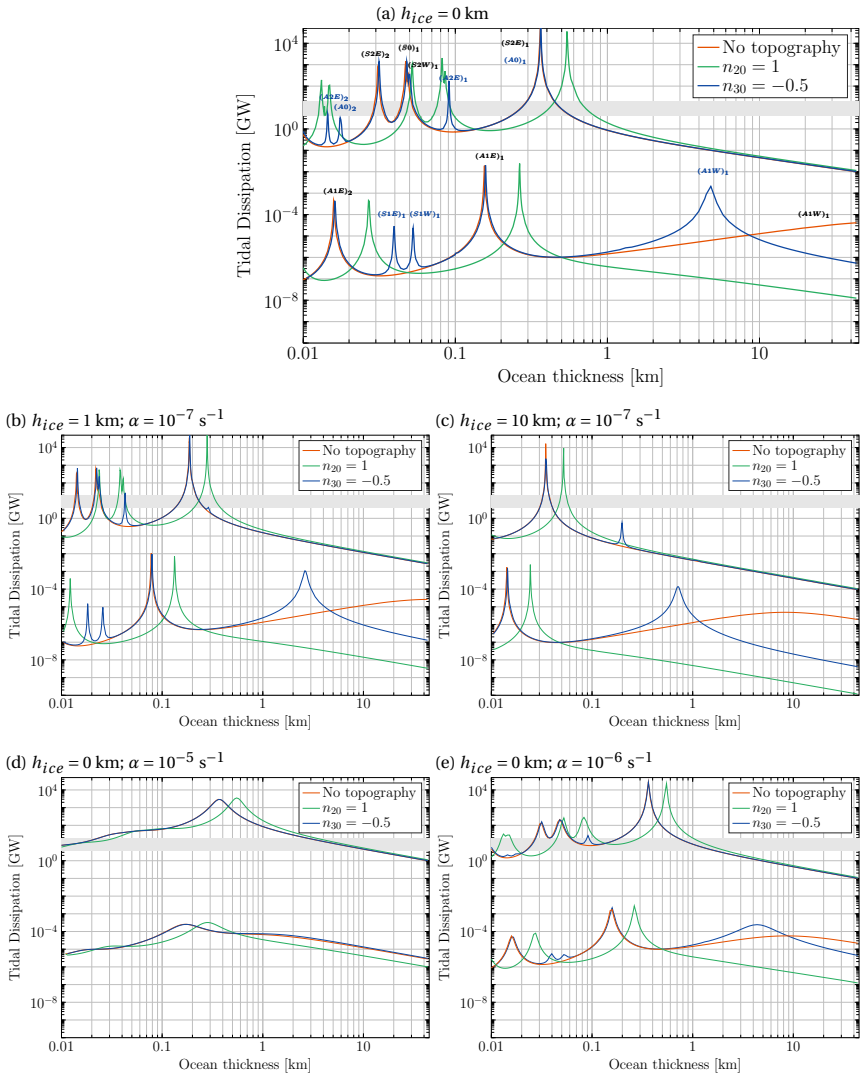

Figure 3.4 Tidal dissipation for different ocean thicknesses for an ocean of constant thickness and oceans with degree two and three thickness topography. Each panel shows tidal dissipation due to the obliquity tide and eccentricity tide with the curves for the obliquity tide corresponding to lower values of tidal dissipation. The different panels show the solution for different ice shell thicknesses (0,1 and 10) km and Rayleigh coefficient $(10^{-5}, 10^{-6}, 10^{-7})$ s^{-1}. In (a) the different resonances are labelled, those excited due to antisymmetric topography are indicated in blue. The horizontal grey band corresponds to the observed thermal output of Enceladus (*Spencer et al.*, 2013)

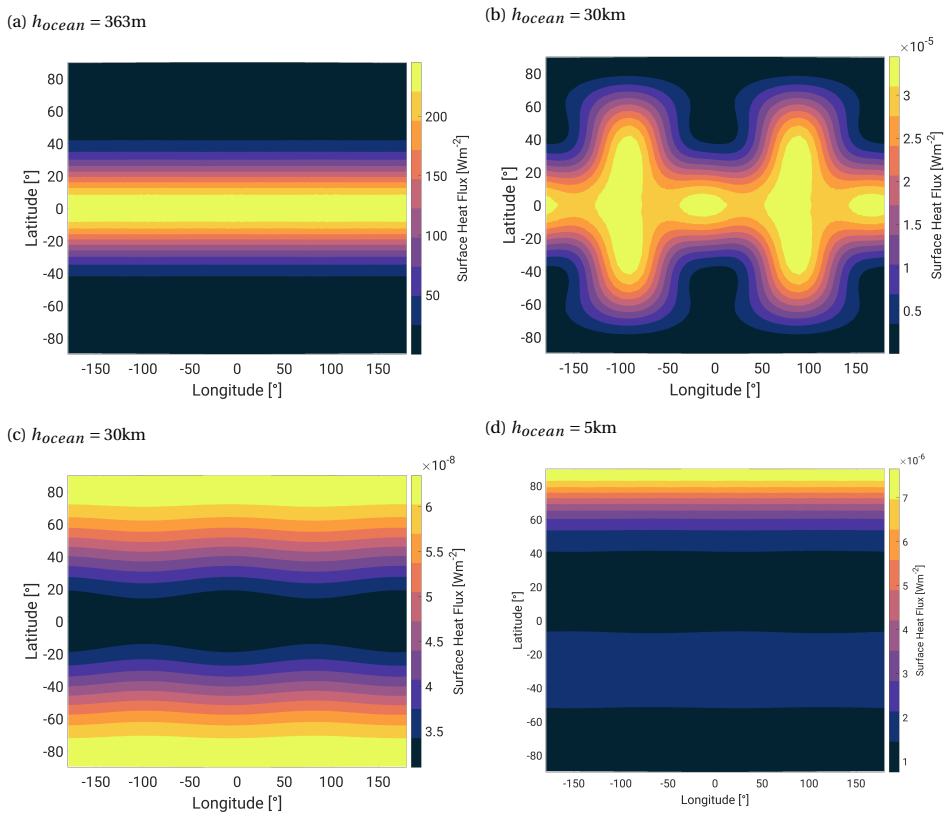

Figure 3.5 Time-averaged tidal dissipation patterns for the eccentricity (a,b) and obliquity tide (c,d) in an ice-free ocean. (a,b,c) show dissipation patterns for an ocean of constant thickness while (d) correspond to an ocean with degree three topography

3.4.2. OCEAN OF VARIABLE THICKNESS

Using gravity, topography and libration data *Beuthe et al.* (2016) *Čadek et al.* (2016) and *Hemingway and Mittal* (2019) showed that Enceladus' ice shell has degree two and three thickness changes resulting in ocean thickness variations of the same type. As explained in Section 3.2, our model uses an ice shell of constant thickness; ocean thickness variations are therefore implicitly given by sea-floor topography. We consider an ocean with thickness variations of the same kind as those inferred for Enceladus' ice shell:

$$h = \hat{h}(1 + n_{20}P_{20} + n_{30}P_{30}) \tag{3.16}$$

where $\hat{h}$ is the average ocean thickness and P_{20} and P_{30} are respectively the degree two and three order zero Legendre functions. These two types of ocean topography are shown in Figure 3.1. Their effect will be studied separately.

The values of n_{20} and n_{30} depend on ocean and ice shell geometry. For a 38 km thick ocean and an ice shell of 22.8 km, *Beuthe et al.* (2016) obtains values for n_{20} and n_{30} equal to ~ 0.3 and ~ -0.1, respectively. To make the effect of variable ocean thickness more evident we use higher nominal values of n_{20} and n_{30} equal to 1 and -0.5, respectively.

We start by considering how symmetric ocean thickness changes affects the ocean response. We compute tidal dissipation due to the eccentricity and the obliquity tide, the results are shown in Figure 3.4. Some differences are apparent when comparing the tidal response to that of an ocean without topography. Firstly, the same resonant peaks characteristic of an ocean of constant thickness are observed, however, they are shifted towards thicker oceans. For the case of an ocean with a free-surface the $(SE2)_1$ resonance moves from a 363 to a 550 m deep ocean. Secondly, we observe that, oppositely to what occurs when the ocean is uniform, tidal dissipation decreases with increasing ocean thickness for the obliquity tide, which suggests that the Rossby-Haurwitz mode $(A1W)_1$ is not efficiently excited in an ocean with degree two topography.

Some further insight can be obtained by considering the eigenmodes of the system when topography is included. Figure 3.3b, shows the eigenfrequencies of the system for $n_{20} = 1$. We observe that the general appearance of the spectrum is not very different from that of a uniform ocean. The ocean thicknesses at which the gravity modes cross the tidal frequency line change, which translates in the shift of resonance peaks observed in Figure 3.4. In contrast, the Rossby-Haurwitz $(A1W)_1$ mode approaches a frequency lower than the forcing frequency in the thick ocean limit, which diminishes the role of this mode. As we did before for different ice shell thicknesses, we track the $(A1W)_1$ and the $(S2E)_1$ modes for different values of n_{20} (Figure 3.6 b). The $(S2E)_1$ resonance gradually shifts towards thicker oceans as n_{20} increases and the asymptotic Rossby-Haurwitz eigenfrequency decreases.

We move now to the case of oceans with antisymmetric ocean thickness changes. The dissipation curve corresponding to an ocean with antisymmetric thickness variations is similar to that of an ocean of constant thickness (Figure 3.4). However, we observe that new resonant peaks corresponding to new modes appear (labelled in blue in Figure 3.4). We will first discuss the effect of degree three topography in the modes already present in the constant thickness ocean response and then examine the new modes.

With the exception of the $(A1W)_1$ mode, the modes also excited for a constant thickness ocean occur for roughly the same ocean thickness as in the constant ocean thickness case. This fact contrasts with degree two topography, where we observe a shift in the resonance peaks towards thicker ocean. The different behaviour can be understood by examining the geographical patterns of the gravity modes excited by the eccentricity and obliquity tide (Figures 3.9 and 3.10). We observe that these modes are confined to low and mid latitude regions. Thus, it can be expected that the ocean thickness in this latitudinal range will control the tidal response. Looking at Figure 3.1 it is evident that an ocean with degree two topography deviates from an ocean of constant thickness in low and mid latitudes. For $n_{20} > 0$ the ocean is thinner than the average ocean thickness; this means that at low and mid latitudes an ocean thickness similar to that for which the gravity modes are excited for a constant thickness ocean will be attained for a higher $\hat{h}$,

explaining the shift towards higher $\hat{h}$ in the resonant peaks. In contrast, ocean thickness variations at low and mid latitudes for degree three topography are small (Figure 3.1). This results in the terms related with ocean thickness variations in Equations (3.8) to be small and results in gravity mode resonances occurring approximately for the same average ocean thickness ($\hat{h}$) as in the constant thickness ocean.

In contrast, the $(A1W)_1$ mode (Figure 3.2 b) is not confined to low latitudes and thus the previous argument does not apply. The ocean response is more affected by degree three thickness variations, which are large at high latitudes. As in the constant thickness ocean, we observe that the $(A1W)_1$ mode eigenfrequency asymptotically approaches a constant frequency in the limit $h \to \infty$ in Figure 3.3c. However, this asymptotic frequency is higher than the tidal frequency. Therefore the mode crosses the tidal frequency line and as a consequence dissipation due to the $(A1W_1)$ mode reaches a maximum and then decreases with increasing ocean thickness. We obtain tidal dissipation patterns for this mode and compare them with the same mode for a uniform ocean (Figure 3.5 c,d). Degree three topography results in anti-symmetric tidal dissipation patterns, tidal dissipation is enhanced in north polar regions, where the ocean is shallow. This simply follows from mass conservation, Eq. (3.6b); currents are stronger in shallower regions, which results in higher energy dissipation. Although this mechanism presents a new way to introduces anti-symmetries in tidal dissipation patterns it does not agree with Enceladus heat flux being higher at the Southern Hemisphere.

As mentioned before, new modes are excited when the antisymmetric topography is considered. The new modes are shown in Figure 3.11. As opposed to the two previous cases we notice that antisymmetric modes $(A2E)_{1,2}$ and $(A0)_{1,2}$ are excited by the symmetric eccentricity tidal forcing and the symmetric modes $(S1E)_1$ and $(S1W)_1$ are excited by the antisymmetric obliquity forcing. Figure 3.3c shows the eigenfrequencies of the modes excited by the eccentricity and obliquity tide. Indicated in dark blue are the new modes that appear due to the degree three order zero topography. The $(A0)_1$ resonance is particularly interesting. For an ice-free ocean, its resonance thickness is the same as that of the $(S2E)_1$ mode and thus it is shadowed by this mode in the dissipation curve. Adding an ice shell separates the two modes and the $(A0)_1$ mode becomes visible in the dissipation curves (Figures 3.4b,c) to the right of the $(S2E)_1$ resonance peak for the 1 and 10 km thick ice shells.

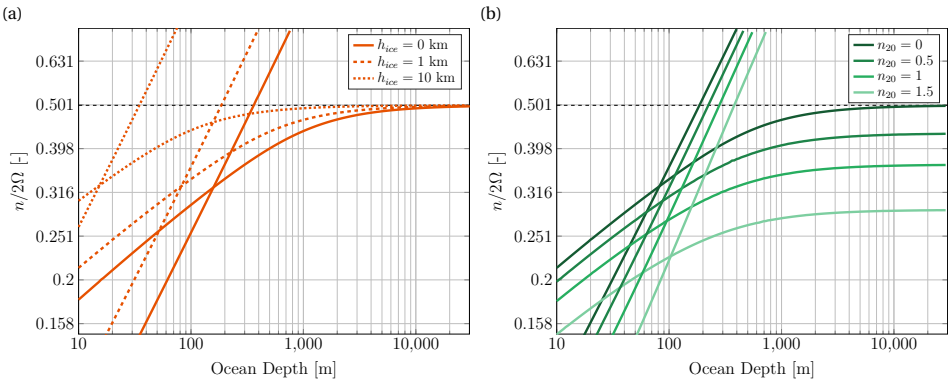

Figure 3.6 Eigenfrequencies for the $(S2E)_1$ (straight lines) and $(A1W)_1$ (bended lines) modes for an ocean of constant thickness and different ice shell thicknesses (a), and an ocean with a 1 km ice shell and different amplitudes (n_{20}) of degree two topography.

3.5. CONCLUSIONS

In this paper we present a new numerical model to solve ocean tides in subsurface oceans with variable thickness. We solve the Laplace Tidal Equations for an ocean of variable thickness coupled with an elastic membrane of constant thickness. We use the Boundary PDE module of the commercial finite element software Comsol Multiphysics ®. The equations are spatially discretised using quadratic triangular elements and integrated in time using the Generalized Alpha algorithm. We benchmark the model against the solution of the LTE for an ocean of constant thickness obtained by *Matsuyama* (2014) using a spectral method. We show that the model converges to the analytic solutions of *Matsuyama* (2014) provided that sufficiently small time steps and mesh size are used.

We use this model to study tides in Enceladus' subsurface ocean. We start with the thoroughly studied case of an ocean of constant thickness to identify characteristics in the system that help us understand the response for an ocean with variable thickness (e.g *Beuthe*, 2016; *Hay and Matsuyama*, 2019; *Tyler*, 2008). As in previous studies, we find that the ocean response to the eccentricity and obliquity tide is characterised by a series of resonant peaks where tidal dissipation surpasses Enceladus's observed heat flux (*Spencer et al.*, 2013) but does not agree with the observed distribution of heat. The resonant peaks can be related to the eigenmodes of the system. The equatorially symmetric eccentricity tide excites symmetric modes while the anti-symmetric obliquity tide excites anti-symmetric modes. All the excited modes are gravity-waves modes except for the westward propagating Rossby-Haurwitz mode that corresponds to a vorticity (or Class 2) mode. Gravity mode resonances occur for oceans that are thinner (few hundred meters) compared to the average ocean thickness of around 30 km estimated using gravity, libration and altimetry data (*Beuthe et al.*, 2016; *Čadek et al.*, 2016; *Hemingway and Mittal*, 2019). The Rossby-Haurwitz mode is excited by the obliquity tide for thick oceans, which results in an increase of tidal heating with ocean thickness for the obliq-

uity tide.

We then explore the effect of degree two and three meridional ocean thickness variations in the ocean response. We observe that the equatorially symmetric degree two topography does not add additional resonant modes to the ocean response. However, the resonant ocean thicknesses for the gravity wave modes are shifted to thicker oceans than those of an ocean of uniform thickness. This shift does not push the resonant ocean thickness to a value close to Enceladus' estimated ocean thickness. The antisymmetric degree three topography can activate new resonant modes. We observe that equatorially symmetric modes can be excited by the antisymmetric obliquity tide and antisymmetric modes are excited by the symmetric eccentricity tide.

Topography also affects the excitation of Rossby-Haurwitz waves. For degree two topography, Rossby-Haurwitz waves have a frequency lower than the tidal frequency, which limits the excitation of these waves by the obliquity tide. With degree three topography, the maximum dissipation due to the Rossby-Haurwitz mode occurs for thinner oceans than in the constant ocean thickness case. Additionally, degree three topography results in anti-symmetric dissipation patterns, but maxima are attained at the north polar regions and not the south polar regions as observed by Cassini. These results have important implications as the Rossby-Haurwitz mode has been suggested to play a major role in preventing subsurface oceans in Europa (*Tyler*, 2008), Enceladus (*Tyler*, 2009) or Triton (*Chen et al.*, 2014; *Hay and Matsuyama*, 2019; *Nimmo and Spencer*, 2015) from freezing. We show that an uneven ocean diminishes the amount of tidal heating produced through the excitation of Rossby-Haurwitz waves. These results are similar to those of *Tyler* (2011), who already pointed out that the Rossby-Haurwitz wave amplitude is greatly reduced in the case of an Enceladan ocean confined to the South Pole.

This study illustrates the importance of topography in controlling the tidal response of subsurface oceans. However, very little information on ocean thickness variations is available for icy moons. In the case of Enceladus, gravity, libration and altimetry data suggest degree two and three variations in the ice shell thickness (*Beuthe et al.*, 2016; *Čadek et al.*, 2016; *Hemingway and Mittal*, 2019). For Europa these lateral variations could be smaller (*Nimmo et al.*, 2007) and they are unknown for other ocean worlds. Very little is known about seafloor topography, however low gravity objects like Enceladus can potentially support large topographic relief. Future missions such as JUICE or Europa Clipper might help to estimate ocean thickness for some of these bodies leading to a better understanding of tides in subsurface oceans.

Our numerical model has some limitations that should be pointed out. Firstly, it does not include self-gravity and the ocean is assumed to be covering a rigid core. *Matsuyama* (2014) showed that including the effect of self-gravity and considering a deformable core results in a shift of gravity mode resonances to thicker oceans. Moreover, self-gravity slightly enhances tidal dissipation per unit time due to the obliquity tide for thick oceans (*Hay and Matsuyama*, 2019). However, these two elements do not add new modes to the ocean response. Similar effects are expected if self-gravity and a deformable core would be added to our model. Secondly, while our ocean model includes meridional thickness variations through a thickness dependent phase speed we model the ice shell as an elastic membane of constant thickness. This implies that ocean thickness variations are due

to seafloor topography instead of ice shell thickness variations. *Běhounková et al.* (2017); *Souček et al.* (2019) considered the response of Enceladus' ice shell of variable thickness above an ocean that is in hydrostatic equilibrium. Their ice shell model is 20 km thick on average and varies from about 5 km in the SPT to more than 30 km near the equator, additionally the Tiger Stripes are included as weak regions in the SPT. They showed that, when forced with the eccentricity tide, ice thickness variations lead to a higher amplitude of surface displacements in the SPT compared with a uniformly thick ice shell. Based on our results, we expect that this would result in the excitation of the antisymmetric ocean modes as happens with the degree three seafloor topography considered here.

Another point that deserves further attention is the validity of the Laplace Tidal Equations in the context of subsurface oceans. The Laplace Tidal Equations are derived from the Navier-Stokes equations assuming: (1) a perfectly homogeneous fluid; (2) horizontal length-scale of the problem larger than vertical length-scale; and (3) small perturbations relative to a state of uniform rotation (e.g., *Gerkema et al.*, 2008; *Hendershott*, 1981; *Miles*, 1974). Considering the little amount of information about the composition of subsurface oceans and the premise that they are heated from below it seems reasonable to make the assumption that subsurface oceans are neutrally buoyant (*Vance and Goodman*, 2009) and thus justify (1). However, depending on the ocean salinity, the ocean might be stably stratified (*Melosh et al.*, 2004; *Vance and Brown*, 2005). In that case, internal gravity waves might develop. The effect of stratification has been considered by *Tyler* (2011) who used a scaling law to relate the baroclinic and barotropic ocean response and suggested that baroclinic tides in a stratified ocean could close Enceladus' energy budget. However, it is not clear how the baroclinic response would be excited. The effect of stratification in the ocean response to tides could be further investigated by using a multilayered shallow-water system. Moreover, the flow of the barotropic tide over topography can result in the excitation of internal gravity waves (*Egbert and Ray*, 2003). The barotropic response of the ocean obtained with our model could be used as starting point to study the excitation of the baroclinic tide through this mechanism.

Assumption (2) leads to the hydrostatic and traditional approximations, which filter internal waves from the solution. The LTE have been widely used to study tides on Earth and successfully explain ~ 70% of tidal dissipation in the ocean, the remaining part being due to internal waves excited in regions of rough topography (*Egbert and Ray*, 2000, 2003). Taking the radius and ocean thickness as horizontal and vertical length-scales, respectively, we find that the ratio between vertical and horizontal length-scales is ~ 0.15 for Enceladus as compared to ~ 0.001 for Earth. *Rovira-Navarro et al.* (2019) and *Rekier et al.* (2019) showed that internal inertial waves can be excited in Enceladus but found dissipation due to internal waves to be generally small in the linear regime for oceans of constant thickness. However, non-linear terms neglected under assumption (3) in the Navier-Stokes equations can induce domain filling turbulence (*Lemasquerier et al.*, 2017; *Wilson and Kerswell*, 2018). The effect of topography on the propagation of inertial waves as well as in triggering turbulence in subsurface oceans remains to be studied.

3.6. APPENDIX A: MESH SELECTION AND MODEL BENCHMARK

We study the effect of the time step and mesh resolution in the FEM model. To do so, we consider the results of *Matsuyama* (2014) who solved the LTE for an ice-free ocean using a spectral method. We use the solutions obtained with a Rayleigh coefficient of $2.7 \cdot 10^{-7}$ s^{-1}. We start by considering the effect of the time step. We select a thick ocean, as it implies a more stringent CFL condition. We consider a 9937 m thick ocean and use a mesh with $N = 848$ elements (Figure 3.7). For this mesh size and ocean thickness, a time step of $0.01\,T_{En}$ would be needed to fulfil the CFL criteria. We run the model for 300 Enceladan orbits with different time steps and compute the average tidal dissipation using Eq. (3.12) for each orbital period. The results are shown in Figure 3.8a. For all the different time steps the solution converges to a value of tidal dissipation, however accuracy increases with decreasing time step.

To study the effect of mesh size we select two ocean thicknesses; one close to a resonance peak ($h_o = 30.35$ m) and one far from a resonance peak ($h_o = 500.18$ m) and run the model for 300 Enceladan orbits using different meshes ranging from 246 to 2814 elements (Figure 3.7) and a time step of $0.008\,T_{En}$. Figure 3.8 b and c show the surface average tidal dissipation for the different meshes. We see that for the ocean thickness far from a resonance peak all the meshes converge towards the solution of *Matsuyama* (2014). In contrast, for the resonant ocean thickness, a higher resolution mesh is needed to converge to the solution.

Based on the previous results we chose to use a time step of $0.008\,T_{En}$ and a mesh with 848 elements. To assess the numerical error obtained with this model configuration we compute tidal dissipation for subsurface oceans with thickness ranging from 10m to 10km and compare the results with those of *Matsuyama* (2014). We observe a very good agreement between the FEM model and analytic results. For most ocean thicknesses errors are smaller than 3%, however close to resonant peaks errors can be as as high as 20%.

(a) $N = 246$

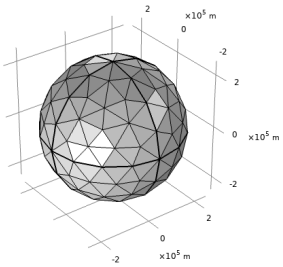

(b) $N = 464$

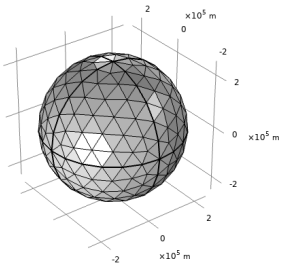

(c) $N = 834$

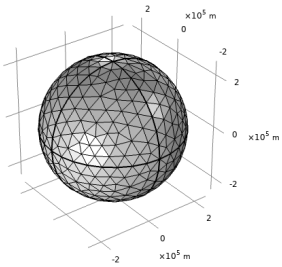

(d) $N = 2814$

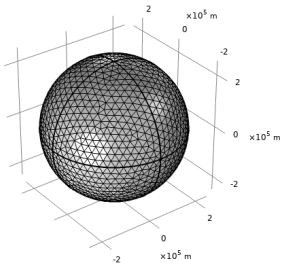

Figure 3.7 Meshes used for the benchmark of the FEM code against analytical results

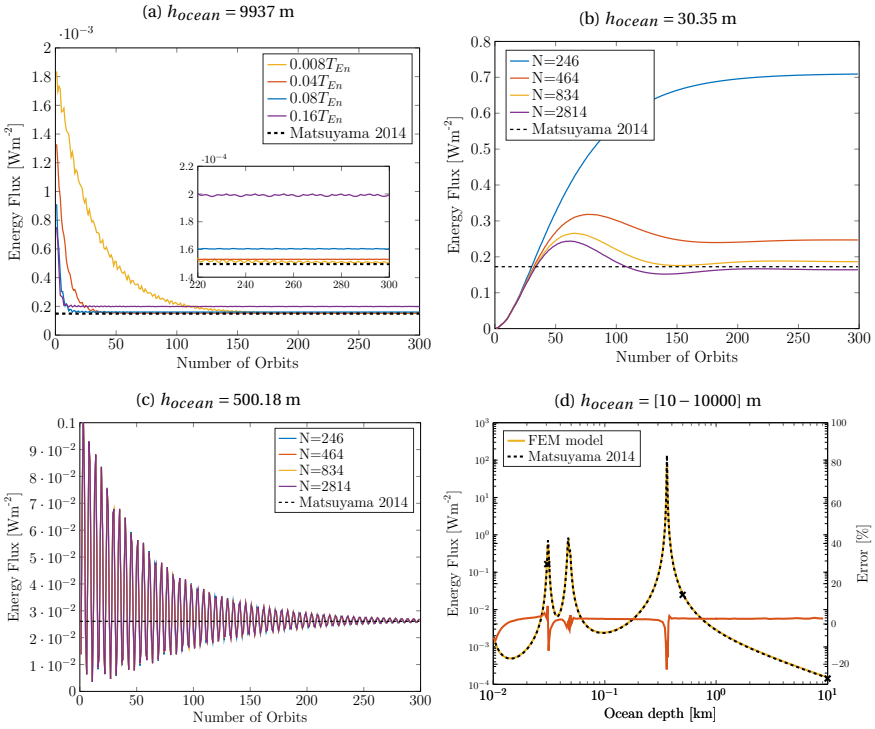

Figure 3.8 (a,b,c) Surface average dissipation obtained using the FEM model for different mesh sizes (represented by number of elements N) and time steps for three different ocean thicknesses. The dashed line corresponds to the analytic solution of *Matsuyama* (2014). (d) Comparison of the FEM solution obtained with $N = 848$ and a time step of $0.008T_{En}$ and the analytic solutions for ocean thickness between 10 and 10000 m, the error is shown in red and the ocean thicknesses corresponding to the numerical tests of panels a,b and c are indicated with a black crosses.

3.7. APPENDIX B: RESONANT MODES

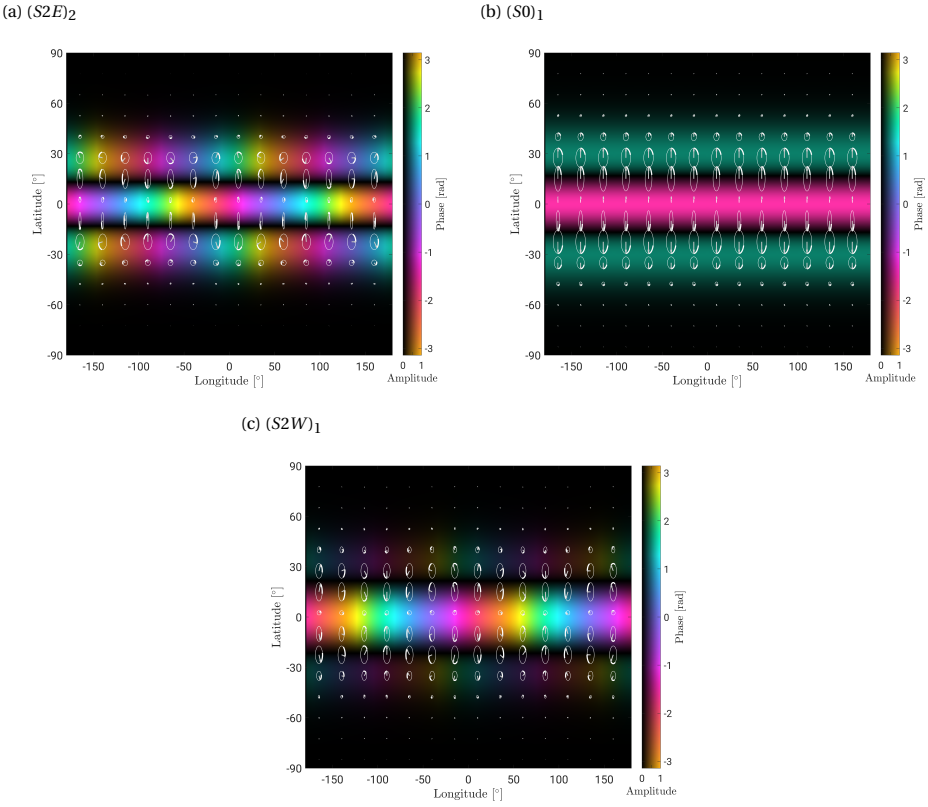

Figure 3.9 Symmetric eigenmodes that can be excited by the eccentricity tide. .

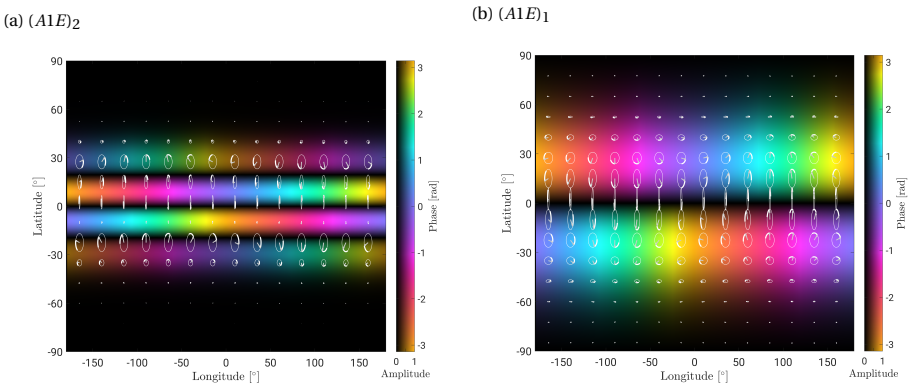

Figure 3.10 Antisymmetric modes excited by the obliquity tide.

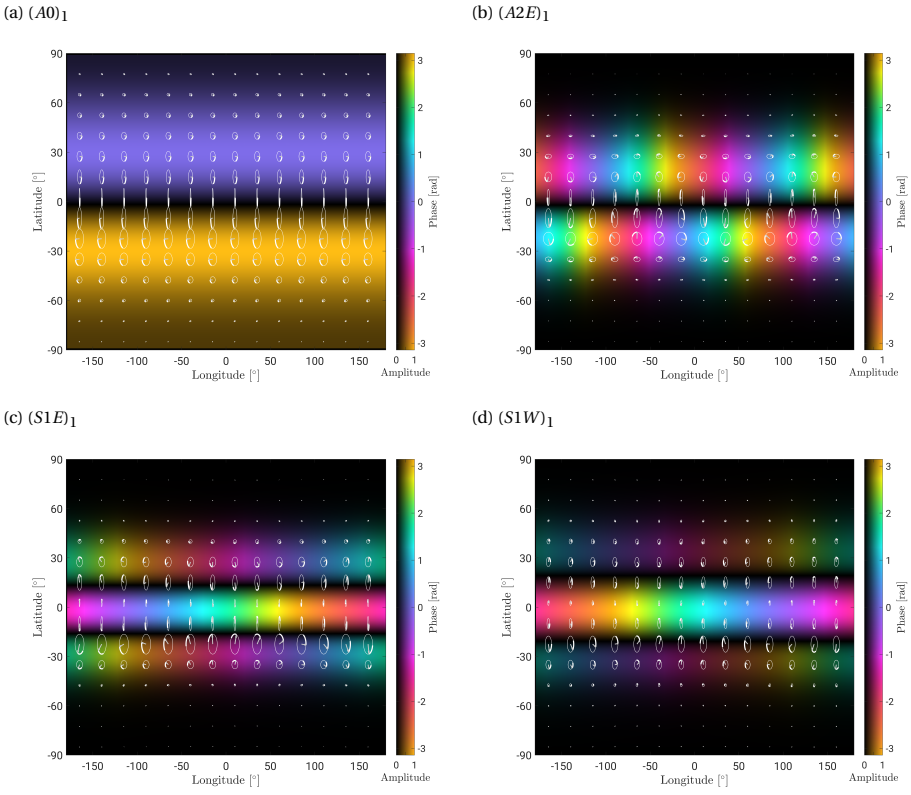

Figure 3.11 Same as Figure 3.2 but for four of the extra modes excited by degree three order zero ocean thickness variations.

4

Do Tidally-Generated Inertial Waves Heat the Subsurface Oceans of Europa and Enceladus?

M. Rovira-Navarro ,M. Rieutord, T. Gerkema, L. R.M. Maas, W. van der Wal,B. Vermeersen

Some of the moons of the outer Solar System harbour subsurface liquid oceans. Tidal dissipation plays an important role in preventing these oceans from freezing. In the past, most studies considered only tidal dissipation in the solid layers of these bodies (rock and ice). Recently, new studies considering tidal dissipation in the oceans of these moons have appeared. All of them make use of the shallow water approximation. However, the use of this approximation might not be adequate. Here we consider the linear non-hydrostatic three dimensional response of these oceans to tidal forcing with the full Coriolis force. To do so we consider an ocean of homogeneous density contained within a perfectly spherical shell and neglect the effect of the ice shell. We force the ocean with a time changing tidal potential and observe patterns of periodic inertial waves that take energy from the global tidal forcing and focus it along thin shear layers that propagate in the fluid. We

An earlier version of this chapter is published in Icarus (*Rovira-Navarro et al.*, 2019): Rovira-Navarro, M., Rieutord, M., Gerkema, T., Maas, R.M., van der Wal, W., & Vermeersen, B. (2019), Do tidally-generated inertial waves heat the subsurface oceans of Europa and Enceladus?, Icarus, 321, 126 – 140.

focus on Europa and Enceladus, showing that inertial waves result in fluid flows of significant amplitude (a few cm/s*). Nevertheless, we find that under the previously mentioned assumptions tidal dissipation due to inertial waves is several orders of magnitude smaller than Europa's radiogenic heating and Enceladus' observed heat flux. Finally, we propose additional dissipation mechanisms that might play a relevant role in Europa and Enceladus and could be further investigated.*

4.1. INTRODUCTION

Evidence for underground water reservoirs in some of the moons of the outer Solar System has accumulated over the last few decades. The existence of a subsurface water body in Europa was first hypothesised by *Cassen et al.* (1979). They argued that radiogenic and tidal heating could melt Europa's interior and form an ocean. The hypothesis was confirmed when *Khurana et al.* (1998) and *Kivelson et al.* (2000) reported variations of the magnetic field in Europa associated with an induced magnetic field and showed that a layer of subsurface salty water is consistent with these observations. The existence of a subsurface ocean is also consistent with the complex geology of Europa's surface (e.g., *Pappalardo et al.*, 1999).

The case of Enceladus is markedly different. This tiny moon of Saturn, its radius being just over 250 km, features vigorous geological activity. Cassini flybys revealed water plumes emanating from long parallel cracks (nicknamed tiger-stripes) on the South Pole (*Porco et al.*, 2006; *Spencer et al.*, 2006). The detection of salt-rich grains in the plumes (*Postberg et al.*, 2009, 2011) and evidence of hydrothermal activity within the moon (*Hsu et al.*, 2015) indicate that the plumes originate from an underground water reservoir. The observed forced libration of Enceladus' surface reveals that the ocean is not only restricted to the moon's southern pole but it completely decouples the ice shell from the moon's rocky mantle (*Thomas et al.*, 2016).

Far away from the Sun, these oceans cannot be maintained by solar irradiation. Another heat source is therefore needed to prevent them from freezing; this heat source is most likely tidal dissipation. Due to orbital resonances with Io and Ganymede, Europa orbits Jupiter in an eccentric orbit. Similarly, in the Saturnian system, Enceladus' eccentricity is maintained by an orbital resonance with Dione. The orbital eccentricity results in a time-varying tidal potential that raises a prominent tide. The moons' obliquity results in additional latitudinal librations of the tidal bulge. Most studies focused on studying tidal dissipation in the solid layers of Europa and Enceladus (e.g., *Ojakangas and Stevenson*, 1989; *Roberts and Nimmo*, 2008). These studies show that the Europan ocean can be maintained by tidal and radiogenic heating; thermal models suggest that the ocean might be around 100 km thick (*Hussmann et al.*, 2002). This is, however, not the case of Enceladus, where tidal and radiogenic heating in the solid parts of the moon are not sufficient to prevent a global ocean from freezing (*Běhounková et al.*, 2017; *Tobie et al.*, 2008) unless Enceladus has an unconsolidated rocky core (*Choblet et al.*, 2017).

By analogy with Earth, where most tidal energy dissipation occurs in the ocean, it has been suggested that tidal dissipation within the ocean plays a major role. *Tyler* (2008) was the first to propose that oceanic tidal currents could heat the moons of the outer Solar System. *Tyler* (2008) considered the response of an ice-free shallow ocean of constant density. He solved the Laplace Tidal Equations (LTE) using the method of *Longuet-Higgins* (1968) for the different tidal constituents. He showed that Europa's obliquity excites planetary Rossby waves of considerable amplitude and suggested that this mechanism might close Enceladus' thermal energy budget (*Tyler*, 2009). However, it was later found that the obliquity of Enceladus is too small for this mechanism to generate enough tidal heating (*Chen and Nimmo*, 2011). *Tyler* (2014) and *Hay and Matsuyama* (2017) also

showed that the eccentricity tide can generate sufficient tidal heating but only for unrealistically shallow oceans. Subsequent studies considered the effect that the ice shell has on oceanic tidal dissipation and concluded that the ice crust further dampens the ocean response (*Beuthe*, 2016; *Matsuyama et al.*, 2018).

A possible criticism to the previous studies is the assumption of an ocean of constant density. An unstratified ocean filters out internal gravity waves which have an important role in tidal dissipation and mixing in Earth's ocean (*Garrett*, 2003). There is little information about the stratification of Europa's and Enceladus' oceans. The ocean is heated from the bottom by tidal and radiogenic heat within the silicate mantle, likely creating a well-mixed convecting ocean (*Goodman and Lenferink*, 2012; *Goodman et al.*, 2004; *Soderlund et al.*, 2013). Nevertheless, under certain conditions the ocean might be stratified (*Melosh et al.*, 2004; *Vance and Brown*, 2005). We do not challenge the assumption of an unstratified ocean and focus on the other assumptions underlying the LTE.

The main assumption of the LTE is that the ocean is in hydrostatic equilibrium, currents are predominantly horizontal. Because vertical currents are assumed to be small, the hydrostatic approximation is often used together with the traditional approximation, which consists in neglecting the terms of the Coriolis force linked to vertical motions in the ocean (*Gerkema et al.*, 2008). For an unstratified ocean these assumptions hold as long as the ratio of the characteristic vertical and horizontal length scales is small (see *Vallis* (2006)). Using the ocean thickness and body's radius as a measure of vertical and horizontal length scales, respectively, higher ratios are obtained for Europa and Enceladus than for Earth (~ 0.06 and ~ 0.15 versus ~ 0.001). It is therefore expected that the neglected vertical velocity is of more relevance in these bodies, making the LTE incomplete to describe tidal currents in Europa's and Enceladus' subsurface oceans.

Without the hydrostatic and traditional approximations, new kinds of waves are possible in the unstratified oceans of the icy moons, the so-called internal inertial (gyroscopic) waves (*Bretherton*, 1964; *Greenspan.*, 1969; *Maas*, 2001; *Stern*, 1963; *Stewartson*, 1971). These waves have properties that are markedly different from those of the more familiar surface waves (*Maas*, 2005) and have been suggested to be of importance for tidal dissipation in giant planets and binary stars (*Lainey et al.*, 2017; *Ogilvie and Lin*, 2004; *Rieutord and Valdettaro*, 1997, 2010; *Rieutord et al.*, 2001). In this study, we want to take the young field of "planetary oceanography" one step further by exploring the relevance of inertial waves for tidal dissipation in the icy moons.

We consider an ocean contained within a deformable spherical shell and study tidally induced inertial waves for different ocean thicknesses. Our main goal is to quantify the amount of tidal heating that is generated by these waves to assess whether they are a significant component in the thermal energy budget of these moons. Additionally, we compare the flow amplitude of inertial waves to that of surface gravity waves obtained with the LTE and consider the footprint that they might have on the satellites' surface. To do so we solve the linearised incompressible Navier-Stokes equations for the different components of the eccentricity and obliquity tide using the spectral methods developed to study inertial waves in an astrophysical context (stars and giant planets) (e.g., *Ogilvie and Lin*, 2004; *Rieutord and Valdettaro*, 1997, 2010).

The text is structured as follows: Section 4.2 introduces inertial waves and presents their main properties, in Section 4.3 we give the mathematical formulation of the problem, we introduce the tidal potential and then explain how the linearised Navier-Stokes equations are forced with this tidal forcing. Afterwards, the results are shown and discussed (Section 4.4) and conclusions are presented (Section 4.5)

4.2. PROPERTIES OF INTERNAL INERTIAL WAVES

To understand the properties of internal inertial waves we start by considering a simplified situation. We consider an inviscid fluid of constant density (ρ_0) inside a container rotating with angular velocity $\boldsymbol{\Omega}$. For this situation, the mass and momentum conservation equations, written in a co-rotating frame, are given by (e.g., *Le Bars et al.*, 2015):

$$\nabla \cdot \boldsymbol{u} = 0, \tag{4.1a}$$

$$\frac{\partial \boldsymbol{u}}{\partial t} + \boldsymbol{u} \cdot \nabla \boldsymbol{u} + 2\boldsymbol{\Omega} \times \boldsymbol{u} = -\nabla W. \tag{4.1b}$$

$\boldsymbol{u}$ is the fluid's velocity, W is a reduced pressure that contains the fluid pressure, the body's gravity potential and other possible conservative body forces. We neglect nonlinear terms and seek plane wave solutions of the form:

$$\boldsymbol{u} = Re\left[\tilde{\boldsymbol{u}} \mathrm{e}^{\mathrm{i}(\boldsymbol{k}\cdot\boldsymbol{x}+\omega t)}\right], \tag{4.2}$$

with $\boldsymbol{k}$ the wavevector, $\tilde{\boldsymbol{u}}$ the wave amplitude and ω the wave frequency. Introducing this trial solution to Eq. (4.1) we obtain a dispersion relation of the form:

$$\omega^2 = 4\Omega^2 \left(\frac{k_z^2}{k_x^2 + k_y^2 + k_z^2} \right), \tag{4.3}$$

where z is parallel to the rotational axis and x, y normal to it. This dispersion relation is markedly different from that of the more familiar surface-gravity waves. While for surface waves the frequency of the wave only depends on the magnitude of the wavenumber, for internal inertial waves it only depends on the angle that the wavevector forms with the rotational axis. The group velocity, ($\boldsymbol{c_g} = \frac{\partial \omega}{\partial \boldsymbol{k}}$) is perpendicular to the wavevector $\boldsymbol{k}$. Energy propagates along surfaces of constant slope, which form an angle θ with the rotational axis:

$$\theta = \arcsin\left(\frac{\omega}{2\Omega}\right), \tag{4.4}$$

the so-called characteristics (see Figure 4.1a).

These properties lead to a fundamental difference in how inertial waves behave upon reflection as compared to surface waves (e.g., *Maas*, 2005). When a monochromatic surface wave packet encounters a surface it reflects specularly without changing its wave-

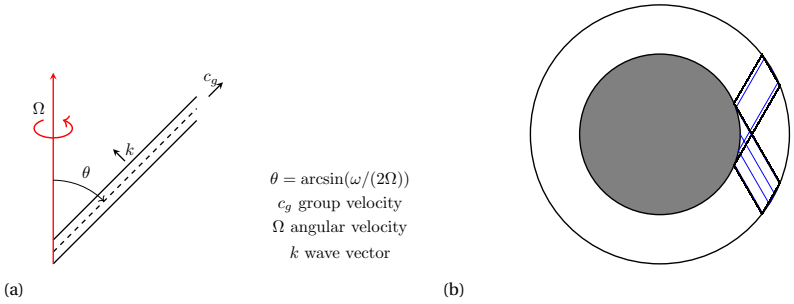

Figure 4.1 Inertial wave propagation. The wave packet propagates with group velocity $\boldsymbol{c_g}$ following characteristics that form an angle θ with the rotational axis. The wavevector $\boldsymbol{k}$ is perpendicular to the group velocity(a). (b) Depending on the container's geometry a wave packet (blue) can converge towards a periodic trajectory (black).

length. In contrast, an internal inertial wave packet reflects keeping the wavevector inclination with respect to the rotational axis constant. Upon reflection, the wavelength can change. Depending on the container's geometry this can lead to focusing of the wave packet, which becomes an efficient mechanism to transport energy from large to small scales.

The focusing properties of inertial waves can result in wave attractors. As its name indicates, wave attractors are trajectories in which energy accumulates. For ocean geometries that have focusing trajectories, two wave packets originating at different locations will converge towards the same trajectory (Figure 4.1b). Wave attractors have the peculiarity of focusing the energy of a large-scale forcing to smaller scales regardless of the nature and location of the excitation. This phenomenon has been observed in the laboratory, both for internal gravity waves (e.g., *Brouzet et al.*, 2016; *Maas et al.*, 1997) and internal inertial waves (e.g., *Maas*, 2001; *Manders and Maas*, 2003, 2004).

As it is of special relevance for astrophysical and geophysical applications, the propagation of inertial waves in spherical containers has been widely studied (e.g., *Bretherton*, 1964; *Bryan*, 1889; *Greenspan.*, 1969; *Ogilvie*, 2009; *Rieutord and Valdettaro*, 1997; *Stern*, 1963; *Stewartson*, 1971, 1972). The response of an inviscid fluid inside an spherical container is given by well-behaved eigenmodes (*Bryan*, 1889). However when a nucleus is added, wave attractors can develop, which lead to singularities; velocity increases without bound along the attractor (*Stewartson*, 1971). Something similar happens at the critical latitude (Θ_c), the latitude at which a characteristic is tangent to the nucleus, where the velocity also develops a singularity (*Rieutord et al.*, 2001). In reality, viscosity prevents the development of such singularities. The result is the development of prominent internal shear layers that propagate in the fluid domain following the characteristics where a significant amount of energy can be dissipated.

4.3. PROBLEM FORMULATION

4.3.1. THE TIDAL POTENTIAL

The obvious candidate for the generation of inertial waves in the oceans of the icy moons is the tidal potential caused by the obliquity and eccentricity of the moons. We can express the tidal potential in terms of the orbital elements of the satellite (*Jara-Orué and Vermeersen*, 2011):

$$\phi = -(nR)^2 \left(\frac{r}{R}\right)^2 \left\{\phi_0 + \phi_{ns} + \phi_{e0} + \phi_{e2} + \phi_{o1}\right\}, \tag{4.5}$$

where n is the mean motion of the satellite given by $n^2 = GM_p/a^3$, G is the universal gravitational constant, M_p the mass of the planet and a the semi-major axis of the satellite's orbit. As we are considering tidally locked satellites, n is the same as the rotational frequency of the satellite (Ω). R is the satellite's radius and r the distance from the center of the satellite to the considered point inside the satellite. The different components of the tidal potential are (*Jara-Orué and Vermeersen*, 2011):

$$\phi_0 = -\frac{1}{2}P_{2,0}(\cos\theta) + \frac{1}{4}P_{2,2}(\cos\theta)\cos\big(2\varphi\big), \tag{4.6a}$$

$$\phi_{ns} = -\frac{1}{2}P_{2,2}(\cos\theta)\sin\big(2\varphi + \Omega_{ns}t\big)\sin(\Omega_{ns}t), \tag{4.6b}$$

$$\phi_{e0} = -\frac{3e}{2}P_{2,0}(\cos\theta)\cos(nt), \tag{4.6c}$$

$$\phi_{e2} = \frac{e}{4}P_{2,2}(\cos\theta)\left[3\cos\big(2\varphi\big)\cos(nt) + 4\sin\big(2\varphi\big)\sin(nt)\right], \tag{4.6d}$$

$$\phi_{o1} = P_{2,1}(\cos\theta)\sin(\epsilon)\cos\big(\varphi\big)\sin(\Phi + nt). \tag{4.6e}$$

θ and φ are the co-latitude and longitude in the body-fixed reference frame, respectively. ϕ_0 is the static component of the tidal potential, ϕ_{ns} arises due to non-synchronous rotation. The eccentricity tide is given by ϕ_{e0}, which is caused by the variation in distance between the planet and the satellite; and ϕ_{e2}, caused by the east/west libration of the position of the subplanet point on the moon's surface. On the other hand, the obliquity tide, ϕ_{o1}, is the result of the latitudinal libration of the subplanet point due to the satellite's obliquity. $P_{l,m}$ are the associated Legendre polynomials of degree l and order m and Φ, e and ϵ are the argument of pericenter, the eccentricity and the obliquity of the moon, respectively. We only consider degree two terms of the tidal potential, as the amplitude of the other components rapidly decreases with increasing degree as $(r/a)^l$.

The non-axisymmetric term of the eccentricity tide (ϕ_{e2}) and the obliquity tide (ϕ_{o1}) can be further divided in a westward (ϕ_{e2w}, ϕ_{o1w}) and an eastward (ϕ_{e2e}, ϕ_{o1e}) propagating wave:

$$\phi_{e2} = \phi_{e2e} + \phi_{e2w} = \frac{7e}{8} P_{2,2}(\cos\theta)\cos(2\varphi - nt) - \frac{e}{8} P_{2,2}(\cos\theta)\cos(2\varphi + nt), \tag{4.7}$$

$$\phi_{o1} = \phi_{o1e} + \phi_{o1w} = -\frac{\sin(\epsilon)}{2} P_{2,1}(\cos\theta)\sin(\varphi - nt - \Phi) + \frac{\sin(\epsilon)}{2} P_{2,1}(\cos\theta)\sin(\varphi + nt + \Phi). \tag{4.8}$$

For this study we consider the different components of the eccentricity and obliquity tide and ignore the non-synchronous rotation of the satellite. We also ignore the static component of the tidal potential as it does not induce a dynamic ocean response. The relevant physical parameters of Europa and Enceladus are given in Table 4.1.

	Europa	Enceladus
R [km]	1565.0	252.3
M [kg]	$4.797 \cdot 10^{22}$	$1.0805 \cdot 10^{20}$
ρ_{av} [kgm^{-3}]	2990	1606
g [ms^{-2}]	1.31	0.11
Ω [rads^{-1}]	$2.05 \cdot 10^{-5}$	$5.31 \cdot 10^{-5}$
e [-]	0.0094	0.0047
ϵ [deg]	< 0.1	< 0.0015
$z_{e0}^{(eq)}$ [m]	11.08	11.50
$z_{e2e}^{(eq)}$ [m]	19.39	20.13
$z_{e2w}^{(eq)}$ [m]	2.77	2.88
$z_{o2e}^{(eq)}$ [m]	1.03	0.003
$z_{o2w}^{(eq)}$ [m]	1.03	0.003
Φ [deg]	0	0
ρ_o [kgm^{-3}]	1000	1000

Table 4.1 Physical parameters for Europa and Enceladus. Radius (R), mass (M), average density (ρ_{av}), surface gravity (g) and rotational rate (Ω) are obtained from: https://ssd.jpl.nasa.gov/?horizons and *Chen et al.* (2014). The obliquity (ϵ) of Europa and Enceladus are obtained assuming that the moons are in a Cassini state (*Baland et al.*, 2012; *Chen and Nimmo*, 2011). The maximum amplitude of the different components of the equilibrium tide are computed considering a non-self gravitating ice-free ocean surrounding an infinitely rigid core (Eq. (4.17)) and using the maximum value of the satellites' obliquity. The argument of pericenter (Φ) and ocean density (ρ_o) are assumed to be 0 and 1000 kgm^{-3}, respectively.

4.3.2. GOVERNING EQUATIONS AND ASSUMPTIONS

In contrast to Section 4.2, we now consider the fluid to be viscous and expand the reduced pressure in its different components. The equations of motion can be written as:

$$\nabla \cdot \boldsymbol{u} = 0, \tag{4.9a}$$

$$\frac{\partial \boldsymbol{u}}{\partial t} + \boldsymbol{u} \cdot \nabla \boldsymbol{u} + 2\boldsymbol{\Omega} \times \boldsymbol{u} = -\frac{1}{\rho_0}\nabla p' + \frac{1}{\rho_0}\nabla \cdot \boldsymbol{\tau} - \nabla\phi - \nabla\phi'. \tag{4.9b}$$

The primed quantities denote deviations from hydrostatic equilibrium. ϕ' represents the gravitational potential of the body, p' is the fluid pressure and τ the stress tensor of the fluid, which we assume to follow Stokes' constitutive law:

$$\boldsymbol{\tau} = \mu(\nabla \boldsymbol{u} + \nabla \boldsymbol{u}^T), \tag{4.10}$$

where μ is the dynamic molecular viscosity. We further use perturbation theory and consider the different quantities to be small. Under such consideration the non-linear advective term $(\boldsymbol{u} \cdot \nabla \boldsymbol{u})$ is neglected. The validity of this assumption will be discussed later (Section 4.5). We introduce an effective viscosity μ_{eff}, which is higher than the molecular viscosity of the fluid and accounts for non-modelled small-scale dissipation mechanisms (e.g., turbulent mixing, interactions of waves with turbulent convection, etc.).

Finally, we obtain the non-dimensional form of the equations of motion by using the inverse of the satellite's rotational frequency $(2\Omega)^{-1}$ and the satellite radius (R) as time and length scales respectively:

$$\hat{\nabla} \cdot \hat{\boldsymbol{u}} = 0, \tag{4.11a}$$

$$\frac{\partial \hat{\boldsymbol{u}}}{\partial \hat{t}} + \boldsymbol{e_z} \times \hat{\boldsymbol{u}} = -\hat{\nabla}\hat{W} + E\hat{\nabla}^2\hat{\boldsymbol{u}}, \tag{4.11b}$$

with $\boldsymbol{e_z}$ the direction of the satellite's rotational axis, W again the reduced pressure:

$$W = \frac{p'}{\rho_o} + \phi + \phi' \tag{4.12}$$

and the non-dimensional variables (indicated with a hat) and parameters defined as:

$$\boldsymbol{u} = 2\Omega R\hat{\boldsymbol{u}}, \tag{4.13a}$$

$$W = 4\Omega^2 R^2 \hat{W}, \tag{4.13b}$$

$$E = \frac{\mu_{eff}}{2\rho\Omega R^2}, \tag{4.14a}$$

$$\hat{\omega} = \frac{n}{2\Omega}. \tag{4.14b}$$

We have introduced the non-dimensional Ekman number (E), which gives the ratio of viscous to Coriolis forces; and the non-dimensional frequency ($\hat{\omega}$), which, since the problem is forced at the diurnal tidal frequency, equals 0.5. In the discussion that follows we use the non-dimensional equations; to avoid cumbersome notation we drop the hat from the variables.

As a starting point we assume that the moons have a free surface. If the surface wave speed ($\sqrt{gh}$, with g the satellite's surface gravity and h the ocean depth) is high enough so that the ocean adjusts quickly to forces varying at the tidal potential frequency, we can assume that the radial displacement of the ocean surface is given by the equilibrium tide (*Ogilvie*, 2009; *Tyler*, 2008). This assumption breaks down if the ocean is too shallow, in that case surface gravity waves dominate the ocean response and other kinds of resonances occur (*Matsuyama et al.*, 2018). For the icy moons, the surface wave speed is high enough as long as the oceans are thicker than 0.78 km or 1.6 km for Europa and Enceladus, respectively. With ocean thicknesses of ~ 100 km (*Hussmann et al.*, 2002) and ~ 38 km (*Beuthe et al.*, 2016) for Europa and Enceladus respectively, the previous assumption seems reasonable for the problem at hand.

We follow the approach of *Ogilvie* (2005) and *Rieutord and Valdettaro* (2010) and split the fluid response into two components: the equilibrium tide $\boldsymbol{u}^{(eq)}$ plus a dynamical tide $\boldsymbol{u}^{(d)}$. By using this decomposition, Eq. (4.11) becomes:

$$\frac{\partial \boldsymbol{u}^{(d)}}{\partial t} + \boldsymbol{e_z} \times \boldsymbol{u}^{(d)} = -\nabla W + E\nabla^2 \boldsymbol{u}^{(d)} + \boldsymbol{f}^{(eq)}. \tag{4.15}$$

$\boldsymbol{f}^{(eq)}$ is an inertial force associated with the equilibrium tide given by:

$$\boldsymbol{f}^{(eq)} = -\frac{\partial \boldsymbol{u}^{(eq)}}{\partial t} - \boldsymbol{e_z} \times \boldsymbol{u}^{(eq)}. \tag{4.16}$$

Note that the dynamic tide is forced indirectly through the equilibrium tide as it does not satisfy the momentum equation (*Ogilvie and Lin*, 2004). If we consider a non self-gravitating ocean around an infinitely rigid core with a free-surface the equilibrium tide is simply given by:

$$\boldsymbol{z}^{(eq)}_{l,m} = -\frac{\phi_{l,m}}{g}\boldsymbol{e_r}, \tag{4.17}$$

where $\phi_{l,m}$ is the degree l order m component of the tidal potential. The maximum amplitude of the equilibrium tide for Europa and Enceladus for the different tidal components is given in Table 4.1. If the effect of self-gravitation, the finite rigidity of the core or the presence of an ice-shell is considered the equilibrium tide can be obtained as:

$$\boldsymbol{z}^{(eq)}_{l,m} = -Z_{l,m}\frac{\phi_{l,m}}{g}\boldsymbol{e_r}, \tag{4.18}$$

with $Z_{l,m}$ being an admittance factor. *Matsuyama et al.* (2018) showed that an ice shell dampens the response of the ocean resulting in $Z_{l,m}$ to be smaller than or close to 1. In particular, for realistic ice shell thicknesses, the admittance is close to 1 for Europa while it can be more than one order of magnitude smaller for Enceladus. In this work, we assume the ocean to follow the equilibrium tide of an ice-free, non self-gravitating ocean in a satellite with a infinitely rigid core (Eq. (4.17)). By doing so, we obtain an upper bound of tidal dissipation due to inertial waves in a spherical shell shaped ocean.

We assume the system to have a response with the same frequency as the forcing tidal potential and thus we consider the different fields to be proportional to $e^{i\omega t}$. By doing so we can eliminate time from the equations of motion and we are left with the system:

$$\nabla \cdot \boldsymbol{u}^{(\boldsymbol{d})} = 0, \tag{4.19a}$$

$$i\omega \boldsymbol{u}^{(\boldsymbol{d})} + \boldsymbol{e_z} \times \boldsymbol{u}^{(\boldsymbol{d})} = -\nabla W + E\nabla^2 \boldsymbol{u}^{(\boldsymbol{d})} + \boldsymbol{f}^{(\boldsymbol{eq})}, \tag{4.19b}$$

$$\boldsymbol{f}^{(\boldsymbol{eq})} = -i\omega \boldsymbol{u}^{(\boldsymbol{eq})} - \boldsymbol{e_z} \times \boldsymbol{u}^{(\boldsymbol{eq})}. \tag{4.19c}$$

We solve Equations (4.19) in a spherical shell, assuming no-slip boundary conditions at the fluid-solid interfaces ($\boldsymbol{u_d} = 0$).

4.3.3. NUMERICAL APPROACH

We solve Equations (4.19) for the different constituents of the equilibrium tide (Eq. (4.17)). As we did with the tidal potential, we expand the equilibrium tide into its different constituents: the order 0 eccentricity tide ($\boldsymbol{u}^{(\boldsymbol{eq})}_{\boldsymbol{e0}}$), and the eastward and westward components of the order 2 eccentricity tide and order 1 obliquity tide ($\boldsymbol{u}^{(\boldsymbol{eq})}_{\boldsymbol{e2e}}$,$\boldsymbol{u}^{(\boldsymbol{eq})}_{\boldsymbol{e2w}}$ and $\boldsymbol{u}^{(\boldsymbol{eq})}_{\boldsymbol{o1e}}$,$\boldsymbol{u}^{(\boldsymbol{eq})}_{\boldsymbol{o1w}}$) (see Appendix 4.6). We then solve Equations (4.19) using $\omega = 0.5$ and $\omega = -0.5$ for the westward and eastward propagating components respectively.

We use the method of *Rieutord and Valdettaro* (1997, 2010), which is detailed in Appendix 4.6. We make use of the spherical symmetry of the problem and expand the velocity and reduced pressure fields using L spherical harmonics in the horizontal direction. The resulting equations are discretised in the radial direction using Chebyshev polynomials on $N+1$ Gauss-Lobatto collocation nodes. By doing so, Eq. (4.19) and the boundary conditions result in an algebraic system of $(L-m+1)(N+1)$ linear equations. The associated matrix of this linear system is block-tridiagonal, and the system is solved using classical LU-factorization of a banded matrix. Except where otherwise indicated, the resolution, given by L and N, is chosen so that the truncation error is less than $\sim 10^{-4}$.

We are specially interested in computing tidal dissipation due to the tidally-induced flows. We compute the amplitude of tidal dissipation as (e.g., *Ogilvie and Lin*, 2004):

$$\hat{D}_v = 2E \int_V c^*_{ij} c_{ij} \, dV, \tag{4.20}$$

where c_{ij} are the elements of the rate-of-strain tensor, $c_{ij} = \frac{1}{2}(\partial_i u_j + \partial_j u_i)$. We expand Eq. (4.20) using spherical harmonics as indicated in Appendix 4.7.

4.4. RESULTS

4.4.1. PARAMETER REGIME

The two parameters that control the fluid response are the ocean thickness and the Ekman number. We characterise the thickness of the ocean using the ratio of the inner to outer ocean radius, η. Europa's and Enceladus' ocean thicknesses are still not known. To understand the effect of ocean geometry on the propagation of inertial waves, we explore the range $\eta = 0.3 - 0.99$, which corresponds to ocean thicknesses ranging from 1095.5 to 15.7 km for Europa and 176.6 to 2.5 km for Enceladus. For this range we use a resolution of $\Delta\eta = 0.005$, which is equivalent to ocean thickness changes of 7825 m for Europa and 1262 m for Enceladus. However, current estimates suggest an η of ~ 0.93 (*Hussmann et al.*, 2002) for Europa and ~ 0.85 (*Beuthe et al.*, 2016) for Enceladus. It is for this reason that we further explore the range $\eta = 0.8 - 0.99$ using a $\Delta\eta$ of 0.0005.

The Ekman number depends on the fluid viscosity (Eq. (4.14)). If we compute the Ekman number using the molecular viscosity of water we obtain a value of 10^{-14} and 10^{-13} for Europa and Enceladus respectively. These low Ekman numbers require currently unattainable resolutions. In any case, when linearising the equations of motion we have introduced a new effective dynamic viscosity (μ_{eff}) that accounts for small-scale dissipation mechanisms. Given our limited knowledge about these oceans it is difficult to estimate the appropriate value of this parameter. It is however expected that the effective viscosity will be orders of magnitudes higher than the molecular viscosity (e.g., *Ogilvie and Lin*, 2004). In the following experiments we explore a wide range of Ekman numbers ($E = 10^{-4} - 10^{-10}$) to account for this uncertainty.

We first study the propagation of inertial waves for different ocean thicknesses and Ekman numbers and explain the main characteristics in terms of the properties defined in Section 4.2 such as wave attractors and the critical latitude singularity (Section 4.4.2). Afterwards, we focus on tidal dissipation and quantify the relevance of inertial waves for Europa's and Enceladus' thermal energy budget (Section 4.4.3)

4.4.2. WAVE ATTRACTORS AND THE CRITICAL LATITUDE SINGULARITY

As explained in Section 4.2 the response of the fluid is dominated by the convergence of wave packets towards wave attractors and the critical latitude singularity. We start by studying the structure of wave attractors that are excited by tidal forcing. As the moons are phase-locked, the frequency of the forcing equals the rotational frequency of the moon, hence, the angle that the characteristics form with the vertical is 30° (Figure 4.1a). We use ray-tracing to study the propagation of energy in meridional planes of the fluid domain. The intersection of the characteristic surfaces with a meridional plane are straight lines (rays) along which energy propagates. We launch a wave packet from a point on the inner sphere without zonal velocity and follow its propagation along the characteristics until it converges towards an attractor in the same meridional plane. Note that when a wave packet is launched with a zonal component it may end up trapped in a meridional plane or escape meridional trapping and reflect endlessly around the domain (*Rabitti and Maas*, 2014, 2013). However, because of the symmetry of the tidal

potential with respect to rotation around the z axis we focus on wave attractors in the meridional plane.

We launch a wave ray from a point equatorward of the critical latitude (5°) and one poleward (85°). The latitude of the last 100 inner boundary reflections are then noted and shown in a Poincaré plot in Figure 4.2a. Additionally, we compute the Lyapunov exponent, which measures the asymptotic rate at which two neighbouring rays converge:

$$\Lambda = \lim_{N\to\infty} \sum_{n=1}^{N} log \left| \frac{d\Theta_{n+1}}{d\Theta_n} \right|. \tag{4.21}$$

$d\Theta$ is the angular distance between the reflection points of two neighbouring characteristics. High (in absolute value) Lyapunov exponents mean highly attracting wave attractors while a Lyapunov exponent equal to 0 indicates non-attracting trajectories. The Lyapunov exponent for different ocean geometries is displayed in Figure 4.2b.

We distinguish between two types of attractors: equatorial attractors, trapped equatorward of the critical latitude, and polar attractors, with reflections outside the previously mentioned interval. As can be seen in Figure 4.2a, the shape of the attractor depends on the ratio of inner to outer ocean radius (η). For some ocean geometries, attractors with few reflections (short attractors) and high (in absolute value) Lyapunov exponents exist. This is the case of the band $[0.5775, 0.6545]$ and $[0.7235, 0.7420]$. In the first case, both equatorial and polar attractors exist, while for the second only polar attractors appear. The peak for $\eta = 0.6545$ corresponds to an attractor with reflections infinitesimally close to the critical latitude, where there is nearly infinite focusing. For such attractors, the Lyapunov exponent goes to minus infinity as resolution in η increases (*Rieutord et al.*, 2001).

For $\eta < 0.57$, there are non-attracting periodic trajectories with a Lyapunov exponent close to 0. In fact, it can be shown that for $\eta \leq 0.5$ all trajectories associated with the frequency $n/2\Omega = 0.5$ are strictly periodic and have a Lyapunov exponent equal to 0 (*Rieutord et al.*, 2001). For these ocean geometries if a ray is launched from the inner sphere it will eventually return to the same point after some reflections, explaining the horizontal lines in Figure 4.2a.

The response of the fluid is characterised by the opposing effects of wave focusing and viscous diffusion. The focusing effect of the geometry tends to focus energy towards small scales ultimately leading to a singularity along the wave attractor. On the other hand, viscosity diffuses the velocity countering the geometrical focusing effect and the development of wave attractors. As we will now see, these two competing effects determine whether a wave attractor is excited for a particular ocean geometry or not.

We start by choosing two ocean geometries with a high (in absolute value) Lyapunov exponent, $\eta = 0.63$ and $\eta = 0.73$, and force the fluid with the axisymmetric eccentricity tidal component for two different Ekman numbers, 10^{-7} and 10^{-9}. To achieve a truncation error less than $\sim 10^{-4}$, we use a resolution of $L = 500$ and $N = 200$ for $E = 10^{-7}$ and $N = 200$ and $L = 1200$ for $E = 10^{-9}$. A meridional cut of the sphere showing the amplitude of the kinetic energy and viscous dissipation is shown in Figure 4.3. For this tidal com-

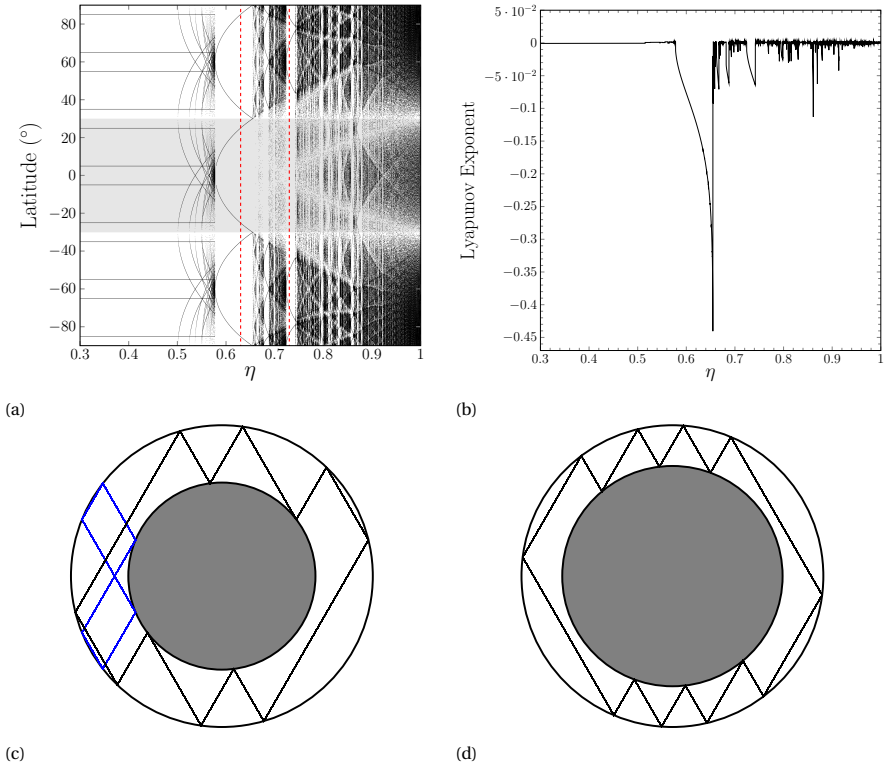

Figure 4.2 Poincaré plot (a) and Lyapunov exponent (b) for a forcing frequency of $n/(2\Omega) = 0.5$. In (a) the latitude of the last 100 reflection points on the inner sphere for rays launched from ±5° and ±85° latitude are indicated for different inner to outer ocean radius ratios (η). The shaded region indicates reflections equatorward of the critical latitude. Two specific ocean geometries for which short, highly attractingwave attractors exist ($\eta = 0.63, 0.73$) are indicated in red and shown in (c) and (d), respectively. (b) gives the Lyapunov exponent for the polar attractors.

ponent the plots are independent of the meridional cut. Also superimposed, we show the wave attractors characteristic of these two ocean geometries.

As can be seen, in both cases wave attractors are generated. Internal shear layers are clearly observed along the attractors where both kinetic energy and viscous dissipation are enhanced. As in *Rieutord and Valdettaro* (2010) we observe the importance of the critical latitude singularity for producing the attractor. The attractor seems to be "fed" by the shear layer emanating from for critical latitude. As expected, as the Ekman decreases the internal shear layer becomes thinner.

We also explore the behaviour of the fluid for ocean geometries with a low (in absolute value) Lyapunov exponent. In such cases, the critical latitude singularity dominates the flow (*Ogilvie*, 2009; *Ogilvie and Lin*, 2004; *Rieutord and Valdettaro*, 2010). We distinguish two cases: ocean geometries where periodic non-focusing trajectories exist (e.g., $\eta = 0.35, 0.5$), $\Lambda = 0$, and geometries with long weakly-attracting wave attractors (e.g., $\eta = 0.75, 0.8815$), $\Lambda < 0$. For the first case, the shear layer emitted from the critical latitude propagates following the characteristics and widens slowly due to viscous dissipation and the lack of focusing (Figures 4.4a-4.4b). In contrast, for the second case we observe the focusing of the shear layer upon reflection (Figures 4.4c-4.4e).

For $\eta = 0.75$ and 0.8815 we observe that as the ray approaches the polar regions both kinetic energy and dissipation are enhanced (*Rieutord and Valdettaro*, 1997). The effect of changing the Ekman number is similar to that reported for those cases where wave attractors appear. It is expected that if the Ekman number is sufficiently small the focusing effect will prevail over viscous diffusion leading to the generation of long wave attractors for $\eta = 0.75$ and 0.8815 similar to those observed for $\eta = 0.63$ and 0.73. However, the low Ekman number for which this transition occurs requires resolutions currently computationally unattainable.

The case of $\eta = 0.8815$ is especially interesting as it corresponds to an Enceladan ocean thickness of around 30 km, which is close to current estimates for Enceladus (*Beuthe et al.*, 2016; *Čadek et al.*, 2016; *Thomas et al.*, 2016). For this ocean thickness we compute the maximum velocity amplitude of inertial tides and study the possible manifestation of inertial waves on Enceladus' surface. We find that the maximum velocity amplitude varies from 0.5 to 3 cm/s for Ekman numbers ranging from 10^{-7} to 10^{-10}. Moreover, the maximum velocity amplitude is always encountered in polar regions. These currents are stronger than those induced by the eccentricity tide under the shallow water approximation, which for realistic ocean thicknesses have a magnitude of around 1 mm/s (*Tyler*, 2009).

Vermeersen et al. (2013) suggested that wave attractors in a polar ocean basin could be the origin of Enceladus' tiger-stripes; here we investigate this hypothesis for the present configuration (an unstratified global ocean of constant depth). Interaction between the fluid and the ice shell are likely to occur at the inertial waves reflection points, where we observe enhanced dissipation. For a 30 km thick ocean, we observe that the pressure at these points is in the order of ~ 1 Pa. Moreover, we can estimate the melting rate of the ice shell at these points by assuming that all the energy dissipated in a ray is focused there and does not radiate outwards. We obtain a maximum melting rate in the

order of 1 m every 10 kyr. Even though it is unclear how inertial waves would interact with the ice shell, these numbers suggest that in an ocean of constant thickness it is unlikely that tidally-excited inertial waves could be the origin of observed surface features, such as the tiger stripes. More work is needed to study if other ocean geometries can result in enhanced energy focusing and higher stresses.

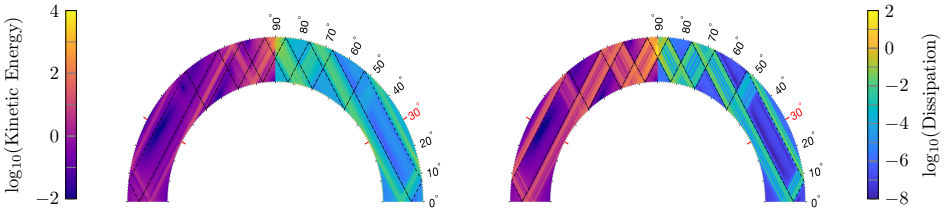

(a) $E = 10^{-7}$, $\eta = 0.73$ (b) $E = 10^{-9}$, $\eta = 0.73$

(c) $E = 10^{-7}$, $\eta = 0.63$ (d) $E = 10^{-9}$, $\eta = 0.63$

Figure 4.3 Non-dimensional kinetic energy (left quadrant) and viscous dissipation (right quadrant) amplitude due to the degree two, order zero eccentricity tide for two ocean geometries where short wave attractors exist. The patterns are shown for different Ekman number (E) and inner to outer ocean radius ratio (η). Polar and equatorial wave attractors are superimposed in black and green, respectively, and the critical latitude is indicated in red. A logarithmic scale is used both for kinetic energy and viscous dissipation. The maximum values of the non-dimensional colour-scale correspond to a kinetic energy of 0.65 $\mathrm{J\,m^{-3}}$ and 4.69 $\mathrm{J\,m^{-3}}$; and a viscous dissipation of 0.26 $\mu\mathrm{W\,m^{-3}}$ and 4.97 $\mu\mathrm{W\,m^{-3}}$ for Europa and Enceladus, respectively.

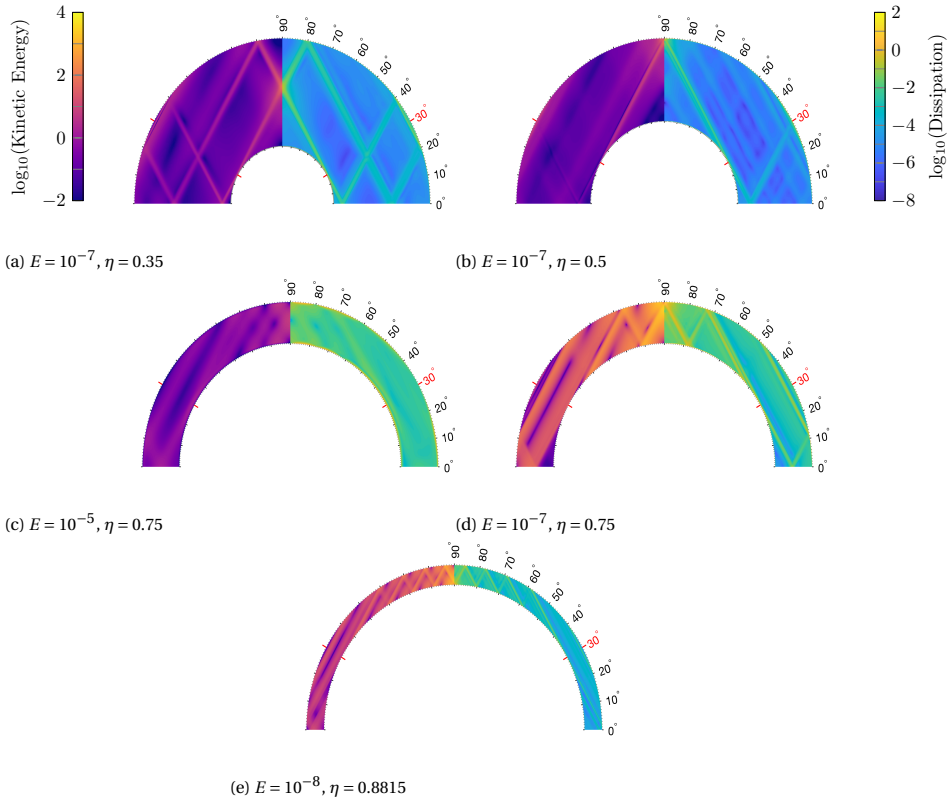

(a) $E = 10^{-7}$, $\eta = 0.35$

(b) $E = 10^{-7}$, $\eta = 0.5$

(c) $E = 10^{-5}$, $\eta = 0.75$

(d) $E = 10^{-7}$, $\eta = 0.75$

(e) $E = 10^{-8}$, $\eta = 0.8815$

Figure 4.4 Same as Figure 4.3 but for ocean geometries with a small Lyapunov exponent. Rays emanating from the critical latitude (and not wave attractors) dominate the flow response.

4.4.3. TIDAL DISSIPATION

The main focus of this work is to study tidal dissipation within Europa and Enceladus. We start by assuming an Ekman number of 10^{-7} and compute tidal dissipation for the different tidal constituents and different ocean thickness ($\eta = 0.3 - 1$) as detailed in Appendix 4.7. To strengthen our conclusions, we then analyse the effect of varying the Ekman number on the degree-two order-zero tidal constituent. For the different shell geometries, we first vary the Ekman number between $10^{-4} - 10^{-8}$. We then study the asymptotic behaviour of dissipation with decreasing Ekman number for some relevant shell geometries for which we use an Ekman number as low as 10^{-10}.

TIDAL DISSIPATION FOR THE DIFFERENT TIDAL COMPONENTS

Dissipation due to tidally induced inertial waves in Europa and Enceladus for $E = 10^{-7}$, is shown in Figure 4.5. As a reference, we also indicate the estimated value of radiogenic

heating in Europa (*Hussmann et al.*, 2010) and the observed thermal output of Enceladus' tiger stripes (*Spencer et al.*, 2013).

It can be seen that the values of the tidal dissipation are well below the reference values for both Europa and Enceladus. Moreover, when we consider the region of the plot that corresponds to likely values of ocean thickness on Europa and Enceladus, $\eta > 0.9$ (*Anderson et al.*, 1998; *Hussmann et al.*, 2002) and $\eta > 0.8$ (*Beuthe et al.*, 2016; *Čadek et al.*, 2016; *Thomas et al.*, 2016), respectively, we observe that the values of tidal dissipation are several orders of magnitude smaller than radiogenic heating in Europa and the observed heat flux in Enceladus. Nevertheless, it is interesting to study the contribution of the different tidal constituents. We see that the axisymmetric eccentricity and eastward tide dominate the fluid response. Moreover, the order one obliquity tide produces considerably lower tidal dissipation, especially in Enceladus. This fact follows from the small amplitude of this tidal component as compared with the others (see Table 4.1) .

For most tidal constituents the tidal dissipation curve is markedly spiky (Figure 4.5). There are values of η for which dissipation is enhanced by more than one order of magnitude. The complex system of internal-shear layers that arise due to the singularities of the problem results in different values of dissipation for different ocean geometries. This is not the case of the westward propagating obliquity tide whose dissipation is given by a much smoother curve. This is because for a degree two, order one forcing the equations of motion admit a purely toroidal solution (*Rieutord and Valdettaro*, 1997), the so called "spin-over" mode. This solution is an exact solution of the equations of motion in case stress-free boundary conditions are used.

However, when no-slip boundary conditions are used for the westward obliquity tide the "spin-over" mode disappears. The use of no-slip boundary conditions results in the development of an oscillatory Ekman layer at the solid-liquid boundary. The thickness of this Ekman layer scales with $\approx E^{1/2}$, however at the critical latitude it thickens and scales as $\sim E^{2/5}$ over a region of width $\sim E^{1/5}$ (*Hollerbach and Kerswell*, 1995; *Kerswell*, 1995). The thickening of the Ekman layer breaks the symmetry of the problem and launches inertial waves that propagates in the interior. However, the resulting internal shear layers are weaker in this case than those generated by the other tidal constituents, dissipation is dominated by the Ekman layer that forms in the solid-liquid boundary, which is less dependent on the shell geometry.

DEPENDENCE OF TIDAL DISSIPATION ON EKMAN NUMBER

We study the dependence of tidal dissipation with Ekman number. For a given ocean thickness (η) we distinguish three different cases depending on the behaviour of viscous dissipation in the limit $E \to 0$. Dissipation can increase, decrease or become asymptotically constant. We call the first and second cases resonance and anti-resonance, respectively, after *Rieutord and Valdettaro* (2010). As we will see, the last case is associated with the appearance of a wave attractor Note that this definition differs from the classic definition of a resonance, commonly associated with the excitation of eigenmodes.

We start by varying the Ekman number from 10^{-4} to 10^{-8} for the axisymmetric eccentricity tide (Figure 4.6). For high Ekman numbers ($E = 10^{-4}, 10^{-5}$) the flow is domi-

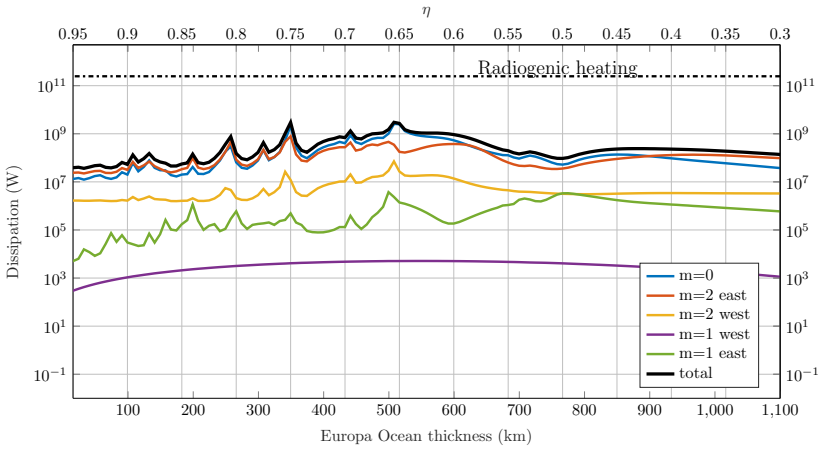

(a)

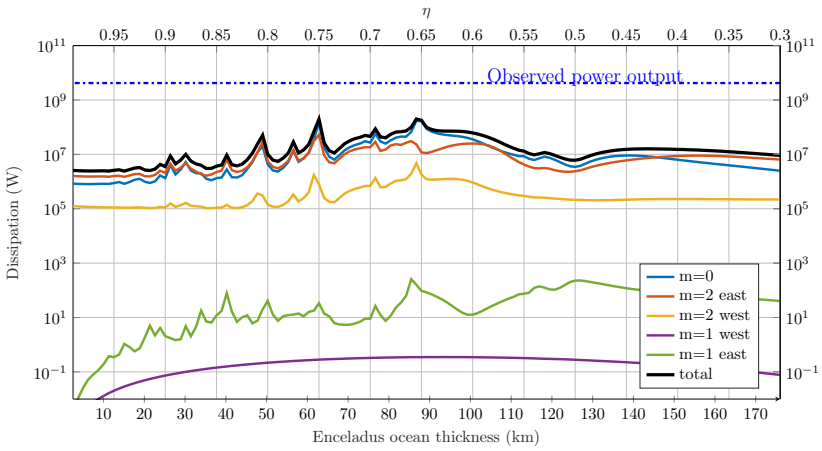

(b)

Figure 4.5 Tidal dissipation amplitude due to tidally excited inertial waves in Europa (a) and Enceladus (b). The ocean is assumed to be within a spherical shell of constant thickness (inner to outer ocean radius ratio, η). All values are computed using $E = 10^{-7}$. The axisymmetric and non-axisymmetric components of the eccentricity tide ($m = 0$ and $m = 2$) as well as the obliquity tide ($m = 1$) are considered. As reference, an estimate of Europa's radiogenic heating and the power radiated from Enceladus tiger stripes are indicated.

nated by the Ekman boundary layer formed at the solid-fluid boundary and not internal shear layers and wave attractors (see Figure 4.4c). For such cases the dissipation curve is smooth, similarly to the westward order one obliquity tide. As the Ekman number decreases, internal shear layers and wave attractors become the dominant features of the fluid response and the curve becomes more spiky.

We see that for small values of η dissipation decreases with Ekman number, an anti-resonance. The behaviour becomes more complicated for thinner oceans for which resonances occur for some values of η (e.g., 0.75, 0.807, 0.8415, 0.8815), moreover, we see that these cases correspond to local maxima of tidal dissipation (in η). We select some representative cases of η in which we observe wave attractors ($\eta = 0.63$ and 0.73), anti-resonances ($\eta = 0.35$) or resonances ($\eta = 0.76$ and 0.8815) for further study. For these cases we further explore the change of dissipation as the Ekman number decreases (Figure 4.7). We use an Ekman number as low as 10^{-10}, which requires enhanced resolution ($L = 2000$, $N = 350$) to achieve a truncation error of $\sim 10^{-3}$.

For a thick ocean ($\eta = 0.35$), dissipation decreases with decreasing Ekman number. Dissipation approximately follows a power law of the form $\sim E^{0.35}$. As explained, for this ocean geometry, strictly non-attracting periodic trajectories exist. *Rieutord and Valdettaro* (2018) have shown that in such a situation the fluid responds to the excitation with a flow characterised by an ever increasing wavenumber that ultimately, when E=0, inhibits any response. This is actually the anti-resonance associated with the periodic trajectory $\omega = \sin(\pi/6)$.

We now consider the two cases with highly attracting short wave attractors, $\eta = 0.63$ and $\eta = 0.73$, depicted in Figure 4.3. Figure 4.7 shows that for these two cases dissipation tends towards an asymptotic limit. In a wave attractor there is a balance between focusing and diffusion. As the Ekman number is reduced, the thickness of the internal shear layer is reduced and the velocity gradient increased in such a way that dissipation remains constant. This situation is similar to that observed in *Ogilvie* (2005) who showed the asymptotic convergence of dissipation in wave attractors in a rectangular container. It is also interesting to note that the asymptotic limit is reached at higher Ekman numbers for $\eta = 0.63$ than for $\eta = 0.73$. Figure 4.3 shows that the $\eta = 0.73$ attractor is longer and less attracting, viscous dissipation acts along a longer distance and prevents the attractor from developing for high Ekman number.

Finally, we focus on two cases where a resonance occurs ($\eta = 0.75$ and 0.8815). These resonances are of special relevance if the Ekman number of Europa's and Enceladus' ocean is very low, for example close to that given by the molecular viscosity of water ($10^{-14} - 10^{-13}$). In such a case, if a resonant state is attained, dissipation could be considerably higher than the values computed for Ekman numbers several orders of magnitude higher. As seen in Figure 4.7, for these two cases dissipation increases with decreasing Ekman number until it reaches a maximum and then starts to decrease again. This behaviour can be understood by analysing the resonance peaks in Figure 4.6b. We see that as the Ekman number decreases the curve becomes more spiky, the resonance peak narrows. If the exact η for which the resonance occurs is not chosen, dissipation will decrease with decreasing Ekman number as the resonance peak becomes narrower. As is evident from this plot, our current resolution does not allow us to resolve the exact

value of η at which dissipation reaches its maximum.

Higher resolution is needed in our explored parameter space to find the exact resonant values of η. It is likely that at these exact resonant ocean geometries the actual dissipation for an Ekman number close to that given by the molecular viscosity of water ($E = 10^{-13} - 10^{-14}$) is several orders of magnitude higher than what we find in Figure 4.6. However, we need to recall that as the Ekman number decreases the resonance peak becomes narrower, thus a resonance would only occur over a very narrow range of ocean thicknesses. For instance, we see that by using $\Delta\eta = 126$ m for Enceladus or 783 m for Europa the resonance peak for $\eta = 0.8815$ at an Ekman number of 10^{-9} is already missed. It seems impossible that the ocean of Europa or Enceladus is of the thickness precisely required for such resonances to occur, specially since this would require the sea-floor and ice shell to be devoid of topographical features of higher amplitude than the previously mentioned resolution.

4.5. DISCUSSION AND CONCLUSIONS

In this work we analyse for the first time tidal dissipation due to inertial waves in Europa and Enceladus. We consider tides caused by the eccentric orbit of these satellites as well as their obliquity. We consider an ocean contained within a spherical shell and use a spectral method to compute tidal dissipation for different ocean thicknesses and dynamic viscosity coefficients (given by the Ekman number). We neglect the effect of the ice shell and argue that our results represent an upper bound estimate for tidal dissipation for an ice-covered moon.

We find that dissipation depends strongly on ocean thickness and Ekman number. One of the challenges in computing tidal dissipation is the scarcity of information about Europa and Enceladus oceans. For instance, the effective viscosity, which depends on small-scale dissipative processes, is not known. It is for this reason that we analyse the behaviour of the fluid for a wide range of Ekman numbers. For a given ocean thickness we distinguish three different scenarios depending on the behaviour of dissipation with Ekman number. If a wave attractor is excited, an asymptotic limit is reached where dissipation is independent of viscosity. Otherwise, there can be an anti-resonance or resonance depending on the ocean geometry. Anti-resonant states, where we observe a decrease of dissipation with decreasing Ekman number, are attained for unrealistically thick oceans; while resonant states, where dissipation increases with decreasing Ekman number, are common for shallower oceans.

After analysing the effect of changing the ocean thickness and viscosity we conclude that under the aforementioned assumptions, tidal dissipation due to inertial waves is several orders of magnitude smaller than Europa's radiogenic heating and Enceladus' observed heat flux and thus does not play an important role in preventing these oceans from freezing. Still, we observe that the induced tidal currents can be one order of magnitude stronger than those obtained using the Laplace Tidal Equations (e.g., *Tyler*, 2008, 2009). We find that for a 30 km thick Enceladan ocean tidal currents of amplitude 3 cm/s are excited. We also consider the possible interaction of inertial waves and the ice shell and conclude that for global oceans of constant thickness it is unlikely that inertial waves

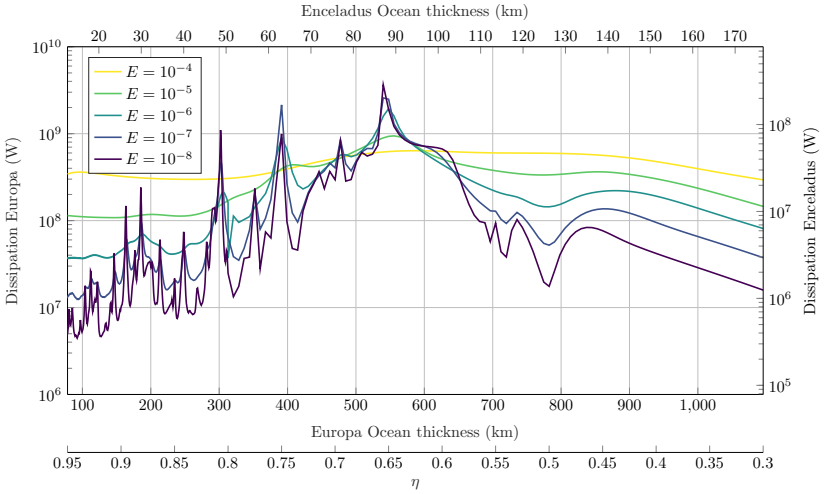

(a)

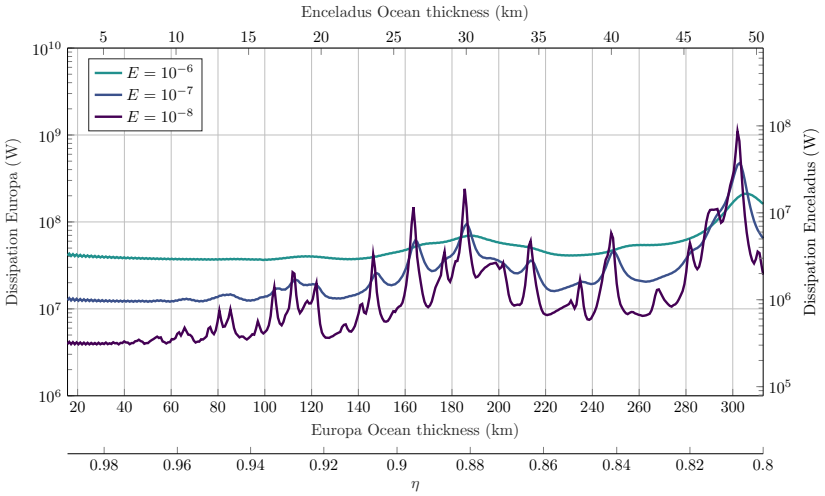

(b)

Figure 4.6 (a) Tidal dissipation amplitude in an ocean contained within a spherical shell due to inertial waves excited by the degree-two order-zero eccentricity tide. The forcing frequency equals the rotational frequency of the body. Dissipation is given for varying ocean thickness, varying values of inner to outer ocean radius ratios (η) and Ekman number ranging from 10^{-4} to 10^{-8}. (b) is a zoom-in of (a) for the most relevant range of ocean thicknesses for Europa and Enceladus ($\eta = 0.8 - 1$).

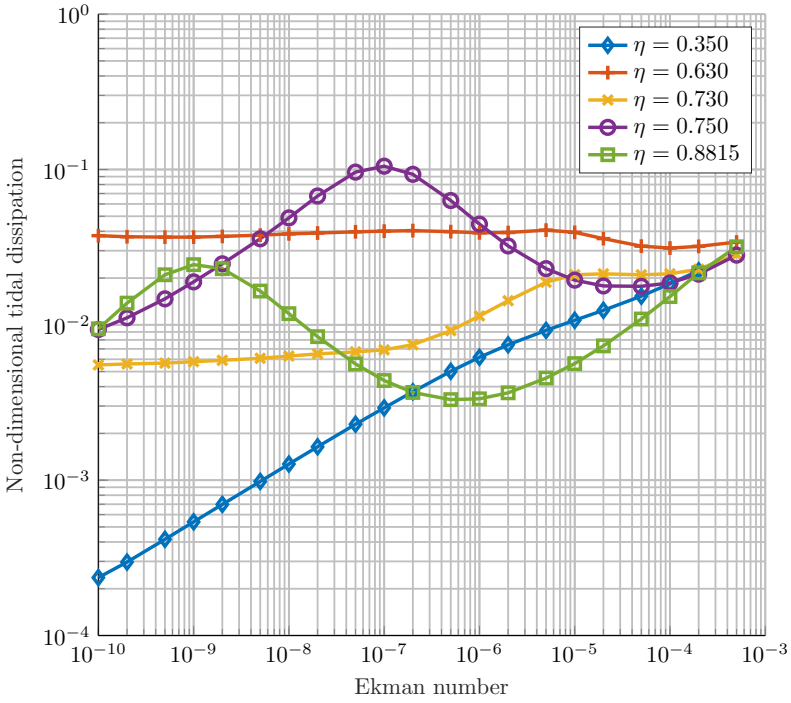

Figure 4.7 Non-dimensional tidal dissipation amplitude, as defined in Eq. (4.35), as a function of Ekman number for different representative inner to outer ocean radius ratio (η) for the degree-two order-zero eccentricity tidal compinent. $\eta = 0.63, 0.73$, corresponds to an ocean with wave attractors with high (in absolute value) Lyapunov exponent; for $\eta = 0.35$ there is an antiresonance; and $\eta = 0.75, 0.8815$ correspond to two resonant states. The markers indicate the different numerical experiments performed.

could result in observable surface features.

The difficulty in explaining Enceladus' present state through tidal dissipation in its solid parts (ice and mantle) have led to a focus on tidal dissipation within the ocean in the past years. However, so far tidal dissipation estimations using the Laplace Tidal Equations have resulted in low values of tidal dissipation for Enceladus' estimated ocean thickness (*Hay and Matsuyama*, 2017; *Matsuyama et al.*, 2018; *Tyler*, 2014). It was suggested that internal inertial waves might produce enough additional tidal dissipation. Here we show that the direct generation of inertial waves in a spherical shell does not provide significant additional heat to prevent the ocean from freezing either.

However, the discussion on tidal heating in the subsurface oceans of the icy moons is far from settled. In our study we have made several assumptions that need to be revisited. We have assumed the ocean to be (1) unstratified, (2) of constant-thickness (no topography), and (3) we have neglected non-linear effects. Each of these elements are

discussed in the next paragraphs.

We are limited by the absence of direct observations of the extraterrestrial oceans. We do not have any information about their density structure, thus, we can only apply our knowledge of similar environments on Earth to make an educated guess. Following the suggestions of *Goodman and Lenferink* (2012); *Goodman et al.* (2004) we have considered the ocean to be convectively mixed. However, under some circumstances the ocean can be stratified (*Melosh et al.*, 2004; *Vance and Brown*, 2005). In a stratified ocean, internal gravity waves, which play an important role in tidal dissipation on Earth (*Garrett*, 2003), can also be generated, adding a new possible source of tidal dissipation.

In this study we consider an ocean contained within a spherical shell. However, it is expected that Enceladus' and Europa's ocean basins deviate from this idealised shape. It is known, for example, that Enceladus' ocean does not have a constant thickness. On the contrary, the ice shell thickness varies from 7 km at the south pole to 24 km at the equator (*Beuthe et al.*, 2016; *Čadek et al.*, 2016). Moreover, due to rotation and tidal deformations both Europa and Enceladus have the shape of a triaxial ellipsoid (e.g., *Nimmo et al.*, 2007; *Thomas*, 2010). Wave attractors also exist in more general ocean basins. We expect that the conversion of large-scale tides into small scale inertial waves will be facilitated by additional topographic variations. Inertial waves for complex ocean geometries is an exciting topic for future work.

Besides, the barotropic tide given by the LTE highly depends on the ocean's basin geometry. The interaction of the barotropic horizontal currents with topography excites internal waves. On Earth most tidal dissipation occurs on the shallow continental shelf where barotropic currents have a higher amplitude, but an additional $\sim 30\%$ of tidal dissipation occurs in the oceanic ridges due to the excitation of internal waves (*Egbert and Ray*, 2000, 2003). The effect of topography on both the barotropic and internal tide should be further studied.

Finally, in this study we have used perturbation theory, we have ignored the non-linear terms in the momentum equations. The use of non-linear terms would change the behaviour of the fluid. For example, inertial waves could interact with the underling convective flow. Another possible interaction is that of inertial waves with a mean-flow excited by libration, which can lead to the well-known elliptic instability (*Kerswell*, 2002). This flow instability gives rise to fully three dimensional turbulence, which might enhance dissipation and change its geographical pattern. Both Europa and Enceladus might be subject to this instability (*Lemasquerier et al.*, 2017). Further experimental and numerical work is needed to understand the relevance of this phenomenon in heating the icy moons and shaping their surface.

4.6. APPENDIX A: NUMERICAL APPROACH EXPANDED

We solve Equations (4.19) using the spectral method of *Rieutord and Valdettaro* (1997). We expand the different fields using vector spherical harmonics:

$$\boldsymbol{u}^{(\boldsymbol{d})} = \sum_{l=0}^{\infty} \sum_{m=-l}^{l} \left[u_m^l(r) \boldsymbol{R}_{\boldsymbol{l}}^{\boldsymbol{m}} + v_m^l(r) \boldsymbol{S}_{\boldsymbol{l}}^{\boldsymbol{m}} + w_m^l(r) \boldsymbol{T}_{\boldsymbol{l}}^{\boldsymbol{m}} \right] \tag{4.22a}$$

$$W = \sum_{l=0}^{\infty} \sum_{m=-l}^{l} W_m^l(r) Y_l^m(\theta, \varphi) \tag{4.22b}$$

with:

$$\boldsymbol{R}_{\boldsymbol{l}}^{\boldsymbol{m}} = Y_l^m \boldsymbol{e_r} \qquad \boldsymbol{S}_{\boldsymbol{l}}^{\boldsymbol{m}} = \nabla Y_l^m \qquad \boldsymbol{T}_{\boldsymbol{l}}^{\boldsymbol{m}} = \nabla \times \boldsymbol{R}_{\boldsymbol{l}}^{\boldsymbol{m}} \tag{4.23}$$

where Y_l^m are normalized spherical harmonics, which satisfy the following orthogonal relations:

$$\int_{4\pi} \boldsymbol{R}_{\boldsymbol{l}}^{\boldsymbol{m}} \cdot \boldsymbol{S}_{\boldsymbol{l}'}^{\boldsymbol{m}'} \, d\Omega = \int_{4\pi} \boldsymbol{S}_{\boldsymbol{l}}^{\boldsymbol{m}} \cdot \boldsymbol{T}_{\boldsymbol{l}'}^{\boldsymbol{m}'} \, d\Omega = \int_{4\pi} \boldsymbol{T}_{\boldsymbol{l}}^{\boldsymbol{m}} \cdot \boldsymbol{R}_{\boldsymbol{l}'}^{\boldsymbol{m}'} \, d\Omega = 0 \tag{4.24a}$$

$$\int_{4\pi} \boldsymbol{R}_{\boldsymbol{l}}^{\boldsymbol{m}} \cdot \boldsymbol{R}_{\boldsymbol{l}'}^{\boldsymbol{m}'*} \, d\Omega = \delta_{ll'} \delta_{mm'} \tag{4.24b}$$

$$\int_{4\pi} \boldsymbol{S}_{\boldsymbol{l}}^{\boldsymbol{m}} \cdot \boldsymbol{S}_{\boldsymbol{l}'}^{\boldsymbol{m}'*} \, d\Omega = \int_{4\pi} \boldsymbol{T}_{\boldsymbol{l}}^{\boldsymbol{m}} \cdot \boldsymbol{T}_{\boldsymbol{l}'}^{\boldsymbol{m}'*} \, d\Omega = l(l+1) \delta_{ll'} \delta_{mm'}. \tag{4.24c}$$

Using the previous expansion the continuity equation becomes:

$$v_m^l = \frac{1}{l(l+1)r} \frac{\partial r^2 u_m^l}{\partial r}. \tag{4.25}$$

Taking the curl of Eq. (4.15) to eliminate the potential and introducing Eq. (4.25) we get the following Equations for the $\boldsymbol{R}_{\boldsymbol{l}}^{\boldsymbol{m}}$, and $\boldsymbol{T}_{\boldsymbol{l}}^{\boldsymbol{m}}$ velocity components:

$$\begin{aligned} E\Delta_l w_m^l + \left(\frac{im}{l(l+1)} - i\omega \right) w_m^l = \\ -A(l,m) r^{l-1} \frac{d}{dr} \left(\frac{u_m^{l-1}}{r^{l-2}} \right) - A(l+1,m) r^{-l-2} \frac{d}{dr} \left(r^{l+3} u_m^{l+1} \right) + f_R, \end{aligned} \tag{4.26a}$$

$$\begin{aligned} E\Delta_l \Delta_l (r u_m^l) + \left(\frac{im}{l(l+1)} - i\omega \right) \Delta_l (r u_m^l) = \\ B(l,m) r^{l-1} \frac{d}{dr} \left(\frac{w_m^{l-1}}{r^{l-1}} \right) + B(l+1,m) r^{-l-2} \frac{d}{dr} \left(r^{l+2} w_m^{l+1} \right) + f_T; \end{aligned} \tag{4.26b}$$

with:

$$A(l,m)=\frac{1}{l^2}\sqrt{\frac{l^2-m^2}{4l^2-1}},\quad B(l,m)=l^2(l^2-1)A(l,m);\quad \Delta_l=\frac{1}{r}\frac{d^2}{dr^2}r-\frac{l(l+1)}{r^2}. \tag{4.27}$$

The forcing terms f_R and f_T are given by :

$$f_R=-\frac{r}{l(l+1)}\int_{4\pi}\nabla\times\boldsymbol{f}^{(eq)}\cdot\boldsymbol{R}_l^{m*}\,d\Omega \tag{4.28a}$$

$$f_T=\int_{4\pi}\nabla\times\boldsymbol{f}^{(eq)}\cdot\boldsymbol{T}_l^{m*}\,d\Omega \tag{4.28b}$$

The values of f_T and f_R are obtained for the different tidal constituents. We need to obtain the non-dimensional components of the different constituents of the equilibrium tide $\boldsymbol{u_{eq}}$ in terms of spherical harmonics. We compute their amplitude by taking the time derivative of Equation (4.6) and using the definition of the equilibrium tide given in Eq. (4.16). We write the resulting expressions using the previously defined normalised spherical harmonics $Y_{l,m}$:

$$\boldsymbol{u_{e0}^{(eq)}}=-\mathrm{i}\frac{3}{2}\sqrt{\frac{\pi}{5}}\frac{\omega^2 eR}{g}r^2\boldsymbol{R_2^0}=k_{e0}\mathrm{i}r^2\boldsymbol{R_2^0} \tag{4.29a}$$

$$\boldsymbol{u_{o1e}^{(eq)}}=-\sqrt{\frac{3\pi}{5}}\frac{\omega^2 R\sin\epsilon}{2g}r^2\boldsymbol{R_2^1}=k_{o1e}r^2\boldsymbol{R_2^1} \tag{4.29b}$$

$$\boldsymbol{u_{o1w}^{(eq)}}=-\sqrt{\frac{3\pi}{5}}\frac{\omega^2 R\sin\epsilon}{2g}r^2\boldsymbol{R_2^1}=k_{o1w}r^2\boldsymbol{R_2^1} \tag{4.29c}$$

$$\boldsymbol{u_{e2e}^{(eq)}}=-\mathrm{i}\frac{7}{4}\sqrt{\frac{6\pi}{5}}\frac{\omega^2 eR}{g}r^2\boldsymbol{R_2^2}=k_{e2e}\mathrm{i}r^2\boldsymbol{R_2^2} \tag{4.29d}$$

$$\boldsymbol{u_{e2w}^{(eq)}}=-\mathrm{i}\frac{1}{4}\sqrt{\frac{6\pi}{5}}\frac{\omega^2 eR}{g}r^2\boldsymbol{R_2^2}=k_{e2w}\mathrm{i}r^2\boldsymbol{R_2^2}. \tag{4.29e}$$

Introducing Eq. (4.29) into Eq. (4.28) we can get the values of f_R and f_T for $m=0$, $m=1$ and $m=2$ components, ($f_R^0, f_T^0, f_R^1, f_T^1$ and f_R^2, f_T^2).

$$f_R^0=k_{e0}\mathrm{i}\frac{r^2}{\sqrt{35}}\delta_{l,3}-k_{e0}\mathrm{i}\frac{r^2}{\sqrt{15}}\delta_{l,1},\quad f_T^0=6k_{e0}\omega r\delta_{l,2} \tag{4.30a}$$

$$f_R^1=k_{o1}\frac{2r^2}{3}\sqrt{\frac{2}{35}}\delta_{l,3}-k_{o1}\frac{r^2}{2}\sqrt{\frac{3}{15}}\delta_{l,1},\quad f_T^1=-6k_{o1}\mathrm{i}r(\omega+\frac{1}{2})\delta_{l,2} \tag{4.30b}$$

$$f_R^2=k_{e2}\mathrm{i}\frac{r^2}{\sqrt{63}}\delta_{l,3},\quad f_T^2=6k_{e2}\omega r\delta_{2,l}+6k_{e2}r\delta_{l,2}. \tag{4.30c}$$

k_{e2e} (k_{o1e}) or k_{e2w} (k_{o1w}) should be used in the place of k_{e2} (k_{o1}) depending if we solve for the westward or eastward wave. Note that the constant k contains information about the physical characteristics of each moon. Due to the fact that the PDEs are linear we solve the system for $k = 1$ and multiply the solution by the corresponding value of k to obtain the solution for each configuration.

By inspecting Equations 4.26 it is clear that the different orders are decoupled, but there exists a coupling between degrees. However, not all the degrees are coupled, symmetric ($\boldsymbol{X}_m^+$) and antisymmetric ($\boldsymbol{X}_m^-$) modes with respect to the equator are decoupled and can be solved independently.

$$\boldsymbol{X}_m^+ = \begin{bmatrix} u_m^m \\ w_m^{m+1} \\ u_m^{m+2} \\ w_m^{m+3} \\ \vdots \end{bmatrix} \qquad \boldsymbol{X}_m^- = \begin{bmatrix} w_m^m \\ u_m^{m+1} \\ w_m^{m+2} \\ u_m^{m+3} \\ \vdots \end{bmatrix}. \tag{4.31}$$

Note that for the $m = 0$ and $m = 2$ tidal components the $\boldsymbol{X}_0^+$ and the $\boldsymbol{X}_2^+$ solutions are excited, respectively, while $m = 1$ excites the $\boldsymbol{X}_1^-$ solution.

The partial differential equations 4.26 are discretised in the radial direction using the Chebyshev polynomials on the Gauss-Lobatto collocation nodes (see Section 4.3.3). More details about this method can be found in *Rieutord and Valdettaro* (1997).

4.7. APPENDIX B: TIDAL DISSIPATION COMPUTATION

We expand Eq. (4.20) as:

$$\hat{D}_v = E \int_\eta^1 d(r) r^2 dr, \tag{4.32}$$

where $d(r)$ is the dissipation in a spherical layer with radius r. We can write the previous equation using the spherical harmonic decomposition of the velocity (Eq. (4.22)):

$$d(r) = \sum_{l=0}^{L} \sum_{m=-L}^{L} 3 \left| \frac{\partial u_m^l}{\partial r} \right|^2 + l(l+1)(|s_m^l|^2 + |t_m^l|^2) + (l-1)l(l+1)(l+2) \frac{|v_m^l|^2 + |w_m^l|^2}{r^2}, \tag{4.33}$$

with:

$$s_m^l = \frac{\partial v_m^l}{\partial r} + \frac{u_m^l - v_m^l}{r} \tag{4.34a}$$

$$t_m^l = r \frac{\partial}{\partial r} \frac{w_m^l}{r}. \tag{4.34b}$$

(e.g., *Rieutord*, 1987). The total value of $\hat{D}_v$ is obtained by numerically integrating Eq. (4.32). Finally, we obtain the dimensional value as:

$$D_v = 8k^2 \rho_o n^3 R^5 \hat{D}_v \tag{4.35}$$

where k depends on the tidal component considered and is given by Eq. (4.29).

5

THE TIDES OF ENCELADUS' POROUS CORE

M. ROVIRA-NAVARRO , R. KATZ , Y. LIAO, W. VAN DER WAL, F. NIMMO

The inferred density of Enceladus' core, together with evidence of hydrothermal activity within the moon, suggests that the core is porous. Tidal dissipation in an unconsolidated core has been proposed as the main source of Enceladus' geological activity. However, the tidal response of its core has generally been modeled assuming it behaves viscoelastically rather than poroviscoelastically. In this work, we analyze the poroviscoelastic response to better constrain the distribution of tidal dissipation within Enceladus.

A poroviscoelastic body has a different tidal response than a viscoelastic one; pressure within the pores alters the stress field and induces a Darcian porous flow. This flow represents an additional pathway for energy dissipation. Using Biot's theory of poroviscoelasticity, we develop a new framework to obtain the tidal response of a spherically symmetric, self-gravitating moon with porous layers and apply it to Enceladus. We show that the boundary conditions at the interface of the core and overlying ocean play a key role in the tidal response. The ocean hinders the development of a large-amplitude Darcian flow, making negligible the Darcian contribution to the dissipation budget. We therefore infer that Enceladus' core can be the source of its geological activity only if it has a low rigidity and a very low viscosity. A future mission to Enceladus could test this hypothe-

This chapter is published in the Journal of Geophysical Research: Planets (*Rovira-Navarro et al.*, 2022): Rovira-Navarro, M., Katz, R. F., Liao, Y., van der Wal, W., & Nimmo, F. (2022). The Tides of Enceladus' Porous Core. Journal of Geophysical Research: Planets, 127, e2021JE007117.

sis by measuring the phase lags of tidally induced changes of gravitational potential and surface displacements.

5.1. INTRODUCTION

When Voyager 1 and Voyager 2 flew by Enceladus they revealed a surprisingly young and active world (*Smith et al.*, 1982). More than two decades later, the Cassini spacecraft discovered water plumes erupting from Enceladus' South Polar Terrain (SPT) (*Porco et al.*, 2006), showed that the SPT radiates ~ 10 GW of energy to space (*Howett et al.*, 2011), and demonstrated that Enceladus has a global subsurface ocean (*Postberg et al.*, 2011; *Thomas et al.*, 2016) .

Explaining the high geological activity of Enceladus remains challenging (*Nimmo et al.*, 2018). The moon's activity is linked to diurnal tides (e.g., *Yoder*, 1979). Enceladus is currently in a 2 : 1 mean-motion orbital resonance with Dione that forces its orbital eccentricity, causing time-varying tides that periodically deform the moon. As Enceladus is not perfectly elastic, part of the tidal energy is transformed into heat, a process known as tidal heating. Energy dissipation in Enceladus is ultimately dependent on tidal dissipation in Saturn. Dissipation within the planet causes a phase-lag in Saturn's tidal bulge; consequently, rotational energy is transferred to Enceladus and Dione where part of it is dissipated (e.g., *Nimmo et al.*, 2018).

Astrometric observations of the Saturnian system can be used to constrain the phase-lag of Saturn's tidal bulge and estimate the amount of energy dissipated in the moons (*Meyer and Wisdom*, 2007). They suggest that Enceladus is in orbital and thermal equilibrium (*Fuller et al.*, 2016; *Lainey et al.*, 2012). If the moon is in thermal equilibrium, ice-shell thickness estimates combined with measurements of the SPT thermal flux can be used to obtain the total energy produced within the moon, which adds up to ~ 35 GW (*Hemingway et al.*, 2018). However, explaining where and how this much energy is dissipated within Enceladus has been problematic (e.g., *Nimmo et al.*, 2018), giving rise to Enceladus' energy puzzle.

Enceladus' ice shell is most likely brittle and conductive, limiting the amount of heat that can be dissipated within it to about 1 GW (*Beuthe*, 2019; *Souček et al.*, 2019). Frictional heating along Enceladus' tiger stripes can contribute an additional $0.1 - 1$ GW of energy dissipation (*Pleiner Sládková et al.*, 2021), but, overall, tidal heating in the ice-shell can only account for roughly 10% of the observed SPT thermal output. Ocean tides have been proposed as an additional heating mechanism (*Tyler*, 2011), but they only become important if Enceladus has an orbital obliquity two orders of magnitude higher than the expected value (*Chen and Nimmo*, 2011); or the ocean is unrealistically thin, radially stratified or turbulent (*Chen et al.*, 2014; *Hay and Matsuyama*, 2019; *Matsuyama*, 2014; *Rekier et al.*, 2019; *Rovira-Navarro et al.*, 2019, 2020; *Tyler*, 2020; *Wilson and Kerswell*, 2018). Modelling the core as a purely solid, viscoelastic body, tidal dissipation produced within it can only account for the observed thermal output if the core has a viscosity of $\eta_c < 10^{13}$ Pa s, much lower than that characteristic of rock. Because of this, substantial tidal dissipation in the core was first disregarded. However, *Roberts* (2015) and *Choblet et al.* (2017) recently suggested that a low viscosity can be attained if Ence-

ladus' core is porous.

An Enceladan porous core is consistent with observations. The density of the core inferred from gravity data, 2.4 $\mathrm{g\,cm^{-3}}$ (e.g., *Beuthe et al.*, 2016), is low compared to that of the minerals expected to form the bulk of the core (*Choblet et al.*, 2017). Furthermore, the detection of salt-rich particles (*Postberg et al.*, 2009, 2011), silicon-rich nanoparticles (*Hsu et al.*, 2015) and molecular hydrogen (*Waite et al.*, 2017) in material ejected by Enceladus' plumes suggests that the ocean interacts with the silicate core in hydrothermal systems. Taken together, these observations suggest that the moon's core is a porous, water-saturated matrix of silicates or loosely packed rock pieces through which water can circulate.

Even though *Roberts* (2015) and *Choblet et al.* (2017) attributed Enceladus' activity to a porous core, they did not explicitly model how a porous core responds to tides. Instead, they modelled the core as a viscoelastic, rocky solid. The response of a porous, permeable, water-saturated body to tidal forces differs from that of a pure solid. The deformation of the matrix induces a flow of water through the permeable interior, which in turns affects the response of the solid matrix and modifies the dissipation in the solid. Furthermore, the viscous flow of water through the pores adds an additional source of dissipation that may not be negligible.

While the tidal response of solid and liquid layers have been thoroughly examined (e.g., *Beuthe*, 2016; *Chen et al.*, 2014; *Jara-Orué and Vermeersen*, 2011; *Kaula*, 1964; *Love*, 1911; *Matsuyama et al.*, 2018; *Renaud and Henning*, 2018; *Rovira-Navarro et al.*, 2019; *Segatz et al.*, 1988; *Tyler*, 2008), the tidal response of bodies with porous layers has been subjected to much less scrutiny. *Wang et al.* (1999) estimated energy dissipation due to tidally-induced flows in Earth's permeable seafloor and showed it to be negligible; *Vance et al.* (2007) applied the same approach to Enceladus' hydrothermal systems and reached a similar conclusion for the icy moon. *Liao et al.* (2020) developed a more complete approach based on Biot's theory of poroviscolasticity (*Biot*, 1941) and argued that the interaction between solid and liquid phases lead to a heat production that can easily exceed 10 GW and thus solve Enceladus' energy puzzle.

The model presented by *Liao et al.* (2020) included several simplifications that require further examination: (1) only the tidal response of the core was considered instead of that of the whole moon (core, ocean and ice shell); (2) the authors forced the problem via an imposed surface strain derived from viscoelastic models and only considered one component of the eccentricity tide instead of forcing the core with the complete tidal potential; (3) the authors neglected the effect of self-gravity, the body force arising from the tidal deformation itself; and (4) they assumed that the displacement field was irrotational.

In this paper, we relax the assumptions of *Liao et al.* (2020) and develop a self-consistent model to compute the tidal deformation and fluid flow of self-gravitating bodies with porous layers (Section 5.2) that can be applied to Enceladus and other bodies with internal porous layers. The new approach is an extension of the standard theory of tides for self-gravitating viscoelastic bodies (*Love*, 1906; *Peltier*, 1974; *Sabadini et al.*, 2016; *Saito*, 1974; *Takeuchi et al.*, 1962) to bodies with poroviscoelastic layers. We apply

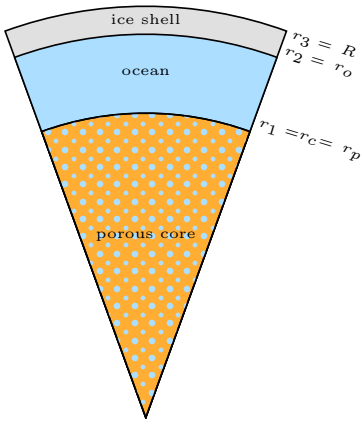

Figure 5.1 Interior structure of Enceladus consisting of three layers: a porous core, a subsurface ocean and an ice shell. The porous core boundary is assumed to be permeable.

the new model to Enceladus (Section 5.3), and examine the circumstances under which sufficient tidal dissipation can be produced within the core to explain the thermal energy radiated by the moon. In Section 5.4 we conclude that Darcy dissipation is likely negligible in Enceladus' thermal budget, leaving a low-viscosity, low-rigidity core as the most plausible avenue for substantial tidal dissipation in the rocky core. We propose how future missions could test this hypothesis.

5.2. METHODS

Our aim is to obtain the linear, periodic, tidal response of a body with internal porous layers to a tidal perturbation. We assume the moon is composed of N spherically symmetric layers of uniform properties. The boundary between a layer i and $i+1$ is at radius r_i. We consider layers that are either purely liquid, purely solid, or a contiguous solid matrix with a permeable network of liquid-filled pores. We use a viscoelastic model of the solid. The model can include as many layers as required to approximate the interior structure of the moon under consideration. Figure 5.1 shows the interior structure that is thought to be valid for Enceladus, consisting of an icy shell, a subsurface ocean and a porous core.

Liao et al. (2020) applied Biot's theory of poroviscoelasticity to the tidal problem. However, the present work is the first derivation of a self-consistent model of body tides in porous media; we therefore provide a detailed formulation of the problem, highlight key assumptions, and explain how it differs from the standard tidal theory for viscoelastic solids and the work of *Liao et al.* (2020). To this end, we start by presenting the governing equations for porous media in detail, show how they reduce to those of a pure solid, and discuss how internal liquid layers are modelled (Section 5.2.1); then we introduce the tidal potential and boundary conditions (Section 5.2.2); and, finally, sketch the

solution method (Section 5.2.3), leaving full details of the mathematical formulation to the Appendices.

5.2.1. GOVERNING EQUATIONS

We use the volume-averaged mass and momentum conservation equations for a parcel of the moon. The parcel contains a solid and a liquid phase of densities ρ_s and ρ_l and volumes V_s and V_l, respectively. The parcel is at least one order of magnitude bigger than the typical grain size. This way, we can use continuum mechanics rather than explicitly modelling the microphysical interactions of grains within the parcel. Thus the variables that follow should be understood as averages. The porosity of the parcel is simply defined as the ratio between the liquid (V_l) and total (V) volumes:

$$\Phi = \frac{V_l}{V}. \tag{5.1}$$

The mass conservation equations for the liquid and solid phases can be written as (e.g., *Ganesan and Poirier*, 1990)

$$\frac{\partial \Phi \rho_l}{\partial t} + \nabla \cdot \left[\Phi \rho_l \boldsymbol{v}_l\right] = 0, \tag{5.2a}$$

$$\frac{\partial (1-\Phi) \rho_s}{\partial t} + \nabla \cdot \left[(1-\Phi) \rho_s \boldsymbol{v}_s\right] = 0. \tag{5.2b}$$

Eqs. (5.2a) and (5.2b) can be added to obtain

$$\frac{\partial \rho}{\partial t} + \nabla \cdot \left[\rho_l \boldsymbol{q} + \rho \boldsymbol{v}_s\right] = 0. \tag{5.3}$$

ρ is the bulk density, $\rho = \Phi\rho_l + (1-\Phi)\rho_s$; and $\boldsymbol{q}$ is the segregation flux given by the relative velocity of the liquid phase with respect to the solid phase, $\boldsymbol{q} = \Phi(\boldsymbol{v}_l - \boldsymbol{v}_s)$. We additionally introduce the variation of fluid content, defined as the amount of liquid entering the solid frame per unit of the solid frame (*Cheng*, 2016),

$$\zeta = \Phi \nabla \cdot (\boldsymbol{u}_s - \boldsymbol{u}_l), \tag{5.4}$$

with $\boldsymbol{u}$ being a displacement vector.

The momentum equation in a frame rotating with the moon's angular velocity (Ω) is given by (*Mckenzie*, 1984)

$$\Phi \rho_l \left(\frac{\mathrm{D}\boldsymbol{v}_l}{\mathrm{D}t} + 2\boldsymbol{\Omega} \times \boldsymbol{v}_l \right) = \nabla \cdot \Phi \boldsymbol{\sigma}_l - \Phi \rho_l \nabla \phi - \boldsymbol{F}, \tag{5.5a}$$

$$(1-\Phi) \rho_s \left(\frac{\mathrm{D}\boldsymbol{v}_s}{\mathrm{D}t} + 2\boldsymbol{\Omega} \times \boldsymbol{v}_s \right) = \nabla \cdot (1-\Phi) \boldsymbol{\sigma}_s - (1-\Phi) \rho_s \nabla \phi + \boldsymbol{F}. \tag{5.5b}$$

$\boldsymbol{\sigma}$ is the stress tensor, ϕ is a potential that includes gravitational forces and the centrifugal force. $\boldsymbol{F}$ is an interaction force between the solid and liquid phases given by

$$\boldsymbol{F} = \Phi \frac{\eta_l}{\kappa} \boldsymbol{q} - p \nabla \Phi. \tag{5.6}$$

p is the pore pressure and η_l is the liquid viscosity. κ is the matrix permeability, which depends on the geometry of the solid matrix. For a solid matrix made of uniform, spherical grains of size d_g, a commonly used expression is the Kozeny-Carman law (*Carman*, 1997; *Kaviany*, 1995):

$$\kappa = \frac{\Phi^3}{180(1-\Phi)^2} d_g^2 \tag{5.7}$$

The inertial terms in the momentum equations (Eq. (5.5)) can be neglected. For the solid phase, high viscosity and the long period of tidal forces as compared to seismic waves imply that the solid is in quasi-equilibrium. In a porous medium, the interaction force is generally larger than inertial terms in (5.5b), which in turn results in a small Reynolds number. Summing the two momentum equations, an equation for the bulk or total stress is obtained

$$\nabla \cdot \boldsymbol{\sigma} - \rho \nabla \phi = 0, \tag{5.8}$$

with the total stress tensor being

$$\boldsymbol{\sigma} = (1-\Phi)\boldsymbol{\sigma}_s + \Phi \boldsymbol{\sigma}_l. \tag{5.9}$$

We assume that deviatoric stresses in the liquid fluctuate on the pore scale and hence they volume-average to zero, except for their contribution to the interaction force (5.6). The stress tensor of the liquid phase is thus isotropic and given by the pore pressure,

$$\boldsymbol{\sigma}_l = -p\boldsymbol{I}, \tag{5.10}$$

with $\boldsymbol{I}$ being the identity matrix. Using the interaction force expression, the liquid phase momentum equation reduces to Darcy's law,

$$\boldsymbol{q} = -\frac{\kappa}{\eta_l}\left(\nabla p + \rho_l \nabla \phi\right). \tag{5.11}$$

Note that if the porosity is zero, we recover the mass and momentum conservation equations for a solid.

A constitutive equation relating the stress tensor and pore pressure to kinematic variables is needed. We define the strain tensor as

$$\boldsymbol{\epsilon} = \frac{1}{2}\left[\nabla \boldsymbol{u} + (\nabla \boldsymbol{u})^T\right], \tag{5.12}$$

where $\boldsymbol{u}$ is the volume average of the solid displacement ($\boldsymbol{u}_s$). The stress and strain tensors can be split into a mean and a deviatoric component:

$$\boldsymbol{\sigma} = -P\boldsymbol{I} + \boldsymbol{\sigma}^d, \tag{5.13a}$$

$$\boldsymbol{\epsilon} = \epsilon^M \boldsymbol{I} + \boldsymbol{\epsilon}^d, \tag{5.13b}$$

with $\epsilon^M = \mathrm{tr}(\boldsymbol{\epsilon})/3$ and $P = -\mathrm{tr}(\boldsymbol{\sigma})/3$; tensile stress is taken to be positive.

In a compressible poroviscoelastic solid, deformation is associated with an effective stress $\boldsymbol{\sigma}'$ (*Biot*, 1941; *Cheng*, 2016),

$$\boldsymbol{\sigma}' = \boldsymbol{\sigma} + \alpha p \boldsymbol{I}. \tag{5.14}$$

α is Biot's constant, the meaning of which will become evident later. We consider that the material is viscoelastic. Different rheological laws can be used to consider the behaviour of a viscoelastic material (e.g., *Renaud and Henning*, 2018). We consider the Maxwell model, in which case effective stress and strain are related as

$$\frac{\mathrm{d}\boldsymbol{\sigma'}}{\mathrm{d}t} + \frac{\mu}{\eta}\boldsymbol{\sigma'} - \frac{1}{3}\frac{\mu}{\eta}\mathrm{tr}(\boldsymbol{\sigma'})\boldsymbol{I} = 2\mu\frac{\mathrm{d}\boldsymbol{\epsilon}}{\mathrm{d}t} + \left(K - \frac{2}{3}\mu\right)\frac{\mathrm{d}\,\mathrm{tr}(\boldsymbol{\epsilon})}{\mathrm{d}t}\boldsymbol{I}, \tag{5.15}$$

or, in terms of total stress,

$$\frac{\mathrm{d}\boldsymbol{\sigma}}{\mathrm{d}t} + \frac{\mu}{\eta}\boldsymbol{\sigma} - \frac{1}{3}\frac{\mu}{\eta}\mathrm{tr}(\boldsymbol{\sigma})\boldsymbol{I} = 2\mu\frac{\mathrm{d}\boldsymbol{\epsilon}}{\mathrm{d}t} + \left(K - \frac{2}{3}\mu\right)\frac{\mathrm{d}\,\mathrm{tr}(\boldsymbol{\epsilon})}{\mathrm{d}t}\boldsymbol{I} - \alpha\frac{\mathrm{d}p}{\mathrm{d}t}\boldsymbol{I}. \tag{5.16}$$

Here, μ and η are the shear modulus and viscosity of the two-phase aggregate, respectively. The Maxwell model does not capture the anelastic behaviour of ice and silicates, which can become especially important when the forcing period is much smaller than the Maxwell time η/μ (*Efroimsky*, 2012b). It is for this reason that recent studies have considered the Andrade rheological model (*Andrade and Trouton*, 1910) for ices (*Castillo-Rogez et al.*, 2011; *Gevorgyan et al.*, 2020; *Rambaux et al.*, 2010; *Rhoden and Walker*, 2022; *Shoji et al.*, 2013) and silicates (*Bierson and Nimmo*, 2016; *Efroimsky*, 2012b; *Renaud and Henning*, 2018; *Walterová and Běhounková*, 2017). In 5.10 we discuss how more complex rheology models can be incorporated into our theory and demonstrate this using the Andrade model.

One further constitutive equation relates the pore pressure with the isotropic strain and the variation of fluid content as (*Cheng*, 2016),

$$p = \frac{K_u - K}{\alpha}\mathrm{tr}(\boldsymbol{\epsilon}) + \frac{K_u - K}{\alpha^2}\zeta, \tag{5.17}$$

where K_u and K are the bulk modulus of the material in undrained ($\zeta = 0$) and drained ($p = 0$) conditions, respectively. These are effective properties of the two-phase medium; the drained modulus depends on the mechanical properties of the solid matrix; in contrast, the undrained modulus depends on both the properties of the liquid and the solid phases. If the material is microscopically homogeneous and isotropic, K, K_u and α can be obtained using the bulk modulus of the solid K_s and liquid K_l phases, and the *bulk modulus of porosity* K_Φ, which measures the resistance to grain rearrangement, (e.g., *Cheng*, 2016),

$$\alpha = \frac{1 + \Phi(1-\Phi)^2 K_\Phi/K_s}{1 + (1-\Phi)^2 K_\Phi/K_s,} \tag{5.18a}$$

$$K = \frac{(1-\Phi)^3 K_\Phi / K_s}{1+(1-\Phi)^2 K_\Phi / K_s} K_s = (1-\alpha) K_s, \tag{5.18b}$$

$$K_u = K + \frac{K_l (K_s - K)^2}{K_l (K_s - K) + \Phi K_s (K_s - K_l)}. \tag{5.18c}$$

With this definition, it becomes apparent that the Biot parameter α relates the resistance to compression of the solid constituent and the porous matrix. A strong porous matrix has a small α while an easily deformable matrix has an α close to 1. If the solid is much less compressible than the frame, $K_\Phi / K_s \to 0$ and therefore $\alpha \to 1$.

The previous set of constitutive equations define a material that, upon a stress perturbation, exhibits an elastic response and viscous creep. Moreover, a perturbation produces a pore pressure field that drives Darcian porous flow. Viscous creep and Darcian flow result in energy dissipation. The rate of volumetric tidal dissipation averaged over a tidal cycle due to these two processes is (e.g., *Liao et al.*, 2020)

$$\dot{E}_{v,solid} = \frac{1}{T} \int_0^T \left(\boldsymbol{\sigma} : \frac{\partial \boldsymbol{\epsilon}}{\partial t} + p \frac{\partial \zeta}{\partial t} \right) \mathrm{d}t, \tag{5.19a}$$

$$\dot{E}_{v,liquid} = \frac{1}{T} \int_0^T \frac{\eta_l}{\kappa} (\boldsymbol{q} \cdot \boldsymbol{q}) \, \mathrm{d}t, \tag{5.19b}$$

respectively.

If the body has an internal liquid layer (i.e., ocean), alternate equations are required for that layer. We assume internal liquid layers are inviscid, incompressible and in hydrostatic equilibrium. If this is the case the radial displacements follow equipotential surfaces,

$$\boldsymbol{u} \cdot \boldsymbol{e}_r = -\phi / g, \tag{5.20}$$

except at solid-liquid interfaces, where this might be hindered (*Jara-Orué and Vermeersen*, 2011). $\boldsymbol{e}_r$ is the radial unit vector, and g the gravitational acceleration. Under these assumptions, surface (e.g., *Hay and Matsuyama*, 2017; *Matsuyama*, 2014; *Rovira-Navarro et al.*, 2020; *Tyler*, 2011) and internal waves (*Rekier et al.*, 2019; *Rovira-Navarro et al.*, 2019) are excluded from the solution.

In all layers, the gravitational potential of the body can be computed using Poisson's equation,

$$\nabla^2 \phi = 4\pi G \rho. \tag{5.21}$$

5.2.2. TIDAL FORCING AND BOUNDARY CONDITIONS

We consider a synchronously rotating moon of radius R with an orbital frequency n and eccentricity e. As the obliquity of Enceladus is expected to be very small (*Chen and Nimmo*, 2011), we focus on eccentricity tides and ignore obliquity tides. The tidal potential at a point with co-latitude and longitude θ, φ located at radial distance r from the center of the moon is given by (e.g., *Jara-Orué and Vermeersen*, 2011; *Kaula*, 1964)

$$\phi^T(r,\theta,\varphi) = (nR)^2 e\left(\frac{r}{R}\right)^2 \mathrm{Re}\left\{\left(3\sqrt{\frac{\pi}{5}}\mathscr{Y}_2^0(\theta,\varphi) - 3\sqrt{\frac{3\pi}{5}}\mathscr{Y}_2^2(\theta,\varphi) + 4\sqrt{\frac{3\pi}{5}}\mathrm{i}\mathscr{Y}_2^{-2}(\theta,\varphi)\right)\exp(\mathrm{i}nt)\right\} + O(e^2). \tag{5.22}$$

$\mathscr{Y}_l^m$ are normalized, real spherical harmonics of degree l and order m (Eq. 5.36).

To solve the previous set of equations, boundary conditions at the moon's surface are required. The normal and shear stress at the surface are zero,

$$\sigma_{rr}(R) = \sigma_{r\theta}(R) = \sigma_{r\phi}(R) = 0. \tag{5.23}$$

The potential, ϕ, is continuous at the surface but its gradient is not. Using Poisson's equation and applying Gauss' theorem for an infinitesimal control volume surrounding the surface layer, we find

$$\int_S \nabla\phi \cdot \boldsymbol{e}_r \, dS = 4\pi G \int_S \int_{R-\delta}^{R+\delta} \rho \, \mathrm{d}r \, \mathrm{d}S. \tag{5.24}$$

We note that *Liao et al.* (2020) considered only the zonal component of the tidal potential ($m = 0$). Furthermore, the tidal forcing was imposed via a prescribed strain at the surface of the core instead of via the tidal potential ϕ^T as explained here, and the no-stress boundary conditions (Eq. (5.23)) were not used. The distinct effect of each of these boundary conditions will be explored in Section 5.3.

Additional boundary conditions must be prescribed at internal boundaries. For the core–ocean and ocean–ice shell interfaces, we use the boundary conditions discussed in *Jara-Orué and Vermeersen* (2011) and given in 5.5. Nevertheless, an additional boundary condition should be provided at the porous layer interface (r_p). Two different boundary conditions can be considered: no radial Darcy flux

$$\boldsymbol{q}(r_p) \cdot \boldsymbol{e}_r = 0, \tag{5.25}$$

or force balance and continuity of fluid pressure. In the latter case, the ocean pressure at the core surface is balanced by the radial component of the stress tensor and the pore pressure equals the ocean pressure,

$$\sigma_{rr}(r_p) = -P_{ocean}, \quad p(r_p) = P_{ocean}, \tag{5.26}$$

which implies $p(r_p) + \sigma_{rr}(r_p) = 0$. For Enceladus, we consider that the core–ocean boundary is permeable and thus use the second boundary condition.

5.2.3. PERTURBATION THEORY AND SOLUTION METHOD

To make the analysis tractable, we linearize the equations of motion using perturbation theory. We split the density, stress tensor and potential force into a background and a

perturbed component. The background component corresponds to the pre-stressed, hydrostatic state arising from the self-gravity of the body; the perturbed component is the result of the time-dependent tidal potential,

$$\boldsymbol{\sigma} = -P_0 \boldsymbol{I} + \boldsymbol{\sigma}^{\Delta}, \tag{5.27a}$$

$$p = p_0 + p^{\Delta}, \tag{5.27b}$$

$$\rho = \rho_0 + \rho^{\Delta}, \tag{5.27c}$$

$$\rho_l = \rho_{l,0} + \rho_l^{\Delta}, \tag{5.27d}$$

$$\phi = \phi_0 + \phi^{\Delta}. \tag{5.27e}$$

Here, ϕ_0 is the gravitational potential of the unperturbed body and ϕ^{Δ} includes both the perturbing tidal potential and the potential arising from self-gravitation of the perturbed body. In the unperturbed state, Eqs. (5.8) and (5.11) are given by:

$$\nabla P_0 + \rho_0 \nabla \phi_0 = 0, \tag{5.28a}$$

$$\nabla p_0 + \rho_{l,0} \nabla \phi_0 = 0, \tag{5.28b}$$

with $\nabla \phi_0 = g \boldsymbol{e}_r$.

Using the previous definitions and linearizing by assuming that the products of perturbation variables are negligible, the momentum equations can be written as:

$$\nabla \cdot \boldsymbol{\sigma}^{\Delta} - \nabla \left(\rho_0 g \boldsymbol{u} \cdot \boldsymbol{e}_r \right) - \rho_0 \nabla \phi^{\Delta} - \rho^{\Delta} g \boldsymbol{e}_r = 0, \tag{5.29a}$$

$$\boldsymbol{q} = -\frac{\kappa}{\eta_l} \left(\nabla p^{\Delta} + \rho_{l,0} \nabla \phi^{\Delta} + g \rho_l^{\Delta} \boldsymbol{e}_r \right). \tag{5.29b}$$

The mass conservation equation can be obtained by linearizing Eq. (5.3) and assuming that under small displacements the Lagrangian and Eulerian derivatives are approximately equal,

$$\frac{\rho^{\Delta}}{\rho_0} = -\nabla \cdot \boldsymbol{u} + \frac{\rho_{l,0}}{\rho_0} \zeta. \tag{5.30}$$

Similarly, using the definition of the variation in liquid content (Eq. (5.4)), and the segregation flux, we obtain:

$$\frac{\partial \zeta}{\partial t} = -\nabla \cdot \boldsymbol{q}. \tag{5.31}$$

Finally, the density change of the liquid phase can be obtained using the definition of the liquid bulk modulus,

$$\frac{\rho_l^{\Delta}}{\rho_{l,0}} = \frac{p^{\Delta}}{K_l}. \tag{5.32}$$

The perturbed gravitational potential is obtained by solving the linearized Poisson's equation,

$$\nabla^2 \phi^{\Delta} = 4\pi G \rho^{\Delta}. \tag{5.33}$$

Eqs. (5.29)–(5.33) reduce to those used in *Liao et al.* (2020) if the solid and liquid phases are assumed to be massless ($\rho_0, \rho_{l,0} = 0$). If the layer is purely solid ($\Phi = 0, \alpha = 0$), we recover the classic equations used for a viscoelastic solid (*Sabadini et al.*, 2016).

To obtain the tidal response of the body, the momentum equations (5.29), mass conservation equations (5.30) and (5.31), and Poisson's equation (5.33) together with constitutive equations (5.16) and (5.17) should be solved under appropriate boundary conditions (Section 5.2.2). As the tidal forcing is periodic, we solve the equations of motion in the Fourier domain. We assume a solution proportional to $\exp(int)$ and transform the previous set of equations to the Fourier domain. Because of the symmetry of the problem, we solve the previous set of equations using spherical harmonics. We obtain stress and strain tensors, the pore pressure and Darcy flow, and we compute tidal dissipation in the solid and liquid phases using Eq. (5.19). Further details can be found in Sections 5.8–5.5.

5.3. APPLICATION TO ENCELADUS

To understand how the predictions of this model differ from the previous treatment of *Liao et al.* (2020) we consider three different cases: (1) Enceladus' core forced via a prescribed surface strain as in *Liao et al.* (2020); (2) Enceladus' core with a free surface and forced with the tidal potential; and (3) a complete model of Enceladus consisting of a porous core, an ocean, and an ice shell, forced with the tidal potential. We begin by examining the simpler cases 1 and 2 to illustrate the effect of the boundary conditions used by *Liao et al.* (2020) (Section 5.3.1) and then move to the more complex, multilayered model to show how the ocean and ice shell affect the core's tidal response (Section 5.3.2).

We assume a core density of 2.4 $\mathrm{g\,cm^{-3}}$ consistent with gravity observations (*Beuthe et al.*, 2016). *Choblet et al.* (2017) obtained a core porosity of $20-30\%$ for realistic core compositions; we use a value of 20%. For a consolidated silicate core, the shear modulus is $\sim 1-10$ GPa and the viscosity is $\sim 10^{20}$ Pas or higher at low homologous temperature. However, if the core is unconsolidated, it can become weaker and the shear modulus and viscosity can be orders of magnitude lower than the typical values of silicates (*Choblet et al.*, 2017; *Goldreich and Sari*, 2009; *Nimmo et al.*, 2018). The parameters used are summarized in Table 5.1.

5.3.1. CORE-ONLY MODEL

Liao et al. (2020) studied the response of Enceladus' core to a prescribed radial strain imposed at the core's surface (in this section, $R = r_c$). The strain was given by a degree-2 order-0 field of the form: $\epsilon_{rr}(R,\theta,\varphi) = \epsilon(R) Y_2^0$. The amplitude of the strain was estimated from the theory of viscoelastic tides (*Murray and Dermott*, 2000). For a homogeneous body in which rigidity dominates over self-gravity, the maximum radial strain attained at

Quantity	Symbol	Value	Units
Surface radius	R	252.1	km
Mass	M	$1.08 \cdot 10^{20}$	kg
Ocean thickness [(1)]	h_{ocean}	38	km
Ice shell thickness [(1)]	h_{ice}	23	km
Average core's density[(1)]	ρ_{core}	2422	$\mathrm{kg\,m^{-3}}$
Ocean's density	ρ_{ocean}	1000	$\mathrm{kg\,m^{-3}}$
Ice viscosity [(2)]	η_{ice}	$1 \cdot 10^{18}$	Pa s
Ice shear modulus [(2)]	μ_{ice}	3.3	GPa
Ice bulk modulus	K_{ice}	33	GPa
Core shear modulus	μ_s	$0.01 - 10$	GPa
Core solid phase bulk modulus [(3)]	K_s	10	GPa
Core viscosity	η_s	$10^{10} - 10^{20}$	Pa s
Biot's constant	α	$0 - 1$	–
Water viscosity[(3)]	η_l	$1.9 \cdot 10^{-3}$	Pa s
Water bulk modulus [(3)]	K_l	2.2	GPa
Core permeability[(3)]	κ	$10^{-8} - 10^{-4}$	$\mathrm{m^2}$
Core porosity	Φ	0.2	-
Eccentricity	e	0.0047	-
Orbital Period	T	33	h

Table 5.1 Enceladus physical and mechanical properties. [(1)] *Beuthe et al.* (2016); [(2)] *Hussmann and Spohn* (2004); [(3)] *Liao et al.* (2020).

the poles is $\epsilon_{rr}(R,0°) = \frac{9}{4\pi}\frac{n^2}{\rho G}e\frac{5}{3} \mid k_2 \mid$, where $k_2 = \frac{3/2}{1+19\hat{\mu}/2\rho g R}$ is the gravitational potential Love number and $\hat{\mu}$ is the complex rigidity. Additionally, *Liao et al.* (2020) assumed the displacement field to be irrotational, $\nabla \times \boldsymbol{u} = 0$, and considered the solid and liquid to be massless, $(\rho, \rho_l) = 0$. For case 1 we make the same assumptions.

Liao et al. (2020) found that for Biot parameter $\alpha \to 1$, tidal dissipation is enhanced as compared to standard viscoelastic models. In what follows, we assess whether this still holds when the core is forced via the tidal potential rather than via a prescribed surface strain. We first take a fixed core permeability ($\kappa = 10^{-8}$ m^2), and compute tidal dissipation for different values of core viscosity and Biot parameter α. Changing α for a given porosity is equivalent to changing the ratio between the bulk modulus of porosity and the solid bulk modulus (Eq. (5.18)), as α approaches 1 the porous matrix becomes more compressible. Afterwards, we study the role of the core's permeability. While we keep the porosity fixed, we note that variations in porosity between $0.2 - 0.3$ result in changes of α and κ much smaller than the ranges explored below (Eqs. (5.7,5.18)).

Figure 5.2 shows total tidal dissipation in the core for different values of Biot parameter α and core viscosity η_s for cases 1 and 2. For case 1, we reproduce the results of *Liao et al.* (2020). For $\alpha = 0.95$ tidal dissipation features two peaks, one at a core viscosity of $\sim 10^{11}$ Pa s, also characteristic of the viscoelastic response, and another one attained at higher core viscosity $\sim 10^{15}$ Pa s, only characteristic of the poroviscoelastic model. Around the two peaks, most of the energy dissipation occurs in the solid phase, as shown by the thin lines. As core viscosity increases further, dissipation in the solid decreases but the total dissipation remains high due to Darcy dissipation. This dissipation occurs in a shallow layer close to the core's surface (Figure 5.3c), where a strong pressure gradient develops that drives flows of up to 2×10^{-5} m s^{-1}. The second dissipation peak is the result of the compressibility of the porous matrix. As $\alpha \to 1$, the drained bulk modulus decreases (Eq. (5.18a)), the second peak becomes more prominent, and Darcy dissipation also increases.

For case 2, forcing by the tidal potential, the second dissipation peak is not present (heavy dashed line in Fig. 5.2). Tidal dissipation reaches its maximum at the same core viscosity as in the non-porous, viscoelastic case and then decreases as viscosity increase until Darcy dissipation becomes dominant. However, as opposed to (1), the amount of heat resulting from Darcy dissipation is less sensitive to the porous-matrix compressibility and, more importantly, it is severely reduced. The prominent pressure gradients characteristic of case 1 do not develop and the maximum flow velocities attained are reduced by two orders of magnitude. This suggests that explaining Enceladus' thermal budget in terms of poroviscoelastic dissipation may be more problematic. However, a highly permeable core may mitigate this to some extent.

The permeability dictates how easily water can flow through the core. Figure 5.3a,b show the total amount of internal heat production for cases 1 and 2 for different values of core permeability. As before, for both cases we observe the high dissipation band characteristic of a viscoelastic core with a low viscosity ($\sim 10^{11}$ Pa s). As core viscosity increases Darcian dissipation becomes dominant and the total tidal dissipation becomes independent of core viscosity. In this regime, dissipation increases with permeability and the flow velocity is controlled by the dimensionless number $\Omega_D = nR^2\eta_l/\kappa\mu$, which can

be understood as a ratio between the timescale of Darcy flow ($R^2\eta_l/\kappa\mu$) and of the tidal perturbation ($1/n$). When $\Omega_D \ll 1$, high flow velocities are attained ($\boldsymbol{q} \propto \Omega_D^{-1}$, Eq. (5.11)) which in turn results in high values of tidal dissipation ($\dot{E}_{liquid} \propto \Omega_D^{-1}$, Eq. (5.19b)). We note that when Ω_D becomes very high, some of the terms in the equations (for example, the term A_{87} in Eq. (5.53)) can become very large, causing numerical problems. This limits the lowest value of permeability we can attain under our current formulation to $\sim 10^{-9}$ m^2. Nevertheless, we derive an analytical expression for Darcian dissipation in the limit of an incompressible porous matrix and liquid (5.9) that presents good agreement with the numerical results (Figure 5.2) and shows that Darcian dissipation can be expected to further decrease for lower permeability values.

While dissipation increases with permeability in both cases, Darcy dissipation in the tidally forced case is lower than in the case where a surface strain is prescribed. In case (1), a high surface stress follows from the imposed strain, producing a large gradient in pore pressure and driving high-amplitude Darcian flow; in contrast, in case (2) the no-stress boundary conditions prevent this from occurring. To produce an amount of heat similar to that observed, a permeability of $\kappa > 10^{-5}$ m^2 is required (Figure 5.3b). These are high permeability values compared to the permeability of Earth's hydrothermal systems, which can reach values of about 10^{-8} m^2 (*Lauer et al.*, 2018). However, it is possible that Enceladus' core does not resemble such a system, but is instead akin to an unconsolidated rubble pile. In that case, Enceladus' core would be made up of loosely packed material through which water can easily circulate.

If Enceladus' core has a porosity of $\sim 0.2-0.3$, a permeability of $\sim 10^{-5}$ m^2 requires grain sizes of about ~10–50 cm (Eq. (5.7)). This blocky structure could be the relic of a violent formation process such as Enceladus forming after a series of collisions of a previous generation of moons (*Asphaug and Reufer*, 2013; *Ćuk et al.*, 2016).

5.3.2. MULTI-LAYERED MODEL

We now move to the more realistic multi-layered model consisting of a porous core, a subsurface ocean and an ice shell (case 3). Although Enceladus' ice shell is of variable thickness (e.g., *Beuthe et al.*, 2016; *Čadek et al.*, 2016; *Hemingway and Mittal*, 2019), we consider an ice shell of constant thickness equal to its average value. For the core radius, core density, and ice and ocean thicknesses we use values in agreement with gravity, shape and libration data (*Beuthe et al.*, 2016). We keep these values and the rheological properties of the ice constant and vary the properties of Enceladus' core (Table 5.1).

As in the previous cases, we compute the tidal response of the moon for different values of core viscosity and permeability. The results are shown in Figure 5.4; they demonstrate that the presence of an ocean reduces the tidal response of the core. As in cases (1) and (2), we find a peak in tidal dissipation for a core viscosity of $\sim 10^{11}$ Pa s. Around this value, tidal heating is compatible with Enceladus' thermal output. However, the high-dissipation band is narrower than for cases (1) and (2)—the presence of an ocean and an ice crust reduces the tidal deformation of the core (*Beuthe*, 2015). Most importantly, the amount of Darcian dissipation is drastically reduced.

As opposed to case (2), Darcian dissipation is small even for a highly permeable core.

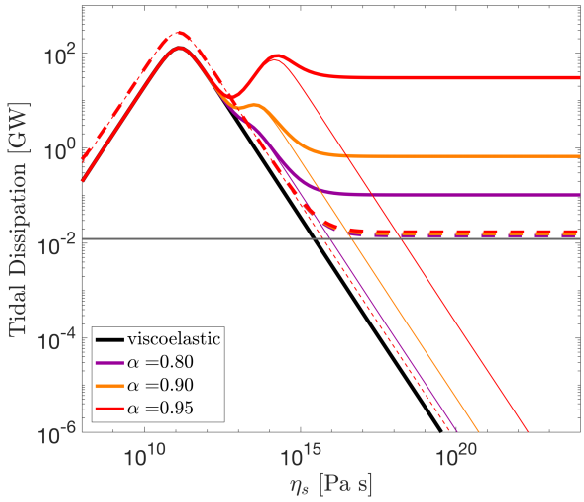

Figure 5.2 Tidal dissipation in Enceladus' core when forced with a prescribed surface strain (solid lines) or the tidal potential (dashed line) for different values of Biot coefficient α. The thin lines indicate tidal dissipation in the solid layer, the gray line shows the amount of Darcy dissipation for incompressible solid and liquid phases obtained using Eq (5.80).

The reduction in Darcian dissipation is due to the presence of the overlying ocean and ice shell. They impose a non-zero pressure at the core surface that largely balances the forcing of the tidal potential. The Darcian flow q is driven by the modified pressure $p^* = p^\Delta + \rho_{l,0}\phi^\Delta$ (Eq. 5.29b). Without an ocean, the pressure at the surface p^Δ is 0 and the tidal force drives the Darcian flow, $p^* = \rho_{l,0}\phi^\Delta$. In contrast, if there is an overlying ocean and ice shell, the pressure at the core–ocean boundary is not zero. To understand this, consider a core that is just covered by an ocean. Under our assumptions, the ocean surface follows the equilibrium tide $-\phi^\Delta/g$ while the core–ocean boundary has a radial displacement of u. As a result, the pressure perturbation at the core–ocean boundary is $p^\Delta = \rho_{l,0}g(-u-\phi^\Delta/g)$. This ocean pressure partially compensates the driving tidal potential, leading to a modified pressure p^* proportional to the the core radial displacement $-\rho_{l,0}gu$. Writing this in terms of h_2, the radial displacement Love number, $p^* = \rho_{l,0}h_2\phi^\Delta$. Because of its rigidity, the radial displacement of the core is generally much smaller than the equilibrium tide ($h_2 \ll 1$), explaining why Darcy dissipation is greatly reduced when considering an ocean-covered core.

The presence of an ice shell above the ocean inhibits the ocean surface from following the equilibrium tide by imposing a pressure load. If the ice shell is completely rigid (no surface displacements), the pressure load compensates the equilibrium tide and is given by $-\rho_{l,0}\phi^\Delta$. Hence the ice shell imposes a pressure equivalent to that imposed by the water column in an ice-free ocean, leading to the same reduction in effective pressure at the core. 5.9 provides analytical solutions for an incompressible core with and

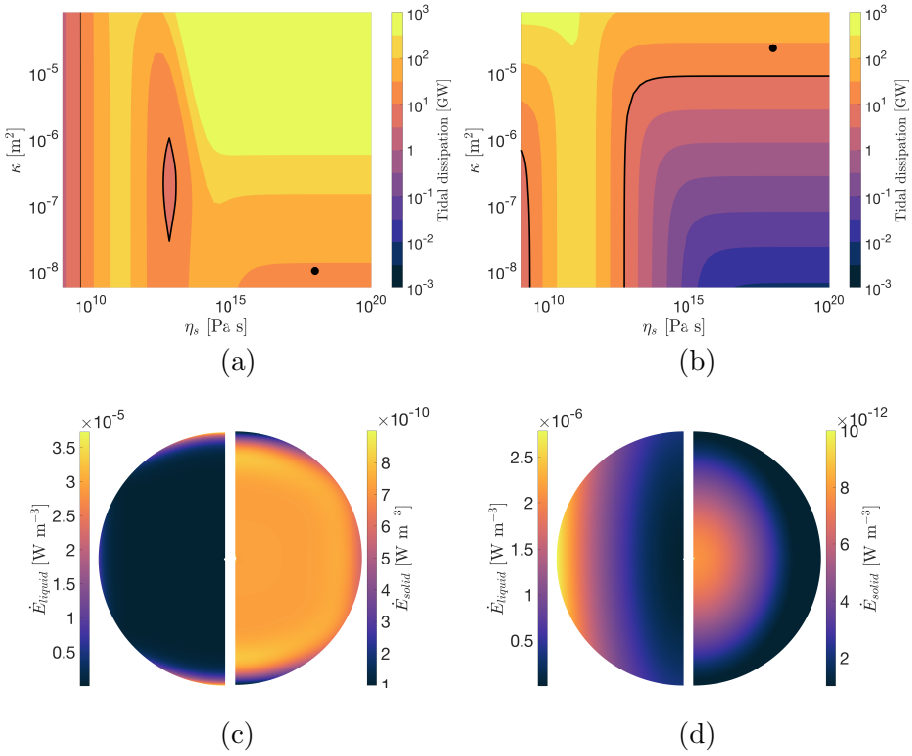

Figure 5.3 Total tidal dissipation in an Enceladan core with a free surface for various values of core viscosity and permeability. In (a) the core is forced via a prescribed strain field of order degree 2 and order 0, in (b) via the tidal potential. The contour for $\dot{E} = 10$ GW is indicated in both plots. (c) and (d) show tidal dissipation in the liquid and solid phases for a meridional cut at longitude 0° for the two points indicated in (a) and (b). Both points have a viscosity of 10^{18} Pa s and result in the same amount of tidal dissipation (28 GW). For all cases we assume $\mu = 1$ GPa, $K_s = 10$ GPa, $K_l = 2.2$ GPa and $\alpha = 0.95$.

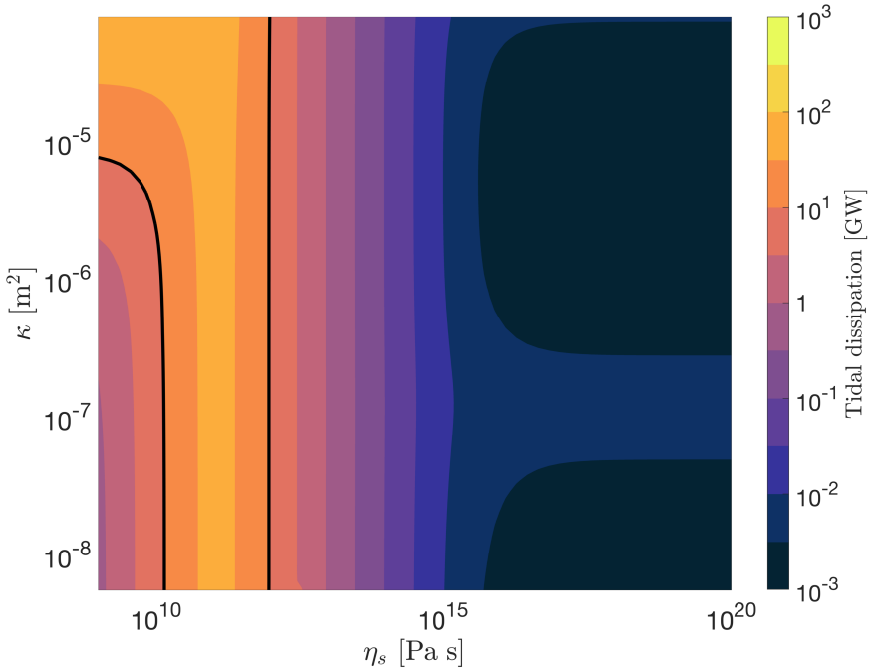

Figure 5.4 Total tidal dissipation in Enceladus' core for different values of core viscosity and permeability. We assume $\mu = 1$ GPa, $K_s = 10$ GPa, $K_l = 2.2$ GPa and $\alpha = 0.95$.

without a free surface that further demonstrate the role of the pressure at the core–ocean boundary.

5.3.3. AN UNCONSOLIDATED CORE

In light of the reduced tidal dissipation in Enceladus' porous core in comparison to the findings of *Liao et al.* (2020), we reconsider the low viscosity band where dissipation is enhanced. In all cases, we found that tidal dissipation peaks at $\sim 10^{11}$ Pa s. Close to this viscosity value, the amount of heat dissipated within the core is compatible with Enceladus' observed thermal output. Such a low viscosity is incompatible with the viscosity characteristics of silicates (*Roberts and Nimmo*, 2008). However, *Choblet et al.* (2017) proposed that low effective viscosity values can be attained if Enceladus' core is unconsolidated. If this is the case, friction between grains can give rise to substantial dissipation. We next reconsider this hypothesis and discuss its plausibility and remaining unknowns.

If strains are small, a granular material essentially behaves as a monolith. The grains deform elastically and stresses are transmitted at the grain boundaries. Some viscous deformation can also occur mainly due to diffusion creep. Under higher strains, grain–grain sliding becomes important and, combined with inter-granular friction, it can result in enhanced energy dissipation (*Lambe and Whitman*, 1969). Instead of using μ and η_s to characterise the rheology, a granular material is normally characterized in terms of an effective shear modulus (μ_{eff}) and a damping coefficient (υ) (e.g., *Choblet et al.*, 2017; *Seed et al.*, 1986). These two variables are related to the shear modulus and the solid viscosity introduced before as

$$\mu = \frac{\mu_{eff}}{\sqrt{1-4\upsilon^2}}, \tag{5.34a}$$

$$\eta_s = \frac{\mu_{eff}}{2n\upsilon}. \tag{5.34b}$$

Figure 5.5 shows the amount of tidal dissipation in the core as function of μ_{eff} and υ. For $\upsilon > 0.1$ more than 10 GW can be generated in Enceladus' core, provided the shear modulus is low enough. The values of the damping coefficient and effective shear modulus depend on factors that include the amplitude of the deviatoric strain, the confining pressure, and the forcing frequency (*Faul and Jackson*, 2005; *Lambe and Whitman*, 1969; *Seed et al.*, 1986).

Goldreich and Sari (2009) showed that the effective rigidity of an unconsolidated body is smaller than that of a monolith due the concentration of stresses in sharp contact points. They proposed that the shear modulus is controlled by the curvature radius at these contact points, which in turn depends on the yield strain of the material ϵ_Y, and showed that the effective rigidity of an unconsolidated body can be estimated as $\mu_{eff} = \left(\frac{2g\rho R}{19}\frac{\mu}{\epsilon_Y}\right)^{1/2}$, with R and g the surface radius and gravity and ρ the bulk density. This expression is consistent with an increase in shear modulus with confining pressure seen in the laboratory (*Goddard*, 1990). Using values representative of Enceladus's core

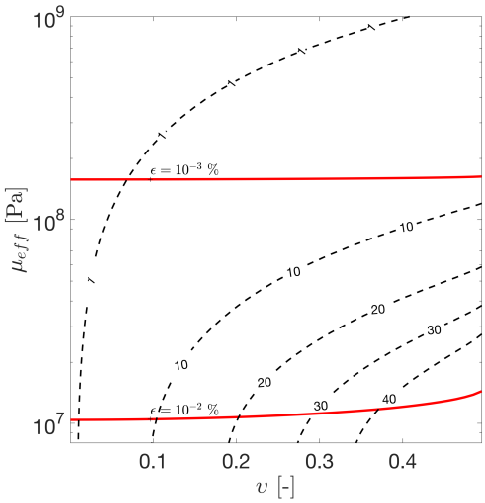

Figure 5.5 Total tidal dissipation in Enceladus' core for different values of core effective shear modulus and damping coefficient. A viscoelastic core and ice shell are assumed. The red lines indicate the maximum deviatoric strain attained within the core.

5

($\mu \sim 1$ GPa, $\epsilon_Y = 10^{-2}$), we find $\mu_{eff} \sim 0.7$ GPa—a value much higher than that required to attain high values of tidal dissipation for moderate values of damping coefficient υ (Figure 5.5).

Laboratory experiments can also be used to bound υ and μ_{eff}. If the material experiences high deviatoric strains, υ increases. Laboratory data shows a pronounced increase of υ for $\epsilon > 0.01\%$; υ can reach values higher than 0.15 for $\epsilon > 0.1\%$ (e.g., *Rollins et al.*, 1998; *Seed et al.*, 1986). For Enceladus' tidal amplitude, these high strains are only attained if the material has a low effective shear modulus ($\mu_{eff} \sim 10^7 - 10^8$ Pa) (Figure 5.5). The shear modulus increases with increasing overburden pressure and decreases with the amplitude of the deviatoric strain. For small strains ($\epsilon < 0.001\%$), the shear modulus of typical sand mixtures at Enceladus' core pressure (5–50 MPa) is on the order of 10^9 Pa (*Seed et al.*, 1986), incompatible with enhanced dissipation. Strains on the order of 0.01–0.1% can reduce the effective shear modulus by around 50% (*Rollins et al.*, 1998; *Seed et al.*, 1986). Furthermore, the effective shear modulus is expected to decrease and the damping coefficient to increase at lower forcing frequencies (*Faul and Jackson*, 2005). Unfortunately, laboratory data is only available for a frequency range (0.01–1 Hz) much higher than Enceladus' tidal frequency ($\sim 10^{-5}$Hz). It remains to be seen if such changes are sufficient to access the high-dissipation region of Figure 5.5. Laboratory experiments at Enceladus-like conditions (high confining pressure, low forcing frequency) are required to assess whether Enceladus' core is in the highly deformable state required for the generation of the observed thermal activity.

A more direct measurement of Enceladus' core viscosity could be provided by a future Enceladan mission. Due to the viscosity of the core and the ice shell, their tidal

responses are characterised by phase lags with respect to the forcing. The ice-shell and core phase lags affect the gravity field and the surface displacements of the moon in different ways. Because the ocean decouples the ice shell from the core, the phase lag of the moon's surface displacement is mostly dependent on the viscosity of the ice shell; in contrast, the phase lag of the moon's gravity field depends on both the viscosity of the core and the ice shell. A low-viscosity core leads to a large gravity phase lag but has a much smaller effect on the surface-displacement phase lag; in contrast, a low viscosity ice shell produces phase lags in the gravity field and surface displacements of similar magnitude. Therefore, by measuring the difference between gravity and surface displacement phase lags, we can distinguish between a low-viscosity and a high-viscosity core. *Hussmann et al.* (2016) proposed this strategy to constrain Europa's core viscosity and the viscosity of high-pressure ice layers within Ganymede; a similar technique could be used for Enceladus (*Marusiak et al.*, 2021).

The gravity and surface-displacement phase lags are given by the phase lags of the gravitational and radial displacement Love numbers k_2 and h_2. Figure 5.6 shows the difference in gravity and surface-displacement phase lags $\xi_{k_2} - \xi_{h_2}$. If the core has a low viscosity, phase-lag differences up to 50° are attained. This also holds if the more complex Andrade rheology is considered (5.10). The gravity phase lag ξ_{k_2} could be measured by precise tracking of a single or dual orbiter around Enceladus (e.g., *Ermakov et al.*, 2021). The surface-displacements phase lag ξ_{h_2} could be measured using a laser or radar altimeter (*Steinbrügge et al.*, 2015, 2018). Such measurement would help to constrain Enceladus' core viscosity and settle the long-standing puzzle of where Enceladus' heat is coming from.

5.4. CONCLUSIONS

Several observations suggest that Enceladus' core likely is a porous silicate matrix throughout which water can permeate. The tidal response of a porous core is expected to be markedly different from that of a non-porous one: the presence of pores renders the body more compressible, pressure within the pores can alter the stress field, and water can flow within the core adding an additional dissipation mechanism. For a non-porous core, tidal dissipation is only high if the core has a rigidity and a viscosity significantly lower than those expected for a monolithic silicate core. Recently, *Liao et al.* (2020) presented an analysis of the tidal response of Enceladus' porous core using Biot's theory of poroviscoelasticity and showed that poroviscoelastic effects can increase tidal dissipation for core properties compatible with those of silicates.

Liao et al. (2020) cautioned that their model relies in some assumptions that required further scrutiny: they considered the tidal response only of the core and ignored the overlying ocean and ice shell, neglected the effects of self-gravity, and forced the problem via a prescribed surface strain rather than via the tidal potential. In this paper, we extended the model of *Liao et al.* (2020) by combining the theory of poroviscoelasticity (e.g., *Biot*, 1941; *Cheng*, 2016) with the theory commonly used to obtain the tidal deformation of viscoelastic, self-gravitating bodies (e.g., *Love*, 1906; *Sabadini et al.*, 2016).

With this theory, we assessed the relevance of the assumptions made by *Liao et al.*

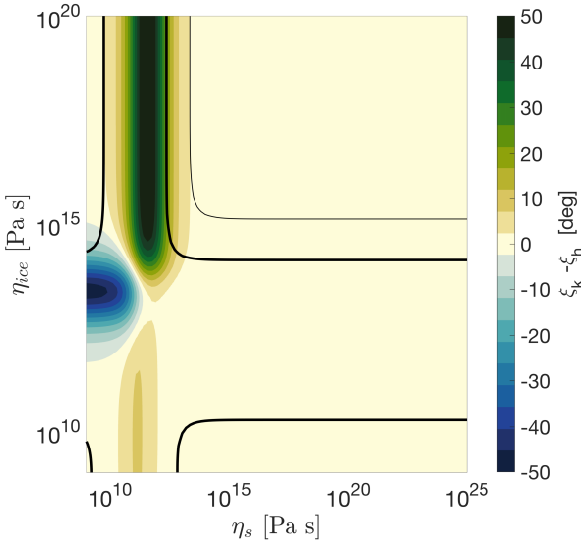

Figure 5.6 Difference in gravity and surface displacements phase lags for different values of core and ice shell viscosity. The thick and thin black contours show combinations of parameters for which tidal heating is 10 and 1 GW, respectively. A shear modulus of 1 GPa is assumed for the core; the properties of the ice shell are those given in Table 5.1, except for the viscosity, which we vary.

(2020), and studied the subspace of core properties for which tidal heating can explain Enceladus' thermal output. We started by considering a model of Enceladus' core without an overlying ocean and ice shell and showed that the boundary conditions at the core boundary play a central role. If the core is forced via a prescribed radial strain — as done in *Liao et al.* (2020)— tidal dissipation in both the solid and liquid phases can be orders of magnitude higher compared to that given by standard viscoelastic models. However, if a free surface is assumed (no-stress) and the core is forced via a tidal body force, dissipation in both liquid and solid phases is reduced. In this scenario, Enceladus' thermal output can only be explained by tidal dissipation in the solid phase if the core viscosity is very low ($\eta_s \sim 10^9$–10^{12} Pa s) compared to that characteristic of silicates or via Darcian dissipation in the fluid if the core is highly permeable ($\kappa > 10^{-5}$ m^2). We then considered a more realistic multi-layered model consisting of a porous core, a subsurface ocean and an ice-shell. We showed that the presence of a hydrostatic ocean hinders the tidal response of the core. More importantly, tidal dissipation due to Darcy flow is severely reduced, making it complicated to reconcile a rocky core with Enceladus' thermal output.

Dissipation within the solid phase can still account for Enceladus' thermal output if the core is weak and has a low viscosity. This requirement appears to be incompatible with a monolithic, silicate core. Yet *Choblet et al.* (2017) ascribed the low shear modulus and viscosity to grain–grain friction in a fragmented core akin to a rubble pile. While it is true that a low viscosity can arise from this process, it only occurs if the tidal strain is sufficiently large, which requires a low shear modulus that is difficult to reconcile with laboratory experiments (*Rollins et al.*, 1998; *Seed et al.*, 1986). However, available laboratory data is not representative of Enceladus' core conditions, which points to the need for further laboratory work. Alternatively, we show that a future Enceladus mission could probe the core's viscosity by measuring the phase lag of tidally-induced changes in the gravity field and surface deformation.

Other tidally active worlds might also have porous regions. Vigorous tidal heating can partially melt the mantle of a planet or a moon forming a porous sublayer filled with magma. Galileo's magnetometer data suggests that Io has a partially molten asthenosphere with a melt fraction of 20% (*Khurana et al.*, 2011) (although alternative explanations have been proposed for the magnetometer data (*Blöcker et al.*, 2018; *Roth et al.*, 2017)). Io is the closest example of a magma-rich world (*Khurana et al.*, 2011; *Peale et al.*, 1979; *Spencer et al.*, 2020), but extrasolar worlds experiencing higher levels of tidal heating might also be common (e.g., *Peters and Turner*, 2013; *Rovira-Navarro et al.*, 2021). So far, attempts to compute the tidal response of bodies with a partially molten asthenosphere have either used the theory of viscoelasticity (e.g., *Fischer and Spohn*, 1990; *Segatz et al.*, 1988), or the Laplace tidal equations commonly employed to model ocean tides (*Hay et al.*, 2020; *Tyler et al.*, 2015). Our model opens the door to study the tidal response of these worlds in a new light.

5.5. APPENDIX A: SOLUTION METHOD

We solve Eqs.(5.29-5.33) in the Fourier domain. Using the spherical symmetry of the problem, we decompose the Fourier-transformed variables using spherical harmonics. Scalar fields such as $\hat{\phi}^{\Delta}$, $\hat{\rho}^{\Delta}$ are written using normalized real spherical harmonics ($\mathscr{Y}_l^m$) of degree l and order m as

$$\hat{\phi}^{\Delta}(r,\theta,\varphi) = \hat{\phi}^{\Delta}_{lm}(r)\mathscr{Y}_l^m(\theta,\varphi), \tag{5.35a}$$

$$\hat{\rho}^{\Delta}(r,\theta,\varphi) = \hat{\rho}^{\Delta}_{lm}(r)\mathscr{Y}_l^m(\theta,\varphi), \tag{5.35b}$$

with

$$\mathscr{Y}_l^m = \begin{cases} (-1)^m\sqrt{2}\sqrt{\dfrac{2l+1}{4\pi}\dfrac{(l-|m|)!}{(l+|m|)!}}P_l^{|m|}(\cos\theta)\sin\big(|m|\varphi\big), & \text{if } m<0 \\ \sqrt{\dfrac{2l+1}{4\pi}}P_l^m(\cos\theta), & \text{if } m=0 \\ (-1)^m\sqrt{2}\sqrt{\dfrac{2l+1}{4\pi}\dfrac{(l-m)!}{(l+m)!}}P_l^m(\cos\theta)\cos\big(m\varphi\big), & \text{if } m>0 \end{cases} \tag{5.36}$$

P_l^m are associated Legendre polynomials of degree l and order m.

The vector fields are similarly expanded using vector spherical harmonics:

$$\hat{\boldsymbol{u}}(r,\theta,\varphi) = \hat{u}_{lm}(r)\boldsymbol{R}_l^m + \hat{v}_{lm}(r)\boldsymbol{S}_l^m, \tag{5.37a}$$

$$\hat{\boldsymbol{q}}(r,\theta,\varphi) = \hat{q}_{lm}(r)\boldsymbol{R}_l^m + \hat{s}_{lm}(r)\boldsymbol{S}_l^m. \tag{5.37b}$$

$\hat{u}_{lm}$ and $\hat{q}_{lm}$, and $\hat{v}_{lm}$ and $\hat{s}_{lm}$ are the radial and tangential components of the displacement and flow field, respectively, and $\boldsymbol{R}_l^m$ and $\boldsymbol{S}_l^m$ are vector spherical harmonics,

$$\boldsymbol{R}_l^m = \mathscr{Y}_l^m\boldsymbol{e}_r, \quad \boldsymbol{S}_l^m = \nabla_{\theta,\varphi}\mathscr{Y}_l^m. \tag{5.38}$$

Using the previous definitions and the constitutive equations, the governing equations can be cast into a first order differential equation of the form

$$\frac{\mathrm{d}\hat{\boldsymbol{y}}}{\mathrm{d}r} = \boldsymbol{A}\hat{\boldsymbol{y}}. \tag{5.39}$$

$\boldsymbol{A}$ is a matrix given in 5.6 and $\hat{\boldsymbol{y}}$ is a vector containing 8 radial functions:

$$\hat{y}_1 = \hat{u}_{lm} \tag{5.40a}$$

$$\hat{y}_2 = \hat{v}_{lm} \tag{5.40b}$$

$$\hat{y}_3 = \hat{\lambda}\hat{\epsilon}^V_{lm} - \alpha\hat{p}^{\Delta}_{lm} + 2\hat{\mu}\frac{\mathrm{d}\hat{u}_{lm}}{\mathrm{d}r} \tag{5.40c}$$

$$\hat{y}_4 = \hat{\mu}\left(\frac{\mathrm{d}\hat{v}_{lm}}{\mathrm{d}r} - \frac{\hat{v}_{lm}}{r} + \frac{\hat{u}_{lm}}{r}\right) \tag{5.40d}$$

$$\hat{y}_5 = \hat{\phi}^{\Delta}_{lm} \tag{5.40e}$$

$$\hat{y}_6 = \frac{\mathrm{d}\hat{\phi}^{\Delta}_{lm}}{\mathrm{d}r} + \frac{l+1}{r}\hat{\phi}^{\Delta}_{lm} + 4\pi G\rho_0\hat{u}_{lm} - \frac{4\pi G\rho_{l,0}\kappa}{\mathrm{i}n\eta_l}\left(\frac{\mathrm{d}}{\mathrm{d}r}\left(\hat{p}^{\Delta}_{lm} + \rho_{l,0}\hat{\phi}^{\Delta}_{lm}\right) + \frac{g\rho_{l,0}}{K_l}\hat{p}^{\Delta}_{lm}\right) \tag{5.40f}$$

$$\hat{y}_7 = \hat{p}^{\Delta}_{lm} \tag{5.40g}$$

$$\hat{y}_8 = \frac{\mathrm{d}}{\mathrm{d}r}\left(\hat{p}^{\Delta}_{lm} + \rho_{l,0}\hat{\phi}^{\Delta}_{lm}\right) + \frac{g\rho_{l,0}}{K_l}\hat{p}^{\Delta}_{lm} \tag{5.40h}$$

$\hat{\epsilon}_{lm}$ is the divergence of the displacement vector given by

$$\hat{\epsilon}^{V}_{lm} = \frac{\mathrm{d}\hat{y}_1}{\mathrm{d}r} + \frac{2}{r}\hat{y}_1 - \frac{l(l+1)}{r}\hat{y}_2. \tag{5.41}$$

and $\hat{\mu}$ and $\hat{\lambda}$ are the complex rigidity and complex drained first Lamé parameter,

$$\hat{\mu} = \mu\frac{1}{1 - \frac{\mathrm{i}\mu}{\eta n}}, \tag{5.42a}$$

$$\hat{\lambda} = K - \frac{2}{3}\hat{\mu}. \tag{5.42b}$$

Note that the radial functions $\hat{y}_{1-8}$ are the same radial functions commonly used to solve the viscoelastic tidal problem (e.g., *Sabadini et al.*, 2016) except that two extra variables ($\hat{y}_7$ and $\hat{y}_8$) are added, and $\hat{y}_6$ is modified. $\hat{y}_1$ and $\hat{y}_2$ are respectively the radial and tangential displacements, $\hat{y}_3$ and $\hat{y}_4$ correspond to the radial and tangential components of the stress tensor (σ^{Δ}_{rr}, $\sigma^{\Delta}_{\theta r}$), $\hat{y}_5$ is the disturbing potential, and $\hat{y}_6$ is the so-called potential stress. $\hat{y}_7$ is the pore pressure and $\hat{y}_8$ is proportional to the radial component of Darcy flow.

For incompressible internal liquid layers, it is sufficient to solve Laplace's equation. The problem can be similarly cast into a matrix form

$$\frac{\mathrm{d}\hat{\boldsymbol{z}}}{\mathrm{d}r} = \boldsymbol{A}_o\hat{\boldsymbol{z}} \tag{5.43}$$

where $\boldsymbol{z} = (\hat{z}_5, \hat{z}_6)^T$ and z_5 and z_6 are two radial functions corresponding to the perturbing potential and potential stress in the ocean:

$$\hat{z}_5 = \hat{\phi}^{\Delta}_{lm}, \tag{5.44a}$$

$$\hat{z}_6 = \frac{\mathrm{d}\hat{\phi}^{\Delta}_{lm}}{\mathrm{d}r} + \left(\frac{l+1}{r} - \frac{4\pi G\rho_0}{g}\right)\hat{\phi}^{\Delta}_{lm}. \tag{5.44b}$$

$\boldsymbol{A}_o$ follows from Poisson's equation and is given in 5.6.

The surface boundary conditions, Eqs. (5.23-5.26), should be written in terms of the y functions. The stress boundary conditions at the surface are easily obtained. In contrast the boundary condition for the gradient of the tidal potential requires some

further discussion. Using Eq. (5.30) for the perturbing density, the Fourier-transformed Eq. (5.31) and the divergence theorem, Eq. (5.24) can be written as

$$\frac{\partial\hat{\phi}^{\Delta}(R+\delta)}{\partial r}-\frac{\partial\hat{\phi}^{\Delta}(R-\delta)}{\partial r}=4\pi\rho_0 G\hat{\boldsymbol{u}}\cdot\boldsymbol{e}_r+4\pi G\frac{\rho_{l,0}}{ni}\hat{\boldsymbol{q}}\cdot\boldsymbol{e}_r. \tag{5.45}$$

We split the perturbing potential into the self-gravity and the tidal potential components (ϕ^G, ϕ^T). In order to fulfill Poisson's equation outside of the body ($r > R$), ϕ^G should be of the form

$$\hat{\phi}^G(r)=\phi^G(R)\left(\frac{r}{R}\right)^{-l-1}. \tag{5.46}$$

Furthermore for a tidal forcing of degree l we have

$$\hat{\phi}^T(r)=\phi^T(R)\left(\frac{r}{R}\right)^{l}. \tag{5.47}$$

Plugging (5.46, 5.47) into (5.45), expanding the different fields in spherical harmonics, using Darcy's law to compute $\boldsymbol{q}$ (Eq. (5.29b)), and taking the limit $\delta \to 0$, we get

$$\hat{y}_6(R)=\frac{2l+1}{R}, \tag{5.48}$$

where we have assumed a unit tidal forcing, $\phi^T_{lm}(R) = 1$. In a similar way, it can be shown that $\hat{y}_6$ is continuous at solid interfaces. The continuity of $\hat{y}_6$ and the fact that the boundary condition at the surface for the tidal forcing adopts a simple form, make using $\hat{y}_6$ convenient. Together with the stress boundary condition, the surface boundary conditions are

$$\hat{y}_3(R)=0, \tag{5.49a}$$

$$\hat{y}_4(R)=0, \tag{5.49b}$$

$$\hat{y}_6(R)=\frac{2l+1}{R}. \tag{5.49c}$$

As explained in Section 5.2.2 these boundary conditions are different than those used by *Liao et al.* (2020). Using our notation, *Liao et al.* (2020) surface boundary conditions translate to:

$$\frac{\mathrm{d}\hat{y}_1(R)}{\mathrm{d}r}=\hat{\epsilon}_{rr,0}, \tag{5.50a}$$

$$\frac{\mathrm{d}\hat{y}_2(R)}{\mathrm{d}r}+\frac{\hat{y}_2(R)-\hat{y}_1(R)}{r}=0, \tag{5.50b}$$

$$\hat{y}_6(R)=0. \tag{5.50c}$$

(5.50a) imposes a prescribed strain of amplitude $\hat{\epsilon}_{rr,0}$, (5.50b) imposes an irrotational displacement field, and (5.50c) sets the gravitational tidal perturbation to 0.

The boundary condition at the porous layer interfaces (5.25,5.26) are simply:

$$\hat{y}_8 = 0, \tag{5.51a}$$

$$\hat{y}_3 + \hat{y}_7 = 0. \tag{5.51b}$$

Continuity of $\hat{y}_1 - \hat{y}_6$ is assumed at the solid layers boundaries. In case an internal liquid layer is present, additional boundary conditions are introduced at solid-liquid interfaces: the tangential stress vanishes, the radial stress is given by the difference between the radial displacement and an equipotential surface and the disturbing potential is continuous but the potential stress is not (*Greff-Lefftz et al.*, 2000; *Jara-Orué and Vermeersen*, 2011):

$$\hat{y}_4(r) = 0, \tag{5.52a}$$

$$\hat{y}_1(r) - \frac{\hat{y}_3(r)}{g(r)\rho_{ocean}} + \frac{\hat{y}_5(r)}{g(r)} = 0, \tag{5.52b}$$

$$\hat{y}_5(r) - \hat{z}_5(r) = 0, \tag{5.52c}$$

$$\hat{y}_6(r) - \hat{z}_6(r) - 4\pi G\rho_{ocean}\left(\hat{y}_1(r) + \frac{\hat{z}_5(r)}{g(r)}\right) = 0. \tag{5.52d}$$

Starting from the center of the moon or the liquid core-mantle boundary (if the body in question has a liquid core), the previous equations are integrated radially using a Runge-Kutta-4 integrator (see 5.7). Once the radial functions are obtained for the different components of the tidal potential, the displacement, flux, stress and strain fields can be computed as explained in 5.8.

5.6. APPENDIX B: PROPAGATION MATRIX

The non-zero elements of the propagation matrix $\boldsymbol{A}$ are:

$$
\begin{aligned}
A_{11} &= -2\frac{\hat{\lambda}}{(2\hat{\mu}+\hat{\lambda})r} \\
A_{12} &= l(l+1)\frac{\hat{\lambda}}{(2\hat{\mu}+\hat{\lambda})r} \\
A_{13} &= \frac{1}{2\hat{\mu}+\hat{\lambda}} \\
A_{17} &= \frac{\alpha}{2\hat{\mu}+\hat{\lambda}} \\
\\
A_{21} &= -\frac{1}{r} \\
A_{22} &= \frac{1}{r} \\
A_{24} &= \frac{1}{\hat{\mu}} \\
\\
A_{31} &= \frac{4}{r}\left(\frac{\hat{\mu}}{r}\frac{3\hat{\lambda}+2\hat{\mu}}{2\hat{\mu}+\hat{\lambda}} - \rho_0 g\right) + \frac{2g\alpha\rho_{l,0}}{r}\left(\frac{-\hat{\lambda}}{2\hat{\mu}+\hat{\lambda}}+1\right) \\
A_{32} &= -\frac{l(l+1)}{r}\left(\frac{2\hat{\mu}}{r}\frac{2\hat{\mu}+3\hat{\lambda}}{2\hat{\mu}+\hat{\lambda}} - \rho_0 g\right) + \frac{l(l+1)g\rho_{l,0}\alpha}{r}\left(\frac{\hat{\lambda}}{2\hat{\mu}+\hat{\lambda}}-1\right) \\
A_{33} &= \frac{1}{2\hat{\mu}+\hat{\lambda}}\left(-\frac{4\hat{\mu}}{r}+g\alpha\rho_{l,0}\right) \\
A_{34} &= \frac{l(l+1)}{r} \\
A_{35} &= -\rho_0\frac{l+1}{r} \\
A_{36} &= \rho_0 \\
A_{37} &= \frac{\alpha}{2\hat{\mu}+\hat{\lambda}}\left(-\frac{4\hat{\mu}}{r}+\rho_{l,0}g\alpha\right) + g\rho_{l,0}\left(\frac{\Phi}{K_f}+\frac{\alpha-\Phi}{K_s}\right) \\
A_{38} &= \frac{4\pi G\rho_{l,0}\rho_0\kappa}{\mathrm{i}n\eta_f} \\
\\
A_{41} &= -\frac{1}{r}\left(\frac{\hat{\mu}}{r}\left(2+\frac{4\hat{\lambda}}{2\hat{\mu}+\hat{\lambda}}\right)-\rho_0 g\right) \\
A_{42} &= \frac{2\hat{\mu}}{r^2}\left(l^2+l-1+\frac{l(l+1)\hat{\lambda}}{(2\hat{\mu}+\hat{\lambda})}\right)
\end{aligned}
\tag{5.53}
$$

$$A_{43} = -\frac{1}{r}\left(1 - \frac{2\hat{\mu}}{2\hat{\mu}+\hat{\lambda}}\right)$$
$$A_{44} = -\frac{3}{r}$$
$$A_{45} = \frac{\rho_0}{r}$$
$$A_{47} = 2\frac{\alpha\hat{\mu}}{r(2\hat{\mu}+\hat{\lambda})}$$

$$A_{51} = -4\pi G\rho_0$$
$$A_{55} = -\frac{l+1}{r}$$
$$A_{56} = 1$$
$$A_{58} = \frac{4\pi G\rho_{l,0}\kappa}{\mathrm{i}n\eta_l}$$

$$A_{61} = -\frac{4\pi(l+1)G\rho_0}{r}$$
$$A_{62} = \frac{4\pi l(l+1)G\rho_0}{r}$$
$$A_{65} = -\frac{4\pi l(l+1)G\rho_{l,0}^2\kappa}{\mathrm{i}n\eta_l r^2}$$
$$A_{66} = \frac{(l-1)}{r}$$
$$A_{67} = -\frac{4\pi l(l+1)G\rho_{l,0}\kappa}{\mathrm{i}n\eta_l r^2}$$
$$A_{68} = \frac{4\pi G(l+1)\rho_{l,0}\kappa}{\mathrm{i}n\eta_l r}$$

$$A_{71} = 4\pi G\rho_{l,0}\rho_0$$
$$A_{75} = \rho_{l,0}\frac{(l+1)}{r}$$
$$A_{76} = -\rho_{l,0}$$
$$A_{77} = -\frac{g\rho_{l,0}}{K_l}$$
$$A_{78} = 1 - \frac{4\pi G\rho_{l,0}^2\kappa}{\mathrm{i}n\eta_l}$$

$$
\begin{aligned}
A_{81} &= \frac{2\mathrm{i}\alpha n\eta_l}{\kappa r}\left(1-\frac{\hat{\lambda}}{2\hat{\mu}+\hat{\lambda}}\right)\\
A_{82} &= -\frac{\mathrm{i}l(l+1)\alpha n\eta_l}{\kappa r}\left(1-\frac{\hat{\lambda}}{2\hat{\mu}+\hat{\lambda}}\right)\\
A_{83} &= \frac{\mathrm{i}\alpha n\eta_l}{\kappa(2\hat{\mu}+\hat{\lambda})}\\
A_{85} &= \frac{l(l+1)\rho_{l,0}}{r^2}\\
A_{87} &= \frac{l(l+1)}{r^2}+\frac{\mathrm{i}n\eta_l}{\kappa}\left(\frac{\alpha^2}{2\hat{\mu}+\hat{\lambda}}+\frac{\Phi}{K_f}+\frac{\alpha-\Phi}{K_s}\right)\\
A_{88} &= \frac{-2}{r}
\end{aligned}
$$

5

The propagation matrix of a non-porous incompressible material is recovered if $\alpha = 0, \Phi = 0, \rho_{l,0} = 0$ and $\hat{\lambda} \to \infty$. Also, by turning-off self-gravity ($\rho_0, \rho_{l,0} = 0$) the equations used in (*Liao et al.*, 2020) are recovered.

For the ocean propagator matrix $\boldsymbol{A}_o$, we have *Saito* (1974):

$$
\begin{aligned}
A_{o,11} &= \frac{4\pi G\rho_0}{g}-\frac{l+1}{r}\\
A_{o,12} &= 1\\
A_{o,21} &= \frac{2(l-1)}{r}\frac{4\pi G\rho_0}{g}\\
A_{o,22} &= \frac{l-1}{r}-\frac{4\pi G\rho_0}{g}
\end{aligned}
\tag{5.54}
$$

5.7. APPENDIX C: PROPAGATING THE SOLUTION

We start integrating Eq. (5.39) at the center of the body ($r_0 = 0$), or at the core-mantle interface ($r_0 = r_c$) if the moon has a liquid core. In either case, three integration constants $\boldsymbol{C}_0 = (C_1, C_2, C_3)^T$ are introduced. The solution at r_0 is $\hat{\boldsymbol{y}} = \boldsymbol{B}_0\boldsymbol{C}_0$. $\boldsymbol{B}_0$ is a matrix. If the body does not have a liquid core it is given by

$$\boldsymbol{B}_0 = \begin{pmatrix} 0 & 0 & 0 \\ 0 & 0 & 0 \\ 1 & 0 & 0 \\ 0 & 1 & 0 \\ 0 & 0 & 0 \\ 0 & 0 & 1 \\ 0 & 0 & 0 \\ 0 & 0 & 0 \end{pmatrix}, \tag{5.55}$$

otherwise, if the body has a liquid core, it is (*Sabadini et al.*, 2016)

$$\boldsymbol{B}_0 = \begin{pmatrix} -\frac{3r_c^{l-1}}{4\pi G\rho_c} & 0 & 1 \\ 0 & 1 & 0 \\ 0 & 0 & \frac{4\pi G\rho_c^2 r_c}{3} \\ 0 & 0 & 0 \\ r_c^l & 0 & 0 \\ 2(l-1)r_c^{l-1} & 0 & 4\pi G\rho_c \\ 0 & 0 & 0 \\ 0 & 0 & 0 \end{pmatrix}, \tag{5.56}$$

with ρ_c and r_c the density and core radius. An integration constant C_4 is introduced for the porous layer so that $y_7(r_p) = C_4$. At interfaces between solid layers continuity implies that

$$\hat{\boldsymbol{y}}^i(r_i) = \boldsymbol{P}\hat{\boldsymbol{y}}^{i-1}(r_i) + \delta_{ip}\boldsymbol{B}_{porous}C_4, \tag{5.57}$$

where δ_{ip} is the Kronecker delta, the superscript indicates the layer index –p being the index of the porous layer– and $\boldsymbol{P}$ and $\boldsymbol{B}_{porous}$ are two matrices given by

$$\boldsymbol{P} = \begin{pmatrix} 1 & 0 & 0 & 0 & 0 & 0 & 0 & 0 \\ 0 & 1 & 0 & 0 & 0 & 0 & 0 & 0 \\ 0 & 0 & 1 & 0 & 0 & 0 & 0 & 0 \\ 0 & 0 & 0 & 1 & 0 & 0 & 0 & 0 \\ 0 & 0 & 0 & 0 & 1 & 0 & 0 & 0 \\ 0 & 0 & 0 & 0 & 0 & 1 & 0 & 0 \\ 0 & 0 & 0 & 0 & 0 & 0 & 0 & 0 \\ 0 & 0 & 0 & 0 & 0 & 0 & 0 & 0 \end{pmatrix}, \tag{5.58}$$

and

$$\boldsymbol{B}_{porous} = (0,0,0,0,0,0,1,0)^T. \tag{5.59}$$

If an internal ocean is present, additional integration constants are introduced. At the ocean base, the solution is given by

$$\boldsymbol{z}(r_o) = \boldsymbol{I}\boldsymbol{C}_{ocean} \tag{5.60}$$

with $\boldsymbol{C}_{ocean} = (C_5, C_6)^T$. At the upper-boundary of the ocean (r_o), the solution is:

$$\boldsymbol{y}(r_o) = \boldsymbol{B}_{ice}\boldsymbol{C}_{ice} \tag{5.61}$$

with $\boldsymbol{C}_{ice} = (C_7, C_8, C_9, C_{10})^T$ and $\boldsymbol{B}_{ice}$ being

$$\boldsymbol{B}_{ice} = \begin{pmatrix} 1 & 0 & -\frac{1}{g(r_o)} & 0 \\ 0 & 1 & 0 & 0 \\ \rho_{ocean} g(r_o) & 0 & 0 & 0 \\ 0 & 0 & 0 & 0 \\ 0 & 0 & 1 & 0 \\ 0 & 0 & 0 & 1 \\ 0 & 0 & 0 & 0 \\ 0 & 0 & 0 & 0 \end{pmatrix}. \tag{5.62}$$

Note that $\boldsymbol{y}(r_o)$ already satisfies the boundary conditions (5.52a,b).

The integration constants $C_1 - C_{10}$ are obtained by propagating the solution (5.39) and (5.43) and applying the boundary conditions (5.49,5.51), and (5.52) if the moon has an internal liquid layer.

5.8. APPENDIX D: BUILDING THE SOLUTION

Once the radial functions $(\boldsymbol{y}, \boldsymbol{z})$ are obtained, they can be used to build the complete solution. The displacement and flow fields are:

$$\hat{\boldsymbol{u}}(r,\theta,\varphi) = \hat{y}_1 \boldsymbol{R}_l^m + \hat{y}_2 \boldsymbol{S}_l^m, \tag{5.63a}$$

$$\hat{\boldsymbol{q}}(r,\theta,\varphi) = -\frac{\kappa}{\eta_f}\hat{y}_8 \boldsymbol{R}_l^m - \frac{\kappa}{\eta_f}\frac{1}{r}\left(\hat{y}_7 + \rho_f \hat{y}_5\right)\boldsymbol{S}_l^m. \tag{5.63b}$$

Similarly, the different components of the strain tensor are given by:

$$\hat{\epsilon}^{\Delta}_{rr}(r,\theta,\varphi) = \frac{\mathrm{d}\hat{y}_1}{\mathrm{d}r}\mathscr{Y}_l^m, \tag{5.64a}$$

$$\hat{\epsilon}^{\Delta}_{\theta\theta}(r,\theta,\varphi) = \frac{1}{r}\left\{\left[\hat{y}_1 - \frac{l(l+1)}{2}\hat{y}_2\right]\mathscr{Y}_l^m + \frac{\hat{y}_2}{2}\mathscr{X}_l^m\right\}, \tag{5.64b}$$

$$\hat{\epsilon}^{\Delta}_{\varphi\varphi}(r,\theta,\varphi) = \frac{1}{r}\left\{\left[\hat{y}_1 - \frac{l(l+1)}{2}y_2\right]\mathscr{Y}_l^m - \frac{\hat{y}_2}{2}\mathscr{X}_l^m\right\}, \tag{5.64c}$$

$$\hat{\epsilon}^{\Delta}_{r\theta}(r,\theta,\varphi) = \frac{1}{2}\left[\frac{\mathrm{d}\hat{y}_2}{\mathrm{d}r} + \frac{\hat{y}_1 - \hat{y}_2}{r}\right]\frac{\partial\mathscr{Y}_l^m}{\partial\theta}, \tag{5.64d}$$

$$\hat{\epsilon}^{\Delta}_{r\varphi}(r,\theta,\varphi) = \frac{1}{2}\left[\frac{\mathrm{d}\hat{y}_2}{\mathrm{d}r} + \frac{\hat{y}_1 - \hat{y}_2}{r}\right]\frac{1}{\sin\theta}\frac{\partial\mathscr{Y}_l^m}{\partial\varphi}, \tag{5.64e}$$

5

$$\hat{\epsilon}^{\Delta}_{\theta,\varphi}(r,\theta,\varphi) = \frac{\hat{y}_2}{2r}\mathcal{Z}^m_l, \tag{5.64f}$$

with

$$\mathcal{X}^m_l = 2\frac{\partial^2 \mathcal{Y}^m_l}{\partial\theta^2} + l(l+1)\mathcal{Y}^m_l, \tag{5.65a}$$

$$\mathcal{Z}^m_l = 2\frac{\partial}{\partial\theta}\left(\frac{1}{\sin\theta}\frac{\partial \mathcal{Y}^m_l}{\partial\varphi}\right). \tag{5.65b}$$

The different components of the stress tensor are:

$$\hat{\sigma}^{\Delta}_{rr} = \hat{\lambda}\hat{\epsilon}^V_{lm}\mathcal{Y}^m_l + 2\hat{\mu}\hat{\epsilon}^{\Delta}_{rr} - \alpha\hat{y}_7\mathcal{Y}^m_l, \tag{5.66a}$$

$$\hat{\sigma}^{\Delta}_{\theta\theta} = \hat{\lambda}\hat{\epsilon}^V_{lm}\mathcal{Y}^m_l + 2\hat{\mu}\epsilon^{\Delta}_{\theta\theta} - \alpha\hat{y}_7\mathcal{Y}^m_l, \tag{5.66b}$$

$$\hat{\sigma}^{\Delta}_{\varphi\varphi} = \hat{\lambda}\hat{\epsilon}^V_{lm}\mathcal{Y}^m_l + 2\hat{\mu}\hat{\epsilon}^{\Delta}_{\varphi\varphi} - \alpha\hat{y}_7\mathcal{Y}^m_l, \tag{5.66c}$$

$$\hat{\sigma}^{\Delta}_{r\theta} = 2\hat{\mu}\hat{\epsilon}^{\Delta}_{r\theta}, \tag{5.66d}$$

$$\hat{\sigma}^{\Delta}_{r\varphi} = 2\hat{\mu}\hat{\epsilon}^{\Delta}_{r\varphi}, \tag{5.66e}$$

$$\hat{\sigma}^{\Delta}_{\theta\varphi} = 2\hat{\mu}\hat{\epsilon}^{\Delta}_{\theta\varphi}, \tag{5.66f}$$

The variation in fluid content ζ can be obtained using

$$\hat{\zeta} = \alpha\hat{\epsilon}^V_{lm}\mathcal{Y}^m_l + \frac{\alpha^2}{K_u - K_d}\hat{p}^{\Delta}_{lm}\mathcal{Y}^m_l. \tag{5.67}$$

The approach presented above allows us to obtain the internal response of a moon to a unit tidal forcing of degree l and order m ($\phi^T = \mathcal{Y}^m_l$). For a satellite in an eccentric orbit, the tidal potential contains terms of degree 2 and orders 0, −2 and 2 (Eq. (5.22)). As the equations are linear, to obtain the tidal response we can compute the radial functions for $l = 2$ and combine them considering the amplitude of the different terms. To obtain the total tidal response for a given field $\hat{a}$ (e.g., displacement vector, stress tensor, strain tensor, etc.), we use

$$\hat{a}(r,\theta,\varphi) = (nR)^2 e\left(3\sqrt{\frac{\pi}{5}}\hat{a}_{02}(r,\theta,\varphi) - 3\sqrt{\frac{3\pi}{5}}\hat{a}_{22}(r,\theta,\varphi) + 4\sqrt{\frac{3\pi}{5}}\mathrm{i}\hat{a}_{2-2}(r,\theta,\varphi)\right), \tag{5.68}$$

where a_{ml} are the solution for degree l and order m. The solution in the time domain is

$$\begin{aligned} a(r,\theta,\varphi,t) = (nR)^2 e\,\mathrm{Re}\Big\{&\Big(3\sqrt{\frac{\pi}{5}}\hat{a}_{02}(r,\theta,\varphi) \\ &- 3\sqrt{\frac{3\pi}{5}}\hat{a}_{22}(r,\theta,\varphi) + 4\sqrt{\frac{3\pi}{5}}\mathrm{i}\hat{a}_{2-2}(r,\theta,\varphi)\Big)\exp(\mathrm{i}nt)\Big\}. \end{aligned} \tag{5.69}$$

Once the solution is obtained, we can compute the volumetric energy dissipated in the solid,

$$\dot{E}_{v,solid} = -\frac{n}{2}\left[\mathrm{Re}(\hat{\boldsymbol{\sigma}}^{\Delta}) : \mathrm{Im}(\hat{\boldsymbol{\epsilon}}^{\Delta}) - \mathrm{Im}(\hat{\boldsymbol{\sigma}}^{\Delta}) : \mathrm{Re}(\hat{\boldsymbol{\epsilon}}^{\Delta}) + \mathrm{Re}(\hat{p}^{\Delta})\,\mathrm{Im}(\hat{\zeta}) - \mathrm{Im}(\hat{p}^{\Delta})\,\mathrm{Re}(\hat{\zeta})\right], \tag{5.70}$$

and liquid phase,

$$\dot{E}_{v,liquid} = \frac{1}{2}\frac{\eta_l}{\kappa}\left(|\hat{q}_r|^2 + |\hat{q}_\theta|^2 + |\hat{q}_\varphi|^2\right). \tag{5.71}$$

The total energy dissipated in the solid and the liquid is obtained by numerically integrating Eqs. (5.70,5.71). Alternatively, it can also be found by plugging the radial functions ($\hat{\boldsymbol{y}}$) into (5.63,5.64 and 5.66) and then using Eqs (5.70,5.71). Using that

$$\int_S \boldsymbol{R}_l^m \cdot \boldsymbol{R}_{l'}^{m'}\,\mathrm{d}S = \delta_{l,l'}\delta_{m,m'} \tag{5.72}$$

and

$$\int_S \boldsymbol{S}_l^m \cdot \boldsymbol{S}_{l'}^{m'}\,\mathrm{d}S = l(l+1)\delta_{l,l'}\delta_{m,m'}, \tag{5.73}$$

we obtain the angular averaged of the volumetric power ($\dot{E}_s$):

$$\begin{aligned}\dot{E}_{s,solid}(r) = \frac{\mathrm{Im}(\hat{\mu})n}{8\pi r^2}\Big(&\frac{4}{3}\Big|r\frac{\mathrm{d}\hat{y}_1}{\mathrm{d}r} - \hat{y}_1 + l(l+1)\hat{y}_2\Big|^2 \\ &+ l(l+1)\left|\frac{r\hat{y}_4}{\hat{\mu}}\right|^2 + l(l+1)(l(l+1)-2)|\hat{y}_2|^2\Big)\end{aligned} \tag{5.74a}$$

$$\dot{E}_{s,liquid}(r) = \frac{1}{8\pi r^2}\frac{\kappa}{\eta_l}\left(r^2|\hat{y}_8|^2 + l(l+1)|\hat{y}_7 + \rho_{l,0}\hat{y}_5|^2\right) \tag{5.74b}$$

The first expression is equivalent to that obtained by *Beuthe* (2013) and *Tobie et al.* (2005) for a viscoelastic body. The total tidal dissipation $\dot{E}_t$ can then be obtained by performing the radial integral of (5.74):

$$\dot{E}_t = 4\pi\int_0^R r^2\dot{E}_s\mathrm{d}r. \tag{5.75}$$

For a tidal forcing of the type given by Eq. (5.22), we find

$$\dot{E}_{t,solid} = \frac{336\pi^2}{5}n^5R^4e^2\int_0^R r^2\dot{E}_{s,solid}\mathrm{d}r. \tag{5.76a}$$

$$\dot{E}_{t,liquid} = \frac{336\pi^2}{5}\frac{n^4R^4\kappa}{\eta_l}e^2\int_0^R r^2\dot{E}_{s,liquid}\mathrm{d}r. \tag{5.76b}$$

5.9. APPENDIX E: INCOMPRESSIBLE CORE SOLUTION

If we consider that both the liquid and the porous matrix are incompressible ($K_s \to \infty$, $K_l \to \infty$), we can obtain an analytical expression for the flow field in the porous layer.

Mass conservation implies that $\zeta \to 0$ (Eq. (5.31)), and the pore pressure field can simply be obtained by solving the Laplace equation (Eq. (5.29))

$$\nabla^2(p^\Delta + \rho_{l,0}\phi^\Delta) = \nabla^2 p^* = 0. \tag{5.77}$$

with p^* a modified pressure. Solving Laplace's equation in spherical coordinates we find

$$p^* = (A_l r^l + B_l r^{-l-1})\mathscr{Y}_l^m(\theta,\varphi), \tag{5.78}$$

where $\mathscr{Y}_l^m$ is a spherical harmonic of degree l and order m and A_l and B_l are two integration constants to be found using the boundary conditions. The solution should be regular at $r = 0$, which implies that $B_l = 0$. Additionally, at the boundary we impose the boundary conditions given by (5.26) to find A_l. If there is no ocean, we have $p^*(r_1) = \rho_{l,0}\phi^\Delta(r_1)$; in contrast, if there is an ocean, we have $p^*(r_1) = P_{ocean}(r_1) + \rho_{l,0}\phi^\Delta(r_1)$. The pressure at the core-ocean boundary is given by the difference between the equipotential surface $-\phi^\Delta/g$ and the radial displacement at the core ocean-boundary $u_r(r_1)$ (Eqs. 5.52). Using these boundary conditions, we can obtain A_l for a core with a free surface or one overlaid by an ocean:

$$A_l^{free} = \frac{\rho_{l,0}\phi_l^\Delta(r_1)}{r_1^l}; \quad A_l^{ocean} = -h_l(r_1)\frac{\rho_{l,0}\phi_l^\Delta(r_1)}{r_1^l}, \tag{5.79}$$

where h_l is the radial displacement Love number.

We can now use Eq. (5.76b) to compute the total amount of Darcian dissipation,

$$\dot{E}^{free}_{liquid,t} = \frac{84}{5}\pi\frac{R_c^5\rho_{l,0}^2 n^4 \kappa e^2}{\eta_l}, \tag{5.80a}$$

$$\dot{E}^{ocean}_{liquid,t} = \frac{84}{5}h_2^2(R_c)\pi\frac{R_c^5\rho_{l,0}^2 n^4 \kappa e^2}{\eta_l}. \tag{5.80b}$$

The previous expressions provide a good approximation to the compressible cases presented in Section 5.3 (see Figure 5.2). Bearing in mind that $|h_l(r_1)| \ll 1$, we find that Darcy dissipation is severely reduced by the presence of an ocean.

5.10. APPENDIX F: ANDRADE RHEOLOGY

Alternative rheology laws can be introduced using the correspondence principle. If Andrade rheology is considered, the complex shear modulus (Eq. 5.42), is given by

$$\hat{\mu} = \left(\frac{1}{\mu} - \frac{\mathrm{i}}{\eta n} + \frac{\mu^{\beta-1}\beta!}{(\mathrm{i}\eta\chi n)^\beta}\right)^{-1}. \tag{5.81}$$

β is a constant that takes values between $0.1 - 0.4$ (e.g., *Renaud and Henning*, 2018) and χ a parameter that depends on the ratio between the anelastic and the Maxwell time

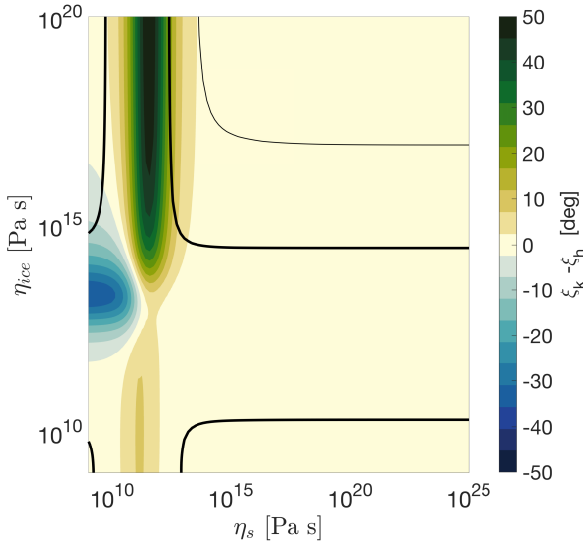

Figure 5.7 Same as Figure 5.6 but for Andrade rheology.

(*Efroimsky*, 2012b). If diffusion creep dominates, $\chi \approx 1$, which is commonly assumed for ices (*Castillo-Rogez et al.*, 2011; *Rhoden and Walker*, 2022; *Shoji et al.*, 2013).

We obtain Figure 5.7 using the Andrade rheology and $\beta = 0.3$ and $\chi = 1$ for both ice and rock. As in *Shoji et al.* (2013), we find that the Andrade rheology increases tidal dissipation in the ice shell for viscosities with a Maxwell time higher than the forcing frequency. The difference in phase-lag remains similar as those found using the Maxwell model (Section 5.3.3).

6

TIDALLY HEATED EXOMOONS AROUND GAS GIANTS

M. ROVIRA-NAVARRO , W. VAN DER WAL, T. STEINKE, D. DIRKX

Thousands of exoplanets have been discovered; however, the detection of exomoons remains elusive. Tidally heated exomoons have been proposed as candidate targets for observation; vigorous tidal dissipation can raise the moon's surface temperature, making direct imaging possible; and cause widespread volcanism that can have a signature in transits. We assess whether the required amounts of tidal dissipation can be attained and how long it can be sustained. In a first step, we look at the thermal state of a super-Io for different orbital configurations. We show that close-in exomoons with moderate ($e \sim e_{Io}$) to high ($e \sim 0.1$) orbital eccentricities can feature surface heat fluxes one to three orders of magnitude higher than that of Io if heat transfer is dominated by heat piping or the moon has a magma ocean. In a second step, we investigate the longevity of a super-Io. The free eccentricity of an isolated close-in exomoon is quickly dampened due to tides; high orbital eccentricities can be maintained if the moon is in a mean-motion resonance with another moon and the planet is highly dissipative. However, this scenario leads to fast orbital migration. For a Mars-sized exomoon, we find that tides alone can raise the surface temperatures to more than 400 K *for ten million* yr*, and surface heat fluxes higher than that of Io can be maintained for billions of years. Such tidally active bodies are expected to feature more vigorous volcanic activity than Io. The material outgassed via volcanism might be detected in transits.*

An earlier version of this chapter is published in the Planetary Science Journal (*Rovira-Navarro et al.*, 2021): Rovira-Navarro, M., van der Wal, W., Steinke, T., & Dirkx, D. (2021), Tidally heated exomoons around gas giants, The Planetary Science Journal, 2(3), 119.

6.1. INTRODUCTION

With the list of confirmed exoplanets continually growing, it is no surprise that the search for exomoons has started to gain momentum. The small size of the satellites with respect to their host planets makes their detection challenging. However, with improvements in observation capabilities and novel detection methods, the observation of exomoons is now within reach. Several techniques have been proposed for the detection of exomoons (e.g., *Heller*, 2017). These methods include transits (*Ben-Jaffel and Ballester*, 2014; *Hippke*, 2015; *Kipping*, 2009; *Kipping et al.*, 2015; *Teachey and Kipping*, 2018; *Teachey et al.*, 2017), microlensing (*Bennett et al.*, 2014; *Han and Han*, 2002), cyclotron radio emissions (*Noyola et al.*, 2014, 2016), pulsar timing variations (*Lewis et al.*, 2008) and direct imaging (*Cabrera, J. and Schneider, J.*, 2007; *Heller, R.*, 2016; *Peters and Turner*, 2013).

Tidally heated exomoons are promising targets in the exomoon hunt (e.g., *Ben-Jaffel and Ballester*, 2014; *Heller*, 2017; *Oza et al.*, 2019; *Peters and Turner*, 2013). Tidal dissipation within an exomoon can heat its interior and result in vigorous observable geologic activity. Io, the innermost Galilean satellite, is a good archetype. Although it has a radius four times smaller than that of Earth, tides raised by Jupiter result in an intrinsic surface heat flux roughly 30 times higher than that of Earth (*Lainey et al.*, 2009; *Turcotte and Schubert*, 2014). Tidal dissipation drives widespread volcanism, which in turn is responsible for the formation of a secondary atmosphere that extends over more than 400 Jupiter radii (*Mendillo et al.*, 1990). Among the outgassed material, there is sodium and potassium, which have not been detected in the gaseous envelopes of gas giants and thus can be used as a proxy for volcanic activity within a planetary system (*Johnson and Huggins*, 2006; *Oza et al.*, 2019). Moreover, the interaction of the outgassed secondary atmosphere with Jupiter's magnetosphere produces Io's plasma torus. While Io is unique in the Solar System, objects with similar or higher levels of internal heating, super-Ios, might be common. In fact, it is possible that these kinds of objects have already been detected. *Ben-Jaffel and Ballester* (2014) suggested that the early ingress of close-in exoplanets WASP-12b and HD 189733b observed in the UV can be explained by the presence of a plasma torus, and *Oza et al.* (2019) proposed that Na signatures in the spectra of the hot Jupiter WASP-49b are evidence of a tidally heated exomoon. If confirmed, these exomoons are likely very different from Io, though; due to the close proximity of the planet to the star, surface temperatures are between 1000 and 3000 K, and tidal dissipation is the result of stellar tides. Transits of temperate/cold gas giants are less likely than transits of close-in giant planets, as they orbit further away from the star and thus have smaller transit probabilities (*Dalba et al.*, 2015). However, cold gas giants suited for transit spectroscopy have already been identified, for example, HIP 41378 f (*Becker et al.*, 2018).

In extreme cases, tidal heating can exceed solar irradiation and have an observable footprint in the surface temperature. *Peters and Turner* (2013) proposed that a super-Io orbiting a cold gas giant could be directly imaged using current and planned telescopes. For this to happen, the moon should have a highly eccentric and/or a short-period orbit around a cold planet. *Peters and Turner* (2013) concluded that Earth-sized exomoons with surface temperatures higher than 600 or 300 K could be detected with the Spitzer Space Telescope and future telescopes such as the James Webb Space Telescope

or SPICA, respectively. The high surface temperatures needed to observe tidally heated exomoons require surface heat fluxes on the order of 500 $\mathrm{W m^{-2}}$, 2 orders of magnitude higher than current values of Io. It remains uncertain if such extreme cases of super-Ios can exist. Furthermore, while episodes of extreme tidal heating might occur, the odds of detecting a super-Io are higher the longer it remains active. Motivated by the prospects of detecting a super-Io around a cold gas giant, we ask the question of under which conditions can a super-Io persist. The question can be further split into (1) what is the possible thermal state of a super-Io?; and (2) how long can a super-Io persist in an observable state?

In Section 6.2, we tackle the first question. We investigate thermal equilibrium states of exomoons of different sizes. While bigger exomoons are more prone to becoming super-Ios, current formation models limit the permissible size of exomoons around gas giants to approximately the size of Mars (*Heller and Pudritz*, 2015a,b). We push this limit and consider exomoons ranging from Io to Earth sizes and identify thermal states for which the amount of generated internal heat equals the amount of heat removed from the interior. We consider rocky exomoons with Io-like structure and composition. To account for the high temperatures reached within the mantle of a super-Io, our model allows for the formation of a sublayer of melt (Section 6.2.1). We compute tidal dissipation using the viscoelastic theory for self-gravitating bodies (e.g., *Peltier*, 1974; *Wu and Peltier*, 1982) using Andrade rheology (Section 6.2.2) and compare it with estimates of heat removed from the mantle (Section 6.2.3) via convection or melt advection (heat piping) to find thermal equilibria states. We first apply the model to Io and find that it can successfully explain its thermal state. Equipped with this model, we compute surface temperatures and heat fluxes for a range of fixed eccentricities and orbital periods to assess whether these bodies could be directly imaged or could exhibit vigorous tidal activity and have substantial exospheres.

In Section 6.3, we tackle the second question: how long can a super-Io live? Instead of considering fixed values for orbital period and eccentricity, we take into account the feedback between tidal dissipation, internal structure, and orbital parameters. We consider two scenarios: an isolated moon-planet system and a system with two exomoons where orbital resonances can occur. Orbital resonances are common in the solar system (e.g., *Peale*, 1976) and are responsible for the high geological activity featured by some of the outer planet moons. Classic examples of resonances in the solar system include Janus-Epimetheus, Mimas-Tethys, and Enceladus-Dione in the Saturnian system and the Laplace resonance involving the three inner Galilean moons. We consider the 2:1 mean-motion resonance and study the thermal-orbital evolution of a Mars-sized exomoon in more detail.

6.2. THERMAL STATES OF A SUPER-IO

6.2.1. INTERIOR STRUCTURE AND RHEOLOGY

We consider three different moons with radii equal to $(1,2,4)\cdot R_{Io}$, which represent Io and roughly Mars- and Earth-sized exomoons. The moons are assumed to be spherically symmetric and made of concentric layers with uniform mechanical and thermal

properties (Figure 6.1). Each moon is assumed to have a metallic core of density ρ_c and radius R_c, and a silicate rocky layer with density ρ_s, which is a standard composition for bodies in this size range. The ratio of the surface (R) and core (R_c) radii is assumed to be the same for the three exomoons and equal to the value estimated for a sulfur-rich Io core, 0.52 (*Anderson et al.*, 1996a). We note that the core ratio could be different for other exomoons; however, the core size has a small effect on our conclusions (see Section 6.2.2).

The outer rocky layer consists of an elastic lithosphere where heat is transferred via conduction and heat piping and a convective mantle (see Section 6.2.3). In the elastic lithosphere, the temperature decreases linearly to the surface temperature T_{surf}. Inside the convective mantle, the temperature follows an adiabat (*Turcotte and Schubert*, 2014):

$$\frac{dT}{dP} = \frac{\alpha T}{\rho C_c}. \tag{6.1}$$

α and C_c are the thermal expansivity and the heat capacity, respectively (see Table 6.1). As an example, for a characteristic mantle temperature of 1800 K, the adiabatic temperature gradient is ≈ 9 KGPa^{-1}.

For sufficiently high mantle temperatures, the local mantle temperature can exceed the local solidus temperature at a given depth. When this occurs, a partially molten sublayer is formed (see Figure 6.1). The average melt fraction ($\overline{\Phi}$) of the layer is computed as

$$\overline{\Phi} = \frac{\overline{T} - \overline{T_s}}{\overline{T_l} - \overline{T_s}}, \tag{6.2}$$

with $\overline{T}$ being the average temperature of the layer. $\overline{T_s}$ and $\overline{T_l}$ are the averages of the pressure-dependent solidus and liquidus temperatures (*Takahashi*, 1990),

$$T_s = 1409.15 + 134.2P - 6.581P^2 + 0.1054P^3 \tag{6.3}$$

$$T_l = 2035 + 57.46P - 3.487P^2 + 0.00769P^3, \tag{6.4}$$

with the pressure in gigapascals. When a slope of $\mathrm{d}T_{s,l}/\mathrm{d}P = 10$ KGPa^{-1} is reached, we assume that the solidus and liquidus temperature increase linearly with pressure (*Reese et al.*, 1999).

The lithosphere is assumed to behave elastically, and the viscosity of the mantle depends on the temperature following an Arrhenius relation,

$$\eta = \eta_s \exp\left(\frac{E_a}{R_g \overline{T_s}}\left(\frac{\overline{T_s}}{\overline{T}} - 1\right)\right), \tag{6.5}$$

where η_s is the viscosity at the solidus temperature, E_a is the activation energy and, R_g is the ideal gas constant. We do not consider the change of activation energy with pressure, which leads to an increase of activation energy with depth (*Karato and Wu*, 1993), and we assume a constant viscosity for the layer. This can result in an underestimation of

the activation energy of the mantle. For example, the activation pressure at Mars' mantle varies between 300 KJ mol^{-1} close to the surface to 540 KJ mol^{-1} in the mid-mantle (*Nimmo and Stevenson*, 2000). We expect this variation to have a small effect in our first-order modelling.

The presence of melt weakens the mantle and results in a decrease of viscosity. For the sublayer of melt, we parameterize the decrease of viscosity with melt fraction ($\overline{\Phi}$) following *Moore* (2003) and *Henning et al.* (2009) and the change of shear modulus with melt fraction using the fit of *Fischer and Spohn* (1990) and *Shoji and Kurita* (2014) to laboratory experiments made by *Berckhemer et al.* (1982):

$$\eta = \eta_s \exp\left(\frac{E_a}{R_g \overline{T}_s}\left(\frac{\overline{T}_s}{\overline{T}} - 1\right)\right)\exp\left(-B\overline{\Phi}\right), \tag{6.6}$$

$$\mu = 10^{\frac{\mu_1}{\overline{T}-\overline{T}_s+1600}} - \mu_2. \tag{6.7}$$

The value of B can range from 10 to 40 for a strong or weak mantle, respectively (*Henning et al.*, 2009). We adopt an intermediate value $B = 25$ consistent with laboratory experiments (*Mei et al.*, 2002). For the layers without melt, we assume a constant shear modulus μ_0. μ_1 is an empirical constant, and μ_2 is adjusted so that the shear modulus is continuous at the solidus temperature.

The melt fraction increases with temperature until the disaggregation point is reached. When this occurs, the asthenosphere does not behave as a viscoelastic solid anymore, and it should be modeled as a magma ocean. We assume that this occurs when $\overline{\Phi} > 0.45$ (e.g., *Moore*, 2003). Although we do not model heat transport and tidal dissipation in this regime, we discuss this aspect further in Sections 6.2.2 and 6.2.3.

6.2.2. INTERNAL HEAT

We consider two mechanisms of internal heat generation: radiogenic heating and tidal dissipation. Radiogenic heating is computed assuming chondritic composition of the mantle (*Schubert et al.*, 1986) and that the age of the body is the same as the age of the Solar System.

Due to tidal interactions with the planet, regular moons evolve into a 1:1 spin orbit resonance (become tidally locked) soon after formation (e.g., *Peale*, 1999). If the orbit is eccentric or the moon has a nonzero obliquity, tidal forces result in periodic deformations of the moon. As the moon is not perfectly elastic, energy is dissipated in the interior. The total amount of tidal dissipation is (e.g., *Cassen et al.*, 1980; *Makarov and Efroimsky*, 2014; *Segatz et al.*, 1988)

$$\dot{E} = -\mathrm{Im}(k_2)\frac{(nR)^5}{G}\left(\frac{21}{2}e^2 + \frac{3}{2}\sin^2\theta\right) \tag{6.8}$$

where R is the radius of the body, n is the orbital frequency, G is the universal gravitational constant, and e and θ are the moons' eccentricity and obliquity, and $\mathrm{Im}(k_2)$ is the

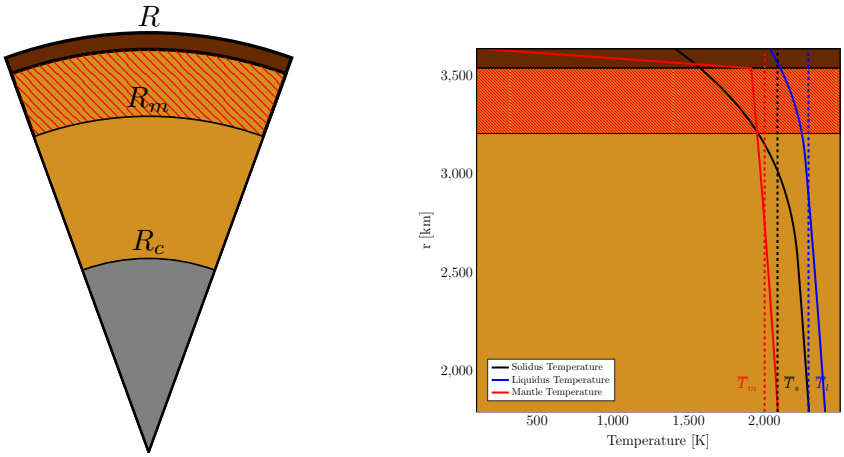

(a) (b)

Figure 6.1 Interior structure of the moons. (a) A metallic core is surrounded by a silicate layer. The silicate layer is further subdivided into a conductive and a convective layer. For high mantle temperatures, a sublayer of melt is formed beneath the lithosphere (red pattern). (b) Solidus and liquidus temperature profiles for a Mars-sized exomoon and a characteristic temperature profile. The average solidus, liquidus, and mantle temperatures are shown by dashed lines.

imaginary component of the k_2 Love number, which is related to the quality factor (Q) as $|\,\mathrm{Im}(k_2)\,| = |\,k_2\,|\,/Q$. We assume that the moon is in a Cassini state with small obliquity, as is the case for Io (*Baland et al.*, 2012), and neglect the contribution of obliquity to the thermal budget. We note that the previous equation is accurate to second order in eccentricity. For high orbital eccentricities, terms of order $O(e^4)$ should be added. High-order terms start to have a noticeable effect for $e > 0.1$ and orders-of-magnitude differences can arise for very high eccentricities ($e > 0.6$; *Renaud et al.*, 2021). Additionally, for $e > 0.1$ higher-order spin-orbit resonances might occur (*Makarov*, 2012; *Renaud et al.*, 2021; *Walterová and Běhounková*, 2020), which results in nonsynchronous rotation and increased tidal dissipation before the moon's orbit is circularized.

The value of $\mathrm{Im}(k_2)$ depends on the internal structure and rheology of the body and the tidal frequency. It can be computed using the viscoelastic theory for self-gravitating bodies (*Peltier*, 1974; *Sabadini et al.*, 2016; *Wu and Peltier*, 1982). By using the correspondence principle (*Peltier*, 1974), the equations of motion governing the deformation of each layer can be transformed to the Fourier domain and written as a set of differential equations of the form

$$\frac{d\tilde{\boldsymbol{Y}}}{dr} = A\tilde{\boldsymbol{Y}}. \tag{6.9}$$

$\tilde{\boldsymbol{Y}}$ is a vector containing the Fourier-transformed radial and tangential displacements ($\tilde{y}_1$,$\tilde{y}_2$), the radial and shear stress ($\tilde{y}_3$, $\tilde{y}_4$), the gravitational potential ($\tilde{y}_5$), and the so-called potential stress ($\tilde{y}_6$). A is a matrix given in Appendix 6.5. We use the matrix propagator method of *Sabadini et al.* (2016) and *Jara-Orué and Vermeersen* (2011) to solve Equation (6.9) under appropriate boundary conditions (Appendix 6.5).

To use the correspondence principle, a rheological law relating stress and strain is needed. Different rheological models have been developed for the study of tidally active bodies (e.g., *Renaud and Henning*, 2018); the viscoelastic behavior of the material depends on its shear modulus μ and viscosity η. The simplest and most commonly used is the Maxwell model. The response is characterized by the so-called Maxwell time (η/μ). When the tidal period is close to the Maxwell time, tidal dissipation is enhanced. For much shorter forcing periods, the body behaves as an elastic body, while for much longer forcing periods the body responds as viscous fluid. While the Maxwell model has been widely used for the study of tidally active bodies (e.g., *Fischer and Spohn*, 1990; *Henning et al.*, 2009; *Moore*, 2003; *Segatz et al.*, 1988), it does not properly capture the complex behavior of olivine observed in laboratory experiments (*Jackson and Faul*, 2010; *McCarthy and Castillo-Rogez*, 2013). In particular, the Maxwell model does not incorporate the anelastic transient creep deformation mechanism that describes the viscoelastic behavior of the material over time-scales shorter than the Maxwell time, which are relevant for tidal dissipation. The Andrade rheology model (*Andrade and Trouton*, 1910) has been particularly successful in capturing this behaviour and has been adopted in recent studies of tidally active bodies of the Solar System (e.g., *Bierson and Nimmo*, 2016; *Castillo-Rogez et al.*, 2011; *Gevorgyan et al.*, 2020) and other planetary systems (e.g., *Renaud and Henning*, 2018; *Walterová and Běhounková*, 2017). These studies have shown the dramatic influence that changing the rheology from Maxwell to Andrade can have on tidal dissipation models. We use the more realistic Andrade rheology as baseline for this study and briefly compare it with the classic Maxwell model to illustrate the differences between the two and the implications they have for the thermal-orbital evolution of a moon (Section 6.2.4 and Appendix 6.8).

The Fourier-transformed shear modulus can be defined in terms of the creep function $\tilde{J}$:

$$\tilde{\mu} = \tilde{J}^{-1}. \tag{6.10}$$

For the Andrade rheology, the Fourier transform of the creep function ($\tilde{J}$) is (*Efroimsky*, 2012b)

$$\tilde{J} = \frac{1}{\mu} - \frac{i}{\eta n} + \frac{\mu^{\alpha-1}}{(i\zeta\eta n)^{\alpha}}\alpha!. \tag{6.11}$$

The first two terms of Eq. (6.11) correspond to the elastic and steady-state creep response characteristic of the Maxwell model, and the last term accounts for the transient creep response included in the Andrade model. Here ζ and α are two empirical parameters that characterize the transient creep response. The value of α for olivine is constrained to vary from 0.1 to 0.5 (e.g, *Gribb and Cooper*, 1998; *Jackson et al.*, 2004). We use an in-

termediate value of 0.3. The value of ζ depends on the ratio between the anelastic and the Maxwell time-scales. It can have a dependence on forcing frequency, as the dominant anelastic deformation mechanism might change depending on the forcing period. However, accurate characterization of the deformation mechanisms in this regime is not available, and we make the assumption that diffusion dominates the anelastic response (e.g., *Renaud and Henning*, 2018; *Shoji and Kurita*, 2014; *Walterová and Běhounková*, 2020). In that case, both timescales are equal and $\zeta \approx 1$ (*Efroimsky*, 2012b). We caution that for high frequencies or high-stress situations, other deformation mechanisms, such as boundary sliding and dislocation unpinning, might become dominant, resulting in an underestimation of tidal dissipation.

The value of $\mathrm{Im}(k_2)$ depends on the core size, which can differ for different exomoons. However, its effect is small. We find that for an Io-sized exomoon dissipation can vary by a factor of two for a core-size range of 0.1–0.5 if a constant-viscosity mantle is assumed. If a low-viscosity asthenosphere is present, the core size has a smaller effect and changes the dissipation by less than 5%.

When the disaggregation point is reached, the viscoelastic theory for tides cannot be applied. Previous studies of tidal dissipation (e.g *Fischer and Spohn*, 1990; *Moore*, 2003; *Renaud and Henning*, 2018) assumed that when the disaggregation point is reached, viscosity is reduced to that of the liquidus, and dissipation drops dramatically. However, dynamic tides in magma oceans can produce dissipation rates equal to or higher than those observed on Io (*Tyler et al.*, 2015). Tidal dissipation in a magma ocean depends on weakly constrained parameters, such as the magma-ocean dissipation time-scale. Instead of explicitly modeling tidal dissipation in the magma ocean we assume that once the disaggregation point is attained, tidal dissipation remains constant.

6.2.3. HEAT TRANSPORT

The heat generated in the interior of the body via radiogenic heating and tidal dissipation is transported through the mantle of the moon to the surface and radiated to space. While most studies on tidally heated moons and planets consider heat transport via convection only (e.g., *Fischer and Spohn*, 1990; *Henning et al.*, 2009; *Hussmann and Spohn*, 2004; *Renaud and Henning*, 2018), heat transport via heat piping has been proposed to be the heat transport mechanism prevalent in Io (*Moore*, 2001, 2003; *O'Reilly and Davies*, 1981) and Earth's early history (*Moore and Webb*, 2013). Here, we consider both convection (Section 6.2.3) and heat piping (Section 6.2.3) as possible heat transfer mechanisms. We do not model heat transfer in the magma-ocean regime but briefly discuss it in Section 6.2.3.

MANTLE CONVECTION

Due to the strong dependence of viscosity on temperature, most terrestrial planets in the Solar System are in the stagnant-lid convection regime. The only notable exception is Earth, where plate tectonics provides a more efficient way to remove internal heat (*Korenaga*, 2013; *Schubert et al.*, 2001). To estimate the heat transport due to mantle convection, we assume that the exomoon is in the stagnant-lid regime. Tidal heating

might trigger plate tectonics (*Zanazzi and Triaud*, 2019). In such a case, the cold near-surface material is recycled, making heat transfer more between 20 and 100 times more efficient than heat transport in the stagnant-lid regime and resulting in lower mantle temperatures (*Nimmo and Stevenson*, 2000).

In the stagnant-lid regime, the body's interior is divided into a well-mixed adiabatic convective layer beneath a much stiffer conductive layer (*Morris and Canright*, 1984; *Reese et al.*, 1999; *Schubert et al.*, 1979; *Solomatov*, 1995). The conductive layer is subdivided into a thermal boundary layer, where viscosity decreases by around three orders of magnitude, and an immobile stagnant lid. We assume the conductive layer (thermal boundary layer+lid) to behave elastically (see Section 6.2.1). The amount of heat transported via convection in the mantle can be parameterized as

$$q = k\frac{\Delta T}{D_m}Nu, \tag{6.12}$$

where k is the thermal conductivity of the mantle, ΔT the temperature increase within the convective layer, D_m is the thickness of the convective layer, and Nu is the Nusselt number. In the stagnant-lid regime, the Nusselt number depends on the Rayleigh number (Ra) and the Frank-Kamenetskii parameter θ (e.g., *Reese et al.*, 1999; *Schubert et al.*, 2001):

$$Ra = \frac{g\alpha\rho D_m^3 \Delta T}{\kappa\eta(T_m)}, \tag{6.13}$$

$$\theta = \frac{\Delta T E_a}{R_g T_m^2}. \tag{6.14}$$

For Newtonian viscosity, scaling arguments lead to (*Reese et al.*, 1999; *Solomatov*, 1995)

$$Nu \approx a\theta^{-4/3}Ra^{1/3}, \tag{6.15}$$

with $a \approx 0.5$ being a nondimensional parameter (*Reese et al.*, 1999). Inserting Eqs. (6.14,6.15) into Eq. (6.12), the heat flux transported via convection can be obtained (*Nimmo and Stevenson*, 2000; *Shoji and Kurita*, 2014):

$$q_m \approx \frac{k}{2}\left(\frac{\rho g\alpha}{\kappa\eta}\right)^{1/3}\gamma_c^{-4/3}, \tag{6.16}$$

with

$$\gamma_c = \frac{E_a}{R_g T_m^2}. \tag{6.17}$$

For typical mantle conditions, γ_c is of order ≈ 0.01 (*Nimmo and Stevenson*, 2000). The thickness of the elastic lithosphere (D_l) is computed as

$$D_l = k\frac{T_m - T_{surf}}{q_m}, \tag{6.18}$$

where T_{surf} is the surface temperature. In the heat-pipe regime, the thickness of the lithosphere and its thermal structure differs from that of the stagnant-lid regime (*Kankanamge and Moore*, 2019; *Spencer et al.*, 2020); the effect on the total tidal dissipation is expected to be negligible.

HEAT PIPING

As the mantle temperature increases and melt starts to form (Section 6.2.1), heat piping becomes a more efficient heat transport mechanism than convection. Melt is segregated from the solid mantle and advected upward due to its positive buoyancy. An equilibrium can be reached in which the amount of melt advected upward is compensated for by the melt generated by tidal heating. *Moore* (2001) developed a model to study heat piping in Io that can be used to compute how much heat can be transported via heat piping inside a rocky body. We follow the approach of *Moore* (2001) and *Bierson and Nimmo* (2016) and compute heat transport via heat piping by solving mass conservation and using Darcy's law for porous media (see Appendix 6.6) in the sublayer of melt. The amount of heat transport via heat piping depends on two parameters: the permeability exponent n, and the scale velocity γ. γ depends on the grain size (b), the density contrast between melt and solid matrix ($\Delta\rho$), the surface gravity (g), the melt's viscosity (η_l), and a constant (τ) closely linked to the permeability exponent (*Moore*, 2001):

$$\gamma = \frac{b^2 \Delta\rho g}{\tau \eta_l}. \tag{6.19}$$

Heat transport efficiency increases with increasing γ and decreasing n. The value of n is typically taken to be between 2 and 3 (*Katz*, 2008). For Io, *Moore* (2001) estimated γ to range between 10^{-5} and 10^{-6}. We consider both a low- and a high-efficiency melt transport scenario with $n = 3$ and $\gamma/g = 10^{-6}/g_{Io}$ and $n = 2$ and $\gamma/g = 10^{-5}/g_{Io}$, respectively. By doing so, we are assuming that grain sizes, melt viscosity, and density contrasts are similar for the range of body sizes considered in this study.

CONVECTION IN A MAGMA OCEAN

When the disaggregation point is reached, the sublayer of melt behaves as a magma ocean. The viscosity of a magma ocean is very low (~ 0.1 Pas), rendering heat transport via convection very efficient (*Solomatov*, 2007). As for the tidal response, we do not model heat transport in this regime. We assume that heat transport in a magma ocean is sufficiently efficient to remove all of the internal heat.

6.2.4. THERMAL EQUILIBRIUM STATES

STABLE AND UNSTABLE EQUILIBRIUM STATES

The thermal state of an exomoon depends on the balance between heat generated in the interior of the body and removed through the lithosphere. The evolution of the mantle temperature can be modeled via a simple equation (e.g., *Fischer and Spohn*, 1990; *Shoji and Kurita*, 2014):

Parameter	Units	Formula/Value	Definition
R_g	$\mathrm{J\,mol^{-1}\,K}$	8.3144	Universal gas constant
R_{Io}	km	1821	Radius Io
ρ_m	$\mathrm{kg\,m^{-3}}$	3542	Mantle density
ρ_c	$\mathrm{kg\,m^{-3}}$	5150	Core density [1]
$\frac{R_c}{R}$	-	0.5206	Surface core radius ratio [1]
α	$\mathrm{K^{-1}}$	$2\cdot10^{-5}$	Thermal expansivity modulus[2]
k	$\mathrm{W\,m^{-1}K^{-1}}$	4	Thermal conductivity [2]
κ	$\mathrm{m^3s^{-1}}$	10^{-6}	Thermal diffusivity [3]
C_c	$\mathrm{J\,kg^{-1}K^{-1}}$	1142	Heat capacity
E_a	$\mathrm{kJ\,mol^{-1}}$	300	Activation energy[4]
η_s	Pa s	$1\cdot10^{16}$	Mantle solidus viscosity
μ_0	GPa	65	Mantle shear modulus[5]
μ_1	K	$8.2\cdot10^4$	Melt shear modulus coefficient 1[6]
μ_2	-	40.44	Melt Shear modulus coefficient 2
α	-	0.3	Andrade coefficient 1
ζ	-	1	Andrade coefficient 2
B	-	25	Melt fraction Coefficient
n	-	$2-3$	Permeability exponent [7]
γ	-	$\frac{b^2\Delta\rho g}{\tau\eta_l}$	Melt scale velocity
S_4	$\mathrm{W\,m^{-2}}$	50.26	Solar irradiation at Jupiter's orbit
A_{Io}	-	0.52	Io's bond albedo [8]

Table 6.1 Model parameters. (1) *Anderson et al.* (1996a); (2) *Sohl and Spohn* (1997); (3) *Hussmann and Spohn* (2004) ;(4) *Karato and Wu* (1993); (5) *Segatz et al.* (1988); (6) *Fischer and Spohn* (1990); (7) *Moore* (2003); (8) *Simonelli et al.* (2001)

$$V_m \rho C_c (1 + St) \frac{\mathrm{d}T}{\mathrm{d}t} = \dot{Q}_{int} - \dot{Q}_s. \tag{6.20}$$

V_m is the mantle's volume, St is the Stefan number, $\dot{Q}_s$ is the surface heat flow, and $\dot{Q}_{int}$ is the internal heat production, which includes radiogenic and tidal heating. The surface heat flow is the sum of the heat flow transported via convection and heat piping; coupling between the two mechanisms is neglected. We neglect other energy sources, such as primordial heat and heat due to the cooling and solidifying of the core. Neglecting the feedback between interior and orbital evolution for now, we can say that when the total heat production equals the total heat lost, an equilibrium state is reached. A thermal equilibrium state is stable if, for a deviation in mantle temperature, the system tends to restore its equilibrium: $\mathrm{d}\dot{Q}_s/\mathrm{d}T > d\dot{Q}_{int}/\mathrm{d}T$. If the amount of internally generated heat stays constant, the object can remain in this equilibrium state for a long period of time. The number of equilibrium points depends on the rheological model, as well as the prevalent heat transport mechanism (e.g., *Ojakangas and Stevenson*, 1986; *Renaud and Henning*, 2018). As mentioned before, we use the Andrade model as a baseline and compare it with the classic Maxwell model to underline the differences with previous studies of thermal-orbital evolution of rocky moons (e.g., *Fischer and Spohn*, 1990; *Hussmann and Spohn*, 2004; *Moore*, 2003).

Figure 6.2 illustrates the location and stability of equilibrium points for an Io-like exomoon for two different mantle rheology (Maxwell and Andrade) and heat transport (convection and heat piping) mechanisms. For the Maxwell model, tidal dissipation is negligible for low mantle temperatures; as the mantle temperature increases and approaches the melting temperature, tidal dissipation sharply increases. A further increase of mantle temperature leads to the formation of a sublayer of melt. Viscosity further decreases within this layer and thereby causes a further increase of tidal dissipation. Tidal dissipation peaks at T_{res} when the Maxwell time of the asthenosphere equals the forcing period. Finally, additional warming of the mantle induces a decrease of viscosity and shear modulus and detunes the astenosphere from the forcing period. For the Andrade rheology, a similar behavior is observed at high mantle temperatures, but for low mantle temperatures, the transient creep mechanism results in higher heat generation.

Equilibrium points for both models are also indicated in Figure 6.2. In both cases, there is a stable equilibrium point. Moreover, the Maxwell plus convection model has an additional unstable point at $T < T_{res}$. A change in the moon's orbital parameters that reduces the amount of tidal dissipation has very different consequences depending on whether the system is at a stable or an unstable point. In the first case, the moon evolves smoothly from one equilibrium point to the other; in the second, the moon enters a runaway cooling phase. As mentioned earlier, the previous analysis holds if the evolution of the orbit is not considered. When the feedback between interior properties and orbital dynamics is considered, a more complex picture arises. As we will show in Appendix 6.8, the differences in the location and stability of the equilibrium points discussed above for the two models have important consequences for the orbital evolution of a moon/exomoon.

In the following subsections, we adopt the more realistic Andrade model and apply it

first to Io and then to exomoons to obtain the range of orbital parameters for which hot states can be attained.

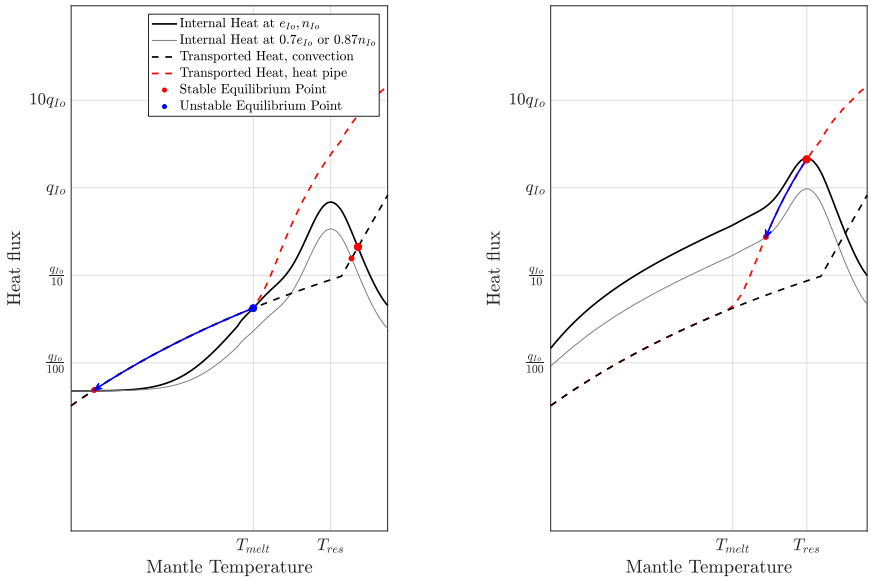

Figure 6.2 Tidal dissipation and transported heat as a function of mantle temperature for an Io-like exomoon. Panel (a) corresponds to a body with Maxwell rheology, while panel (b) corresponds to a body with Andrade rheology. Stable and unstable equilibrium points are indicated in red and blue, respectively. Tidal dissipation is displayed for Io's present eccentricity and orbital frequency; a decrease in eccentricity or orbital frequency changes the amount of tidal dissipation (gray line) and drives the system evolution, as indicated by the blue line.

THE CASE OF IO

Before applying our model to the more general case of an exomoon, we explore its implications for Io and assess whether it can successfully explain its thermal state.

Figure 6.3a shows Io's heat flux and tidal dissipation as a function of mantle temperature. Depending on melt fraction and the prevalent heat transport mechanism, we distinguish three regimes: the stagnant-lid regime, which corresponds to a mantle without a sublayer of melt; the heat-pipe regime, where melt advection dominates heat transfer; and the magma-ocean regime. Tidal dissipation is computed at Io's current orbital period and different eccentricities. When the eccentricity is low, radiogenic heat is the only significant heat source, and thermal equilibrium is reached for a low mantle temperature, $\approx$ 1200 K. As eccentricity increases, the equilibrium state moves to higher mantle

temperatures. For moderate eccentricities ($\sim e_{Io}/2$), the dislocation creep mechanism can lead to situations where $\mathrm{d}\dot{Q}_s/\mathrm{d}T \approx \mathrm{d}\dot{Q}_{int}/\mathrm{d}T$. In such cases, a quasi-equilibrium state can be attained in which temperature varies slowly and the thermal evolution of the system stagnates (*Renaud and Henning*, 2018). For higher eccentricities, new equilibrium configurations appear at higher mantle temperatures. The mantle temperature and stability of such points depend on the considered heat transfer mechanism (see Figure 6.3).

If we consider Io's current eccentricity, we find that heat transported via mantle convection in the stagnant-lid regime is insufficient to remove Io's present heat flux, as also found in *Moore* (2003). In contrast, the equilibrium points obtained for the heat-pipe regime are much closer to Io's observed heat flux. For the high-efficient heat transport scenario, we obtain that an equilibrium point is attained for a model with a 40 km thick asthenosphere with a melt fraction of 0.02. The equilibrium heat flux in this configuration is roughly half of Io's. In the low-efficiency heat-piping model, the equilibrium point is reached at roughly two times Io's observed heat flux for a model with a 330 km asthenosphere with a 0.2 melt fraction. The truth probably lies in-between, but the second scenario is more consistent with the interpretation of Galileo's magnetometer observations as evidence of a near-surface partially molten layer with a 0.2 melt fraction (*Khurana et al.*, 2011). However, this claim has recently been challenged (*Blöcker et al.*, 2018; *Roth et al.*, 2017). For this model, tidal dissipation is mainly focused in the asthenosphere (≈ 90%) and is higher in equatorial regions (Figure 6.4). Assuming that all of the molten rock travels to the surface through channels in the lithosphere, we can estimate the resurfacing rate, which is on the order of 1 $\mathrm{cm\,yr^{-1}}$. This rate is higher than the minimum 0.02 $\mathrm{cm\,yr^{-1}}$ required by the lack of impact craters and consistent with the $0.4-14$ $\mathrm{cm\,yr^{-1}}$ resurfacing rate estimated from surface changes observed during Galileo's mission (*Phillips*, 2000).

VOLCANIC EXOMOONS AND TIDALLY BOOSTED SURFACE TEMPERATURES

We apply the approach used to obtain thermal equilibrium states for Io to the more general case of exomoons of different sizes and orbital parameters. We are primarily interested in estimating the surface heat flux and surface temperature. The average surface temperature can be estimated by considering that the moon is a blackbody with surface temperature T_{surf}:

$$T_{surf}^4 = \frac{1}{\sigma}\left(\frac{(1-A)S}{4} + q_s\right), \tag{6.21}$$

where σ is the Stefan–Boltzmann constant, S is the stellar irradiation, and A the moon's bond albedo. As we are considering volcanic rocky worlds around cold exoplanets, we use Io's albedo A_{Io} and the solar flux at Jupiter's orbit S_4. Localized volcanic activity can result in spatial and temporal variations of surface temperature. Our estimations of surface temperature should be understood as the total thermal output of a rocky exomoon, keeping in mind that how and when this energy is released will depend on the thermal regime of the moon. Moreover, the outgassing of material and formation of a substantial

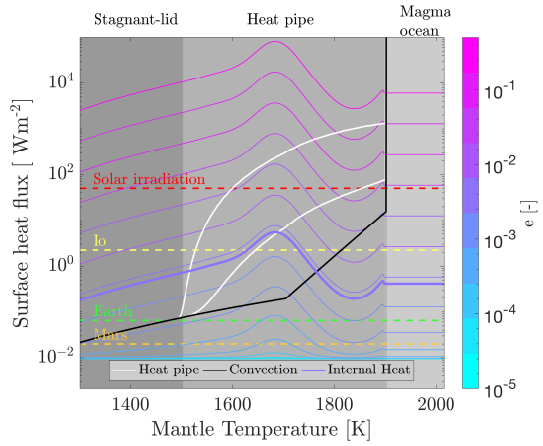

(a) R_{Io}

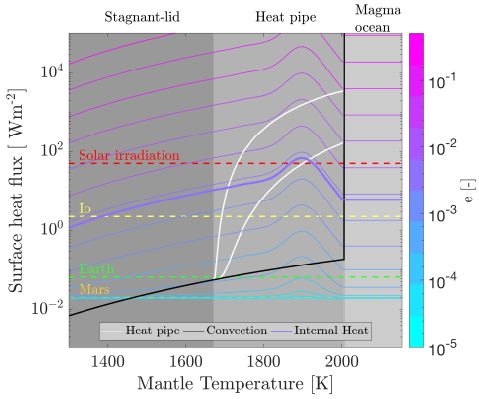

(b) $2R_{Io}$

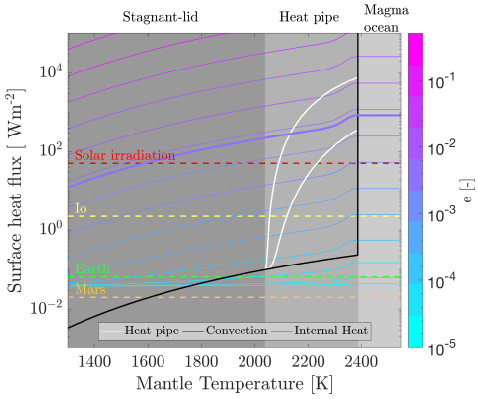

(c) $4R_{Io}$

Figure 6.3 Internal and transported heat in terms of surface heat flux as a function of the average mantle temperature for exomoons of different radii. The internal heat includes both radiogenic and tidal heating. Tidal heating is computed at Io's orbital frequency and shown for a range of orbital eccentricities. The thickest line corresponds to Io's present eccentricity. Three different heat transport regimes are indicated with different shadings; the stagnant-lid regime, the heat-pipe regime and the magma-ocean regime. Heat transported via convection (black line) and heat piping (blue lines) are indicated. For comparison, surface heat fluxes for Mars, Earth, and Io, as well as the solar irradiation at Jupiter's orbit, are also shown.

atmosphere would alter the heat balance of the moon and thus the surface temperature (e.g., *Noack et al.*, 2017).

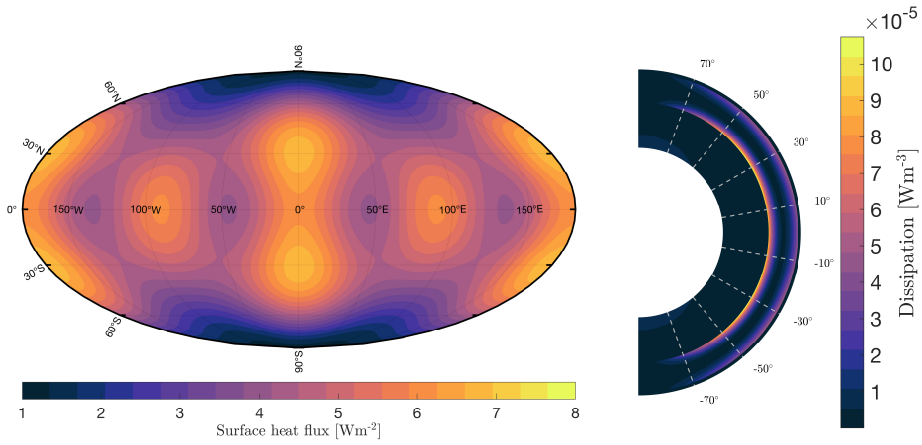

(c) (b)

Figure 6.4 Surface heat flux (a) and internal heat distribution along a meridional cut going through the subjovian point (b) for an Io in thermal equilibrium.

6

We can also estimate the amount of outgassed material ($\dot{M}_o$) and resulting column density. This quantity is closely related to the surface heat flux. A proxy for the outgassing rate can be obtained by considering Io's outgassing rate, $\dot{M}_{o,Io}$, and a tidal efficiency, η_T,

$$\eta_T = \left(\frac{R}{R_{Io}}\right)^2 \frac{q}{q_{Io}} \tag{6.22}$$

as $\dot{M}_o \sim \eta_T \dot{M}_{o,Io}$ (*Oza et al.*, 2019; *Quick et al.*, 2020). The previous expression gives an order-of-magnitude estimate; other factors such as the style of heat transport and volcanism and the mantle composition, are likely to affect the outgassing rate.

We start by considering exomoons of sizes $2R_{Io}$ and $4R_{Io}$ orbiting at Io's orbital frequency (Figure 6.3 (b) and (c)). Some differences with Io (Figure 6.3(a)) are apparent. For bigger exomoons, higher values of tidal dissipation are attained for the same orbital eccentricity. This should not come as a surprise, as tidal dissipation has a strong dependence on body size ($\dot{E} \propto R^5$). In contrast, the heat transported via mantle convection has a smaller dependence on body size (Eq. (6.12)). Heat transport via melt advection quickly becomes the dominant heat transport mechanism as orbital eccentricity increases.

If we consider Io's orbital eccentricity, we find surface heat fluxes more than 1 and 2 orders of magnitude higher than Io for Mars- and Earth-sized exomoon (i.e., $2R_{Io}$ and $4R_{Io}$), respectively. By using the previous proxies, we can infer that these exomoons would likely feature more volcanic activity than Io and produce a plasma torus with column densities $2-3$ orders of magnitude higher than those observed in the Jovian system for a $2R_{Io}$ and $4R_{Io}$ moon, respectively. Additionally, for $R = 4R_{Io}$, we observe that

thermal equilibrium is reached for a surface heat flux above solar irradiation. In such circumstances, the second term in Equation 6.21 becomes important, and tides have a signature in the surface temperature that increases to ~ 300 K.

Figure 6.5 shows the surface heat flux and surface temperature for different combinations of orbital eccentricity and orbital distance. The orbital distance is shown as a function of the Roche limit, $a/a_R = (2\pi\rho_m G)^{1/3}/(3n^2)^{1/3}$, which does not depend on the mass of the orbiting planet. The equilibrium states are obtained for the high-efficiency heat-piping transport scenario. If otherwise, the low-efficiency scenario is considered, similar results follow, but the magma-ocean regime is attained for lower eccentricities and orbital frequencies. As expected, surface heat flux and temperature increase with increasing eccentricity and decreasing orbital distance (Eq. (6.12)). For instance, Io would have a surface temperature of 400 K provided it orbited with its current eccentricity at $a/a_R \approx 2$ or at its current orbital distance with an eccentricity of ≈ 0.1. As body size increases, the subset of orbital parameters for which tides increase the moon's surface temperature grows.

From Figure 6.5, it is clear that, provided an exomoon has a high enough eccentricity and/or orbits close to the planet, super-Ios with intense volcanism and even tidally boosted surface temperatures arise. A question immediately follows: do we expect exomoons to orbit within these regions, and for how long?

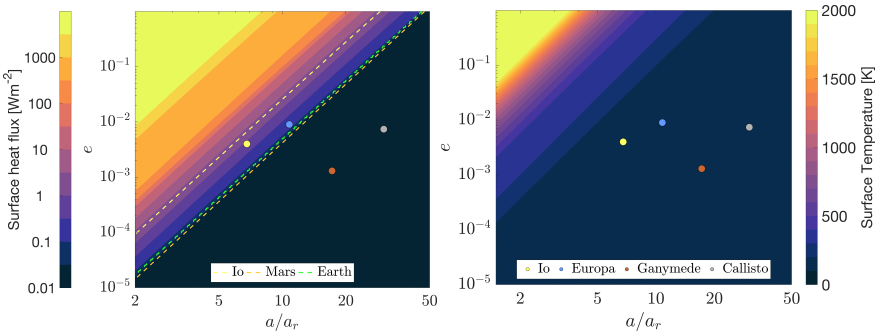

(a) R_{Io}

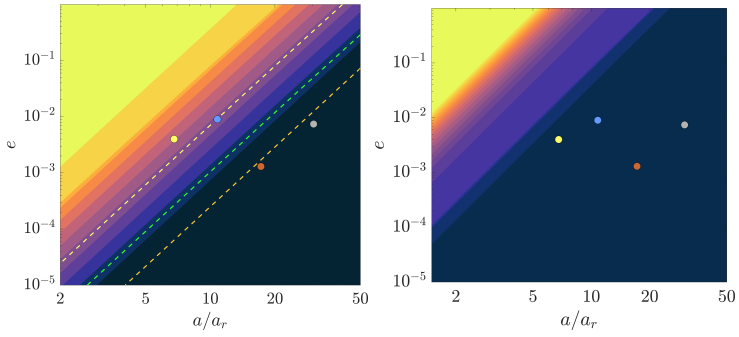

(b) $2R_{Io}$

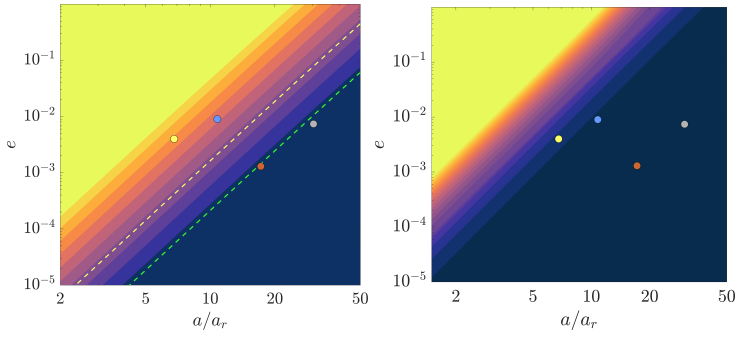

(c) $4R_{Io}$

Figure 6.5 Equilibrium surface heat flux and surface temperature for an Io-sized (a), Mars-sized (b), and Earth-sized (c) exomoon as a function of orbital eccentricity and distance. The orbital parameters of the Galilean moons and the surface heat flux of Io, Mars, and Earth are indicated. The amount of outgassed material compared to Io can be estimated using the heat flux with Eq. (6.22).

6.3. LONGEVITY OF A SUPER-IO

As we have shown in the previous section, for tidally active exomoons to be observable, vigorous tidal dissipation linked to a high orbital eccentricity and/or low orbital period is needed. However, it remains to be seen if these orbital states are attainable, let alone long-lived, so that they provide opportunities for observation. Instead of taking orbital period and eccentricity as constant parameters, as we did in the first part of the paper, in this section we explore the coupling between the interior thermal state of a moon and its orbital parameters. Clearly, we cannot tackle all possible orbital evolution scenarios; we pick two representative cases. We start by considering tidal interactions between a gas giant and an orbiting exomoon in an isolated moon-planet system. Afterwards, we consider how orbital resonances can excite the orbital eccentricity of an exomoon by focusing on the simplest orbital resonance: a 2 : 1 MMR.

6.3.1. ISOLATED MOON-PLANET SYSTEM

As we are considering cold gas giants that, in contrast to close-in exoplanets, are far from their star, we neglect the effect of stellar tides in both the planet and the moon. In an isolated moon-planet system, tidal dissipation within the moon removes energy from the moon orbit and circularizes it. Additionally, tidal dissipation within the planet produces a phase lag in the planets' response to the tide raised by the moon. As a consequence, the moon exerts a torque on the planet that changes the planet's spin rate, and the planet exerts a torque of the same magnitude to the moon that drives orbital migration. The direction of moon migration depends on whether the orbital period of the moon is higher or lower than the rotational period of the planet. We consider that the planet's rotation period is lower than the moon's orbital period. This is justified by the fast rotation rates of the Solar System gas giants and those measured for extrasolar gas giants (*Bryan et al.*, 2018; *Snellen et al.*, 2014). Under the previous assumptions, the change of orbital frequency (n), orbital eccentricity (e), and the planet's spin rate ($\dot{\theta}$) are given by (Appendix 6.7)

$$\frac{1}{n}\frac{\mathrm{d}n}{\mathrm{d}t} = \frac{1}{\tau_n} + \frac{p_e e^2}{\tau_e}, \tag{6.23a}$$

$$\frac{1}{e}\frac{\mathrm{d}e}{\mathrm{d}t} = -\frac{1}{\tau_e}, \tag{6.23b}$$

$$\frac{\mathrm{d}\dot{\theta}}{\mathrm{d}t} = -\frac{3}{2}\frac{GM_m^2 R_p^3}{\kappa M_p a^6}\frac{|\,k_{2,p}\,|}{Q_p}, \tag{6.23c}$$

with $p_e = 57/7$, and where τ_n and τ_e are the orbital migration and circularization timescales and are given by

$$\tau_n^{-1} = -\frac{9}{2}\frac{M_m}{M_p}\left(\frac{R_p}{a}\right)^5 |\,\mathrm{Im}(k_{2,p})\,|\, n = -\frac{9}{2}\frac{M_m}{M_p}\left(\frac{R_p}{a}\right)^5 \frac{|\,k_{2,p}\,|}{Q_p} n \tag{6.24a}$$

$$\tau_e^{-1} = \frac{21}{2}\left(\frac{R_m}{a}\right)^5 \frac{M_p}{M_m} \mid \mathrm{Im}(k_{2,m}) \mid n = \frac{21}{2}\left(\frac{R_m}{a}\right)^5 \frac{M_p}{M_m} \frac{\mid k_{2,m} \mid}{Q_m} n \tag{6.24b}$$

where m and p stand for moon and planet, respectively.

Tidal dissipation within the moon results in orbit circularization and inward orbital migration. The rate at which this occurs depends on the internal structure of the moon via the second-degree Love number $\mathrm{Im}(k_{2,m})$. On the other hand, under the aforementioned assumptions, tidal dissipation within the planet results in outward orbital expansion and despinning of the planet. Combining Eqs. (6.23a) and (6.23c), the change in planet spin rate produced as the moon migrates can be obtained. Unless the moon is very massive and formed very close to the planet, the effects of the moon on the planet's rotation are small. A Mars-like exomoon around Jupiter would slow down Jupiter less than 1% as it migrates from $2a_R$ to $20a_R$. In what follows, we assume $\mathrm{d}\dot{\theta}/\mathrm{d}t \approx 0$, the planet is treated as an infinite source of energy that drives orbit migration. The migration rate depends on how energy is dissipated within the planet, as given by the imaginary component of the planet's second-degree Love number, $\mathrm{Im}(k_{2,p})$. In classical tidal theory, it is considered to be independent of the forcing frequency; we make this assumption and consider a range of frequency independent $\mathrm{Im}(k_{2,p})$. However, new observations indicate a strong dependence of $\mathrm{Im}(k_{2,p})$ on forcing frequency (*Lainey et al.*, 2017, 2020), which has been linked with the excitation of internal waves in the planet's gaseous envelope (e.g., *Ogilvie and Lin*, 2004). The $\mathrm{Im}(k_{2,p})$ spectrum depends on weakly constrained parameters such as the structure and composition of the planet, which in turn can undergo significant changes as the planet evolves. Implicitly, our model assumes that the exomoon does not excite any of the resonant modes in the planet's dissipation spectrum. The incorporation of such effects would require the analysis of a broad range of properties of the giant planet's dissipation spectrum, as no robust bottom-up model of this spectrum can be set up for poorly constrained exoplanet interiors.

Figure 6.6 shows the circularization time-scales as a function of orbital distance for a hot exomoon with a $\mathrm{Im}(k_{2,m})$ similar to that of Io (*Lainey et al.*, 2009). Here, τ_e strongly depends on orbital distance ($\tau_e \propto (a/a_R)^{13/2}$); if the moon is far from the planet ($a/a_R \gtrapprox 20$), the circularization time-scale is more than 1 Gyr. At such orbital distances, tidal dissipation is quite low. However, a highly eccentric ($e > 0.1$) Earth-like exomoon would still experience high levels of tidal dissipation that could even increase the surface temperature to around 500 K (Figure 6.5). Can we imagine a plausible scenario where this could occur? A possible candidate is the capture of a terrestrial-sized planet by a gas giant via the binary-exchange capture process (*Williams*, 2013). The capture process results in highly eccentric orbits compatible with high values of tidal dissipation.

For close-in exomoons, the eccentricities required for high tidal activity are lower (Figure 6.5). However, the circularization time-scales are much shorter, less than a million years for a moon orbiting closer to the planet than Io (Figure 6.5). A sporadic boost in eccentricity could result in high values of tidal dissipation and boost the surface temperature, but such a boost would inevitably be short-lived, lowering the chances of detection. For these moons to exhibit vigorous geological activity for a longer time period, it is necessary that the eccentricity is continuously forced. This can occur via MMRs.

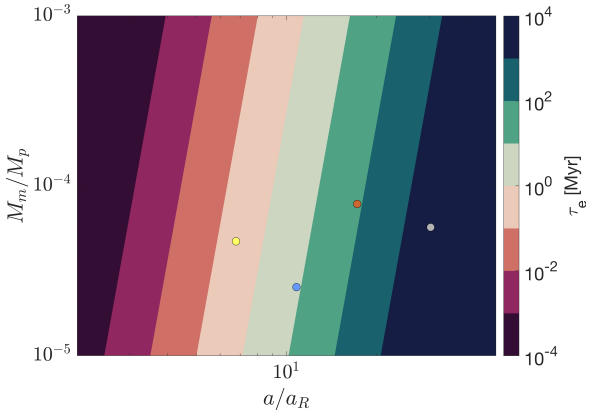

Figure 6.6 The τ_e as a function of orbital distance and moon-to-planet mass ratio for a body with an $|\,\mathrm{Im}(k_{2,m})\,| = 10^{-2}$, similar to Io's present value. The Galilean moons are indicated.

6.3.2. 2:1 MEAN-MOTION RESONANCE

MMRs occur when two moons consistently apply a periodic gravitational perturbation to each other. This happens when the orbital frequencies of the two objects (n_1, n_2) are related via (e.g., *Murray and Dermott*, 2000): $(p+q)n_2 - pn_1 - q\dot{\omega}_1 \approx 0$, where ω_1 is the argument of the pericenter and p and q are two integers. The periodic gravitational forcing alters the orbit of both objects and excites the eccentricity of the moons. As already mentioned, we cannot explore all possible orbital resonances. Thus, we focus on the $2:1$ orbital resonance ($p=1, q=1$).

In a 2:1 orbital resonance, the resonant variable $\nu = n_1 - 2n_2$ is close to zero. Using the perturbing potential up to first order in eccentricity, the equations governing the orbital evolution of the two moons can be obtained (*Yoder and Peale*, 1981):

$$\dot{n}_1 = \frac{n_1}{\tau_{n1}} + \frac{e_1^2 n_1}{\tau_{e1}}\left((3+p_e) + 3\frac{\tau_{e1}}{\tau_{e2}}\frac{M_1}{M_2}\left(\frac{C_2}{C_1}\right)^2 \alpha^{1/2}\right) + 3\frac{M_2}{M_p}\alpha\left(\frac{n_1}{\nu}\right)^2 \dot{\nu}\,(C_1 e_1 - C_2 e_2)\,, \tag{6.25a}$$

$$\begin{aligned}(1+K(e_1,e_2))\,\dot{\nu} = n_1\Bigg[&\frac{1}{\tau_{n1}}\left(1-\frac{\tau_{n1}}{\tau_{n2}}\right) + \frac{e_1^2}{\tau_{e1}}\Bigg((3+p_e) + 12\frac{M_1}{M_2}\alpha^2 \\ &+ \frac{\tau_{e1}}{\tau_{e2}}\left(\frac{M_1}{M_2}\right)^2\left(\frac{C_2}{C_1}\right)^2\left(2(6-p_e)\alpha^{5/2} + 3\frac{M_2}{M_1}\alpha^{1/2}\right)\Bigg)\Bigg],\end{aligned} \tag{6.25b}$$

$$e_1 = -\frac{M_2}{M_p}\frac{n_1}{\nu}\alpha C_1, \quad e_2 = \frac{M_1}{M_p}\frac{n_1}{\nu}\alpha^{3/2} C_2. \tag{6.25c}$$

Here C_1 and C_2 are two constants with values of -1.19 and 0.428, respectively; α is the ratio between the inner and outer moon semi-major axes, which, close to the 2:1 resonance, equals 0.63; and $K(e_1, e_2)$ is a positive number,

$$K(e_1,e_2) = -6\frac{M_p}{M_2}\frac{1}{C_1}\left[\alpha^{1/2} + \left(\frac{C_2}{C_1}\right)^2 \frac{M_1}{M_2}\alpha\right] e_1^3 + 12\frac{M_p}{M_1}\frac{1}{C_2}\left[1 + \left(\frac{C_1}{C_2}\right)^2 \frac{M_2}{M_1}\alpha^{-1/2}\right] e_2^3, \quad (6.26)$$

which is small provided the eccentricities are also small.

Different orbital migration timesscales ($\tau_{n1} \neq \tau_{n2}$) can lead to the convergence of a pair of moons and the assembly of an MMR resonance (Eq. (6.25b), Figure 6.7). This can occur either in the protoplanetary disk via differential orbital decay (Figure 6.7(a)); or, once the protoplanetary disk has dissipated, via differential tidal expansion of the orbit (Figure 6.7(b) and (c)). In the second case, τ_n and τ_e are given by Equation (6.24). In the first case, the orbital evolution is driven by the interactions of the protoplanetary disk with the recently formed moons (*Canup and Ward*, 2002; *Peale and Lee*, 2002). The satellites excite density waves in the protoplanetary disk that cause a torque on the moons and result in inward migration. The protoplanetary disk also dampens the satellite eccentricity. Equation (6.23) can still be used to model the effects of moon protoplanetary disk interactions in the orbital evolution, provided we use $p_e = 3$ and define τ_n and τ_e as (*Goldreich and Schlichting*, 2014):

$$\frac{1}{\tau_n} \sim \left(\frac{M_m}{M_p}\right)\left(\frac{M_d}{M_p}\right)\left(\frac{a}{h}\right)^2 n, \quad (6.27a)$$

$$\frac{1}{\tau_e} \sim \left(\frac{M_m}{M_p}\right)\left(\frac{M_d}{M_p}\right)\left(\frac{a}{h}\right)^4 n, \quad (6.27b)$$

where h/a is the aspect ratio of the disk, and M_d is the disk mass.

As the moons move deeper into the orbital resonance, the orbital eccentricity increases (Eq. (6.25c)). Depending on the ratio of the migration time-scales of the two moons (τ_{n1}/τ_{n2}), two scenarios are possible: the moons (1) cross the orbital resonance or (2) get trapped in it. The first scenario results in a boost of orbital eccentricity that is later circularized in a time-scale τ_e (Figure 6.7(a)). In the second scenario (Figure 6.7(b) and (c)) an equilibrium eccentricity is reached that can persist for a long time.

For MMR assembled via tidal expansion of the orbit once the protoplanetary disk is dissipated, the first scenario can occur provided the outer moon migrates faster than the inner moon. Given the strong dependence of τ_n with orbital distance (Eq. (6.24b)), this requires that $|\,\mathrm{Im}\{(k_{2,p}(n_2))\}\,| > |\,\mathrm{Im}\{(k_{2,p}(n_1))\}\,|$, which can occur under the resonance-locking scenario (e.g., *Fuller et al.*, 2016; *Lainey et al.*, 2020). The boost in orbital eccentricity due to the crossing of the 2 : 1 MMR can be estimated as (*Dermott et al.*, 1988)

$$e_1 = \left(\frac{2\sqrt{6}\frac{M_2}{M_p}\alpha\,|\,C_1\,|}{1+4\frac{M_1}{M_2}\alpha^2}\right)^{1/3} \quad (6.28)$$

We note that similar expressions can be obtained for different values of p and q; thus, Eq. (6.28) gives an order-of-magnitude estimation of the orbital eccentricity boost for other MMRs. Using the previous equation, we can obtain the boost in orbital eccentricity for different values of M_1/M_2 and M_1/M_p. As shown in Figure 6.8, the boost of

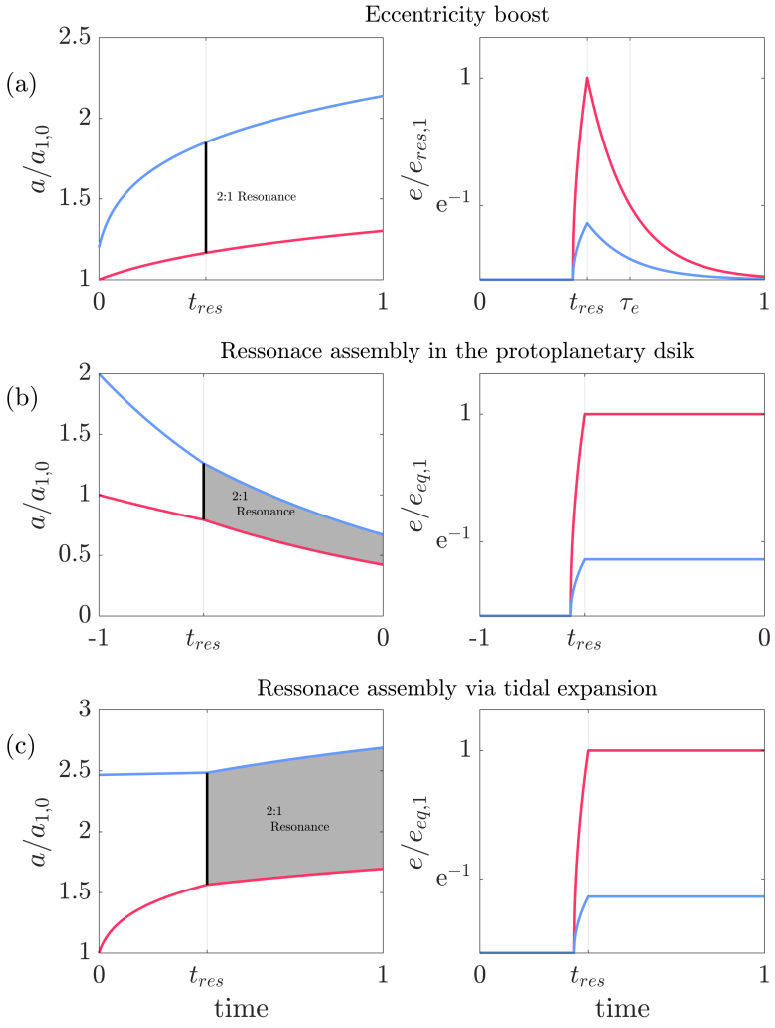

Figure 6.7 Semi-major axis and orbital eccentricity of two moons in a 2 : 1 MMR for different scenarios. In the first scenario, panel (a), $\tau_{n1} > \tau_{n2}$ and the moons go through the resonance but do not get trapped, while in the second scenario, panels (b) and (c), the moons can remain in resonance for a long time. For panel (b) the resonance is assembled in the protoplanetary disk, while in (c) via tidal expansion once the protoplanetary disk dissipates. Note that once the protoplanetary disk dissipates, the system can relax to the equilibrium eccentricity of panel (c) or the orbit is circularized in a time-scale τ_e as shown in panel (a).

orbital eccentricity due to the crossing of a resonance can be close to 0.1. For example, for $M_1/M_2 = 1$ and $M_1/M_p = 10^{-4}$, $e \approx 0.05$. Such an increase in orbital eccentricity could result in vigorous and tidally boosted surface temperatures if resonance crossing occurs when the moon is close to the planet. As an example, a Mars-sized exomoon orbiting between Io and Europa's orbit would experience surface temperatures up to 400 K (Figure 6.5), but the eccentricity would be dampened in less than 10 Myr (Figure 6.6).

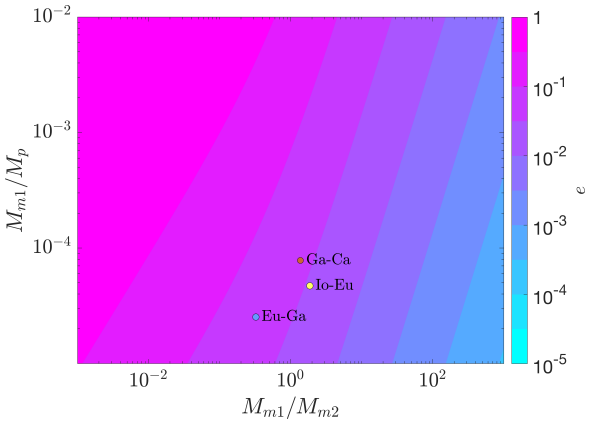

Figure 6.8 Boost in orbital eccentricity due to the crossing of a 2:1 MMR for different ratios of M_1/M_p and M_1/M_2. The locations of the Galilean moons are indicated.

As mentioned before, in the second scenario, the two moons remain caught in an orbital resonance for a long period of time. As the moons move deeper into the orbital resonance, the orbital eccentricity increases (Eq. (6.25c)). The increase of orbital eccentricity results in a phase lag between both moons, which prompts a transfer of angular momentum from one moon to the other. As we will see, under certain conditions, this transfer of angular momentum ensures that both moons migrate at the same rate ($\dot{\nu} = 0$), and an equilibrium eccentricity is reached. The value of the equilibrium eccentricity can be computed as (Eq. (6.29))

$$e_1^2 = -\frac{\tau_{e1}}{\tau_{n1}}\left(1-\frac{\tau_{n1}}{\tau_{n2}}\right)\left((3+p_e)+12\frac{M_1}{M_2}\alpha^2+ \frac{\tau_{e1}}{\tau_{e2}}\left(\frac{M_1}{M_2}\right)^2\left(\frac{C_2}{C_1}\right)^2\left(2(6-p_e)\alpha^{5/2}+3\frac{M_2}{M_1}\alpha^{-1/2}\right)\right)^{-1}. \tag{6.29}$$

The value of the equilibrium eccentricity is proportional to $\sqrt{\tau_e/\tau_n}$, while the prefactor multiplying this ratio differs depending on p and q. The proportionality of the equilibrium eccentricity to $\sqrt{\tau_e/\tau_n}$ remains for different values of p and q (*Dermott et al.*, 1988, Equation 39).

For the assembly of a 2 : 1 MMR in the protoplanetary disk, the existence of such equilibrium eccentricity requires that $M_2 > 2M_1$. The value of the equilibrium eccentricity is $e \sim h/a$. For a disk aspect ratio of the order of ~ 0.1 (*Canup and Ward*, 2002; *Peale and Lee*, 2002), orbital eccentricities of ~ 0.1 can be attained (Figure 6.9). Once the protoplanetary disk dissipates, the eccentricity is dampened on a timescale τ_e or the system relaxes to the equilibrium configuration of the tidally driven scenario.

In case orbital migration is driven by tidal forces, the existence of an equilibrium eccentricity requires that the inner moon migrates faster than the outer moon, $\tau_{n1} < \tau_{n2}$, which, for a frequency-independent $\mathrm{Im}(k_{2,p})$, implies $M_2 < 20M_1$. The forced eccentricity is (Equations (6.29) and (6.24))

$$e^2 \sim \left(\frac{M_m}{M_p}\right)^2 \left(\frac{R_p}{R_m}\right)^5 \frac{\mathrm{Im}(k_{2,p})}{\mathrm{Im}(k_{2,m})}. \tag{6.30}$$

Figure 6.9a shows the forced eccentricity for an Io-like moon in a 2:1 orbital resonance with a second moon. We consider that tidal dissipation is negligible in the outer moon and use $\mathrm{Im}(k_{2,p})$ and $\mathrm{Im}(k_{2,m})$ compatible with those estimated for Jupiter and Io (*Lainey et al.*, 2009). For the planet radius, we use the empirical mass-radius relation of *Bashi, Dolev et al.* (2017). If the inner-to-outer moon mass ratio is too low, the outer moon migrates too fast, and the moons do not get caught in the MMR. On the other hand, if the ratio is high, the forced eccentricity of the inner moon is small. For a mass ratio equal to that of Io and Europa, we obtain a forced eccentricity of approximately half of Io's present eccentricity. This discrepancy is because Io is part of a more complex resonance chain, the Laplace resonance, which can excite higher eccentricities (*Yoder and Peale*, 1981). However, by considering the simple 2 : 1 MMR, we obtain an order of magnitude estimation of the forced eccentricity that can be attained if the moon is part of a more complex resonance chain.

We further consider the case where both moons have equal mass and obtain the forced eccentricity for different moon and planet masses and different values of $\mathrm{Im}(k_{2,p})$ using Eq. 6.29 (Figure 6.9(b)). Moderate-to-high orbital eccentricities ($10^{-3} - 10^{-1}$) that result in high surface heat fluxes are attained, provided that (1) the moon-to planet mass ratio is high and/or (2) the planet is highly dissipative. Configurations with $M_m/M_p > 10^{-4}$ should be regarded with caution, as satellite formation models for giant planets predict $M_m/M_p \sim 10^{-4}$ (*Canup and Ward*, 2006; *Heller and Pudritz*, 2015a,b). This makes Mars-sized exomoons plausible around super-Jovian ($1 - 12M_{♃}$) planets, but the ratio for Earth-sized is only attained well inside the brown dwarf regime , $M_p > 12M_{♃}$ (e.g., *Boss et al.*, 2005).

The value of $\mathrm{Im}(k_{2,p})$ is uncertain and a matter of intense research. Equilibrium tidal theory suggests $|\mathrm{Im}(k_{2,p})| \sim 10^{-13}$ (*Goldreich and Nicholson*, 1977); however, astrometric observations of the Jovian and Saturnian systems indicate that $|\mathrm{Im}(k_{2,♃})| \sim 10^{-5}$ and as high as $|\mathrm{Im}(k_{2,♄})| \sim 10^{-3}$ (*Lainey et al.*, 2009, 2020). High values of $|\mathrm{Im}(k_{2,p})|$ lead to high-equilibrium eccentricity. However, high $|\mathrm{Im}(k_{2,p})|$ implies fast orbital migration (Equation (6.24)). As the moon migrates outwards, tidal dissipation rapidly decreases (Equation (6.8)) limiting the longevity of a super-Io.

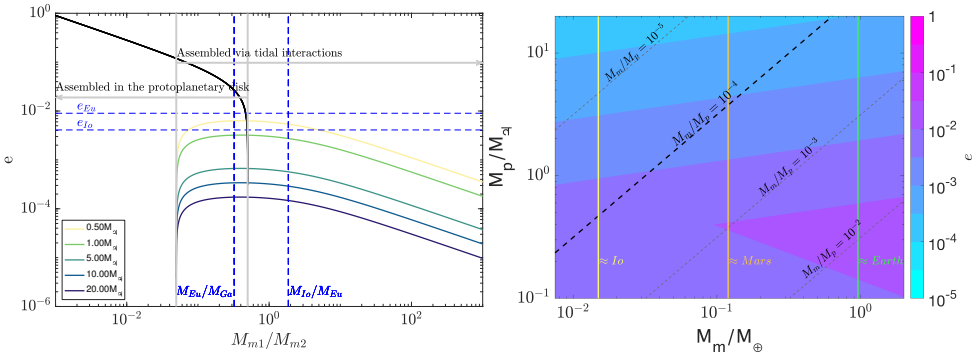

(a) (b)

Figure 6.9 (a) Equilibrium eccentricity of the inner moon in a 2:1 orbital resonance as a function of the ratio of inner and outer moon mass (x-axis). Both resonance assembly in the protoplanetary disk (black line) and via tidal interactions with planets of different sizes are shown. An Io-sized moon with $|\,\mathrm{Im}(k_{2,m})\,|$ compatible with Io and a planet with $|\,\mathrm{Im}(k_{2,p})\,|$ similar to Jupiter are assumed (10^{-2} and 10^{-5}). Tidal dissipation in the outer moon is neglected. For the case in which both moons have the same mass, panel (b) shows the orbital eccentricity for different combinations of planet and moon mass assuming Io- and Jupiter-like values for $\mathrm{Im}(k_{2,m})$ and $\mathrm{Im}(k_{2,p})$. For a different $\mathrm{Im}(k_{2,p})$, the equilibrium eccentricity can be recovered by multiplying the value given in the plot by $\sqrt{|\,\mathrm{Im}(k_{2,p})\,|\,/10^{-5}}$. Different ratios of M_m/M_p are indicated, with $M_m/M_p = 10^{-4}$ consistent with moon formation theory indicated in bold. The vertical lines correspond to the three sizes of bodies considered in this study.

This becomes evident if we study the coupled thermal-orbital evolution of a close-in exomoon. As the formation of a pair of Earth-sized exomoons seems unlikely from moon formation theory, and high values of tidal dissipation are more easily attained for Mars-sized than Io-sized exomoons, we focus on the case of a pair of close-in ($a = 2a_R$) Mars-sized exomoons orbiting a super-Jovian planet ($5M_\oplus$). As shown before, the orbital and thermal evolution of the moon are coupled via the imaginary component of the second-degree Love number ($\mathrm{Im}(k_{2,m})$), which in turn depends on the interior structure. We compute tidal dissipation and heat transfer as explained in Section 6.2.1. The orbital evolution is computed using Equation (6.25) and the thermal evolution using (6.20). The system is integrated forward in time using a two-step Euler method with an adaptive step size. We assume $|\,\mathrm{Im}(k_{2,p})\,|$ is frequency-independent, and we vary its value from 10^{-3} to 10^{-6} and study the thermal-orbital evolution of the exomoons. In all cases, we assume that the moons start deep into the resonance with an eccentricity of 0.01.

The evolution of the exomoons for different values of $|\,\mathrm{Im}(k_{2,p})\,|$ is depicted in Figure 6.10. At the start of the simulation, the high eccentricity combined with the close proximity of the exomoon to the planet results in high tidal dissipation and tidally boosted

surface temperatures. At this time, the moon is in the magma-ocean regime. The moon's eccentricity changes until the equilibrium eccentricity is reached. The value of the equilibrium eccentricity depends on the value of $|\,\mathrm{Im}(k_{2,p})\,|$, with higher values leading to higher values of orbital eccentricity. Meanwhile, the moon migrates at a rate dependent on $\mathrm{Im}(k_{2,p})$, tidal dissipation decreases, and the moon cools down enough to enter the heat-pipe regime. Upon cooling, the value of $\mathrm{Im}(k_{2,m})$ changes and, in a range of 1–10 Myr, a new equilibrium orbital eccentricity is attained.

The close proximity of the moon to the planet combined with high orbital eccentricity results in high surface heat fluxes, as well as tidally boosted surface temperatures. For instance, for $|\,\mathrm{Im}(k_{2,p})\,| = 10^{-4}$, surface heat fluxes of more than 1000 $\mathrm{W\,m^{-2}}$ are attained. Surface temperatures are higher than 400 K for the first 10 Myr. This phase is, however, short-lived due to the fast orbital migration of the moon. Tidal dissipation quickly decreases, the melt fraction in the asthenosphere diminishes, and the moon shifts from the magma-ocean regime to the heat-pipe regime. After 100 Myr surface temperatures are down to 200 K and, after 500 Myr, the contribution of tides to surface temperature is negligible. As the semi-major axis increases, the migration time-scale (τ_n; Equation (6.24)) decreases, but the eccentricity remains nearly constant. A surface heat flux 10–100 times higher than Io is maintained during the first billion years and then decreases to values similar to Io while the moon stays in the heat-pipe regime.

If the planet is less dissipative, the equilibrium eccentricity is lower, but the orbital migration time-scale is reduced. These two factors partly compensate each other; while the eccentricity attained for $|\,\mathrm{Im}(k_{2,p})\,| = 10^{-5,-6}$ is lower than that for $|\,\mathrm{Im}(k_{2,p})\,| = 10^{-3,-4}$, the moon stays closer to the planet during a longer time. As in the more dissipative cases, high surface temperatures are attained during the first million years, but the contribution of tides to surface temperature is negligible after 500 Myr. The surface heat flux stays above that of Io for more than 2 billion years, giving ample time for the outgassing of material and the formation of a secondary atmosphere and plasma torus.

While we observe small-amplitude fast oscillations of the eccentricity at the beginning of our simulation, our models do not feature the pronounced periodic oscillations characteristic of the models of *Hussmann and Spohn* (2004) and *Fischer and Spohn* (1990) for Io. As we show in Appendix 6.8, this is a consequence of the very efficient transfer mechanism included in our model (heat piping) and the use of Andrade rheology, which implies that Io could be in thermal equilibrium instead of in an oscillatory state, as proposed in *Fischer and Spohn* (1990).

6.4. CONCLUSIONS

We started this paper with a clear question — what are the prospects of detecting a super-Io?— and we addressed two important sides of it: where and in which thermal state we can expect to find super-Ios and for how long we expect a super-Io to be tidally active.

To do so, we presented a thermal model of an exomoon. Based on our current knowledge of Io, we considered a multilayered model that allows for the formation of a sublayer of melt in which heat can be transported via melt advection. Our model confirms the

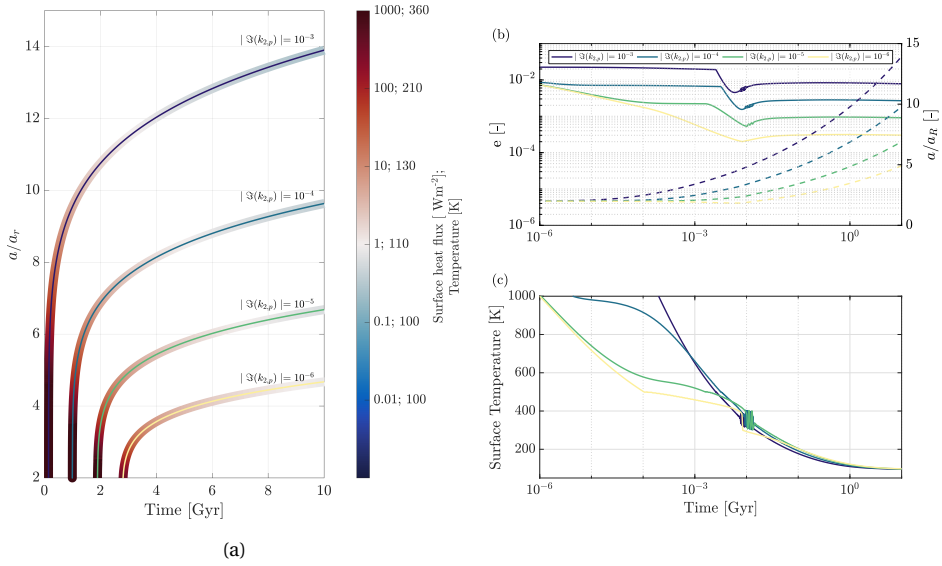

Figure 6.10 Thermal-orbital evolution of a Mars-sized exomoon orbiting around a $5M_{\oplus}$ planet in a 2:1 orbital resonance with an exomoon of the same size. Panel (a) shows the semi-major axis in terms of the Roche limit (y-axis) as a function of time (x-axis). The trajectories are colored according to surface heat flux and surface temperature. Panel (b) shows the detail of the evolution of the eccentricity (solid lines) and semi-major axis (dashed lines), (c) shows the surface temperature using a logarithm time-scale.

findings of *Moore* (2001, 2003) and *Moore and Webb* (2013) that this mechanism plays a crucial role in the heat budget of a tidally heated (exo)moon. We applied our model to Io and found that it can successfully explain its thermal state and is consistent with Galileo's observation hinting at a partially melted asthenosphere (*Khurana et al.*, 2011).

In order to simplify our model, we made some assumptions. As it is commonly done (e.g., *Fischer and Spohn*, 1990; *Henning et al.*, 2009; *Hussmann and Spohn*, 2004; *Renaud and Henning*, 2018; *Shoji and Kurita*, 2014), we used the viscoelastic tidal theory to model tidal dissipation. However, when tidal dissipation is very high, the melt fraction increases and can reach high values. The body is then better described either as a highly porous material consisting of a matrix of rock filled with magma or, for higher melt fractions, a magma ocean with rocky particles in suspension. Our treatment of tidal dissipation and heat transport in the high-melt fraction regime was highly simplified. In such circumstances, the classical theory of viscoelastic tides does not adequately describe the behavior of the body. Advances have been made in understanding the role of porosity (*Liao et al.*, 2020) and tides in a liquid reservoir (e.g., *Hay et al.*, 2020; *Matsuyama et al.*, 2018; *Rovira-Navarro et al.*, 2019; *Tyler et al.*, 2015) for tidal dissipation, yet our knowledge remains limited. Further study of these regimes will be key to understanding Io and

ultimately super-Ios. Additionally, we considered that material properties only vary radially and not laterally. While this assumption allows to get a first-order understanding of Io and super-Ios, unveiling their complex dynamics might require taking into account the complex feedback between tidal dissipation, internal properties, and resulting heterogeneities (*Steinke et al.*, 2020b). In the case of Io, the availability of high-resolution observations justifies this kind of modelling, but we are still very far from this point for exomoons.

We applied our model to exomoons ranging from Io to Earth-sized and found that exomoons orbiting within a few Roche radii of their planet experience high levels of tidal dissipation if they have moderate eccentricities (similar to Io). Thermal equilibrium states with surface heat fluxes higher than those of Io are obtained for a wide range of orbital parameters. For some of theses cases, tidal dissipation is very high, and the thermal budget of the moon is dominated by tidal dissipation, resulting in a high surface temperature that could make direct imaging by future telescopes possible (*Peters and Turner*, 2013).

While our analysis of thermal equilibrium states as a function of orbital parameters showed that super-Ios can result for different orbital configurations, one key question remained: do we expect a population of exomoons to fill this space, and for how long? This question should be tackled from a moon formation and evolution point of view. We addressed the second aspect by considering the coupling between interior structure and orbit evolution of a close-in exomoon.

We showed that an Earth-sized exomoon orbiting far away from the planet ($a/a_R > 20$) with a high eccentricity can remain tidally active for billions of years and speculated that this might happen if such an exomoon is captured via a mechanism known as the binary-exchange capture process (*Williams*, 2013). However, under these circumstances, our assumption of the moon being tidally locked and having a small obliquity could break. Moreover, higher-order eccentricity terms will be become relevant for the orbital evolution of the moon (*Renaud et al.*, 2021). The more general problem of capture and tides for a nonsynchronous rotating moon should be addressed. This opens the door to higher-order spin-orbit resonances, such as a Mercury-type 3 : 2 resonance (e.g., *Dobrovolskis*, 2007; *Makarov*, 2012; *Walterová and Běhounková*, 2020), as well as obliquity tides that can be investigated in future work.

For moons closer to theri planet, circularization time-scales are on the order of million of years, which implies that long-lived super-Ios require active forcing of the eccentricity, for example, via MMRs (e.g., *Peale*, 1976). We considered a super-Io in a 2 : 1 orbital resonance and found a trade-off between high orbital eccentricity and fast orbital migration. We obtained that in order for the forced eccentricity to be high enough for surface temperatures to be dominated by tidal heating, the orbited exoplanet should be highly dissipative (i.e., have a low quality factor). Low quality factors are not compatible with the equilibrium tide theory of *Goldreich and Nicholson* (1977), but are in agreement with the low values measured for Jupiter and Saturn (*Lainey et al.*, 2009, 2020). However, we showed that highly dissipative planets lead to fast orbital migration which limits the amount of time the moon spends near the planet, where tidal dissipation is high. We studied in more detail the case of a Mars-sized exomoon orbiting a super-Jovian planet.

We found that tidal dissipation decreases below solar irradiation ≈ 500 million years after the establishing of the MMR, limiting the window for direct imaging. However, the moon can remain tidally active for billion of years with heat fluxes exceeding those of Io. This implies that a plasma torus denser than that of Jupiter can be expected in the system, which provides an opportunity for detection in transmission spectra (*Johnson and Huggins*, 2006; *Oza et al.*, 2019). Finding a tidally heated exomoon via transit spectroscopy or direct imaging would provide an important constraint on the planet's interior structure due to the relation between the moon's eccentricity and dissipation within the planet.

6.5. APPENDIX A: PROPAGATOR MATRIX TECHNIQUE

A detailed description of the propagator matrix technique for the viscous gravitation problem can be found in *Sabadini et al.* (2016). Here, we give a brief summary of the method. For each layer (i) (1 for the uppermost layer and N for the core), Eq. (6.9) needs to be solved. Matrix A is given by

$$A = \begin{pmatrix} -\frac{2}{r} & \frac{l(l+1)}{r} & 0 & 0 & 0 & 0 \\ -\frac{1}{r} & \frac{1}{r} & 0 & \frac{1}{\tilde{\mu}} & 0 & 0 \\ \frac{4}{r}\left(\frac{3\tilde{\mu}}{r}-\rho g\right) & -\frac{l(l+1)}{r}\left(\frac{6\tilde{\mu}}{r}-\rho g\right) & 0 & \frac{l(l+1)}{r} & -\frac{\rho(l+1)}{r} & \rho \\ -\frac{1}{r}\left(\frac{6\tilde{\mu}}{r}-\rho g\right) & \frac{2(2l^2+2l-1)\tilde{\mu}}{r^2} & -\frac{1}{r} & -\frac{3}{r} & \frac{\rho}{r} & 0 \\ -4\pi G\rho & 0 & 0 & 0 & -\frac{l+1}{r} & 1 \\ -\frac{4\pi G\rho(l+1)}{r} & \frac{4\pi G\rho l(l+1)}{r} & 0 & 0 & 0 & \frac{l-1}{r} \end{pmatrix}. \tag{6.31}$$

l is the spherical degree harmonic, which equals 2 for tidal forcing.

The solution to the previous set of differential equations can be written as

$$\tilde{\boldsymbol{y}}_{\boldsymbol{i}}(r,\omega) = \tilde{Y}_i(r,\omega)\boldsymbol{C}_{\boldsymbol{i}}, \tag{6.32}$$

where ω is the forcing frequency, and Y the so-called fundamental matrix which equals:

$$\tilde{Y}_i(r,\omega) = \begin{pmatrix} \frac{lr^{l+1}}{2(2l+3)} & r^{l-1} & 0 \\ \frac{(l+3)r^{l+1}}{2(2l+3)(l+1)} & \frac{r^{l-1}}{l} & 0 \\ \frac{(l\rho gr+2(l^2-l-3)\tilde{\mu})r^l}{2(2l+3)} & (\rho gr+2(l-1)\tilde{\mu})r^{l-2} & -\rho r^l \\ \frac{l(l+2)\tilde{\mu}r^l}{(2l+3)(l+1)} & \frac{2(l-1)\tilde{\mu}r^{l-2}}{l} & 0 \\ 0 & 0 & -r^l \\ \frac{2\pi G\rho l r^{l+1}}{2l+3} & 4\pi G\rho r^{l-1} & -(2l+1)r^{l-1} \\ \frac{(l+1)r^{-l}}{2(2l-1)} & r^{-l-2} & 0 \\ \frac{(2-l)r^{-l}}{2l(2l-1)} & -\frac{r^{-l-2}}{l+1} & 0 \\ \frac{(l+1)\rho gr-2(l^2+3l-1)\tilde{\mu}}{2(l-1)r^{l+1}} & \frac{\rho gr-2(l+2)\tilde{\mu}}{r^{l+3}} & -\frac{\rho}{r^{l+1}} \\ \frac{(l^2-1)\tilde{\mu}}{(2l-1)r^{l+1}} & \frac{2(l+2)\tilde{\mu}}{l(l+1)r^{l+3}} & 0 \\ 0 & 0 & -\frac{1}{r^{l+1}} \\ \frac{2\pi G\rho(l+1)}{(2l-1)r^l} & \frac{4\pi G\rho}{r^{l+2}} & 0 \end{pmatrix} \tag{6.33}$$

and $\boldsymbol{C_i}$ is a vector of integration constants.

The solution at the surface of the moon ($\tilde{\boldsymbol{y}}(R)$) can be computed by propagating the solution from the core-mantle boundary (R_c) to the surface (R) by imposing continuity at the layers' boundaries:

$$\tilde{\boldsymbol{y}}(\boldsymbol{R},\boldsymbol{\omega}) = \left(\prod_{i=1}^{N-1} \tilde{Y}_i(r_i,\omega)\tilde{Y}_i^{-1}(r_{i+1},\omega)\right) I_c \boldsymbol{C_c}. \tag{6.34}$$

I_c is a matrix that follows from the boundary conditions at the core-mantle boundary and is given by

$$I_c = \begin{pmatrix} -\frac{3R_c^{l-1}}{4\pi G\rho_c} & 0 & 1 \\ 0 & 1 & 0 \\ 0 & 0 & \frac{4}{3}\pi G\rho_c^2 R_c \\ 0 & 0 & 0 \\ R_c^l & 0 & 0 \\ 2(l-1)R_c^{l-1} & 0 & 4\pi G\rho_c \end{pmatrix} \tag{6.35}$$

and $\boldsymbol{C_c}$ is a vector of three integration constants that we obtain by applying the surface boundary conditions:

$$\tilde{y}_3(R,\omega) = 0, \tag{6.36}$$

$$\tilde{y}_4(R,\omega) = 0, \tag{6.37}$$

$$\tilde{y}_6(R,\omega) = \frac{2l+1}{R}. \tag{6.38}$$

The second-degree tidal Love number is

$$k_2 = \tilde{y}_5(R,\omega) - 1 \tag{6.39}$$

6.6. APPENDIX B: HEAT PIPING

The advection of melt in a partially molten asthenosphere can be described using conservation of mass and Darcy's law for porous media (*Moore*, 2001):

$$\nabla \cdot (\Phi v_l) = s, \tag{6.40}$$

$$\nabla \cdot ((1-\Phi) v_s) = -s, \tag{6.41}$$

$$\Phi(v_l - v_s) = \frac{k_\Phi \Delta\rho g}{\eta_l}. \tag{6.42}$$

v_s and v_l are, respectively, the ascend velocities of the solid and liquid phases; Φ is the melt fraction; and k_Φ is the permeability, which depends on the geometry of the porous matrix

$$k_\Phi = \frac{b^2 \Phi^n}{\tau}, \tag{6.43}$$

b is the grain size, n and τ two constants related with the geometry of the matrix, and s is the melt production rate and is related with the volumetric heat rate q_{vol} as

$$s = \frac{q_{vol}}{\rho L}. \tag{6.44}$$

Although heat is not uniformly distributed within the asthenosphere, we assume q_{vol} to be constant within the layer. v_s can be eliminated from Equuation (6.42) to obtain two equations for v_l and Φ:

$$\frac{\mathrm{d}v_l}{\mathrm{d}r} = \frac{q_{vol}}{\Phi\rho L} - v_l\left(\frac{2}{r} + \frac{1}{\Phi}\frac{\mathrm{d}\Phi}{\mathrm{d}r}\right) \tag{6.45}$$

$$\frac{\mathrm{d}\Phi}{\mathrm{d}r}\left[v_l + \gamma\big((n-(n+1)\Phi)\Phi^n\right] = \frac{q_{vol}}{\rho L} - 2(1-\Phi)\Phi\frac{v_l}{r}. \tag{6.46}$$

For different values of volumetric heat (q_{vol}), we integrate the previous set of equations from the bottom of the asthenosphere to the top. The average melt fraction $\overline{\Phi}$ is then computed and a curve relating the average melt fraction ($\overline{\Phi}$) and q_{vol} is obtained.

6.7. APPENDIX C: TIDAL EFFECTS ON ORBIT EVOLUTION

The effects of planet and moon tides on the evolution of a moon-planet system have been widely studied (e.g., *Boué and Efroimsky*, 2019; *Kaula*, 1964). Here we follow

Efroimsky and Williams (2009) and *Boué and Efroimsky* (2019) to obtain the tidal effects on the orbit of a synchronously rotating satellite with low inclination orbiting around a planet spinning at angular rate $\dot{\theta}$. The evolution of the satellite's orbital frequency and eccentricity are given by *Boué and Efroimsky* (2019), Equations (143) and (156), and the change of the planet's spin rate due to moon is given by *Efroimsky and Williams* (2009) Equation (34):

$$\frac{1}{n}\frac{\mathrm{d}n}{\mathrm{d}t} = \frac{9}{2}\mathscr{C}n\left[K_{2,p}(2n-2\dot{\theta}) + \left(-5K_{2,p}(2n-2\dot{\theta}) + \frac{3}{4}K_{2,p}(n) + \frac{1}{8}K_{2,p}(n-2\dot{\theta}) + \frac{147}{8}K_{2,p}(3n-2\dot{\theta}) + 19\mathscr{D}K_{2,m}(n)\right)e^2\right] + O(e^4) + O(i^2) \tag{6.47a}$$

$$\frac{1}{e}\frac{\mathrm{d}e}{\mathrm{d}t} = -n\mathscr{C}\left[-\frac{3}{4}K_{2,p}(2n-2\dot{\theta}) - \frac{3}{16}K_{2,p}(n-2\dot{\theta}) + \frac{147}{16}K_{2,p}(3n-2\dot{\theta}) + \frac{9}{8}K_{2,p}(n) + \frac{21}{2}\mathscr{D}K_{2,m}(n)\right] + O(e^2) + O(i^2) \tag{6.47b}$$

$$\frac{\mathrm{d}\dot{\theta}}{\mathrm{d}t} = \frac{3}{2}\frac{GM_m^2R_p^5}{I_pa^6}\left[(1-5e^2)K_{2,p}(2n-2\dot{\theta}) + \frac{e^2}{4}K_{2,p}(n-2\dot{\theta}) + \frac{49e^2}{4}K_{2,p}(3n-2\dot{\theta})\right] + O(e^4) + O(i^2) \tag{6.47c}$$

m and p stand for moon and planet, respectively. I_p is the planet's moment of inertia ($I = \kappa M_pR_p^2$, with $\kappa = 2/5$ for a homogeneous planet); and $\mathscr{C}$ and $\mathscr{D}$ are two constants that depend on the physical properties of the planet and moon,

$$\mathscr{C} = \frac{M_m}{M_p}\left(\frac{R_p}{a}\right)^5, \tag{6.48a}$$

$$\mathscr{D} = \left(\frac{M_p}{M_m}\right)^2\left(\frac{R_m}{R_p}\right)^5. \tag{6.48b}$$

K_2 are second degree quality functions at frequency ω which are given by:

$$K_2(\omega) = -\mathrm{sign}(\omega)\,\mathrm{Im}[k_2(|\,\omega\,|)] = \mathrm{sign}(\omega)\frac{|\,k_2\,|}{Q} \tag{6.49}$$

where k_2 is the second-degree Love number, and Q is the quality factor. By looking at Equations (6.47a)-(6.47c), it is evident that the leading term is due to semidiurnal tides raised in the planet by the satellite. Moreover, $\mathscr{D} > 1$ and, in general, $|\,K_p\,|$ is several orders of magnitude lower than $|\,K_m\,|$. In such circumstances, and assuming that the spin rate of the planet ($\dot{\theta}$) is higher than the orbital frequency of the moon (n), Eq. (6.47) can be written as:

$$\frac{1}{n}\frac{\mathrm{d}n}{\mathrm{d}t} = \frac{1}{\tau_n} + \frac{p_e e^2}{\tau_e} \tag{6.50a}$$

$$\frac{1}{e}\frac{\mathrm{d}e}{\mathrm{d}t} = -\frac{1}{\tau_e} \tag{6.50b}$$

$$\frac{\mathrm{d}\dot{\theta}}{\mathrm{d}t} = -\frac{3}{2}\frac{GM_m^2 R_p^3}{\kappa M_p a^6}\frac{|\,k_{2,p}\,|}{Q_p} \tag{6.50c}$$

with $p_e = 57/7$. τ_e and τ_n are the damping time-scale for the eccentricity and orbital frequency,

$$\tau_n^{-1} = -\frac{9}{2}\frac{M_m}{M_p}\left(\frac{R_p}{a}\right)^5 |\,\mathrm{Im}(k_{2,p})\,|\, n = -\frac{9}{2}\frac{M_m}{M_p}\left(\frac{R_p}{a}\right)^5 \frac{|\,k_{2,p}\,|}{Q_p} n \tag{6.51a}$$

$$\tau_e^{-1} = \frac{21}{2}\left(\frac{R_m}{a}\right)^5 \frac{M_p}{M_m} |\,\mathrm{Im}(k_{2,m})\,|\, n = \frac{21}{2}\left(\frac{R_m}{a}\right)^5 \frac{M_p}{M_m}\frac{|\,k_{2,m}\,|}{Q_m} n \tag{6.51b}$$

with the moon and planet Love numbers evaluated at n and $2\dot{\theta} - 2n$, respectively. We note that the previous assumption can break in the resonance-locking scenario, where $K_{2,p}(2n - 2\dot{\theta})$ might be similar in magnitude to $K_{2,m}(n)$. Finally, it is important to note that higher-order can become important for high orbital eccentricities ($e > 0.1$; *Renaud et al.*, 2021).

Comparing Eq. (6.50) with the equations used in previous studies (e.g., *Fischer and Spohn*, 1990; *Malhotra*, 1991; *Shoji and Kurita*, 2014; *Yoder*, 1979), we note that those studies use $p_e = 3$ instead of the value obtained above. This discrepancy arises from the incorrect assumption in some past publications that eccentricity damping occurs at constant angular momentum.

6.8. APPENDIX D: IMPLICATIONS OF ANDRADE RHEOLOGY AND HEAT PIPING FOR THE THERMAL-ORBITAL EVOLUTION OF ROCKY MOONS

The thermal-orbital evolution scenarios presented in Section 6.3 are markedly different from those obtained by *Fischer and Spohn* (1990) and *Hussmann and Spohn* (2004) for Io. In *Fischer and Spohn* (1990) and *Hussmann and Spohn* (2004), the thermal-orbital evolution is characterized by a nearly equilibrium phase followed by an oscillatory phase of alternating cold and warm phases and finally a runaway cooling of the body. In contrast, in our model the body evolves following a series of near-equilibrium thermal-orbital states. The difference is due to the use of Andrade rheology instead of Maxwell rheology, as well as from the introduction of a more efficient heat transport mechanism: heat piping. Here, we briefly explore how these two factors affect the thermal-orbital evolution of a rocky exomoon.

The difference can be explained in terms of the location and stability of thermal equilibrium points. To illustrate this point, we consider the thermal-orbital evolution of an Io-sized moon using the two different models presented in Section 6.2.4: (a) Maxwell rheology and heat transport via mantle convection, and (b) Andrade rheology and heat transport via heat piping. In both cases, we consider that the moon starts its evolution at

$a/a_R = 2$ with an initial orbital eccentricity of 10^{-3} in an orbital resonance with a moon of the same size. Due to the close proximity of the moon to the planet, tidal dissipation is high, and a stable equilibrium point with $T > T_{res}$ is reached in both cases. As the moon migrates outward and tidal dissipation decreases, the equilibrium mantle temperature decreases accordingly until the point $T = T_{res}$. This point is unstable for model (a) but stable for model (b). For model (a), further orbital migration starts a runaway cooling phase. As the moon cools downs, $\mathrm{Im}(k_{2,m})$ sharply decreases, which leads to an increase of the orbital eccentricity (Equation (6.29)) and thus tidal dissipation, causing the body to heat up again (Figure 6.11). This process is repeated several times resulting in thermal-orbital oscillations. In contrast, when Andrade rheology and heat piping are included, the equilibrium point is stable, and the moon can evolve following thermal equilibrium states and no oscillatory phase occurs.

This result can also be interpreted in the context of the linear stability analysis presented in *Ojakangas and Stevenson* (1986). *Ojakangas and Stevenson* (1986) showed that the stability and subsequent orbit evolution depend on the exponents of the power dependence of tidal dissipation and heat transport with mantle temperature ($n = \mathrm{d}\ln \dot{Q}_{int}/\mathrm{d}T$ and $m = \mathrm{d}\ln \dot{Q}_s/\mathrm{d}T$). The Andrade rheology and heat piping reduce n and increase m, which brings the system to the stable regime.

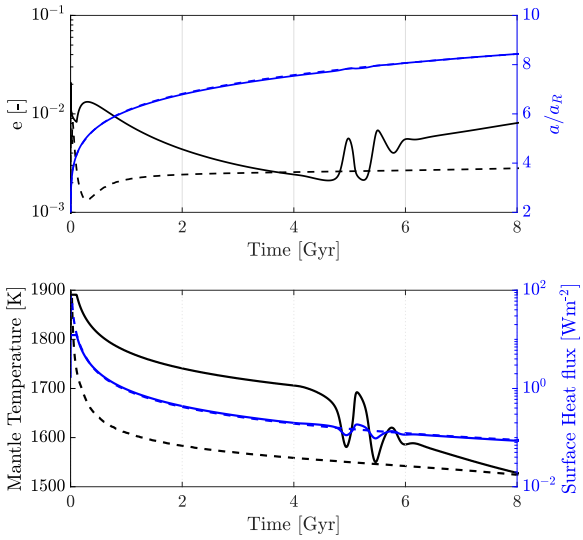

Figure 6.11 Thermal-orbital evolution of an Io-sized exomoon in a 2:1 orbital resonance around a Jovian planet. The solid line corresponds to a model with Maxwell rheology and heat transport dominated by convection, and the dashed line corresponds to Andrade rheology and heat transport dominated by heat piping. In both cases, $|\,\mathrm{Im}(k_{2,p})\,| = 10^{-5}$ is assumed.

7

CONCLUSION AND OUTLOOK

Eliminate all other factors, and the one which remains must be the truth.

—Sir Arthur Ignatius Conan Doyle, *The Sign of the Four*

In chapters 3, 4, 5 and 6, we addressed the research questions introduced in Chapter 1 and discussed in Chapter 2. Here, we gather the answers to those questions, discuss what their broader implications are for our understanding of tidally active moons and identify new research directions towards which the knowledge gained steers us. The chapter is split in four sections. First, we discuss the advances made in the understanding of tides in subsurface oceans (Section 7.1), tides in moons with porous layers (Section 7.2), and summarise our findings regarding tidally active exomoons (Section 7.3). For each of these sections, we recapitulate the research questions, summarise the conclusions obtained in the thesis and then indicate avenues for future research. Finally, in Section 7.4, we widen our outlook and explore how future observations and space missions can contribute to the topics explored in this thesis.

7.1. TIDES IN SUBSURFACE OCEANS

7.1.1. RESEARCH QUESTIONS AND MAIN FINDINGS

The discovery of volcanoes on Io and subsurface oceans in Europa prompted a profound interest in tides in the moons of the outer Solar System. In the post-Voyager era, efforts focused on the study of solid tides (e.g., *Cassen et al.*, 1980; *Ojakangas and Stevenson*, 1989; *Ross and Schubert*, 1987; *Segatz et al.*, 1988) and their link to interior structure and surface features; the role of ocean tides was generally overlooked. *Sagan and Dermott* (1982) speculated about the role that tides in Titan's hydrocarbon lakes might play in

the moon's orbital evolution, but the topic received little attention until *Tyler* (2008) proposed that dynamic ocean tides power the geological activity of icy moons.

Subsequent efforts extended the work of *Tyler* (2008) and applied it to different bodies of the Solar System. Nevertheless, at the core of nearly all these studies two assumptions remained: (1) oceans were assumed to be of constant thickness, and (2) the study of ocean tides relied on the shallow water approximation. In Chapters 3 and 4 we challenged these two assumptions. Below we summarize our main findings and their implications.

THE TIDAL RESPONSE OF OCEANS OF VARYING THICKNESS

To put our results into context, it is instructive to briefly recapitulate the main characteristics of the tidal response of global oceans of constant thickness (for more details see Chapter 3). *Longuet-Higgins* (1968) studied the response of global oceans using the Laplace tidal equations and identified two main types of waves: gravity waves, where gravity is the restoring force; and planetary Rossby waves, where the Coriolis force is the restoring force. He also showed that the eigenmodes and eigenfrequencies of a global ocean depend on the body's radius and the ocean's thickness. If an ocean is forced at one of its eigenfrequencies strong tidal currents are excited, leading to substantial energy dissipation.

Almost half a century later, *Tyler* (2014, 2008, 2009, 2020, 2021) and *Tyler et al.* (2015) applied the approach of *Longuet-Higgins* (1968) to study tides in the water oceans of icy moons and Io's magma ocean. They showed that the high surface wave velocity characteristic of moons with deep subsurface oceans hinders the occurrence of surface gravity wave resonances, which would only occur for much thinner oceans, but that high amplitude Rossby-Haurwitz waves can be excited by the obliquity component of the tidal potential if the obliquity of the moon is large. With the exception of Titan, the obliquity of the moons of the outer Solar System have not been measured. Nevertheless, dissipation is expected to quickly dampen the free obliquity of a moon and bring it to a Cassini state. *Chen and Nimmo* (2011) and *Chen et al.* (2014) used this to compute the obliquity of the moons of the outer Solar System and showed that while obliquity tides could be relevant in moons with substantial obliquity (e.g., Triton), they were unlikely to play a major role in moons with low obliquity (e.g., Enceladus). Since the work of *Tyler* (2008) several improvements have been made in theory of ocean tides in subsurface oceans (e.g., *Beuthe*, 2016; *Hay and Matsuyama*, 2017; *Matsuyama*, 2014; *Matsuyama et al.*, 2018; *Tyler*, 2020), however, the assumption of a global ocean of uniform thickness remained unchallenged.

On Earth, the global ocean scenario is clearly unrealistic. As the tidal wave propagates, it encounters the continents and enters into the shallow seas giving rise to a complex global response. Gravity, rotation and topography data suggest that the oceans of icy moons are global, yet they are not necessarily of uniform thickness. The details of the ice and sea-bed topography are far from certain for most moons, but for Enceladus gravity and topography data evidences long-wavelength ocean thickness variations (*Beuthe et al.*, 2016; *Čadek et al.*, 2016; *Hemingway and Mittal*, 2019) that could play a similar role as that played by continents on Earth. In Chapter 3, we used the Laplace tidal equations to study the response of an Enceladan ocean of variable thickness to the eccentricity and

obliquity tide and tackled the following research question:

1. How does the tidal response of a subsurface ocean of variable thickness differ from that of a constant thickness ocean?

To resolve this question, we studied ocean tides in subsurface oceans of variable thickness representative of Enceladus (*Beuthe et al.*, 2016; *Čadek et al.*, 2016; *Hemingway and Mittal*, 2019): oceans with degree two thickness variations (thinner at the equator and thicker at the poles) and oceans with degree three thickness variations (corresponding to a thicker ocean in the South Polar Terrain as compared to the Northern Hemisphere). As done in previous work, we used the shallow water approximation and considered the Laplace tidal equations, which we solved using the finite element method.

We found that the tidal response of oceans with degree two thickness variations to the eccentricity and obliquity tides is characterized by the same eigenmodes as those characteristic of oceans of constant thickness. Nevertheless, the eigenfrequencies of the modes are different. Therefore, the average ocean thicknesses for which the ocean resonates with the tidal forcing is not the same as that of an ocean of constant thickness. For the eccentricity tide, resonances occur for oceans that have an equatorial ocean thickness similar to that for which the same resonance occurs in a constant thickness ocean. As in the constant thickness ocean counterpart, these resonances occur for thin oceans, < 1 km, and are thus not expected to play a dominant role in Enceladus' > 20 km thick ocean.

For both constant thickness oceans and oceans with degree-two topography, modes excited by the symmetric eccentricity tide are symmetric with respect to the equator while modes excited by the asymmetric obliquity tide are asymmetric. Degree three ocean thickness variations introduce an asymmetry to the problem and make the excitation of asymmetric and symmetric modes by the eccentricity and obliquity tides, respectively, possible. We showed that asymmetric ocean thickness variations can give rise to asymmetric tidal dissipation patterns. Nevertheless the heating patterns we obtained do not agree with the observation of enhanced activity in Enceladus' Southern regions as compared to its Northern regions.

The response of the ocean to the obliquity tide is also influenced by ocean thickness variations. We showed that ocean thickness variations inhibit the excitation of Rossby-Haurwitz planetary waves, which have been credited with powering Europa (*Tyler*, 2008), Enceladus (*Tyler*, 2009) and Triton (*Chen and Nimmo*, 2011; *Nimmo and Spencer*, 2015). Our findings regarding the obliquity tide are particularly relevant for Triton. The high obliquity of this moon makes it susceptible to strong obliquity-forced Rossby-Haurwitz waves (*Chen et al.*, 2014). *Nimmo and Spencer* (2015) showed that obliquity ocean tides can produce heat flux up to 18 $\mathrm{mW\,m^{-2}}$, sufficient to prevent a subsurface ocean from freezing and strong enough to drive convection and yielding in Triton's ice shell compatible with surface observations. As we have seen, ocean thickness variation detunes the ocean from the Rossby-Haurwitz waves' natural frequency. In order for Triton to be powered by obliquity ocean tides, its ocean should be global and fairly uniform in thickness.

OCEAN TIDES BEYOND THE LAPLACE TIDAL EQUATIONS

The assumptions beneath the Laplace tidal equations turn the 3D Navier-Stokes equations into a set of 2D equations that do not have a radial dependence. However, this simplification comes at a cost: internal waves are removed from the solution (Section 2.2.1). Internal waves play an important role in Earth's ocean tidal dissipation (e.g., *Munk*, 1997) and in the tidal response of stars and gas giants (e.g., *Fuller et al.*, 2016; *Ogilvie*, 2014). In Chapter 4, we studied internal inertial waves and examined two research questions:

2. What are the patterns and intensity of ocean currents resulting from tidally induced inertial waves in subsurface oceans?

3. Do tidally induced inertial waves heat the subsurface ocean of Europa and Enceladus?

The properties of internal inertial waves are markedly different from those of surface waves (e.g., *Maas*, 2005). For instance, the dispersion relation for surface waves is of the form $\omega = \omega(|\boldsymbol{k}|)$, where $\boldsymbol{k}$ and ω are the wave vector and frequency, respectively. This means that upon reflection, as the frequency of the wave remains the same, so does the wavelength. In contrast, as we have shown in Chapter 4, the dispersion relation for internal waves is of the from $\omega = \omega(\alpha)$, where α is the orientation of the wave vector. This implies that when a wave reflects, it does so keeping the orientation of the wave vector constant; its wavelength might, however, change. Depending on the geometry of the container, this can result in wave focusing, the accumulation of energy in specific trajectories known as wave attractors. For an inviscid fluid, a singularity develops along these trajectories. However, when viscosity is considered, the competing effects of energy dissipation and wave focusing prevents the development of such singularities. Instead, internal shear layers develop where energy is dissipated.

We studied inertial waves in a simplified geometry representative of a subsurface ocean, a spherical shell. We considered the tidal response of subsurface oceans of different thicknesses to diurnal tides. To solve the linearized Navier-Stokes equations, we expanded them in a series of spherical harmonics and Chebyschev polynomials and obtained the solution using the method of *Rieutord and Valdettaro* (2010).

Wave attractors have been known to exist in spherical shells for a long time (*Israeli*, 1972; *Rieutord et al.*, 2001; *Stern*, 1963; *Stewartson*, 1972). Additionally, in a spherical shell a singularity arises at the critical latitude (where a ray is tangent to the core). In Chapter 4, we investigated whether wave attractors can be formed in subsurface oceans. Wave attractors are characterized by their Lyapunov exponent, which indicates how fast waves converge towards a limiting orbit. A negative Lyapunov exponent means convergence, and thus the formation of a wave attractor; a high (in absolute value) Lyapunov exponent means fast convergence and thus a highly attracting attractor. We found that for geometries with high Lyapunov exponent wave attractors form. On the other hand, for geometries with low Lyaponov exponents, energy dissipation outplays energy focusing and prevents the formation of wave attractors. For these geometries the flow field is characterized by shear layers emanating from the critical latitude that blur after a few reflections from the container's walls. We find the strongest attractors to form for oceans thicker than those expected in Europa and Enceladus, which implies that the critical

latitude singularity dominates the flow field. For an ocean thickness representative of Enceladus, we found that flow velocities of a few $\mathrm{cm\,s^{-1}}$ can result from inertial waves.

We computed how much energy can be dissipated in the internal shear layers characteristic of inertial waves. Energy dissipation strongly depends on ocean geometry and the ratio between viscous and Coriolis forces. For some ocean thicknesses compatible with Enceladus' (21 – 67 km) and Europa's (80 – 170km) estimates (e.g., *Soderlund et al.*, 2020), sharp resonances occur in which energy dissipation is between one or two orders of magnitude higher compared to neighbouring ocean thickness values. However, we found these peaks to be below the amount of heat required to maintain Enceladus' ocean and below Europa's radiogenic heating, evidencing that inertial waves do not likely play a major role in the thermal budget of these two moons. These results were later confirmed by *Rekier et al.* (2019), who also studied inertial waves in Enceladus' ocean due to tides. In contrast to what we did in Chapter 4, they considered the effect of an ice shell on the tidal response and showed that it further reduces the amplitude of inertial waves. *Rekier et al.* (2019) also considered the excitation of inertial waves due to the libration of the ice shell and showed that they produce more energy dissipation than inertial waves excited by tides, albeit still orders of magnitude below Enceladus' observed thermal output.

7.1.2. OUTLOOK

In Section 2.2, we presented an overview of the different approximations that can be used to study ocean tides; we discussed their rationale and argued why some have been traditionally employed. We then challenged two of these assumptions to extend our understanding of ocean tides in extraterrestrial oceans. However, we still relied on two important assumptions: we neglected non-linear terms in the Navier-Stokes equations and assumed an unstratified ocean. Below we discuss what this implies for our results and for future modelling efforts.

Moreover, in our study of liquid tides we did not consider the intricate connection between tides and the orbital evolution of moons (Section 2.3). At the end of this section, we explore in which circumstances liquid tides can have an important effect in the long-term orbital evolution of moons and how future work can account for it.

STIRRING THE OCEAN: TURBULENCE AND INSTABILITIES

Under the assumption of small perturbations, we neglected the advection term $(\boldsymbol{u}\cdot\nabla\boldsymbol{u})$ in the momentum equation for our study of ocean tides (see Table 2.1). This allowed us to linearize the equations of motion and focus our study on tidal waves. However, as noted in Section 2.2.1, this assumption comes at a cost: important phenomena such as wave-breaking, wave-wave and wave-flow interactions are neglected. Here, we briefly discuss when these elements become relevant.

Wave-wave and wave-flow interactions via the $\boldsymbol{u}\cdot\nabla\boldsymbol{u}$ term can give rise to instabilities, wave-breaking and, ultimately, turbulence. The main driver of flow instabilities for moons with internal liquid layers is the moons' libration. As discussed in Section 2.1, tidally locked moons have a frozen tidal bulge that points on average towards the planet. Due to the eccentric orbit of a moon, the subplanet point changes relative to the

frozen tidal bulge producing a gravitational torque that alters the moon's rotation rate: $\Omega = \Omega_0(1 + \epsilon \sin(\Omega_0 t))$, where ϵ is the libration amplitude, which can have a maximum value of $2e$.

Because of the liquid's viscosity, the libration of the moons' outer shell results in the formation of viscous boundary layers at the ocean-ice interface. The boundary layer librates with the shell, while the bulk of the interior remains in solid body rotation. The libration of the outer shell produces oscillations in the boundary layer. If these oscillations are of sufficient amplitude, an instability known as the centrifugal instability might occur, breaking the boundary layer and producing turbulence in the form of longitudinal rolls near the outer boundary (*Noir et al.*, 2009). *Wilson and Kerswell* (2018) suggested that this mechanism is important in Enceladus.

Apart from the centrifugal instability, another instability of importance for librating tidally distorted bodies with internal liquid layers is the elliptical instability (see *Kerswell* (2002) and *Le Bars et al.* (2015) for a review). The elliptical instability occurs when an elongated moon is subject to libration. For a tidally locked moon, the moon's libration together with the equatorial ellipticity of the moon, produces a base-flow characterised by elliptical streamlines along which the fluid oscillates. In the elliptical instability, two inertial waves (as those studied in Chapter 4) interact non-linearly with this base flow feeding energy into each other until waves break and the domain is filled with turbulence.

For an inviscid flow, the triadic interaction of this base-flow with two inertial waves inevitably leads to a flow instability. However, viscous energy dissipation can hinder the growth of the instability and prevent the development of turbulence. Whether this occurs or not depends on the Ekman number of the fluid, the libration amplitude and the elongation of the moon along the tidal axis. Combining laboratory and numerical experiments, *Lemasquerier et al.* (2017) showed that Enceladus' subsurface ocean is prone to the elliptical instability. Europa's ocean might also be, although the uncertainty in its libration amplitude does not allow to obtain a final answer. If this was the case, Enceladus' and Europa's oceans would be turbulent rather than characterized by the wave solutions studied in Chapters 3 and 4; the tidally excited internal waves studied in Ch. 4 would still play a central role in the initiation and maintenance of the turbulent flow.

WHEN TIDES MEET CONVECTION

Tides are not the only driver of ocean currents in subsurface oceans. Tidal and radiogenic heat flux from the seafloor heats the overlying ocean water. As a result those water parcels become buoyant and start to rise towards the ice shell, forming convection cells (Figure 7.1). Because of the non-linear nature of the Navier-Stokes equations, the tidal currents studied in chapters 3 and 4 can be expected to interact with convection. However, until very recently, convective and tidal currents have been studied separately.

The problem of thermal convection in rotating spherical shells has been widely studied in literature due to its myriad of geophysical applications — Earth's core convection, convection in gas giants and stars, etc. (e.g., *Bercovici et al.*, 1989)— but only in the last decade has this problem been explored in the context of subsurface oceans (see *Soder-*

lund et al., 2020, for a review). The flow patterns are controlled by the competition between rotation and thermal forcing (e.g., *Gastine et al.*, 2016). If basal heating is not very high, the Coriolis force organizes the flow in Taylor columns aligned with the rotational axis, which resemble the Taylor columns formed in gas giant atmospheres that produce their characteristic bands. As the intensity of basal heating increases, the flow becomes more turbulent and the Taylor columns are distorted (*Amit et al.*, 2020; *Soderlund*, 2019; *Soderlund et al.*, 2013).

Peak zonal flows due to ocean convection in icy moons are expected to be as high as 10s of $\mathrm{cm\,s^{-1}}$ (*Soderlund*, 2019), higher than the tidal flows predicted in chapters 3 and 4. The effect of convection on tidal currents is difficult to predict. Convection might blur tidal currents, but it is also possible that energy exchange between convective and tidal flows drives flow instabilities similar to those discussed above. Recently, *Hay et al.* (2021) presented a model to study the interaction between convective and tidal currents and pointed towards the first hypothesis. Nevertheless the authors caution that further analysis is needed.

INTERNAL TIDES IN A STRATIFIED OCEAN

Models used to study tidal dynamics in subsurface oceans —including those used in this thesis— often assume a well-mixed unstratified ocean. As opposed to an unstratified ocean, a stratified ocean can support internal gravity waves (see Table 2.1), which offer a new avenue for tidal dissipation. On Earth, internal gravity waves play an important role in energy dissipation and ocean mixing (e.g., *Garrett*, 2003; *Garrett and Munk*, 1979; *Munk*, 1997). It is thus important to reexamine the assumption of unstratified subsurface oceans.

The assumption of a well-mixed unstratified ocean can be justified in view of the ocean convective models discussed in the previous section. As opposed to Earth's ocean, which is heated at its surface by solar radiation, subsurface oceans are heated from below, rendering them unstable to convection —a situation reminiscent of convection in a boiling pot. Nevertheless, this reasoning ignores that, under certain conditions, subsurface oceans can become stratified (e.g., *Vance and Goodman*, 2009).

Below a certain salinity, the maximum density of water is not attained at its melting temperature but slightly above it. As a consequence, a cold buoyant "stratosphere" sandwiched between the ice shell and the warmer convection portion of the ocean can form. This situation is observed in lake Vostok beneath Antarctica ice sheet. The extent of the buoyant stratosphere depends on the ocean salinity and pressure; *Melosh et al.* (2004) estimated this stratosphere to be a few hundred meters thick for Europa.

Stratified oceans can also result from the effects of salinity on the ocean's density. In an ocean of near saturated composition, salt precipitates from hot buoyant parcels as they rise towards the ice shell, enhancing the salinity of the ocean bottom. A regime known as double-diffusion convection can be attained (*Vance and Brown*, 2005; *Vance and Goodman*, 2009). In this regime the ocean is divided into a warm well-mixed salty layer below a colder layer of fresher water, separated by a staircase profile of temperature and salinity. Double-diffusive convection is observed in different terrestrial envi-

ronments such as parts of the Weddell Sea, the ice-covered Antarctic lake Vanda and the Black and Red Seas (*Vance and Goodman*, 2009). The Black sea might be a good analogy of a subsurface ocean, as its sea floor is geothermally heated.

The density profile of subsurface oceans might also change laterally. *Čadek et al.* (2019) noted that variations in hydrostatic pressure at Enceladus' ice-ocean interface cause the ice shell to flow from thicker to thinner regions. Consequently, the current ice shell thickness profile can only be maintained if there are regions of melting and freezing at a rate of a few mm per year (*Čadek et al.*, 2019). If this is the case, a process similar to Earth's ocean overturning circulation might be occurring in Enceladus. Brine rejection and freshwater production due to melting and freezing at the ocean-ice interface can produce complex vertical and horizontal stratification profiles (*Kang et al.*, 2020; *Lobo et al.*, 2021; *Zeng and Jansen*, 2021).

Tyler (2020) modelled baroclinic ocean tides using the concept of an equivalent depth and the Laplace tidal equations. He argued that a stratified ocean can be modelled as an unstratified one with a reduced equivalent ocean thickness that depends on the ocean stratification profile. If the equivalent ocean depth is sufficiently small, the ocean can resonate with the eccentricity tide in a way similar to a thin unstratified ocean and thus lead to high levels of energy dissipation. Further research into the density structure of subsurface ocean will allow to develop more complex models to study tidal waves. If the ocean is partitioned into a discrete number of layers of constant density — e.g., a dense well-mixed interior below a lighter stratosphere— the Laplace tidal equations used in Chapter 3 can be extended to study internal and surface gravity waves in a multi-layered system (see *Vallis*, 2006, Chapter 3). If in contrast density stratification is more gradual, the approach used in Chapter 4 to study internal inertial waves in a spherical shell can be modified to study internal gravity waves (e.g., *Dintras et al.*, 1999).

MOON-MOON TIDES AND RESONANCES

In our study of tides, we considered the diurnal tide raised by the planet. However, in the same way that a planet rises tides in its moons, moons do also rise tides to each other. The tidal amplitude scales with the mass of the tide-rising body, meaning that the strength of moon-moon tides is several orders of magnitude weaker than that of planet tides. However, as opposed to planet tides that have a monochromatic spectra, moon-moon tides occur over a wider spectrum of frequencies. Because of their small amplitude, this spectrum of tides barely affects the response of solid layers, but some of these notes can resonate in the subsurface oceans of icy moons.

As discussed above, if the perturbing tidal potential had a lower orbital period, the thick subsurface oceans of icy moons would not be able to quickly adjust to the eccentricity tide, and tidal resonances would be possible. *Hay et al.* (2020) showed that this might be the case if moon-moon tides are taken into account. Some of the high frequencies characteristic of moon-moon tides can produce resonances in thick subsurface oceans that result in high-amplitude tidal flows and tidal dissipation. *Hay et al.* (2020) focused on the study of moon-moon tides in the Jovian system. A logical extension of their work is to consider the Saturnian system. As discussed above, to study ocean tides in Enceladus' ocean it is important to consider that the ocean is not of constant thick-

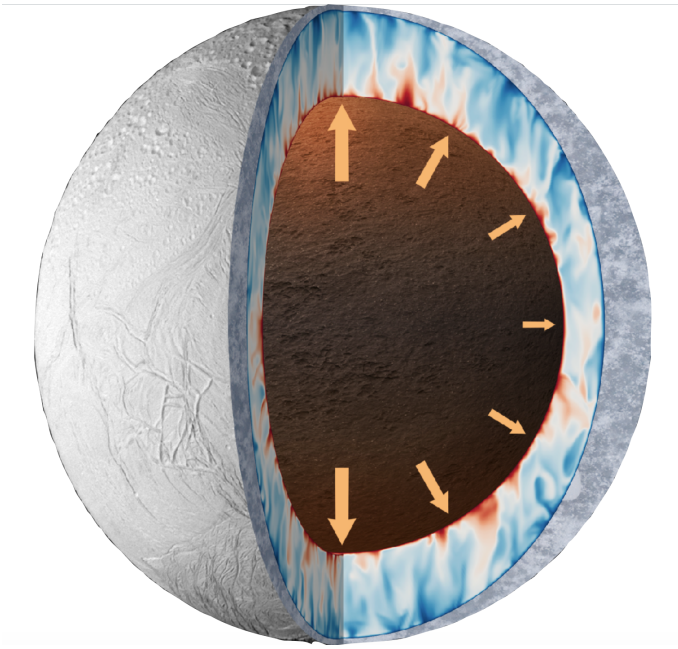

Figure 7.1 Illustration of thermal convection in Enceladus' ocean. Radiogenic and tidal heating in the core heat Enceladus' subsurface ocean and drive ocean convection. The core's heat flux is latitude dependent, as indicated by the arrows. The warm ocean parcels (red) rise towards the moon's ice shell, which is thicker at the equator than at the poles. Illustration courtesy of Jeffrey Nederend (*Nederend et al.*, 2020).

ness; the tools developed in Chapter 3 can be readily applied to study moon-moon tides in oceans of variable thickness. In their study of moon-moon tides, *Hay et al.* (2020) used the Laplace tidal equations and thus ignored internal waves. The method developed to study internal inertial waves excited by diurnal tides presented in Ch. 4 can be employed to study internal inertial waves excited by moon-moon tides and their relevance for the thermal budget of the moon. However, given the results presented in Chapter 4 and in *Rekier et al.* (2019), it seems unlikely that inertial waves excited by moon-moon tides will result in more energy dissipation than surface waves.

OCEAN TIDES AND THERMAL-ORBITAL EVOLUTION

In Chapters 3 and 4, we studied tides in liquid layers. In both cases, we considered the interior and orbital parameters fixed. Nevertheless, we have seen that tidal dissipation modifies the interior structure and orbit of tidally active bodies. Intense episodes of tidal heating can alter the ice shell thickness and change the rheology of rocky and icy layers, as well as cause orbit migration and circularization; giving rise to complex feedbacks (see Section 2.3). The coupling between the tidal response of moons, their interior and orbit has been comprehensively explored in the literature (*Hussmann and Spohn*, 2004; *Ojakangas and Stevenson*, 1986); however, this has always been done neglecting liquid tides. As shown in Chapter 3 and discussed above, the tidal response of subsurface ocean can often be approximated by the equilibrium tide. When this is the case, there is little tidal dissipation in the ocean and the traditional approach of only considering solid tides in the thermal-orbital evolution of moons suffices. Nevertheless, there are two important scenarios in which tides in subsurface ocean might play an important role on the

thermal-orbital evolution of a moon: (1) obliquity tides, and (2) moon-moon tides.

Table 1.1 shows the expected obliquity of different moons. For some moons, their low obliquity keeps tidal dissipation due to ocean tides orders of magnitude below dissipation due to solid tides (e.g., Enceladus and Europa), but, for other satellites with a more substantial obliquity, dissipation due to ocean tides is close to (Callisto and Titan) or even exceeds dissipation due to solid tides (Triton) (see *Chen et al.*, 2014, Table 3). This suggests that ocean tides should be considered when studying the thermal-orbital evolution of at least some icy moons.

As discussed above, moon-moon tides can also provoke resonances in subsurface oceans. If a moon hits one of these resonances tidal dissipation is dramatically enhanced, which can lead to changes in its interior structure (e.g., partial melting of the ice shell) and its orbit (e.g., circularization, inward orbital migration). The dynamical effects of moon-moon tides enrich —and complicate— the possible evolution scenarios of moons with subsurface oceans.

Computing the tidal response of a solid body is simpler and less numerically expensive than computing the tidal response of a body with liquid layers. Spherical harmonics are normally used. For a spherically symmetric solid, a tidal forcing of degree l and order m leads to a tidal response of same degree and order (see chs. 5 and 6). This is not the case for ocean tides: the Coriolis term couples spherical harmonics of different degrees making the computation of the tidal response of the ocean more challenging (chs. 3 and 4). If the role of ocean tides in the long-term thermal-orbital evolution of moons is to be studied, efficient numerical schemes to solve the Laplace tidal equations are necessary. The TROPF software package is capable of computing the tidal response of subsurface ocean very efficiently (*Tyler*, 2019; *Tyler*, 2020, 2021), which opens the door to tackle the questions raised above.

7

7.2. TIDES IN BODIES WITH POROUS AND PARTIALLY MOLTEN LAYERS

7.2.1. RESEARCH QUESTIONS AND MAIN FINDINGS

The challenge of explaining Enceladus' endogenic activity in terms of tidal dissipation in the ice shell and the ocean has led several authors to consider the hypothesis that Enceladus' activity is powered by tidal dissipation in its core. This idea relies in the fact that Enceladus' core density is low, which implies that the core is either a mixture of ice and rock, a porous medium, or made of loosely packed grains. *Roberts* (2015) and *Choblet et al.* (2017) argued that, if this is the case, the core is more susceptible to strong tides and tidal dissipation.

Previous studies used the theory traditionally employed to model solid tides. However, the tidal response of a solid and a porous core are expected to differ (Section 2.2.3). More recently, *Liao et al.* (2020) used the theory of poroviscoelasticity to study the tidal deformation and flow of water throughout Enceladus porous core and showed that poroviscoelastic effects could account for Enceladus' thermal output. They made, however,

some non-trivial assumptions — ignored the overlying ocean and ice shell, the effect of self-gravitation and used a set of simplified boundary conditions — that required further examination. In Chapter 5, we reexamined these assumptions to answer two research questions:

4. How does the presence of a porous layer alter the tidal response of a tidally active moon?

5. What is the contribution of Darcy dissipation to Enceladus' energy budget?

We extended the model of *Liao et al.* (2020) by combining the poroviscoelasticity theory of *Biot* (1941) with the theory of tides for self-gravitating viscoelastic bodies (e.g., *Sabadini et al.*, 2016). We showed that the boundary conditions at the porous layer interface are paramount in controlling the moon's response to tides. If the moon's core is forced via a prescribed strain at its boundary, high pore pressures are attained close to the core's boundary, which in turn drive intense Darcy flow, cause high stresses and produce an amount of tidal dissipation compatible with observations for a wide range of core viscosity and permeability values. In contrast, if the core is forced via a tidal body force and free-stress boundary conditions are prescribed at the core boundary, the parameter space for which the amount of tidal dissipation is consistent with observations is reduced to two scenarios: a low viscosity core with viscosity between 10^{10} and 10^{13} Pa s, or a highly permeable core with a permeability larger than 10^{-5} m^2. The presence of an ocean further reduces the amount of Darcy flow and dissipation in the core, leaving the low-viscosity scenario as the most likely avenue for intense dissipation in Enceladus' core. *Choblet et al.* (2017) suggested this scenario can be reconciled with a silicate core if the core resembles a rubble-pile.

Combining these results with those discussed in the previous section, we can reexamine Enceladus' energy puzzle in a new light (Section 2.3.2). The results presented in Chapters 3 and 4 and summarized in 7.1, together with previous studies of ocean tides in Enceladus (e.g., *Beuthe*, 2020; *Beuthe et al.*, 2016; *Matsuyama*, 2014; *Matsuyama et al.*, 2018; *Rekier et al.*, 2019), show that it is unlikely that tidally induced waves in an unstratified Enceladan ocean dominate the moon's thermal budget. As discussed in Section 7.1.2, the notable exceptions are tides in a stratified ocean, or a highly turbulent ocean.

Alternatively, as proposed by *Choblet et al.* (2017) and examined in Chapter 5, tides in an unconsolidated core can result in an amount of tidal dissipation compatible with Cassini's observations. Nevertheless, this only occurs for rheology parameters at the fringes of what we can expect for granular media: a low shear modulus on the order of 0.01–0.1 GPa, compared to expected values of ~ 1 GPa; or, alternatively, a damping coefficient higher than 0.4, compared to expected values smaller than 0.1 (Section 5.3.3). Nevertheless, we must caution that these bounds rely on laboratory experiments performed at conditions not entirely representative of Enceladus (e.g., higher forcing frequency, lower confining pressure), which implies that laboratory experiments of granular media at Enceladan-like conditions are still needed to settle the debate.

We propose that a future mission might directly probe the rheology of the moon's core by measuring tidal-induced gravitational field changes around the moon and sur-

face displacements. A highly dissipative Enceladan core results in a phase lag between the tidal-induced gravitational field changes and surface displacements that can reach values as high as 50° (Chapter 5). A future JUICE-type mission with precise tracking capabilities and equipped with an altimeter could return this measurement allowing to distinguish between a high and a low-dissipative interior (Section 7.4).

7.2.2. OUTLOOK

In Chapter 5, we developed a model to study the tidal response of a moon with porous layers and applied it to Enceladus. In what follows, we indicate two interesting applications for which the model could be extended: (1) investigate the geochemistry of Enceladus's hydrothermal systems and how it connects to plume observations, and (2) study the tidal response of moons with mushy magma layers.

ENCELADUS AS A CHEMICAL REACTOR

As ocean water circulates through Enceladus' core, it is heated by tidal and radiogenic heat likely forming hydrothermal systems. In these systems, water-rock interactions can prompt complex chemical reactions. Enceladus' porous core might provide a wide range of pressures and temperatures for different chemical processes to occur, turning the moon into a "chemical reactor". Chemical components formed in hydrothermal systems are then dissolved in the ocean and some of them might exit the moon through its plumes. The chemistry of Enceladus' plumes offers a window to its deep interior.

Analyses of the composition of grains and gases expelled by the plumes suggest that there is ongoing hydrothermal activity within Enceladus (*Hsu et al.*, 2015; *Matson et al.*, 2007; *Waite et al.*, 2017). Cassini observations suggest temperatures attained within this system are at least 360K (*Hsu et al.*, 2015) and might be as high as 500–800 K (*Matson et al.*, 2007). Enceladus' hydrothermal systems might resemble those of Earth (e.g., *Hand et al.*, 2020), where life is suspected to have originated (e.g., *Martin et al.*, 2008). High temperatures attained in Enceladus' core can provoke the serpentinization of olivine and the production of H_2 (*Holm et al.*, 2015; *Malamud and Prialnik*, 2013, 2016), which some autotrophic organisms could use to reduce CO_2 and bind carbon. Following serpentinization, chains of chemical reactions can lead to the synthesis of complex organic molecules similar to those observed in Enceladus' plumes (e.g., *Khawaja et al.*, 2019; *Postberg et al.*, 2018).

To study this complex system, the mechanical model presented in Chapter 5 should be substantially extended to include heat transfer between the solid and fluid phases and the ensuing convection of water in hydrothermal systems. This would allow to infer the range of conditions (temperature, pore-pressure, etc.) attained within the core and constrain the chemical reactions likely to occur. This way, a clear connection between tidal dissipation and plume composition can be made. Work in this direction is essential to interpret plume observations and ultimately characterize Enceladus' subsurface habitat.

A MUSHY MAGMA OCEAN

As we have seen in Chapter 6, intense tidal heating might partially melt Io's mantle. Using Galileo's magnetometer observations, *Khurana et al.* (2011) deduced that Io has a ≈ 50 km thick asthenosphere with ≈ 20% melt fraction. While this claim has been recently challenged (*Blöcker et al.*, 2018; *Roth et al.*, 2017), theoretical models of Io's mantle support the formation of a partially molten layer (*Spencer et al.*, 2020).

Traditionally, the tidal response of bodies with melt is modelled using the same approach employed to compute the tidal response of solid bodies after applying a decrease of shear modulus and viscosity to account for the presence of melt (see *Fischer and Spohn* (1990); *Hussmann and Spohn* (2004); *Renaud and Henning* (2018); Chapter 6). In contrast, *Tyler et al.* (2015) modelled tides in Io's asthenosphere by treating it as a magma ocean and using the same Laplace tidal equations we used in Chapter 3 to study tides in subsurface oceans. However, modelling tides in Io's partially molten mantle requires a framework similar to that developed in Chapter 5. The new poroviscoelastic model can help in showing how the asthenosphere of Io or a super-Io responds to tides and whether tides play an important role in magma transport.

Before applying the model to Io, or a super-Io, some aspects would need to be addressed. In Chapter 5, we encountered numerical problems for bodies with a low permeability and a large radius. Io's radius is almost one order of magnitude larger than that of Enceladus', and its permeability is likely lower. Therefore, we can expect this problem to aggravate. The refinement of the numerical method presented in Chapter 5 or the derivation of an analytical solution to the equations presented there might aid in tackling this problem. Additionally, we have assumed the background pressure field to be hydrostatic, this assumption is not appropriate for Io as melt advection and ensuing compaction create a non-hydrostatic background pressure field (*Spencer et al.*, 2020).

7.3. THERMAL-ORBITAL EVOLUTION OF TIDALLY ACTIVE WORLDS AND THE EXOMOON HUNT

7.3.1. RESEARCH QUESTIONS AND MAIN FINDINGS

In the previous sections, we focused on the tidally active moons of the outer Solar System. However, it is reasonable to assume that exoplanets also host tidally active moons. This type of exomoons has been labelled as a promising target for different exomoon-finding techniques. In case of extreme tides, tidal heating can boost the surface temperature of an exomoon making it observable in the mid-infrared (*Peters and Turner*, 2013). Moreover, tidally heated exomoons are expected to spawn vigorous volcanic activity. Volcanic outgassing can feed a substantial exosphere with a characteristic spectral signature detectable using transit spectroscopy (*Oza et al.*, 2019).

In order to assess how likely it is to detect an exomoon experiencing extreme levels of tidal heating — a super-Io — the intricate coupling between tidal dissipation, interior structure and orbital evolution discussed in Chapter 2 needs to be considered. However, previous studies have paid little attention to this aspect. In Chapter 6 we addressed this

issue and tackled two research questions:

6. What is the thermal state of a super-Io?

7. How long can a super-Io persist in an observable state?

We found that three ingredients are required for tidal heating to boost an exomoon's surface temperature: the exomoon needs to be (1) close to its host planet, (2) in a highly eccentric orbit and (3) large. For example, an Io-like exomoon would have a surface temperature of around 400 K if it orbited with its current eccentricity at less than half its current orbital distance, or if it had an eccentricity 25 times higher than its present value. These constraints are less stringent for a Mars and an Earth-sized exomoon: if we were to put Earth in Io's orbit, its tidally boosted surface temperature would be around 300 K.

The high eccentricity and small semi-major axis required to attain high levels of tidal dissipation place constraints on the type of systems that can host a super-Io.If a moon experiences a boost in tidal eccentricity that leads to strong tidal heating, its obit is quickly circularised. This means that the detection window for such an event is small. For instance, if Io exited the Laplace resonance, its orbit would be circularized in a few million years. The high eccentricities required for a super-Io to exist can only be maintained during a long time if they are actively forced. Mean-motion resonances provide a way for this.

In Chapter 6, we showed that thermal-orbital equilibrium configurations exist where rotational energy stored in the planet is transferred to the moon, where it is dissipated. This process is controlled by the tidal response of the planet: the more dissipative the planet is, the higher the moon's eccentricity, favouring super-Ios around dissipative gas giants. However, a highly dissipative planet implies fast orbital migration, which means that super-Ios with tidally boosted surface temperature might only be observable early in the evolution of the planet when the moons are close to the planet and at its brightest, reducing the window for directly imaging an exomoon. A more promising technique for detecting tidally heated exomoons is via transit spectroscopy. We showed that exomoons can remain tidally active for a time-span comparable to the age of the Solar System, providing ample opportunity for exospheres to form.

The thermal-orbital evolution model presented in Chapter 6 also provided new insights into the evolution of Io. Rather than assuming the traditional Maxwell rheology to model the tidal response of a super-Io, we used the more realistic Andrade model (*Andrade and Trouton*, 1910; *Bierson and Nimmo*, 2016; *Castillo-Rogez et al.*, 2011; *Renaud and Henning*, 2018) and included the very efficient heat-piping mechanism to account for heat transfer in bodies with partial melt. The combination of these two elements results in a thermal-orbital evolution notably different to that of classic models. While the evolution of Io in previous models is characterized by an oscillation between warm and cold phases corresponding to oscillations in orbital eccentricity (e.g., *Fischer and Spohn*, 1990; *Hussmann and Spohn*, 2004) that might modulate its volcanic activity, we showed that the combined effect of these two new elements prevent oscillations and result in a smoother thermal-orbital evolution.

Intense tidal heating in such worlds is likely to partially melt the upper mantle, meaning that super-Ios are either in the efficient heat-pipe regime that *Moore* (2001) proposed for Io or have molten magma oceans. Our knowledge about tidal dissipation for bodies with high melt fractions is still poor (Section 7.2.2). The model we presented in Chapter 5 for tides in porous media can help untangle how tides work in this regime.

7.3.2. OUTLOOK

We showed that the larger a moon is, the higher the tidally induced surface heat flux. However, we noted that our current understanding of moon formation processes limits how large a gas giant orbiting exomoon might be. In what follows, we discuss in which circumstances this limit might not apply and how these systems can be studied in the future. We then move to the more general topic of dissipation in gas giants. We discuss how recent developments in this field are changing our understanding of the orbital evolution of the moons of the outer Solar System, and explain what these new findings imply for the results presented in Chapter 6.

CAPTURED EXOMOONS

In the Solar System, the moons-to-planet mass ratio is remarkably similar for all the gas and ice giants, it only varies from $1.1 \cdot 10^{-4}$ to $2.5 \cdot 10^{-4}$ (e.g., *Canup and Ward*, 2006). This limit is the consequence of two competing processes in a protoplanetary disk: the in-flow of material into the protoplanetary disk and satellite loss due to the inward migration of protomoons (*Canup and Ward*, 2006; *Heller and Pudritz*, 2015a,b). On these grounds, we argued that we can expect Mars-sized exomoons around super-Jovian exoplanets, but that systems with larger exomoons are probably less common.

The 10^{-4} ratio contrasts with the still-debated detection of a Neptune-sized exomoon around a Jupiter-sized exoplanet (*Heller, René et al.*, 2019; *Teachey and Kipping*, 2018). However, we should remember that the $\sim 10^{-4}$ limit only applies to the in situ formation of moons around gas giants; other formation mechanisms might render larger exomoons. As an example, for the Earth-Moon system, which likely formed after the impact of a Mars-size protoplanet with the Earth (*Canup and Asphaug*, 2001), the ratio is $\sim 10^{-2}$. Another interesting example of a moon with a different origin is Triton. Triton's peculiar orbit (retrograde and high inclination) suggests that it did not accrete in Neptune's protoplanetary disk but was instead captured. Triton might have been captured due to gas-drag in Neptune's protoplanetary disk (*McKinnon and Leith*, 1995) or, alternatively, later in the Solar System's history via a process known as binary-exchange capture (*Agnor and Hamilton*, 2006). In this scenario one of the members of a binary-planet is captured by a gas giant while the other escapes during a close encounter. *Williams* (2013) suggested that a similar process might result in Earth-sized exomoons around gas giants.

The binary-exchange capture scenario opens the door to interesting evolution pathways. A captured Earth-sized exomoon will likely be in a highly eccentric and oblique orbit and in a state of non-synchronous rotation. These two ingredients are apt to produce strong tides and tidal dissipation (*Renaud et al.*, 2021), making these worlds interesting candidates for detection; but, for how long? Studying the evolution of such a system

requires extending the model presented in Chapter 6 to include high-order eccentricity and inclination terms for computing the tidal response of the moon and its orbital evolution (i.e., Eqs. 2.39,2.52), as well as to consider the spin-orbit evolution of the captured object rather than making the assumption that the moon is tidally locked in a state of synchronous rotation.

RESONANCE LOCKING AND THE THERMAL-ORBITAL EVOLUTION OF MOONS

In Chapter 6, we explicitly computed the frequency-dependent tidal response of the secondary (as given by its quality factor Q and Love numbers k_2). However, for the primary, we assumed a fixed k_2 and Q. Uncertainties in the interior structure of gas giants and stars and the complex dynamics of their gas envelopes make estimating the quality factor of a gas giant challenging. As a consequence, a constant Q has traditionally been assumed for gas giants and stars. Early estimations of tidal dissipation in Jupiter's atmosphere suggested a very high quality factor $Q \sim 10^{13}$ (*Goldreich and Nicholson*, 1977), implying little orbital evolution since the Galilean moons formed. *Yoder* (1979) and *Yoder and Peale* (1981), on the other hand, showed that explaining the thermal activity of Io requires a much lower quality factor, $Q \sim 10^5$, compatible with significant orbital migration of the satellites.

Lainey et al. (2009, 2012, 2017, 2020) recently constrained the quality factors of Saturn and Jupiter using astrometric, and in the case of Saturn, radiometric observations. They showed that tidal dissipation in gas giants is not only higher than expected but also frequency dependent (e.g., the quality factor of Saturn changes by two orders of magnitude at Mimas' and Titan's frequencies). This discovery challenges the constant Q assumption widely used in thermal-orbital evolution models, including the one presented in Chapter 6, and opens new evolution scenarios for gas giant systems. The variation in tidal dissipation with forcing frequency is likely the result of the excitation of resonant internal waves (similar to those studied in Ch. 4 for Europa and Enceladus) in the gas giant's atmosphere (*Ogilvie and Lin*, 2004). The resonance frequency of such waves depends on the interior structure of the planet, which in turn changes over time.

Conceptual models have shown the dramatic influence that a frequency-dependent quality factor can have on the thermal-orbital evolution (*Fuller et al.*, 2016; *Nimmo et al.*, 2018). *Fuller et al.* (2016) presented a new scenario for moon migration known as *resonance locking*. In this scenario, a moon gets *locked* with a resonant mode of the planet, migrating outward at the same rate at which the planet's resonant frequency shifts. When this occurs, fast orbital migration ensues (Figure 7.2).

Resonance locking might be behind some intriguing observations of the moons of the outer Solar System. *Downey et al.* (2020) suggested that Callisto's eccentricity and inclination were recently (~ 0.3 Gyr ago) excited due to the fast migration of Ganymede. A variable Q might also explain the resurfacing of Ganymede and answer some outstanding questions about Saturn's icy moons: *Polycarpe et al.* (2018) suggested that the fast migration of Titan due to resonance locking can explain Iapetus inclined and eccentric orbit. To further address these questions, a full-fledged thermal-orbital evolution model that accounts for a variable Q in the primary is required.

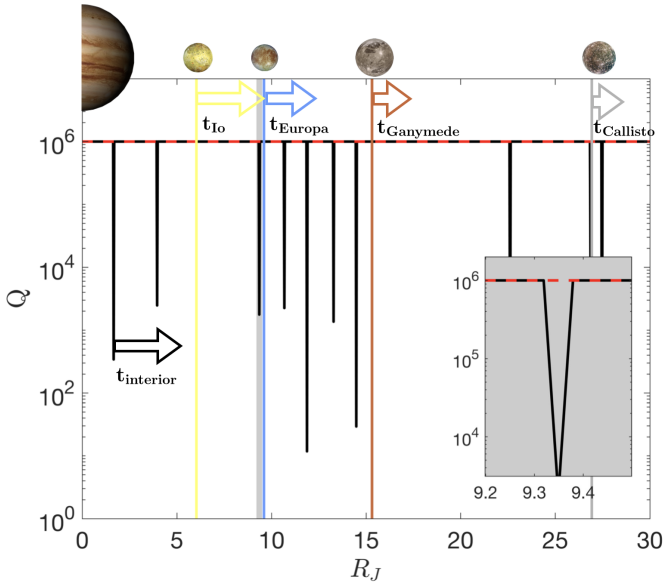

Figure 7.2 Sketch of a quality factor spectrum for Jupiter. The dips in Q correspond to resonant modes. The location of the Galilean moons are indicated, the arrows show the migration of the moons and of the spectra. When a moon hits a resonant mode, fast orbital migration ensues. Resonance locking occurs when a moon's migration time-scale (t_{moon}) is close to the time-scale at which the planet's interior evolves ($t_{interior}$).

Gasman (2021) adapted the model presented in Ch. 6 to study the orbital evolution of two moons caught in a mean-motion resonance under the resonance-locking scenario. Interestingly, she showed that the decrease in effective quality factor that occurs as the moon migrates outward can lead to an increase of orbital eccentricity. This could widen the observability window of tidally heated exomoons. Furthermore, a changing Q opens the possibility of episodes of high eccentricity and heating later in a moon's evolution due to resonance crossing. This contrasts with the constant Q scenario, which predicts the highest levels of tidal dissipation to occur during the early phases of the moon evolution when the planet is at its brightest, and raises the prospects of observing a super-Io.

7.4. AN EXCITING FUTURE

Data collected by the Voyager, Galileo and Cassini-Huygens missions revealed the main characteristics of the Jovian and Saturnian moons, allowing to construct first order models of their interior, and to study the large-scale dynamics of this diverse collection of worlds. While the data returned by these two missions has not been exhausted, and, as pointed out in previous sections, there are still more than enough questions to keep modellers busy for years, the data also underscores the need for more observations. We are now in a better place to formulate questions about these bodies and pinpoint the required observations to tackle them.

In this decade, two missions —JUICE and Europa Clipper— will fly to Jupiter to study its icy moons. The European-led JUICE mission will largely focus on Ganymede (e.g., *Grasset et al.*, 2013). After two Europa flybys and various flybys of Callisto and Ganymede, JUICE will characterize Ganymede from orbit. The American Europa Clipper, on the

other hand, will perform various flybys of Ganymede and Callisto but will focus on Europa (*Bayer et al.*, 2019; *Phillips and Pappalardo*, 2014). Due to the more demanding environment of Europa, Europa Clipper will characterize Europa during approximately 45 flybys of the moon. Using ice penetrating radars, magnetometers, radio science packages, and, in the case of JUICE, an altimeter; the two missions will return a wealth of new geophysical data.

Accurate radio tracking of the spacecrafts will allow to obtain the real part of the gravity Love number k_2 of both Europa and Ganymede —and possibly Callisto— for the first time, as well as high-degree gravity field data. The two spacecrafts will also measure the libration of Europa's and Ganymede's ice shells, and characterize them using ice penetrating radars. Additionally, the GALA altimeter onboard JUICE will be able to very accurately measure the tidal deformations of Ganymede's ice shell yielding the h_2 Love number. These measurements will allow to narrow-down current average ice shell and ocean thickness estimates and infer thickness variations. What this will imply is made evident if we remember that current ice shell thickness estimates for Europa vary between 3 and 30 km (*Soderlund et al.*, 2020) and that there is currently no information about ice shell thickness variations. With this new information, it will be possible to build more realistic interior models of these icy moons to study their ocean and ice shell dynamics.

Europa Clipper and JUICE radiometric and astrometric data — combined with the historical record of astrometric observations — will also help constraining dissipation within Io, Ganymede, Europa and Jupiter (*Dirkx et al.*, 2016; *Hussmann et al.*, 2016). These measurements will give an observational constraint on tidal dissipation against which models could be tested. Precise radio-tracking data of the ongoing Juno spacecraft is already revealing new details about the interior of Jupiter (*Durante et al.*, 2019; *Idini and Stevenson*, 2021; *Stevenson*, 2020). This information is key to decipher how the architecture of gas giant systems arose (Section 7.3) and will improve our capacity to predict what kind of exomoons we are likely to find around different types of exoplanets.

The magnetometer on-board of the spacecrafts will measure the magnetic field around Europa and Ganymede at different frequencies. Similar observations performed by the Galileo spacecraft showed that Europa and Ganymede have subsurface oceans (*Khurana et al.*, 1998; *Kivelson et al.*, 2002). More detailed magnetic field data, complemented with the measurements mentioned above, will allow to identify the ocean-ice shell boundary and, very importantly, constrain the salinity of the respective subsurface oceans (*Vance et al.*, 2021). Better bounds on the ocean salinity, together with improved estimates of the ocean density derived from the combination of gravity, libration and radar data, will provide a clearer picture of ocean stratification, which has immense implications for ocean dynamics (Section 7.1.2). If ocean currents are strong enough, the magnetometers might capture the resulting motionally induced magnetic field and provide the first direct observation of ocean currents in other worlds (*Tyler*, 2011; *Vance et al.*, 2021), making it possible to compare flows obtained from ocean models as those presented in this thesis with data.

The science case for a return to Enceladus is even more pressing (e.g., *Cable et al.*, 2021). Enceladus fits the definition of an habitable world: it has (1) a subsurface ocean of liquid water that is (2) rich in salts and organic compounds, and (3) an accessible

energy source provided by its tidally driven hydrothermal activity (e.g., *Cable et al.*, 2021; *Hand et al.*, 2020). Because of this, the relevant question for Enceladus is not whether it is habitable, but whether it is inhabited. A search-for-life mission to Enceladus will likely carry several instruments for biochemical analysis; however, such a mission will be incomplete if it does not aim at providing the geophysical context in which life might (or might not) have evolved in the moon.

The two most prominent geophysical questions for astrobiology are: (1) How stable is Enceladus' subsurface habitat? (2) How is energy dissipation partitioned between the different layers of the moon? The first question has evident implications for the emergence and evolution of a potential Enceladan biosphere; if Enceladus subsurface ocean freezes and melts down periodically it is less likely that life could emerge and survive. The second question has direct implications for the energy supply of a hypothetical Enceladan ecosystem, which would rely on the chemical components produced in hydrothermal systems.

A single or dual orbiter could provide answers to these two questions (*Ermakov et al.*, 2021; *Marusiak et al.*, 2021). As in the case of the Europa Clipper and JUICE missions, accurate tracking of the spacecrafts' orbit would allow to obtain the gravity Love number k_2. A major achievement would be measuring the phase lag of the tidal response, which would provide a constraint on the present amount of tidal dissipation and settle the debate about whether the moon is in thermal equilibrium (1). If this measurement were complemented with a constraint of the $\mathrm{Im}\{h_2\}$ using an altimeter, we would get unprecedented insight into how tidal dissipation is partitioned between core, ocean an ice (2). *Hussmann et al.* (2016) proposed JUICE could use this same approach for Ganymede, which experiences tides approximately 10 times weaker (Table 7.3). In Chapter 5, we showed how this technique could be also used for Enceladus. Finally, the continuation of astrometric observations of Saturn's moons and radio-tracking of the spacecraft would also help to determine whether the system is in an equilibrium orbital configuration or not (1).

Combined with more precise libration estimations, gravity and altimetry measurements would narrow down the average ocean and ice shell thickness and reveal ice shell and ocean thickness variations. A complementary constraint could also be obtained if the Love numbers for the different components of Enceladus' tide can be separated (*Ermakov et al.*, 2021; *Marusiak et al.*, 2021). This would likely require a GRAIL-style gravity mission. Such a mission would also yield gravity and shape models way beyond what we now have (gravity up to degree 3, shape up to degree 16). Higher-resolution gravity and altimetry measurements could reveal the finer details of the ice shell and to distinguish a conductive from a convective ice shell, which is important for (1). If these measurements were complemented by an independent ice shell thickness constraint (e.g., via the Love numbers, libration, detection of ice-ocean interface with a radar), the core and ice shell gravity signals could be separated allowing to see below the ice shell and constrain the core's topography, which might not be hydrostatic (*Hemingway and Mittal*, 2019; *McKinnon*, 2013). Better information of the ocean's batyhmetry would permit to construct more accurate ocean models to study both tidal and convective currents. For instance, fine details of the ocean bathymetry might reveal regions where the flow of the

barotropic tide over rough topography generates internal waves, a process that plays a crucial role on Earth's oceans (e.g., *Garrett*, 2003; *Munk*, 1997).

In contrast to Jupiter, Saturn's magnetic field is not tilted and thus the techniques used to prove the interior of the Galilean moons cannot be as efficiently used in Enceladus. Nevertheless, the more stable magnetic field experienced by this moon might be an ideal setting to measure magnetic field changes induced by ocean currents (*Marusiak et al.*, 2021).

While Galileo and Cassini-Huygens measured the first order characteristics of the moons of the Jovian and Saturnian systems, our knowledge about Neptune's moon Triton is almost entirely derived from the Voyager 2's 1989 flyby, and is therefore much more limited. The brief encounter was sufficient to unveil an active world with few craters, signs of resurfacing and plumes, and hinted at the existence of a subsurface ocean (*Hansen et al.*, 2021). Triton's unique origin —a captured Kuiper belt object— makes it a very special ocean world candidate, halfway between the Jovian and Saturnian icy moons and the frigid objects of the Kuiper belt. A mission to Triton could resolve if it has an ocean, reveal the processes shaping its unique landscapes, allow to investigate the origin and dynamics of its plumes and provide new clues about its turbulent history. But a Triton mission would also put into context what we know about other icy worlds, the evolutionary pathways that tidally active icy moons can take and their implications for habitability (*Hansen et al.*, 2021). There are currently two proposed missions to Triton; the discovery (New horizons-style) Trident mission (*Frazier et al.*, 2020), which would perform one Triton flyby, and the flagship (Cassini-style) Odyssey mission, which would orbit Neptune for approximately 4 years and perform several flybys of the moon (*Rymer et al.*, 2021, 2020).

Any icy moon mission with surface elements —lander(s), penetrator(s)— would increase the science return. A Europa lander was discussed in the context of the Europa Clipper mission, but was finally discarded. An Europa lander mission might fly after Europa Clipper provides detailed maps of the moon's surface (*Dooley*, 2018; *Pappalardo et al.*, 2013). The science return of an Enceladan mission would also be amplified if it carried a lander or a penetrator (*Balachandran et al.*, 2020; *MacKenzie et al.*, 2021; *Marusiak et al.*, 2021), and a Triton lander has also been proposed to fly as an add-on to the Odyssey mission.

One of the most promising geophysical instruments to put in a lander is a seismometer. Because of tides, icy moons are expected to have a level of seismic activity in the sensitive range of geophones (e.g., *Olsen et al.*, 2021; *Panning et al.*, 2018; *Vance et al.*, 2018). Just as seismography allowed to characterize the interior of Earth, the Moon and now —thanks to Insight— Mars (e.g., *Stähler et al.*, 2021); a seismometer, or network of seismometers, would allow to constrain ice shell and ocean thickness, locate and characterize regions of tectonic activity and convection, as well as study the location and timing of seismic events and its link to tides and interior (e.g., *Marusiak et al.*, 2021). For example, we can expect an Enceladan rubble-pile core such as that discussed in Chapter 5 to generate much more seismic noise than a monolithic one. Radio tracking of a lander would also be ideal to measure tidal deformations and libration and would allow to determine the moon's ephemeris with great precision. A network of magnetometers placed

on the surface could exploit the local magnetic field or use active magnetic sounding to prove different depths of the subsurface and constrain its salinity (*Marusiak et al.*, 2021).

Lingering on the science fiction realm, but closer than we might think, is the in-situ exploration of subsurface oceans. With Earth's oceans remaining still largely unexplored, it is bold to imagine that we might soon *soak our feet* in the waters of an extraterrestrial ocean. Yet, the technology required for such an undertaking is being developed. Cryobots able to penetrate the icy crusts of Europa and Enceladus have already been proposed (*Zimmerman et al.*, 2001) —and some even tested in Earth analogues (*Konstantinidis et al.*, 2015)— and different ocean exploration platforms —buoyant rovers, submarines— are also under study (*Cwik et al.*, 2018; *Ellery*, 2016).

The exploratory work presented in this thesis about super-Ios (Chapter 6) can only be understood when looked at side by side with studies of their Solar System analogue, Io. Our growing understanding of Io and the Jovian system allowed us to speculate about the existence of a similar kind of moon in other planetary systems, and explore what it would take for such a moon to survive for a long time and be observable. A dedicated Io mission would allow to answer standing questions about rocky worlds experiencing high amounts of tidal dissipation, leading to an improvement of the models presented in Chapter 6, and consequently allowing us to fine-tune criteria for the exomoon hunt. The Io Volcano Observer (IVO)[1] is a proposed mission that could provide the answer to these questions (*McEwen et al.*, 2014).

Due to the unforgiving environment of the innermost parts of the Jovian system, IVO would not orbit Io, but, as Europa Clipper, perform a series of Io flybys (around 10) at different instances of Io's tidal period. Accurate tracking of the spacecraft during these flybys would allow to measure Io's changing gravity field and obtain its k_2. A magnetometer on-board would measure the induced magnetic field, libration of the moon surface would also be measured and high resolution thermal maps of the moon's surface obtained. These observations would allow to settle the debate about the amount of magma present within the moon, permit to distinguish where and how tidal dissipation occurs within Io, and shed new light into how heat is transported inside bodies experiencing extreme amounts of internal heating such as Io, super-Ios or the Hadean Earth.

The worlds mentioned above belong to the broader family of tidally active worlds; their characteristics come into sharper focus when they are analyzed together. Because of this, the science return of these missions is greatly amplified when they are combined. Many of the processes shaping these objects are common but operating at different intensities. An evident example is tidal heating, which plays an important role in all of them. Understanding how tidal dissipation changes across the spectrum of tidally active worlds will allow to unravel the divergent evolutionary pathways that these moons followed and find the answer to some of the most compelling questions surrounding these worlds: What makes an icy moon habitable? How much volcanic activity can tides drive? What is the past and the fate of the Laplace resonance? Why do the icy moons of Saturn look so different?

[1] In June 2021, both IVO and Trident Discovery missions were discarded in favour of the two Venus missions, DAVINCI+ and VERITAS.

Looking for synergies between missions is not simply an add-on, but a must, if we want to understand how these moons work. The orbital and internal dynamics of some of them are intimately linked via mean-motion resonances (see Chapter 2). The evolution of these moons cannot be disentangled without considering their interactions. As an example, understanding the dynamics of the moons involved in the Laplace resonance requires constraining the thermal budget of the three innermost Galilean moons and dissipation within Jupiter.

Just as the discovery of the first exoplanet in 1992 transformed planetary sciences; the discovery of exomoons will revolutionize our understanding of planetary systems. Once a sizable population of exomoons is discovered, we will be able to place the moons of the Solar System in a broader context. Rather than having the static picture we now have, we will have access to snapshots of planet-moon systems at different stages of their evolution. This will make it possible to study with more detail the formation and evolution of satellites and to reconstruct the evolution of the moons of the Solar System more precisely. The first tentative —and controversial— detections of exomoons (*Heller, René et al.*, 2019; *Oza et al.*, 2019; *Teachey and Kipping*, 2018; *Teachey et al.*, 2017) together with the proliferation of methods to detect them (*Ben-Jaffel and Ballester*, 2014; *Bennett et al.*, 2014; *Cabrera, J. and Schneider, J.*, 2007; *Han and Han*, 2002; *Heller, R.*, 2016; *Hippke*, 2015; *Kipping*, 2009; *Kipping et al.*, 2015; *Lewis et al.*, 2008; *Noyola et al.*, 2014, 2016; *Peters and Turner*, 2013; *Rovira-Navarro et al.*, 2021; *Teachey and Kipping*, 2018; *Teachey et al.*, 2017) give room for optimism. We might be at the brink of a revolution; with new ground-based telescopes, the James Webb Space Telescope on its way to L2 and rapid improvements in data analysis techniques, this leap might happen in the coming years (e.g., *Heller*, 2017). The playground of those studying natural satellites is about to be expanded.

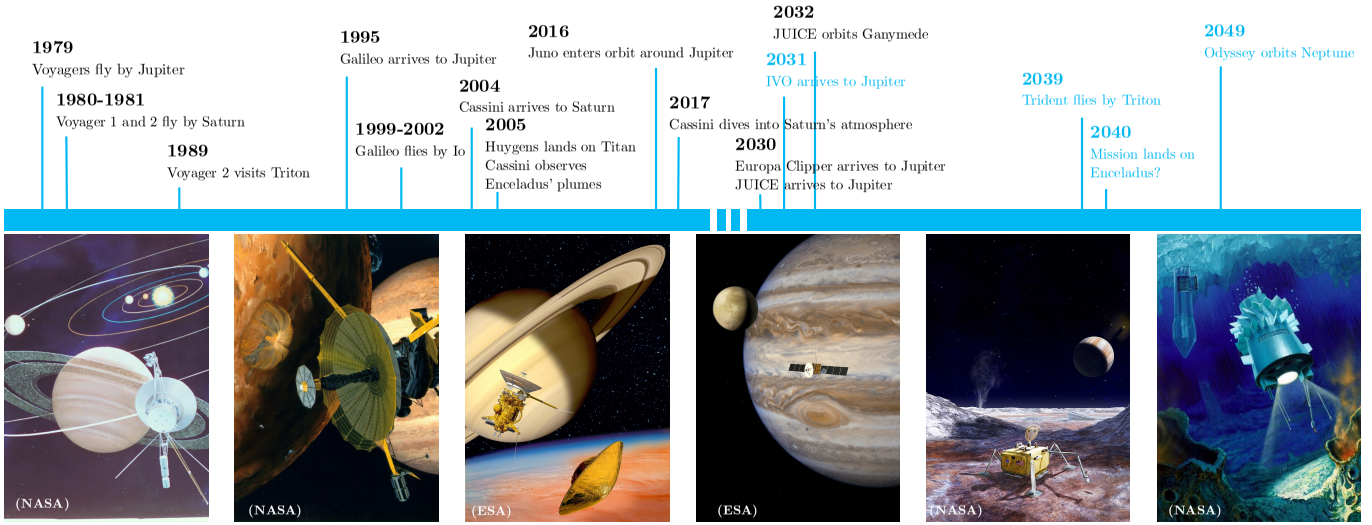

Figure 7.3 A condensed overview of the exploration of the outer Solar System with main indicated. Uncertain dates are shown in blue. Images from NASA and ESA.

REFERENCES

Agnor, C. B. & Hamilton, D. P. (2006), Neptune's capture of its moon Triton in a binary–planet gravitational encounter, *Nature*, *441*(7090), 192–194.

Alterman, Z., Jarosch, H., Pekeris, C. L., & Jeffreys, H. (1959), Oscillations of the earth, *Proc. R. Soc. A*, *252*(1268), 80–95.

Amit, H., Choblet, G., Tobie, G., et al. (2020), Cooling patterns in rotating thin spherical shells - Application to Titan's subsurface ocean, *Icarus*, *338*, 113,509.

Anderson, J., Jacobson, R., McElrath, T., et al. (2001), Shape, mean radius, gravity field, and interior structure of Callisto, *Icarus*, *153*(1), 157 – 161.

Anderson, J. D., Sjogren, W. L., & Schubert, G. (1996a), Galileo gravity results and the internal structure of Io, *Science*, *272*(5262), 709–712.

Anderson, J. D., Lau, E. L., Sjogren, W. L., Schubert, G., & Moore, W. B. (1996b), Gravitational constraints on the internal structure of Ganymede, *Nature*, *384*(6609), 541–543.

Anderson, J. D., Schubert, G., Jacobson, R. A., et al. (1998), Europa's differentiated internal structure: Inferences from four Galileo encounters, *Science*, *281*(5385), 2019–2022.

Andrade, E. N. D. C. & Trouton, F. T. (1910), On the viscous flow in metals, and allied phenomena, *Proc. R. Soc. A*, *84*(567), 1–12.

Asphaug, E. & Reufer, A. (2013), Late origin of the Saturn system, *Icarus*, *223*(1), 544–565.

Balachandran, K., Nathan, E., Rovira-Navarro, M., et al. (2020), A Mission Concept Investigating the Habitability of Enceladus: SILENUS, in Lunar and Planetary Science Conference, Lunar and Planetary Science Conference, p. 1339.

Baland, R.-M., Yseboodt, M., & Van Hoolst, T. (2012), Obliquity of the Galilean satellites: The influence of a global internal liquid layer, *Icarus*, *220*(2), 435 – 448.

Baland, R.-M., Yseboodt, M., & Hoolst, T. V. (2016), The obliquity of Enceladus, *Icarus*, *268*, 12 – 31.

Bashi, Dolev, Helled, Ravit, Zucker, Shay, & Mordasini, Christoph (2017), Two empirical regimes of the planetary mass-radius relation, *Astron. Astrophys.*, *604*, A83.

Bayer, T., Bittner, M., Buffington, B., et al. (2019), Europa Clipper Mission: Preliminary design report, in 2019 IEEE Aerospace Conference, pp. 1–24, doi:10.1109/AERO.2019.8741777.

Becker, J. C., Vanderburg, A., Rodriguez, J. E., et al. (2018), A discrete set of possible transit ephemerides for two long-period gas giants orbiting HIP 41378, *Astron. J.*, *157*(1), 19.

Beghin, C., Sotin, C., & Hamelin, M. (2010), Titan's native ocean revealed beneath some 45km of ice by a Schumann-like resonance, *Cr. Geosci.*, *342*(6), 425 – 433.

Běhounková, M., Tobie, G., Čadek, O., et al. (2015), Timing of water plume eruptions on Enceladus explained by interior viscosity structure, *Nat. Geosci.*, *8*(8), 601–604.

Bêhounková, M., Souček, O., Jaroslav, H., & Čadek, O. (2017), Plume activity and tidal deformation on Enceladus influenced by faults and variable ice shell thickness, *Astrobiology*, *17*(9), 941–954.

Ben-Jaffel, L. & Ballester, G. E. (2014), Transit of exomoon plasma tori: New diagnosis, *Astrophys. J.*, *785*(2).

Bennett, D. P., Batista, V., Bond, I. A., et al. (2014), MOA-2011-BLG-262Lb: A Sub-Earth-Mass Moon Orbiting a Gas Giant Primary or a High Velocity Planetary System in the Galactic Bulge, *Astrophys. J.*, *785*(2), 155.

Berckhemer, H., Kampfmann, W., Aulbach, E., & Schmeling, H. (1982), Shear modulus and q of forsterite and dunite near partial melting from forced-oscillation experiments, *Phys. Earth Planet. Inter.*, *29*(1), 30 – 41, special Issue Properties of Materials at High Pressures and High Temperatures.

Bercovici, D., Schubert, G., Glatzmaier, G. A., & Zebib, A. (1989), Three-dimensional thermal convection in a spherical shell, *J. Fluid Mech.*, *206*, 75–104.

Beuthe, M. (2008), Thin elastic shells with variable thickness for lithospheric flexure of one-plate planets, *Geophys. J. Int*, *172*(2), 817–841.

Beuthe, M. (2013), Spatial patterns of tidal heating, *Icarus*, *223*(1), 308–329.

Beuthe, M. (2015), Tides on Europa: The membrane paradigm, *Icarus*, *248*, 109–134.

Beuthe, M. (2016), Crustal control of dissipative ocean tides in Enceladus and other icy moons, *Icarus*, *280*, 278 – 299.

Beuthe, M. (2018), Enceladus' crust as a non-uniform thin shell: I tidal deformations, *Icarus*, *302*, 145–174.

Beuthe, M. (2019), Enceladus's crust as a non-uniform thin shell: II tidal dissipation, *Icarus*, *332*, 66–91.

Beuthe, M. (2020), Comment on "Heating of Enceladus due to the dissipation of ocean tides" by R. Tyler, *Icarus*, *350*, 113,934.

Beuthe, M., Rivoldini, A., & Trinh, A. (2016), Enceladus's and Dione's floating ice shells supported by minimum stress isostasy, *Geophys. Res. Lett.*, *43*(19), 10,088–10,096.

Bierson, C. J. & Nimmo, F. (2016), A test for Io's magma ocean: Modeling tidal dissipation with a partially molten mantle, *J. Geophys. Res. Planets*, *121*(11), 2211–2224.

Biot, M. A. (1941), General theory of three-dimensional consolidation, *J. Appl. Phys*, *12*(2), 155–164.

Blackledge, B. W., Green, J. A. M., Barnes, R., & Way, M. J. (2020), Tides on other earths: Implications for exoplanet and palaeo-tidal simulations, *Geophys. Res. Lett.*, *47*(12), e2019GL085,746, e2019GL085746.

Blöcker, A., Saur, J., Roth, L., & Strobel, D. F. (2018), Mhd modeling of the plasma interaction with Io's asymmetric atmosphere, *J. Geophys. Res. Planets*, *123*(11), 9286–9311.

Boss, A. P., Butler, R. P., Hubbard, W. B., et al. (2005), Working Group on Extrasolar Planets, *Proc. Int. Astron. Union*, *1*(T26A), 183–186.

Boué, G. & Efroimsky, M. (2019), Tidal evolution of the keplerian elements, *Celest. Mech. Dyn. Astron.*, *131*(7), 30.

Bretherton, F. P. (1964), Low frequency oscillations trapped near the equator, *Tellus*, *16*(2), 181–185.

Brouzet, C., Ermanyuk, E. V., Joubaud, S., Sibgatullin, I., & Dauxois, T. (2016), Energy cascade in internal-wave attractors, *Europhys. Lett.*, *113*(4), 44,001.

Bryan, G. (1889), The waves on a rotating liquid spheroid of finite ellipticity, *Phil. Trans. R. Soc. A*, *180*, 187–219.

Bryan, M. L., Benneke, B., Knutson, H. A., Batygin, K., & Bowler, B. P. (2018), Constraints on the spin evolution of young planetary-mass companions, *Nat. Astron.*, *2*(2), 138–144.

Cable, M. L., Porco, C., Glein, C. R., et al. (2021), The science case for a return to Enceladus, *Planet. Sci. J.*, *2*(4), 132.

Cabrera, J. & Schneider, J. (2007), Detecting companions to extrasolar planets using mutual events, *Astron. Astrophys.*, *464*(3), 1133–1138.

Čadek, O., Tobie, G., Van Hoolst, T., et al. (2016), Enceladus's internal ocean and ice shell constrained from Cassini gravity, shape, and libration data, *Geophys. Res. Lett.*, *43*(11), 5653–5660.

Čadek, O., Souče, O. O., Bêhounková, M., et al. (2019), Long-term stability of Enceladus' uneven ice shell, *Icarus*, *319*, 476 – 484.

Canup, R. M. & Asphaug, E. (2001), Origin of the Moon in a giant impact near the end of the Earth's formation, *Nature*, *412*(6848), 708–712.

Canup, R. M. & Ward, W. R. (2002), Formation of the Galilean satellites: Conditions of accretion, *Astron. J.*, *124*(6), 3404–3423.

Canup, R. M. & Ward, W. R. (2006), A common mass scaling for satellite systems of gaseous planets, *Nature*, *441*(7095), 834–839.

Carman, P. (1997), Fluid flow through granular beds, *Chem. Eng. Res. Des.*, *75*, S32–S48.

Carr, M. H., Belton, M. J. S., Chapman, C. R., et al. (1998), Evidence for a subsurface ocean on Europa, *Nature*, *391*(6665), 363–365.

Cartwright, D. (1999), *Tides: A Scientific History*, Cambridge University Press.

Cassen, P., Reynolds, R. T., & Peale, S. J. (1979), Is there liquid water on Europa?, *Geophys. Res. Lett.*, *6*(9), 731–734.

Cassen, P., Peale, S. J., & Reynolds, R. T. (1980), Tidal dissipation in Europa: A correction, *Geophys. Res. Lett.*, *7*(11), 987–988.

Castillo-Rogez, J. C., Efroimsky, M., & Lainey, V. (2011), The tidal history of Iapetus: Spin dynamics in the light of a refined dissipation model, *J. Geophys. Res. Planets*, *116*(E9).

Castillo-Rogez, J. C., Hemingway, D., Rhoden, A., Tobie, G., & McKinnon, W. B. (2018), Origin and evolution of Saturn's mid-sized moons, in Enceladus and the Icy Moons of Saturn, edited by P. M. Schenk, R. N. Clark, C. J. A. Howett, A. J. Verbiscer, and J. H. Waite, p. 285, doi:10.2458/azu_uapress_9780816537075-ch014.

Chen, E., Nimmo, F., & Glatzmaier, G. (2014), Tidal heating in icy satellite oceans, *Icarus*, *229*, 11 – 30.

Chen, E. M. A. & Nimmo, F. (2011), Obliquity tides do not significantly heat Enceladus, *Icarus*, *214*(2), 779–781.

Cheng, A. H.-D. (2016), *Poroelasticity, Theory and Applications of Transport in Porous Media*, vol. 27, Springer.

Choblet, G., Tobie, G., Sotin, C., et al. (2017), Powering prolonged hydrothermal activity inside Enceladus, *Nat. Astron.*, *1*(12), 841–847.

Chung, J. & Hulbert, G. M. (1993), A time integration algorithm for structural dynamics with improved numerical dissipation: the generalized-α method, *J. Appl. Mech*, *60*(2), 371–375.

Comas Solá, J. (1908), Observations des satellites principaux de Jupiter et de Titan, *Astronomische Nachrichten*, *179*(18), 289.

Comsol Multiphysics® (2012), *Comsol Multiphysics®User's Guide v4.3*, pp. 810–815.

Conrad, J., Nimmo, F., Schenk, P., et al. (2019), An upper bound on Pluto's heat flux from a lack of flexural response of its normal faults, *Icarus*, *328*, 210–217.

Crow-Willard, E. N. & Pappalardo, R. T. (2015), Structural mapping of Enceladus and implications for formation of tectonized regions, *J. Geophys. Res. Planets*, *120*(5), 928–950.

Ćuk, M., Dones, L., & Nesvorný, D. (2016), Dynamical evidence for a late formation of Saturn's moons, *Astrophys. J.*, *820*(2), 97.

Cwik, T., Zimmerman, W., Gray, A., et al. (2018), A technology architecture for accessing the oceans of icy worlds, in 69th International Astronautical Congress, Bremen, Germany.

Czechowski, L. (2006), Parameterized model of convection driven by tidal and radiogenic heating, *Adv. Space Res.*, *38*(4), 788–793.

Dalba, P. A., Muirhead, P. S., Fortney, J. J., et al. (2015), The transit transmission spectrum of a cold gas giant planet, *Astrophys. J.*, *814*(2), 154.

Darwin, G. H. (1880), On the secular changes in the elements of the orbit of a satellite revolving about a tidally distorted planet, *Phil. Trans. R. Soc.*, *171*, 713–891.

de Pater, I., Marchis, F., Macintosh, B. A., et al. (2004), Keck AO observations of io in and out of eclipse, *Icarus*, *169*(1), 250–263, special Issue: Io after Galileo.

de Pater, I., Luszcz-Cook, S., Rojo, P., et al. (2020), ALMA observations of Io going into and coming out of eclipse, *Planet. Sci. J.*, *1*(3), 60.

de Sitter, W. (1931), Jupiter's Galilean Satellites. (George Darwin Lecture, delivered by Professor W. de Sitter, Assoc.R.A.S., on 1931 May 8.), *Mon. Not. R. Astron. Soc.*, *91*(7), 706–738.

Dermott, S. F. & Sagan, C. (1995), Tidal effects of disconnected hydrocarbon seas on Titan, *Nature*, *374*(6519), 238–240.

Dermott, S. F., Malhotra, R., & Murray, C. D. (1988), Dynamics of the Uranian and Saturnian satelite systems: A chaotic route to melting miranda?, *Icarus*, *76*(2), 295–334.

Dintras, B., Rieutord, M., & Valdettaro, L. (1999), Gravito-inertial waves in a rotating stratified sphere or spherical shell, *J. Fluid Mech.*, *398*, 271–297.

Dirkx, D., Lainey, V., Gurvits, L., & Visser, P. (2016), Dynamical modelling of the Galilean moons for the JUICE mission, *Planet. Space Sci.*, *134*, 82–95.

Dobrovolskis, A. R. (2007), Spin states and climates of eccentric exoplanets, *Icarus*, *192*(1), 1 – 23.

Dooley, J. (2018), Mission concept for a Europa lander, in 2018 IEEE Aerospace Conference, pp. 1–10, doi:10.1109/AERO.2018.8396518.

Downey, B. G., Nimmo, F., & Matsuyama, I. (2020), Inclination damping on Callisto, *Mon. Not. R. Astron. Soc.*, *499*(1), 40–51.

Durante, D., Hemingway, D., Racioppa, P., Iess, L., & Stevenson, D. (2019), Titan's gravity field and interior structure after Cassini, *Icarus*, *326*, 123–132.

Efroimsky, M. (2012a), Bodily tides near spin–orbit resonances, *Celest. Mech. Dyn. Astron.*, *112*(3), 283–330.

Efroimsky, M. (2012b), Tidal dissipation compared to seismic dissipation: in small bodies, Earths, and super-Earths, *Astrophys. J.*, *746*(2), 150.

Efroimsky, M. & Williams, J. G. (2009), Tidal torques: a critical review of some techniques, *Celest. Mech. Dyn. Astron.*, *104*(3), 257–289.

Egbert, G. D. & Ray, R. D. (2000), Significant dissipation of tidal energy in the deep ocean inferred from satellite altimeter data, *Nature*, *405*, 775.

Egbert, G. D. & Ray, R. D. (2003), Semidiurnal and diurnal tidal dissipation from TOPEX/Poseidon altimetry, *Geophys. Res. Lett.*, *30*(17).

Ellery, A. (2016), *Case study: Robotic exploration of Europa, In: Planetary Rovers: Robotic Exploration of the Solar System*, pp. 513–539, Springer Berlin Heidelberg.

Ermakov, A. I., Park, R. S., Roa, J., et al. (2021), A recipe for the geophysical exploration of enceladus, *Planet. Sci. J.*, *2*(4), 157.

Faul, U. H. & Jackson, I. (2005), The seismological signature of temperature and grain size variations in the upper mantle, *Earth Planet. Sci. Lett.*, *234*(1), 119–134.

Fischer, H.-J. & Spohn, T. (1990), Thermal-orbital histories of viscoelastic models of Io (J1), *Icarus*, *83*(1), 39 – 65.

Frazier, W., Bearden, D., Mitchell, K. L., et al. (2020), Trident: The path to Triton on a discovery budget, in 2020 IEEE Aerospace Conference, pp. 1–12, doi:10.1109/AERO47225.2020.9172502.

Fuller, J., Luan, J., & Quataert, E. (2016), Resonance locking as the source of rapid tidal migration in the Jupiter and Saturn moon systems, *Mon. Not. R. Astron. Soc.*, *458*(4), 3867–3879.

Gaeman, J., Hier-Majumder, S., & Roberts, J. H. (2012), Sustainability of a subsurface ocean within Triton's interior, *Icarus*, *220*(2), 339–347.

Ganesan, S. & Poirier, D. R. (1990), Conservation of mass and momentum for the flow of interdendritic liquid during solidification, *Metall. Mater. Trans. B*, *21*(1), 173.

Garrett, C. (2003), Internal tides and ocean mixing, *Science*, *301*(5641), 1858–1859.

Garrett, C. & Munk, W. (1979), Internal waves in the ocean, *Annu. Rev. Fluid Mech.*, *11*(1), 339–369.

Gasman, D. (2021), Mean motion resonances in a resonance lock: Stability and evolution, Master's thesis, Delft University of Technology.

Gastine, T., Wicht, J., & Aubert, J. (2016), Scaling regimes in spherical shell rotating convection, *J. Fluid Mech.*, *808*, 690–732.

Gerkema, T. (2019), *An Introduction to Tides*, Cambridge University Press.

Gerkema, T., Zimmerman, J. T. F., Maas, L. R. M., & van Haren, H. (2008), Geophysical and astrophysical fluid dynamics beyond the traditional approximation, *Rev. Geophys*, *46*(2).

Gevorgyan, Y., Boué, G., Ragazzo, C., Ruiz, L. S., & Correia, A. C. (2020), Andrade rheology in time-domain. application to Enceladus' dissipation of energy due to forced libration, *Icarus*, *343*, 113,610.

Gillon, M., Triaud, A. H. M. J., Demory, B.-O., et al. (2017), Seven temperate terrestrial planets around the nearby ultracool dwarf star TRAPPIST-1, *Nature*, *542*(7642), 456–460.

Goddard, J. D. (1990), Nonlinear elasticity and pressure-dependent wave speeds in granular media, *Proc. R. Soc. Lond. A*, *430*(1878), 105–131.

Goldreich, P. & Nicholson, P. D. (1977), Turbulent viscosity and Jupiter's tidal Q, *Icarus*, *30*(2), 301 – 304.

Goldreich, P. & Sari, R. (2009), Tidal evolution of rubble piles, *Astrophys. J*, *691*(1), 54–60.

Goldreich, P. & Schlichting, H. E. (2014), Overstable librations can account for the paucity of mean motion resonances among exoplanet pairs, *Astron. Astrophys.*, *147*(2), 32.

Goodman, J. C. & Lenferink, E. (2012), Numerical simulations of marine hydrothermal plumes for Europa and other icy worlds, *Icarus*, *221*(2), 970 – 983.

Goodman, J. C., Collins, G. C., Marshall, J., & Pierrehumbert, R. T. (2004), Hydrothermal plume dynamics on Europa: Implications for chaos formation, *J. Geophys. Res. Planets*, *109*(E3).

Grasset, O., Dougherty, M., Coustenis, A., et al. (2013), JUpiter ICy moons Explorer (JUICE): An ESA mission to orbit Ganymede and to characterise the Jupiter system, *Planet. Space Sci.*, *78*, 1–21.

Greenberg, R., Geissler, P., Hoppa, G., et al. (1998), Tectonic processes on Europa: Tidal stresses, mechanical response, and visible features, *Icarus*, *135*(1), 64–78.

Greenspan., H. P. (1969), *The Theory of Rotating Fluids*, Cambridge University Press, Cambridge Monographs on Mechanics and Applied Mathematics.

Greff-Lefftz, M., Legros, H., & Dehant, V. (2000), Influence of the inner core viscosity on the rotational eigenmodes of the earth, *Phys. Earth Planet. Inter.*, *122*(3), 187–204.

Gribb, T. T. & Cooper, R. F. (1998), Low-frequency shear attenuation in polycrystalline olivine: Grain boundary diffusion and the physical significance of the Andrade model for viscoelastic rheology, *J. Geophys. Res. Solid Earth*, *103*(B11), 27,267–27,279.

Hamilton, C. W., Beggan, C. D., Still, S., et al. (2013), Spatial distribution of volcanoes on Io: Implications for tidal heating and magma ascent, *Earth Planet. Sci. Lett.*, *361*, 272–286.

Han, C. & Han, W. (2002), On the feasibility of detecting satellites of extrasolar planets via microlensing, *Astrophys. J.*, *580*(1), 490–493.

Hand, K. P., Sotin, C., Hayes, A., & Coustenis, A. (2020), On the habitability and future exploration of ocean worlds, *Space Sci. Rev.*, *216*(5), 95.

Hansen, C. J., Castillo-Rogez, J., Grundy, W., et al. (2021), Triton: Fascinating moon, likely ocean world, compelling destination!, *Planet. Sci. J.*, *2*(4), 137.

Harada, Y. & Kurita, K. (2006), The dependence of surface tidal stress on the internal structure of Europa: The possibility of cracking of the icy shell, *Planet. Space Sci.*, *54*(2), 170–180.

Hartkorn, O. & Saur, J. (2017), Induction signals from Callisto's ionosphere and their implications on a possible subsurface ocean, *J. Geophys. Res. Space Phys.*, *122*(11), 11,677–11,697.

Haurwitz, B. (1940), The motion of atmospheric disturbances on the spherical Earth, *J. Mar. Res*, *3*, 254–267.

Hay, H. C. & Matsuyama, I. (2017), Numerically modelling tidal dissipation with bottom drag in the oceans of Titan and Enceladus, *Icarus*, *281*, 342 – 356.

Hay, H. C. & Matsuyama, I. (2019), Nonlinear tidal dissipation in the subsurface oceans of Enceladus and other icy satellites, *Icarus*, *319*, 68 – 85.

Hay, H. C. F. C., Trinh, A., & Matsuyama, I. (2020), Powering the Galilean satellites with moon-moon tides, *Geophys. Res. Lett.*, *47*(15), e2020GL088,317, e2020GL088317 10.1029/2020GL088317.

Hay, H. C. F. C., Fenty, I., & Pappalardo, R. T. (2021), How do convective and tidal dynamics interact in Europa's subsurface ocean?, in Lunar and Planetary Science Conference, Lunar and Planetary Science Conference, p. 2147.

Hayes, A. G. (2016), The lakes and seas of Titan, *Annu. Rev. Earth Planet. Sci.*, *44*(1), 57–83.

Heller, R. (2017), Detecting and characterizing exomoons and exorings, in Handbook of Exoplanets, edited by H. J. Deeg and J. A. Belmonte, Springer, doi:10.1007/978-3-319-30648-3_35-1.

Heller, R. & Pudritz, R. (2015a), Conditions for water ice lines and Mars-mass exomoons around accreting super-Jovian planets at 1-20 from Sun-like stars, *Astron. Astrophys.*, *578*, A19.

Heller, R. & Pudritz, R. (2015b), Water ice lines and the formation of giant moons around super-Jovian planets, *Astrophys. J.*, *806*(2), 181.

Heller, R. (2016), Transits of extrasolar moons around luminous giant planets, *Astron. Astrophys.*, *588*, A34.

Heller, René, Rodenbeck, Kai, & Bruno, Giovanni (2019), An alternative interpretation of the exomoon candidate signal in the combined Kepler and Hubble data of Kepler-1625, *Astron. Astrophys.*, *624*, A95.

Hemingway, D., Iess, L., Tajeddine, R., & Tobie, G. (2018), The Interior of Enceladus, in Enceladus and the Icy Moons of Saturn, edited by P. M. Schenk, R. N. Clark, C. J. A. Howett, A. J. Verbiscer, and J. H. Waite, p. 79, doi:10.2458/azu_uapress_9780816537075-ch005.

Hemingway, D. J. & Mittal, T. (2019), Enceladus's ice shell structure as a window on internal heat production, *Icarus*, *332*, 111 – 131.

Hendershott, M. C. (1981), Long waves and ocean tides, in Evolution of Physical Oceanography, edited by B. A. Warren and C. Wunsch, pp. 292–341, MIT Press.

Henning, W. G., O'Connell, R. J., & Sasselov, D. D. (2009), Tidally heated terrestial exoplanets: viscoelastic response models, *Astrophys. J.*, *707*(2), 1000–1015.

Hippke, M. (2015), On the detection of exomoons: A Search in Kepler data for The orbital sampling effect and the scatter peak, *Astrophys. J.*, *806*(1), 51.

Hollerbach, R. & Kerswell, R. R. (1995), Oscillatory internal shear layers in rotating and precessing flows, *J. Fluid Mech.*, *298*, 327–339.

Holm, N. G., Oze, C., Mousis, O., Waite, J. H., & Guilbert-Lepoutre, A. (2015), Serpentinization and the formation of H2 and CH4 on celestial bodies (planets, moons, comets), *Astrobiology*, *15*(7), 587–600.

Hoppa, G. V., Tufts, B. R., Greenberg, R., & Geissler, P. E. (1999), Formation of cycloidal features on Europa, *Science*, *285*(5435), 1899–1902.

Hough, S. S. (1898), On the application of harmonic analysis to the dynamical theory of the tides. Part II. on the general integration of Laplace's tidal equations, *Proc. R. Soc. Lond.*, *191*, 139–185.

Howett, C. J. A., Spencer, J. R., Pearl, J., & Segura, M. (2011), High heat flow from Enceladus' south polar region measured using 10–600 cm^{-1} Cassini/CIRS data, *J. Geophys. Res. Planets*, *116*(E3).

Hsu, H.-W., Postberg, F., Sekine, Y., et al. (2015), Ongoing hydrothermal activities within Enceladus, *Nature*, *519*, 207–210.

Hurford, T., Sarid, A., & Greenberg, R. (2007), Cycloidal cracks on Europa: Improved modeling and non-synchronous rotation implications, *Icarus*, *186*(1), 218–233.

Hussmann, H. & Spohn, T. (2004), Thermal-orbital evolution of Io and Europa, *Icarus*, *171*(2), 391 – 410.

Hussmann, H., Spohn, T., & Wieczerkowski, K. (2002), Thermal equilibrium states of Europa's ice shell: Implications for internal ocean thickness and surface heat flow, *Icarus*, *156*(1), 143 – 151.

Hussmann, H., Choblet, G., Lainey, V., et al. (2010), Implications of rotation, orbital states, energy sources, and heat transport for internal processes in icy satellites, *Space Sci. Rev.*, *153*(1), 317–348.

Hussmann, H., Shoji, D., Steinbrügge, G., Stark, A., & Sohl, F. (2016), Constraints on dissipation in the deep interiors of ganymede and europa from tidal phase-lags, *Celest. Mech. Dyn. Astron.*, *126*(1), 131–144.

Idini, B. & Stevenson, D. J. (2021), Dynamical tides in Jupiter as revealed by Juno, *Planet. Sci. J.*, *2*(2), 69.

Iess, L., Rappaport, N. J., Jacobson, R. A., et al. (2010), Gravity field, shape, and moment of inertia of Titan, *Science*, *327*(5971), 1367–1369.

Iess, L., Jacobson, R. A., Ducci, M., et al. (2012), The tides of Titan, *Science*, *337*(6093), 457–459.

Iess, L., Stevenson, D. J., Parisi, M., et al. (2014), The gravity field and interior structure of Enceladus, *Science*, *344*(6179), 78–80.

Israeli, M. (1972), On trapped modes of rotating fluids in spherical shells, *Stud. in Appl. Math.*, *51*(3), 219–237.

Jackson, I. & Faul, U. H. (2010), Grain size-sensitive viscoelastic relaxation in olivine: Towards a robust laboratory-based model for seismological application, *Phys. Earth Planet. Inter.*, *183*(1), 151 – 163, special Issue on Deep Slab and Mantle Dynamics.

Jackson, I., Faul, U. H., Fitz Gerald, J. D., & Tan, B. H. (2004), Shear wave attenuation and dispersion in melt-bearing olivine polycrystals: 1. specimen fabrication and mechanical testing, *J. Geophys. Res. Solid Earth*, *109*(B6).

Jaeger, W. L., Turtle, E. P., Keszthelyi, L. P., et al. (2003), Orogenic tectonism on Io, *J. Geophys. Res. Planets*, *108*(E8).

Jara-Orué, H. M. & Vermeersen, B. L. (2011), Effects of low-viscous layers and a non-zero obliquity on surface stresses induced by diurnal tides and non-synchronous rotation: The case of Europa, *Icarus*, *215*(1), 417 – 438.

Johnson, R. E. & Huggins, P. J. (2006), Toroidal atmospheres around extrasolar planets, *Publ. Astron. Soc. Pac.*, *118*(846), 1136–1143.

Kamata, S., Matsuyama, I., & Nimmo, F. (2015), Tidal resonance in icy satellites with subsurface oceans, *J. Geophys. Res. Planets*, *120*(9), 1528–1542.

Kang, W., Bire, S., Campin, J.-M., et al. (2020), Differing Enceladean ocean circulation and ice shell geometries driven by tidal heating in the ice versus the core.

Kankanamge, D. G. J. & Moore, W. B. (2019), A parameterization for volcanic heat flux in heat pipe planets, *J. Geophys. Res. Planets*, *124*(1), 114–127.

Karato, S.-i. & Wu, P. (1993), Rheology of the upper mantle: A synthesis, *Science*, *260*(5109), 771–778.

Katz, R. F. (2008), Magma Dynamics with the Enthalpy Method: Benchmark Solutions and Magmatic Focusing at Mid-ocean Ridges, *J. Petrol.*, *49*(12), 2099–2121.

Kaula, W. M. (1961), Analysis of gravitational and geometric aspects of geodetic utilization of satellites, *Geophys. J. R. Astron. Soc.*, *5*(2), 104–133.

Kaula, W. M. (1964), Tidal dissipation by solid friction and the resulting orbital evolution, *Rev. Geophys.*, *2*(4), 661–685.

Kaviany, M. (1995), *Principles of Heat Transfer in Porous Media*, second ed., Springer, New York.

Kerswell, R. R. (1995), On the internal shear layers spawned by the critical regions in oscillatory ekman boundary layers, *J. Fluid Mech.*, *298*, 311–325.

Kerswell, R. R. (2002), Elliptical instability, *Annu. Rev. Fluid Mech.*, *34*(1), 83–113.

Khawaja, N., Postberg, F., Hillier, J., et al. (2019), Low-mass nitrogen-, oxygen-bearing, and aromatic compounds in Enceladean ice grains, *Mon. Not. R. Astron. Soc.*, *489*(4), 5231–5243.

Khurana, K. K., Kivelson, M. G., Stevenson, D. J., et al. (1998), Induced magnetic fields as evidence for subsurface oceans in Europa and Callisto, *Nature*, *395*(6704), 777–780.

Khurana, K. K., Jia, X., Kivelson, M. G., et al. (2011), Evidence of a global magma ocean in Io's interior, *Science*, *332*(6034), 1186–1189.

Kipping, D. M. (2009), Transit timing effects due to an exomoon, *Mon. Not. R. Astron. Soc.*, *392*(1), 181–189.

Kipping, D. M., Schmitt, A. R., Huang, X., et al. (2015), The hunt for exomoons with Kepler(HEK). V. A survey of 41 planetary candidates for exomoons, *Astrophys. J.*, *813*(1), 14.

Kirk, R. L., Brown, R. H., & Soderblom, L. A. (1990), Subsurface energy storage and transport for solar-powered geysers on Triton, *Science*, *250*(4979), 424–429.

Kivelson, M., Khurana, K., & Volwerk, M. (2002), The permanent and inductive magnetic moments of Ganymede, *Icarus*, *157*(2), 507–522.

Kivelson, M. G., Khurana, K. K., Russell, C. T., et al. (1996), Discovery of Ganymede's magnetic field by the Galileo spacecraft, *Nature*, *384*(6609), 537–541.

Kivelson, M. G., Khurana, K. K., Russell, C. T., et al. (2000), Galileo magnetometer measurements: A stronger case for a subsurface ocean at Europa, *Science*, *289*(5483), 1340–1343.

Konopliv, A. S., Binder, A. B., Hood, L. L., et al. (1998), Improved gravity field of the moon from Lunar prospector, *Science*, *281*(5382), 1476–1480.

Konstantinidis, K., Flores Martinez, C. L., Dachwald, B., et al. (2015), A lander mission to probe subglacial water on Saturn's moon Enceladus for life, *Acta Astronaut.*, *106*, 63–89.

Korenaga, J. (2013), Initiation and evolution of plate tectonics on Earth: Theories and observations, *Annu. Rev. Earth Planet. Sci.*, *41*(1), 117–151.

Kuiper, G. P. (1944), Titan: a satellite with an atmosphere., *Astrophys. J.*, *100*, 378.

Lainey, V., Arlot, J., Karatekin, Ö., & Van Hoolst, T. (2009), Strong tidal dissipation in Io and Jupiter from astrometric observations, *Nature*, *459*(7249), 957–959.

Lainey, V., Karatekin, Ö., Desmars, J., et al. (2012), Strong tidal dissipation in Saturn and constraints on Enceladus' thermal state from astrometry, *Astrophys. J.*, *752*(1), 14.

Lainey, V., Jacobson, R. A., Tajeddine, R., et al. (2017), New constraints on Saturn's interior from Cassini astrometric data, *Icarus*, *281*, 286 – 296.

Lainey, V., Casajus, L. G., Fuller, J., et al. (2020), Resonance locking in giant planets indicated by the rapid orbital expansion of Titan, *Nat. Astron.*, *4*(11), 1053–1058.

Lambe, T. & Whitman, R. (1969), *Soil Mechanics*, John Wiley.

Lang, K. (2011), *The Cambridge Guide to the Solar System*, 2 ed., Cambridge University press.

Langseth, M. G., Keihm, S. J., & Peters, K. (1976), Revised Lunar heat-flow values., *Lunar and Planetary Science Conference Proceedings*, *3*, 3143–3171.

Laplace, P.-S. (1798), *Traité de mécanique céleste, Tome II, Livre IV, Des oscillations de la mer et de l'atmosphére*.

Lauer, R. M., Fisher, A. T., & Winslow, D. M. (2018), Three-dimensional models of hydrothermal circulation through a seamount network on fast-spreading crust, *Earth Planet. Sci. Lett.*, *501*, 138–151.

Le Bars, M., Cébron, D., & Le Gal, P. (2015), Flows driven by libration, precession, and tides, *Annu. Rev. Fluid Mech.*, *47*(1), 163–193.

Le Verrier, U. J. (1855), Recherches astronomiques: Chapitre IV. - Développement de la fonction qui sert de base au calcul des perturbations des mouvements des planètes., *Annales de l'Observatoire de Paris*, *1*, 258–342.

Lemasquerier, D., Grannan, A. M., Vidal, J., et al. (2017), Libration-driven flows in ellipsoidal shells, *J. Geophys. Res. Planets*, *122*(9), 1926–1950.

Lewis, K. M., Sackett, P. D., & Mardling, R. A. (2008), Possibility of detecting moons of pulsar planets through time-of-arrival analysis, *Astrophys. J.*, *685*(2), L153–L156.

Liao, Y., Nimmo, F., & Neufeld, J. A. (2020), Heat production and tidally driven fluid flow in the permeable core of Enceladus, *J. Geophys. Res. Planets*, *125*(9), e2019JE006,209, e2019JE006209 10.1029/2019JE006209.

Lieske, J. H. (1980), Improved ephemerides of the Galilean satellites, *Astronomy and Astrophysics*, *82*(3), 340–348.

Lindal, G., Wood, G., Hotz, H., et al. (1983), The atmosphere of Titan: An analysis of the Voyager 1 radio occultation measurements, *Icarus*, *53*(2), 348–363.

Lobo, A. H., Thompson, A. F., Vance, S. D., & Tharimena, S. (2021), A pole-to-equator ocean overturning circulation on Enceladus, *Nat. Geosci.*, *14*(4), 185–189.

Longuet-Higgins, M. S. (1968), The eigenfunctions of Laplace's tidal equations over a sphere, *Philos. Trans. Royal Soc. A*, *262*(1132), 511–607.

Lopes, R. M. & Spencer., J. R. (2007), *Io After Galileo*, Springer.

Lorenz, R. D., Stiles, B. W., Kirk, R. L., et al. (2008), Titan's rotation reveals an internal ocean and changing zonal winds, *Science*, *319*(5870), 1649–1651.

Love, A. (1906), *A treatise of the mathematical theory of elasticity*, Cambridge University Press.

Love, A. (1911), *Some problems of geodynamics*, Cambridge University Press.

Lunine, J. I., Stevenson, D. J., & Yung, Y. L. (1983), Ethane ocean on Titan, *Science*, *222*(4629), 1229–1230.

Maas, L. R. M. (2001), Wave focusing and ensuing mean flow due to symmetry breaking in rotating fluids, *J. Fluid Mech.*, *437*, 13–28.

Maas, L. R. M. (2005), Wave attractors: Linear yet nonlinear, *Int. J. Bifurcat. Chaos*, *15*(09), 2757–2782.

Maas, L. R. M., Benielli, D., Sommeria, J., & Lam, F.-P. A. (1997), Observation of an internal wave attractor in a confined, stably stratified fluid, *Nature*, *388*(6642), 557–561.

MacKenzie, S. M., Neveu, M., Davila, A. F., et al. (2021), The Enceladus orbilander mission concept: Balancing return and resources in the search for life, *Planet. Sci. J.*, *2*(2), 77.

Makarov, V. V. (2012), Conditions of passage and entrapment of terrestrial planets in spin-orbit resonances, *Astrophys. J.*, *752*(1), 73.

Makarov, V. V. & Efroimsky, M. (2014), Tidal dissipation in a homogeneous spherical body. ii. Three examples: Mercury, Io, and Kepler-10 b, *Astrophys. J.*, *795*(1), 7.

Malamud, U. & Prialnik, D. (2013), Modeling serpentinization: Applied to the early evolution of enceladus and mimas, *Icarus*, *225*(1), 763–774.

Malamud, U. & Prialnik, D. (2016), A 1-D evolutionary model for icy satellites, applied to Enceladus, *Icarus*, *268*, 1–11.

Malhotra, R. (1991), Tidal origin of the Laplace resonance and the resurfacing of Ganymede, *Icarus*, *94*(2), 399 – 412.

Manders, A. M. M. & Maas, L. R. M. (2003), Observations of inertial waves in a rectangular basin with one sloping boundary, *J. Fluid Mech.*, *493*, 59–88.

Manders, A. M. M. & Maas, L. R. M. (2004), On the three-dimensional structure of the inertial wave field in a rectangular basin with one sloping boundary, *Fluid Dyn. Res.*, *35*(1), 1–21.

Margules, M. (1893), Luftbewegungen in einer rotierenden Sphäroidschale, *Sber. Akad. Wiss.*, *102*.

Martin, W., Baross, J., Kelley, D., & Russell, M. J. (2008), Hydrothermal vents and the origin of life, *Nature Reviews Microbiology*, *6*(11), 805–814.

Marusiak, A. G., Vance, S., Panning, M. P., et al. (2021), Exploration of icy ocean worlds using geophysical approaches, *Planet. Sci. J.*, *2*(4), 150.

Matson, D. L., Ransford, G. A., & Johnson, T. V. (1981), Heat flow from Io (JI), *J. Geophys. Res. Solid Earth*, *86*(B3), 1664–1672.

Matson, D. L., Castillo, J. C., Lunine, J., & Johnson, T. V. (2007), Enceladus' plume: Compositional evidence for a hot interior, *Icarus*, *187*(2), 569–573.

Matsuyama, I. (2014), Tidal dissipation in the oceans of icy satellites, *Icarus*, *242*, 11 – 18.

Matsuyama, I., Beuthe, M., Hay, H. C., Nimmo, F., & Kamata, S. (2018), Ocean tidal heating in icy satellites with solid shells, *Icarus*, *312*, 208 – 230.

McCarthy, C. & Castillo-Rogez, J. C. (2013), Planetary ices attenuation properties, in The Science of Solar System Ices, edited by M. S. Gudipati and J. Castillo-Rogez, pp. 183–225, Springer New York, doi:10.1007/978-1-4614-3076-6_7.

McEwen, A., Turtle, E., Hibbard, K., Reynolds, E., & Adams, E. (2014), Io volcano observer (ivo): Budget travel to the outer solar system, *Acta Astronaut.*, *93*, 539–544.

McEwen, A. S., Keszthelyi, L., Geissler, P., et al. (1998), Active volcanism on Io as seen by Galileo SSI, *Icarus*, *135*(1), 181–219.

Mckenzie, D. (1984), The Generation and Compaction of Partially Molten Rock, *J. Petrol.*, *25*(3), 713–765.

McKinnon, W. B. (1984), On the origin of Triton and Pluto, *Nature*, *311*(5984), 355–358.

McKinnon, W. B. (2013), The shape of enceladus as explained by an irregular core: Implications for gravity, libration, and survival of its subsurface ocean, *J. Geophys. Res. Planets*, *118*(9), 1775–1788.

McKinnon, W. B. (2015), Effect of enceladus's rapid synchronous spin on interpretation of Cassini gravity, *Geophys. Res. Lett.*, *42*(7), 2137–2143.

McKinnon, W. B. & Leith, A. C. (1995), Gas drag and the orbital evolution of a captured Triton, *Icarus*, *118*(2), 392–413.

Mei, S., Bai, W., Hiraga, T., & Kohlstedt, D. (2002), Influence of melt on the creep behavior of olivine basalt aggregates under hydrous conditions, *Earth Planet. Sci. Lett.*, *201*(3), 491 – 507.

Melosh, H., Ekholm, A., Showman, A., & Lorenz, R. (2004), The temperature of Europa's subsurface water ocean, *Icarus*, *168*(2), 498–502.

Mendillo, M., Baumgardner, J., Flynn, B., & Hughes, W. J. (1990), The extended sodium nebula of Jupiter, *Nature*, *348*(6299), 312–314.

Meyer, J. & Wisdom, J. (2007), Tidal heating in Enceladus, *Icarus*, *188*(2), 535–539.

Miles, J. W. (1974), On Laplace's tidal equations, *J. Fluid Mech.*, *66*(2), 241–260.

Moore, W. B. (2001), The thermal state of Io, *Icarus*, *154*(2), 548 – 550.

Moore, W. B. (2003), Tidal heating and convection in Io, *J. Geophys. Res. Planets*, *108*(E8).

Moore, W. B. & Webb, A. A. G. (2013), Heat-pipe Earth, *Nature*, *501*(7468), 501–505.

Morabito, L. A. (2012), Discovery of Volcanic Activity on Io. A Historical Review.

Morabito, L. A., Synnott, S. P., Kupferman, P. N., & Collins, S. A. (1979), Discovery of currently active extraterrestrial volcanism, *Science*, *204*(4396), 972–972.

Morris, S. & Canright, D. (1984), A boundary-layer analysis of benard convection in a fluid of strongly temperature-dependent viscosity, *Phys. Earth Planet. Inter.*, *36*(3), 355 – 373.

Munk, W. (1997), Once again: once again tidal friction, *Prog. Oceanogr.*, *40*(1), 7–35.

Munk, W. & Wunsch, C. (1997), The Moon, of course..., *Oceanography*, *10*(3), 132–134.

Mura, A., Adriani, A., Tosi, F., et al. (2020), Infrared observations of io from juno, *Icarus*, *341*, 113,607.

Murray, C. & Dermott, S. (2000), *Solar System Dynamics*, Cambridge University Press.

Nederend, J., Rovira-Navarro, M., & Pestana, T. (2020), Thermal convection in subsurface oceans with variable thickness: Application to Enceladus., *Earth and Space Science Open Archive*, p. 13.

Nimmo, F. & Bills, B. (2010), Shell thickness variations and the long-wavelength topography of titan, *Icarus*, *208*(2), 896–904.

Nimmo, F. & Spencer, J. (2015), Powering Triton's recent geological activity by obliquity tides: Implications for Pluto geology, *Icarus*, *246*, 2 – 10, special Issue: The Pluto System.

Nimmo, F. & Stevenson, D. J. (2000), Influence of early plate tectonics on the thermal evolution and magnetic field of Mars, *J. Geophys. Res. Planets*, *105*(E5), 11,969–11,979.

Nimmo, F., Thomas, P., Pappalardo, R., & Moore, W. (2007), The global shape of Europa: Constraints on lateral shell thickness variations, *Icarus*, *191*(1), 183 – 192.

Nimmo, F., Porco, C., & Mitchell, C. (2014), Tidally modulated eruptions on Enceladus:Cassini ISS observations and models, *Astron. J.*, *148*(3), 46.

Nimmo, F., Barr, A. C., Běhounková, M., & McKinnon, W. B. (2018), The thermal and orbital evolution of Enceladus: Observational constraints and models., in Enceladus and the Icy Moons of Saturn, edited by P. M. Schenk, R. N. Clark, C. J. A. Howett, A. J. Verbiscer, and J. H. Waite, pp. 79–94, University of Arizona Press, doi:10.2458/azu_uapress_9780816537075-ch005.

Noack, L., Rivoldini, A., & Van Hoolst, T. (2017), Volcanism and outgassing of stagnant-lid planets: Implications for the habitable zone, *Phys. Earth Planet. Inter.*, *269*, 40 – 57.

Noir, J., Hemmerlin, F., Wicht, J., Baca, S., & Aurnou, J. (2009), An experimental and numerical study of librationally driven flow in planetary cores and subsurface oceans, *Phys. Earth Planet. Inter.*, *173*(1), 141–152.

Noyola, J. P., Satyal, S., & Musielak, Z. E. (2014), Detection of exomoons through observation of radio emissions, *Astrophys. J.*, *791*(1), 25.

Noyola, J. P., Satyal, S., & Musielak, Z. E. (2016), On the radio detection of multiple-exomoon systems due to plasma torus sharing, *Astrophys. J.*, *821*(2), 97.

Ogilvie, G. I. (2005), Wave attractors and the asymptotic dissipation rate of tidal disturbances, *J. Fluid Mech.*, *543*, 19–44.

Ogilvie, G. I. (2009), Tidal dissipation in rotating fluid bodies: a simplified model, *Mon. Not. R. Astron. Soc.*, *396*(2), 794–806.

Ogilvie, G. I. (2014), Tidal dissipation in stars and giant planets, *Annu. Rev. Astron. Astrophys.*, *52*(1), 171–210.

Ogilvie, G. I. & Lin, D. N. C. (2004), Tidal dissipation in rotating giant planets, *Astrophys. J.*, *610*(1), 477–509.

Ojakangas, G. & Stevenson, D. (1986), Episodic volcanism of tidally heated satellites with application to Io, *Icarus*, *66*(2), 341 – 358.

Ojakangas, G. W. & Stevenson, D. J. (1989), Thermal state of an ice shell on Europa, *Icarus*, *81*(2), 220 – 241.

Olsen, K. G., Hurford, T. A., Schmerr, N. C., et al. (2021), Projected seismic activity at the tiger stripe fractures on Enceladus, Saturn, from an analog study of tidally modulated icequakes within the Ross Ice Shelf, Antarctica, *Journal of Geophysical Research: Planets*, *126*(6), e2021JE006,862, e2021JE006862 2021JE006862.

O'Reilly, T. C. & Davies, G. F. (1981), Magma transport of heat on Io: A mechanism allowing a thick lithosphere, *Geophys. Res. Lett.*, *8*(4), 313–316.

Oza, A. V., Johnson, R. E., Lellouch, E., et al. (2019), Sodium and potassium signatures of volcanic satellites orbiting close-in gas giant exoplanets, *Astrophys. J.*, *885*(2), 168.

Panning, M. P., Stähler, S. C., Huang, H.-H., et al. (2018), Expected seismicity and the seismic noise environment of Europa, *J. Geophys. Res. Planets*, *123*(1), 163–179.

Pappalardo, R., Vance, S., Bagenal, F., et al. (2013), Science potential from a Europa lander, *Astrobiology*, *13*(8), 740–773, pMID: 23924246.

Pappalardo, R. T., Belton, M. J. S., Breneman, H. H., et al. (1999), Does Europa have a subsurface ocean? Evaluation of the geological evidence, *J. Geophys. Res. Planets*, *104*(E10), 24,015–24,055.

Peale, S., Cassen, P., & Reynolds, R. (1980), Tidal dissipation, orbital evolution, and the nature of Saturn's inner satellites, *Icarus*, *43*(1), 65–72.

Peale, S. J. (1976), Orbital resonances in the Solar System, *Annu. Rev. Astron. Astrophys.*, *14*(1), 215–246.

Peale, S. J. (1999), Origin and evolution of the natural satellites, *Annu. Rev. Astron. Astrophys.*., *37*(1), 533–602.

Peale, S. J. & Lee, M. H. (2002), A primordial origin of the Laplace relation among the Galilean satellites, *Science*, *298*(5593), 593–597.

Peale, S. J., Cassen, P., & Reynolds, R. T. (1979), Melting of Io by tidal dissipation, *Science*, *203*(4383), 892–894.

Peltier, W. R. (1974), The impulse response of a Maxwell Earth, *Rev. Geophys.*, *12*(4), 649–669.

Peters, M. A. & Turner, E. L. (2013), On the direct imaging of tidally heated exomoons, *Astrophys. J.*, *769*(2), 98.

Phillips, C. B. (2000), Voyager and galileo ssi views of volcanic resurfacing on Io and the search for geologic activity on Europa. phd thesis.

Phillips, C. B. & Pappalardo, R. T. (2014), Europa Clipper mission concept: Exploring Jupiter's ocean moon, *Eos, Transactions American Geophysical Union*, *95*(20), 165–167.

Platzman, G. W. (1975), Normal modes of the Atlantic and Indian oceans, *J. Phys. Oceanogr.*, *5*(2), 201–221.

Platzman, G. W. (1978), Normal modes of the world ocean. part I. design of a finite-element barotropic model, *J. Phys. Oceanogr.*, *8*(3), 323–343.

Pleiner Sládková, K., Souček, O., & Běhounková, M. (2021), Enceladus' tiger stripes as frictional faults: Effect on stress and heat production, *Geophysical Research Letters*, *48*(19), e2021GL094,849, e2021GL094849 2021GL094849.

Poinelli, M., Larour, E., Castillo-Rogez, J., & Vermeersen, B. (2019), Crevasse propagation on brittle ice: Application to cycloids on Europa, *Geophys. Res. Lett.*, *46*(21), 11,756–11,763.

Polycarpe, W., Saillenfest, M., Lainey, V., et al. (2018), Strong tidal energy dissipation in Saturn at Titan´s frequency as an explanation for Iapetus orbit, *Astron. Astrophys.*, *619*, A133.

Porco, C. C., Helfenstein, P., Thomas, P. C., et al. (2006), Cassini observes the active South Pole of Enceladus, *Science*, *311*(5766), 1393–1401.

Postberg, F., Kempf, S., Schmidt, J., et al. (2009), Sodium salts in E-ring ice grains from an ocean below the surface of Enceladus, *Nature*, *459*, 1098–1101.

Postberg, F., Schmidt, J., Hillier, J., Kempf, S., & Srama, R. (2011), A salt-water reservoir as the source of a compositionally stratified plume on Enceladus, *Nature*, *474*, 620–622.

Postberg, F., Khawaja, N., Abel, B., et al. (2018), Macromolecular organic compounds from the depths of Enceladus, *Nature*, *558*(7711), 564–568.

Quick, L. C., Roberge, A., Mlinar, A. B., & Hedman, M. M. (2020), Forecasting rates of volcanic activity on terrestrial exoplanets and implications for cryovolcanic activity on extrasolar ocean worlds, *Publ. Astron. Soc. Pac.*, *132*(1014), 084,402.

Rabitti, A. & Maas, L. R. (2014), Inertial wave rays in rotating spherical fluid domains, *J. Fluid Mech.*, *758*, 621–654.

Rabitti, A. & Maas, L. R. M. (2013), Meridional trapping and zonal propagation of inertial waves in a rotating fluid shell, *J. Fluid Mech.*, *729*, 445–470.

Rambaux, N., Castillo-Rogez, J. C., Williams, J. G., & Karatekin, O. (2010), Librational response of Enceladus, *Geophys. Res. Lett.*, *37*(4).

Reese, C., Solomatov, V., & Moresi, L.-N. (1999), Non-newtonian stagnant lid convection and magmatic resurfacing on Venus, *Icarus*, *139*(1), 67 – 80.

Rekier, J., Trinh, A., Triana, S. A., & Dehant, V. (2019), Internal energy dissipation in Enceladus's subsurface ocean from tides and libration and the role of inertial waves, *J. Geophys. Res. Planets*, *124*(8), 2198–2212.

Renaud, J. P. & Henning, W. G. (2018), Increased tidal dissipation using advanced rheological models: Implications for Io and tidally active exoplanets, *Astrophys. J.*, *857*(2), 98.

Renaud, J. P., Henning, W. G., Saxena, P., et al. (2021), Tidal Dissipation in Dual-body, Highly Eccentric, and Nonsynchronously Rotating Systems: Applications to Pluto-Charon and the Exoplanet TRAPPIST-1e, *Planet. Sci. J.*, *2*(1), 4.

Rhoden, A. R. & Walker, M. E. (2022), The case for an ocean-bearing mimas from tidal heating analysis, *Icarus*, *376*, 114,872.

Rieutord, M. (1987), Linear theory of rotating fluids using spherical harmonics part I: Steady flows, *Geophys. Astro. Fluid*, *39*(3), 163–182.

Rieutord, M. & Valdettaro, L. (1997), Inertial waves in a rotating spherical shell, *J. Fluid Mech.*, *341*, 77–99.

Rieutord, M. & Valdettaro, L. (2010), Viscous dissipation by tidally forced inertial modes in a rotating spherical shell, *J. Fluid Mech.*, *643*, 363–394.

Rieutord, M. & Valdettaro, L. (2018), Axisymmetric inertial modes in a spherical shell at low Ekman numbers, *J. Fluid Mech.*, *844*, 597–634.

Rieutord, M., Georgeot, B., & Valdettaro, L. (2001), Inertial waves in a rotating spherical shell: attractors and asymptotic spectrum, *J. Fluid Mech.*, *435*, 103–144.

Roberts, J. H. (2015), The fluffy core of Enceladus, *Icarus*, *258*, 54 – 66.

Roberts, J. H. & Nimmo, F. (2008), Tidal heating and the long-term stability of a subsurface ocean on Enceladus, *Icarus*, *194*(2), 675 – 689.

Rollins, K. M., Evans, M. D., Diehl, N. B., & III, W. D. D. (1998), Shear modulus and damping relationships for gravels, *J. Geotech. Geoenviron. Eng.*, *124*(5), 396–405.

Ross, M. N. & Schubert, G. (1987), Tidal heating in an internal ocean model of Europa, *Nature*, *325*(6100), 133–134.

Rossby, C. (1939), Relation between variations in the intensity of the zonal circulation of the atmosphere and the displacement of the semi-permanent centers of action, *J. Mar. Res*, *2*, 38–55.

Roth, L., Saur, J., Retherford, K. D., et al. (2017), Constraints on Io's interior from auroral spot oscillations, *J. Geophys. Res. Planets*, *122*(2), 1903–1927.

Rothery, D. A. (1999), *Satellites of the outer planets : worlds in their own right*, second edition ed., Oxford University Press.

Rovira-Navarro, M., Rieutord, M., Gerkema, T., et al. (2019), Do tidally-generated inertial waves heat the subsurface oceans of Europa and Enceladus?, *Icarus*, *321*, 126 – 140.

Rovira-Navarro, M., Gerkema, T., Maas, L. R., et al. (2020), Tides in subsurface oceans with meridional varying thickness, *Icarus*, *343*, 113,711.

Rovira-Navarro, M., van der Wal, W., Steinke, T., & Dirkx, D. (2021), Tidally heated exomoons around gas giants, *Planet. Sci. J.*, *2*(3), 119.

Rovira-Navarro, M., Katz, R. F., Liao, Y., van der Wal, W., & Nimmo, F. (2022), The tides of enceladus' porous core, *J. Geophys. Res. Planets*, *127*(5), e2021JE007,117, e2021JE007117 2021JE007117.

Rymer, A., Runyon, K., Vertisi, J., et al. (2021), Neptune and Triton: A flagship for everyone, in Bulletin of the American Astronomical Society, vol. 53, p. 374, doi: 10.3847/25c2cfeb.0b72af56.

Rymer, A. M., Clyde, B., Runyon, K., & Neptune-Odyssey team (2020), Neptune Odyssey: Mission to the Neptune-Triton system, *LPI Contributions*, *2547*, 6031.

Sabadini, R., Vermeersen, B., & Cambiotti, G. (2016), *Global dynamics of the Earth: Applications of viscoelastic relaxation theory to solid-Earth and planetary geophysics: Second edition*, Springer.

Sagan, C. & Dermott, S. F. (1982), The tide in the seas of Titan, *Nature*, *300*, 731 EP –.

Saito, M. (1974), Some problems of static deformation of the Earth, *J. Phys. Earth*, *22*(1), 123–140.

Saur, J., Duling, S., Roth, L., et al. (2015), The search for a subsurface ocean in Ganymede with Hubble Space Telescope observations of its auroral ovals, *J. Geophys. Res. Space Phys.*, *120*(3), 1715–1737.

Schenk, P. M. & Zahnle, K. (2007), On the negligible surface age of Triton, *Icarus*, *192*(1), 135–149.

Schubert, G., Cassen, P., & Young, R. (1979), Subsolidus convective cooling histories of terrestrial planets, *Icarus*, *38*(2), 192 – 211.

Schubert, G., Spohn, T., & Reynolds, R. T. (1986), Thermal histories, compositions and internal structures of the moons of the solar system., in Satellites, pp. 224–292.

Schubert, G., Turcotte, D., & Olson, P. (2001), *Mantle Convection in the Earth and Planets*, Cambridge University Press.

Sears, W. D. (1995), Tidal dissipation in oceans on Titan, *Icarus*, *113*(1), 39 – 56.

Seed, H. B., Wong, R. T., Idriss, I. M., & Tokimatsu, K. (1986), Moduli and damping factors for dynamic analyses of cohesionless soils, *J. Geotech. Eng.*, *112*(11), 1016–1032.

Segatz, M., Spohn, T., Ross, M., & Schubert, G. (1988), Tidal dissipation, surface heat flow, and figure of viscoelastic models of Io, *Icarus*, *75*(2), 187–206.

Shoji, D. & Kurita, K. (2014), Thermal-orbital coupled tidal heating and habitability of Martian-Sized extrasolar planets around M stars, *Astrophys. J.*, *789*(1), 3.

Shoji, D., Hussmann, H., Kurita, K., & Sohl, F. (2013), Ice rheology and tidal heating of enceladus, *Icarus*, *226*(1), 10–19.

Simonelli, D. P., Dodd, C., & Veverka, J. (2001), Regolith variations on Io: Implications for bolometric albedos, *J. Geophys. Res. Planets*, *106*(E12), 33,241–33,252.

Smith, B. A., Soderblom, L. A., Johnson, T. V., et al. (1979a), The Jupiter System Through the Eyes of Voyager 1, *Science*, *204*(4396), 951–972.

Smith, B. A., Soderblom, L. A., Beebe, R., et al. (1979b), The Galilean Satellites and Jupiter: Voyager 2 Imaging Science Results, *Science*, *206*(4421), 927–950.

Smith, B. A., Soderblom, L., Beebe, R., et al. (1981), Encounter with Saturn: Voyager 1 imaging science results, *Science*, *212*(4491), 163–191.

Smith, B. A., Soderblom, L., Batson, R., et al. (1982), A New Look at the Saturn System: The Voyager 2 images, *Science*, *215*(4532), 504–537.

Smith, B. A., Soderblom, L. A., Banfield, D., et al. (1989), Voyager 2 at Neptune: Imaging science results, *Science*, *246*(4936), 1422–1449.

Snellen, I. A. G., Brandl, B. R., de Kok, R. J., et al. (2014), Fast spin of the young extrasolar planet β Pictoris b, *Nature*, *509*(7498), 63–65.

Soderlund, K. M. (2019), Ocean dynamics of outer Solar System satellites, *Geophys. Res. Lett.*, *46*(15), 8700–8710.

Soderlund, K. M., Schmidt, B. E., Wicht, J., & Blankenship, D. D. (2013), Ocean-driven heating of Europa's icy shell at low latitudes, *Nat. Geosci.*, *7*, 16–19.

Soderlund, K. M., Kalousová, K., Buffo, J. J., et al. (2020), Ice-ocean exchange processes in the Jovian and Saturnian satellites, *Space Sci. Rev.*, *216*(5), 80.

Sohl, F. & Spohn, T. (1997), The interior structure of Mars: Implications from SNC meteorites, *J. Geophys. Res. Planets*, *102*(E1), 1613–1635.

Solomatov, V. (2007), 9.04 -Magma oceans and primordial mantle differentiation, in Treatise on Geophysics, edited by G. Schubert, pp. 91 – 119, Elsevier, doi:10.1016/B978-044452748-6.00141-3.

Solomatov, V. S. (1995), Scaling of temperature-and stress-dependent viscosity convection, *Phys. Fluids*, *7*(2), 266–274.

Souček, O., Hron, J., Bêhounková, M., & Čadek, O. (2016), Effect of the tiger stripes on the deformation of Saturn's moon Enceladus, *Geophys. Res. Lett.*, *43*(14), 7417–7423.

Souček, O., Bêhounková, M., Čadek, O., et al. (2019), Tidal dissipation in Enceladus' uneven, fractured ice shell, *Icarus*, *328*, 218 – 231.

Spencer, D. C., Katz, R. F., & Hewitt, I. J. (2020), Magmatic intrusions control Io's crustal thickness, *J. Geophys. Res. Planets*, *125*(6), e2020JE006,443, e2020JE006443 10.1029/2020JE006443.

Spencer, J. R., Sartoretti, P., Ballester, G. E., et al. (1997), The Pele plume (Io): Observations with the Hubble Space Telescope, *Geophys. Res. Lett.*, *24*(20), 2471–2474.

Spencer, J. R., Rathbun, J. A., Travis, L. D., et al. (2000), Io's thermal emission from the galileo photopolarimeter- radiometer, *Science*, *288*(5469), 1198–1201.

Spencer, J. R., Pearl, J. C., Segura, M., et al. (2006), Cassini encounters Enceladus: Background and the discovery of a south polar hot spot, *Science*, *311*(5766), 1401–1405.

Spencer, J. R., Stern, S. A., Cheng, A. F., et al. (2007), Io volcanism seen by new horizons: A major eruption of the tvashtar volcano, *Science*, *318*(5848), 240–243.

Spencer, J. R., Howett, C. J. A., Verbiscer, A., et al. (2013), Enceladus Heat Flow from High Spatial Resolution Thermal Emission Observations, *European Planetary Science Congress*, *8*, EPSC2013-840.

Spohn, T. & Schubert, G. (2003), Oceans in the icy Galilean satellites of Jupiter?, *Icarus*, *161*(2), 456 – 467.

Stähler, S. C., Khan, A., Banerdt, W. B., et al. (2021), Seismic detection of the Martian core, *Science*, *373*(6553), 443–448.

Steinbrügge, G., Stark, A., Hussmann, H., Sohl, F., & Oberst, J. (2015), Measuring tidal deformations by laser altimetry. a performance model for the Ganymede laser altimeter, *Planet. Space Sci.*, *117*, 184–191.

Steinbrügge, G., Schroeder, D., Haynes, M., et al. (2018), Assessing the potential for measuring Europa's tidal Love number h2 using radar sounder and topographic imager data, *Earth Planet. Sci. Lett.*, *482*, 334–341.

Steinke, T. (2021), The curious case of Io: Connections between interior structure, tidal heating and volcanism, Ph.D. thesis, Delft University of Technology.

Steinke, T., van Sliedregt, D., Vilella, K., van der Wal, W., & Vermeersen, B. (2020a), Can a combination of convective and magmatic heat transport in the mantle explain Io's volcanic pattern?, *J. Geophys. Res. Planets*, *125*(12), e2020JE006,521, e2020JE006521 2020JE006521.

Steinke, T., Hu, H., Honing, D., van der Wal, W., & Vermeersen, B. (2020b), Tidally induced lateral variations of Io's interior, *Icarus*, *335*, 113,299.

Stern, M. E. (1963), Trapping of low frequency oscillations in an equatorial "boundary layer", *Tellus*, *15*(3), 246–250.

Stern, S. A. & McKinnon, W. B. (2000), Triton's surface age and impactor population revisited in light of Kuiper belt fluxes: Evidence for small Kuiper belt objects and recent geological activity, *Astron. J.*, *119*(2), 945–952.

Stevenson, D. J. (2020), Jupiter's interior as revealed by Juno, *Annu. Rev. Earth Planet. Sci.*, *48*(1), 465–489.

Stewartson, K. (1971), On trapped oscillations of a rotating fluid in a thin spherical shell, *Tellus*, *23*(6), 506–510.

Stewartson, K. (1972), On trapped oscillations of a rotating fluid in a thin spherical shell ii, *Tellus*, *24*(4), 283–287.

Stiles, B. W., Kirk, R. L., Lorenz, R. D., et al. (2008), Determining Titan's spin state from Cassini radar images, *Astron. J.*, *135*(5), 1669–1680.

Stofan, E. R., Elachi, C., Lunine, J. I., et al. (2007), The lakes of Titan, *Nature*, *445*(7123), 61–64.

Takahashi, E. (1990), Speculations on the Archean mantle: Missing link between komatiite and depleted garnet peridotite, *J. Geophys. Res. Solid Earth*, *95*(B10), 15,941–15,954.

Takeuchi, H., Saito, M., & Kobayashi, N. (1962), Statical deformations and free oscillations of a model Earth, *J. Geophys. Res.*, *67*(3), 1141–1154.

Teachey, A. & Kipping, D. M. (2018), Evidence for a large exomoon orbiting Kepler-1625b, *Sci. Adv.*, *4*(10).

Teachey, A., Kipping, D. M., & Schmitt, A. R. (2017), HEK. VI. on the dearth of Galilean analogs in Kepler, and the exomoon candidate Kepler-1625b I, *Astrophys. J.*, *155*(1), 36.

Terrile, R. & Cook, A. (1981), Enceladus: Evolution and possible relationship with Saturn's E-ring, *Lunar Planet. Sci. (Suuppl. A)*, *12*(10).

Thomas, P. (2010), Sizes, shapes, and derived properties of the Saturnian satellites after the Cassini nominal mission, *Icarus*, *208*(1), 395 – 401.

Thomas, P., Tajeddine, R., Tiscareno, M., et al. (2016), Enceladus' measured physical libration requires a global subsurface ocean, *Icarus*, *264*, 37 – 47.

Thomson, W. (1863), On the rigidity of the Earth, *Proc. R. Soc. Lond.*, *153*, 573–582.

Thomson, W. & Tait, P. (1911), *Natural Philosophy, Vol I, Part II*, Cambridge University Press.

Tobie, G., Mocquet, A., & Sotin, C. (2005), Tidal dissipation within large icy satellites: Applications to Europa and Titan, *Icarus*, *177*(2), 534–549.

Tobie, G., Čadek, O., & Sotin, C. (2008), Solid tidal friction above a liquid water reservoir as the origin of the south pole hotspot on Enceladus, *Icarus*, *196*(2), 642 – 652.

Tokano, T. (2010), Simulation of tides in hydrocarbon lakes on saturn's moon Titan, *Ocean Dyn.*, *60*(4), 803–817.

Turcotte, D. & Schubert, G. (2014), Heat transfer, in Geodynamics, 3 ed., pp. 160–229, Cambridge University Press, doi:10.1017/CBO9780511843877.005.

Tyler, R. (2011), Tidal dynamical considerations constrain the state of an ocean on Enceladus, *Icarus*, *211*(1), 770 – 779.

Tyler, R. (2014), Comparative estimates of the heat generated by ocean tides on icy satellites in the outer Solar System, *Icarus*, *243*, 358 – 385.

Tyler, R. H. (2008), Strong ocean tidal flow and heating on moons of the outer planets, *Nature*, *456*(7223), 770–772.

Tyler, R. H. (2009), Ocean tides heat Enceladus, *Geophys. Res. Lett.*, *36*(15), l15205.

Tyler, R. H. (2019), Introducing the Tidal Response of Planetary Fluids (TROPF) Software Package, in Lunar and Planetary Science Conference, Lunar and Planetary Science Conference, p. 2883.

Tyler, R. H. (2020), Heating of Enceladus due to the dissipation of ocean tides, *Icarus*, *348*, 113,821.

Tyler, R. H. (2021), On the tidal history and future of the Earth–Moon orbital system, *Planet. Sci. J.*, *2*(2), 70.

Tyler, R. H., Henning, W. G., & Hamilton, C. W. (2015), Tidal heating in a magma ocean within Jupiter's moon Io, *Astrophys. J.s*, *218*(2), 22.

Vallis, G. K. (2006), *Atmospheric and Oceanic Fluid Dynamics*, 745 pp., Cambridge University Press.

Vance, S. & Brown, J. (2005), Layering and double-diffusion style convection in Europa's ocean, *Icarus*, *177*(2), 506 – 514.

Vance, S. & Goodman, J. (2009), Oceanography of an Ice-Covered Moon, in Europa, edited by R. T. Pappalardo, W. B. McKinnon, and K. K. Khurana, pp. 459–482, University of Arizona Press.

Vance, S., Harnmeijer, J., Kimura, J., et al. (2007), Hydrothermal systems in small ocean planets, *Astrobiology*, *7*(6), 987–1005, pMID: 18163874.

Vance, S. D., Kedar, S., Panning, M. P., et al. (2018), Vital signs: Seismology of icy ocean worlds, *Astrobiology*, *18*(1), 37–53, pMID: 29345986.

Vance, S. D., Styczinski, M. J., Bills, B. G., et al. (2021), Magnetic induction responses of Jupiter's ocean moons including effects from adiabatic convection, *J. Geophys. Res. Planets*, *126*(2), e2020JE006,418, e2020JE006418 2020JE006418.

Veeder, G. J., Matson, D. L., Johnson, T. V., Blaney, D. L., & Goguen, J. D. (1994), Io's heat flow from infrared radiometry: 1983–1993, *J. Geophys. Res. Planets*, *99*(E8), 17,095–17,162.

Vermeersen, B. L., Maas, L. R., van Oers, S., Rabitti, A., & Jara-Orue, H. (2013), Tidal-induced ocean dynamics as cause of Enceladus' tiger stripe pattern, *AGU Fall Meeting Abstracts*, P53B-1848.

Waite, J. H., Glein, C. R., Perryman, R. S., et al. (2017), Cassini finds molecular hydrogen in the Enceladus plume: Evidence for hydrothermal processes, *Science*, *356*(6334), 155–159.

Walterová, M. & Běhounková, M. (2017), Tidal effects in differentiated viscoelastic bodies: a numerical approach, *Celest. Mech. Dyn. Astron.*, *129*(1), 235–256.

Walterová, M. & Běhounková, M. (2020), Thermal and orbital evolution of low-mass exoplanets, *Astrophys. J.*, *900*(1), 24.

Wang, K. & Davis, E. E. (1996), Theory for the propagation of tidally induced pore pressure variations in layered subseafloor formations, *J. Geophys. Res. Solid Earth*, *101*(B5), 11,483–11,495.

Wang, K., Van Der Kamp, G., & Davis, E. E. (1999), Limits of tidal energy dissipation by fluid flow in subsea formations, *Geophys. J. Int.*, *139*(3), 763–768.

Williams, D. M. (2013), Capture of terrestrial-sized moons by gas giant planets, *Astrobiology*, *13*(4), 315–323, pMID: 23537110.

Wilson, A. & Kerswell, R. R. (2018), Can libration maintain Enceladus's ocean?, *Earth Planet. Sci. Lett.*, *500*, 41 – 46.

Wu, P. (2004), Using commercial finite element packages for the study of earth deformations, sea levels and the state of stress, *Geophys. J. Int.*, *158*(2), 401–408.

Wu, P. & Peltier, W. R. (1982), Viscous gravitational relaxation, *Geophys. J. Int.*, *70*(2), 435–485.

Yoder, C. F. (1979), How tidal heating in Io drives the galilean orbital resonance locks, *Nature*, *279*(5716), 767–770.

Yoder, C. F. & Peale, S. J. (1981), The tides of Io, *Icarus*, *47*(1), 1 – 35.

Zanazzi, J. & Triaud, A. H. (2019), The ability of significant tidal stress to initiate plate tectonics, *Icarus*, *325*, 55 – 66.

Zeng, Y. & Jansen, M. F. (2021), Ocean circulation on enceladus with a high- versus low-salinity ocean, *Planet. Sci. J.*, *2*(4), 151.

Zimmerman, W., Bryant, S., Zitzelberger, J., & Nesmith, B. (2001), A radioisotope powered cryobot for penetrating the Europan ice shell, *AIP Conference Proceedings*, *552*(1), 707–715.

CURRICULUM VITÆ

Marc ROVIRA-NAVARRO

20-03-1993	Born in Barcelona, Spain

EDUCATION

2004-2011	Secondary Education Escola Pia Santa Anna, Mataró, Spain
2011–2015	Bachelor of Aerospace Engineering Polytechnic University of Catalonia, Terrassa, Spain *Thesis*: Study of a New Trajectory Planner for Mars Entry Guidance
2015–2017	Master of Science in Aerospace Engineering (cum laude) Delft University of Technology, Delft, The Netherlands *Thesis*: Studying the Svalbard-Barents-Kara Ice Sheet Using GRACE Observations
2017–2021	PhD Aerospace Engineering Delft University of Technology, Delft, The Netherlands *Thesis*: Tidal Dynamics of Moons with Fluid Layers

List of Publications

Journal Articles

7. **Rovira-Navarro, M.**, Katz, R. F., Liao, Y., van der Wal, W., & Nimmo, F. (2022). The Tides of Enceladus' Porous Core. Journal of Geophysical Research: Planets, 127, e2021JE007117

6. **Rovira-Navarro, M.**, van der Wal, W., Steinke, T., & Dirkx, D. (2021) Tidally heated exomoons around gas giants. *The Planetary Science Journal*, 2, 119

5. Soderlund, K.M., Kalousová, K., Buffo, J.J., Glein, C.R., Goodman, J.C., Mitri, G., Patterson, G.W., Postberg, F., **Rovira-Navarro, M.**, Rückriemen, T., Saur, J., Schmidt, B.E., Sotin, C., Spohn, T., Tobie, G., Van Hoolst, T., Vance, S.D., & Vermeersen, B.(2020) Ice-Ocean Exchange Processes in Outer Solar System Satellites. *Space Science Reviews*, 216, 80

4. **Rovira-Navarro, M.**, Gerkema, T., Maas, L. R. M., van der Wal, W., van Ostayen, R., & Vermeersen, B. (2020) Tides in Subsurface Oceans with Meridional Varying Thickness. *Icarus*, 343, 11371

3. **Rovira-Navarro, M.**, van der Wal, W., Barletta, V.R., Root, B.C., & Sandberg Sørensen, L. (2020) GRACE constraints on Earth rheology of the Barents Sea and Fennoscandia. *Solid Earth*, 11(2), 379-395

2. **Rovira-Navarro, M.**, Rieutord, M., Gerkema, T., Maas, L. R. M., van der Wal, W., & Vermeersen, B. (2019). Do tidally-generated inertial waves heat the subsurface oceans of Europa and Enceladus? *Icarus*, 321, 126–140

1. Barletta, V.R., Bevis, M., Smith, B.E., Wilson, T., Brown, A., Bordoni, A., Willis, M., Khan, S.A., **Rovira-Navarro, M.**, Dalziel, I., Smalley, R., Kendrick, E., Konfal, S., Caccamise, D.J., Aster, R.C., Nyblade, A., & Wiens, D.A. (2018). Observed rapid bedrock uplift in Amundsen Sea Embayment promotes ice-sheet stability. *Science*, 360(6395), 1335-1339

Selected Conference Contributions

8. Kleisioti, K., Dirkx, D., **Rovira-Navarro, M.**, Kenworthy, M. (2021). Could we observe exomoons around β Pictoris b? European Planetary Science Congress 2021, online, 13–24 Sep 2021, EPSC2021-546

7. Nederend, J., **Rovira-Navarro, M.**, Pestana, T. (2020). Thermal convection in subsurface oceans with variable thickness: Application to Enceladus. American Geophysical Union Fall Meeting, December 2020

6. **Rovira-Navarro, M.**, van der Wal, W., Steinke, T., B. Vermeersen, B., and Gerkema, T. (2020). Tidally heated exomoons around cold exoplanets. Lunar and Planetary Science Conference

5. **Rovira-Navarro, M.**, Gerkema, T., Maas, L. R. M., van der Wal, W., van Ostayen, R., and Vermeersen, B. (2019). Tidal dissipation in ice-covered, homogeneous-density oceans of variable thickness. American Geophysical Union Fall Meeting, December 2019.

4. Balachandran, K., Nathan, E., **Rovira-Navarro, M.**, Cappuccio, P., Di, J., Doerksen, K. , Fuchs, J., Gloder, A., Jolitz, R., Li,M. , Limonchik,D. , Massarweh, L., Meszaros, A., Naftalovich, D., Peev, T. and Santra, S. (2019). SILENUS: A Mission Concept Investigating the Habitability of Enceladus. EPSC Abstracts Vol. 13, EPSC-DPS2019-1302-1

3. **Rovira-Navarro, M.**, Sandberg, L., Barletta, V.R., and van der Wal, W. (2017). Is a GIA signal in GRACE data present in the Kara Sea region? Abstract of European Geoscience Union (EGU) General Assembly; Geophysical Research Abstracts, Vol. 19, EGU2017-19152-1

2. Barletta, V.R, **Rovira-Navarro, M.**, Bodoni, A., Bevis, M., Wilson, T., and Willis, M.J. (2017). Sea level contribution from Amundsen Embayment in the last 200 years. Abstract of European Geoscience Union (EGU) General Assembly, Research Abstracts, Vol. 19, EGU2017-9906-2.

1. Duan, G., **Rovira-Navarro, M.**, and Mease, K.D. Trajectory Tracking and Online Replanning for Mars Entry. (2016) AIAA/AAS Astrodynamics Specialist Conference, AIAA SPACE Forum, (AIAA 2016-5444)

AFTERWORD

Seven years ago, I arrived to Delft with a bag full of questions and the idea that I wanted to learn "something about Space". After much rambling through Vermeer-splashed streets, I can say I have definitely learned, but the bag of questions has grown heavier. In the process, I have crossed paths with people who have taught me about science and life and shaped the researcher and person I have become.

In 2016, during my MSc studies, I approached Wouter van der Wal to inquire about the possibility of doing an internship on how melting glaciers and the solid Earth interact. I still remember how nervous I felt siting in his office for the first time. Since then, we have been working together on different topics and that nervous smile of mine has turned into the sincere smile of one who knows he will be listened to. Thanks for encouraging me to explore new ideas, providing good guidance and trusting in me specially when I was unsure about myself. After finishing my MSc, Wouter told me Bert Vermeersen, Leo Maas, Theo Gerkema and himself had an upcoming PhD project about tides in the moons of the outer Solar System and encouraged me to apply. I could not have been more thrilled when I received the news I could take the position.

I want to thank Bert Vermeersen for giving me the opportunity to work in the field of planetary sciences; thanks for entrusting me with this project and encouraging me to pursue my ideas, be bold and independent. I also want to thank Leo Maas and Theo Gerkema for their support. Without their knowledge, guidance and patience to teach me the music of Earth's oceans I could have never dreamt of imagining the waves that echo in extraterrestrial seas. Leo, thanks for welcoming me to Utrecht University, leaving your office I always felt wiser than when I entered; and Theo, thanks for our endless discussions in Yerseke that ranged from tides to Borges and which I always looked forward to.

Throughout this journey I have had the opportunity to meet and work with outstanding people who have shaped how I do and understand science. I want to start with Valentina Barletta, who kindly received me in Copenhagen when I was just starting my career and advised me to be an open and gregarious scientist, I hope this can be felt throughout the thesis. I want to thank my co-authors, Michael Rieutord, Ron van Ostayen, Dominic Dirkx (who also had the patience to read the thesis and provide insightful comments), Teresa Steinke, Richard Katz, Yang Liao and Francis Nimmo and the other exceptional people I have had the pleasure to discuss ideas with during these years: Rob Tyler, Hamish Hay, Tiago Pestana, Jeffrey Nederend, Mikale Beuthe, Jeremy Rekier, Santiago Andrés Triana, Ondřej Čadek, Ondřej Souček, Marie Běhounková, Joe Renaud, etc. As I move to the next step of my career, I hope to keep learning from you all. A special mention goes to Isamu Matsuyama: in my PhD I read your papers with interest and admiration; this admiration has only grown since I got to know you personally. Thanks for

welcoming me to Tucson, tacos and tides are a good mix.

During these years I have been lucky to share my office with excellent researchers who I am proud to call friends. Bas and Teresa, thanks for mentoring and guiding me in the dangerous trade of PhD-ing. Jesse, thanks for all those conversations about soccer (next year Barça will finally make a come-back) and life. I also want to thank the other PhD students of the department: Tim, Jacco, Mao, Yuxin, Haiyang, Gourav, Kartik, Günther, Nick, Dora, Elina, Marie; those cookies and coffee breaks sweetened my weeks. To all the members of the ninth floor of the Aerospace Faculty, thanks for making me feel welcomed and valued.

To my dear friends Lluis and Dani. For some years now we have been pushing each other to try harder and dream further. Space planes, the Moon, quantum physics, the ancient world, the simulation hypothesis, shared books and so much more, you expanded my horizons and fed my curiosity. Thanks for the strolls through Delft, runs, dinners, cafes, board-game nights and the endless conversations about this weird world and the strange profession we have chosen. You made Delft feel like home.

Writing in a room in Brooklyn, I cannot help to think about my family. Dinosaurs, mountains, forests, planets... you never deflected my questions and pushed me to keep asking more and better ones. Because of this, you have seen me grow up in distant countries, but in every word I type your influence is deeply felt. *Gràcies*.

The last words of this thesis are reserved to my wife and daughter, Maria and Rita. Not only has Maria read all the work presented in this thesis in search of of typPos [2] (becoming a world expert on tides in the process), but she has had the patience to endure my pessimism and lighten those cloudy Dutch days. You have seen me grow from high-school student to doctor, you are the "wall where I can lounge" as I walk the endless horizons. Rita, I hope one day you read these pages with wonder and curiosity. No matter how dark it gets, there will always be some beauty waiting to lighten your eyes.

Brooklyn, July 2022 Marc Rovira-Navarro

[2] I wanted to surprise her, so she did not review this part...